Investigation of Porous Metals as Improved Efficiency Regenerators

By:

Erardo Mario Elizondo Luna

A thesis submitted in partial fulfilment of the requirements for the degree of Doctor of Philosophy

The University of Sheffield

Faculty of Engineering

Department of Materials Science and Engineering

March 2016

Acknowledgements

I would like to thank the National Council of Science and Technology of Mexico (CONACyT) for their financial support during this period.

I'm very grateful to my supervisor Dr. Russell Goodall for his guidance, support and encouragement. It has been a great experience working with him, always approachable, dedicating time to discuss my research and experiments, giving valuable suggestions and alternatives to reach an objective.

Special thanks to my supervisor Dr. Robert Woolley for his guidance and advice at different stages during the development of my research; constantly providing suggestions and new ideas to obtain successful results from the experiments that were essential for the completion of this work.

I would like to extend my appreciation to all my colleagues and members of staff at the E-Futures Program, especially Professor Anthony West and Dr. Neil Lowrie for their kindness and generous support. I would like to thank the technical staff, Dr. Lisa Hollands, Mr. Ian Watts, Mr. Kyle Arnold and Mr. Malcolm Nettleship for all their shared experience and assistance.

Thanks to my colleagues Dr. Farzad Barari, Mr. Ahmed Abuserwal, Mr. Francisco Carranza, Mr. Everth Hernandez and Mr. Omar Lopez for their help and suggestions. Thanks as well to my friends in Sheffield, who have given me support and made my PhD experience more enjoyable.

To Dr. Salvador Valtierra, Dr. Mario Gutierrez and Dr. Blanca Esquivel for their recommendation and advice at the beginning of this period in my life.

Finally, I would like to express gratitude to my family, for their understanding and enthusiasm towards my education.

Abstract

In these past few years the subject of porous metals has gained considerable attention. The area of flow and heat transfer behaviour in porous metals used as regenerators is the focus of this work.

A total of 37 porous metal samples have been produced to evaluate their characteristics as regenerators, these include 12 replicated porous metal samples made from commercially pure aluminium using three different NaCl preform particle sizes and two packing methods. The replication method using argon only was improved to become more efficient, tests were done to determine adequate time and temperature for uniform porous metal sample production. In total 4 different protocols (W, X, Y and Z) were developed to produce different levels of porosity (from 61 to 78%) by changing certain variables in the production process.

Other porous metal samples were manufactured with the objective of having a wide range of structures and material comparisons; 7 SS304L wire mesh samples, 3 wire felt samples (Al, Cu and SS304L), to evaluate the effect of pore size, 5 packed sphere samples (Al, AISI 52000 chrome steel, Cu, soda glass and SS420) and 10 additive layer manufactured samples (SS316L and Ti6Al4V) to evaluate the effect of material and porosity levels.

All the samples were tested on pressure drop and heat transfer capabilities, they were compared with the literature using Reynolds and Stanton numbers, the thermal conductivity was also measured, a characteristic that had to be estimated in previous work due to a lack of an experimental test rig, which was developed during this research.

It was found that the best performing ones were the stainless steel wire meshes, the wire felts and the replicated porous metals. Several correlations involving pore size, porosity and material effects were proposed as an aid for designing regenerators obtained from the experimental results. The replicated porous metals have the potential of being used as regenerators if they can be made from high efficiency materials and of a smaller pore size than the ones discussed here, their advantage is that they may be modified to a large range of specifications, being able to replicate the behaviour of other structures.

Table of Contents

Nomenclature

Uppercase Letters

A_{CS}	Cross section area
A_{HT}	Heat transfer or surface area
A_{Sp}	Specific surface area
C	Form drag coefficient
D_0	Insulation transversal length
D_H	Hydraulic diameter
$\mathrm{D_P}$	Pore/Particle diameter
D_R	Regenerator diameter
D_W	Wire diameter
K	Permeability
L	Length
L_1	Upper aluminium piece length
L_2	Lower aluminium piece length
L_C	Characteristic length
L_R	Regenerator length
N	Coordination number
N_{Sph}	Number of Spheres
NTU_R	Regenerator number of transfer units
NTU_W	Wall number of transfer units
Pr	Prandtl number
Q	Heat
Q_C	Heat lost
Q_H	Heat gained
Re	Reynolds number
Re_K	Permeability based Reynolds number
R_{tc}	Regenerator heat capacity to wall heat capacity ratio
St	Stanton number
T_0	Initial temperature
T_a	Adimensional temperature
T_{Air}	Air temperature
T_C	Cold temperature
T_{Ex}	External insulation temperature
T_H	Hot temperature
T_R	Regenerator temperature
V	Volume
V_1	Compressed gas volume
V_2	Expanded gas volume
V_M	Material volume
V_P	Pore volume
V_R	Regenerator or bulk volume
X	Tortuosity

Lowercase Letters

a	Constant
b	Constant

c	Constant
c_{Air}	Air specific heat
c_M	Material specific heat
c_R	Regenerator specific heat
d	Representative unit cell dimension
d_w	Window diameter
h	Convective heat transfer coefficient
i	Instant value in x axis (Crank-Nicolson)
k	Thermal conductivity
k_{Al}	Aluminium thermal conductivity
k_{In}	Insulation material thermal conductivity
k_M	Material thermal conductivity
k_R	Regenerator thermal conductivity
l	Instant value in y axis (Crank-Nicolson)
m_M	Material mass
$\dot{m}$	Mass flow rate
$\dot{m}_{Air}$	Air mass flow rate
r	Radius
t	Time
t_a	Adimensional time
v_D	Superficial velocity
v_ε	Velocity through the pores
x	Independent variable distance
x_a	Adimensional distance
y	Dependent variable distance

Greek Letters

γ	Surface tension
ΔP	Pressure drop
Δx	Distance difference
δi	Diffusion number
ε	Porosity
ε_0	Random packing density
η	Regenerator efficiency
λ_R	Regenerator dimensionless thermal conductivity
λ_W	Wall dimensionless thermal conductivity
μ	Fluid absolute viscosity
π	Pi value (3.141592)
ρ	Density
ρ_M	True density or material density
ρ_R	Regenerator or bulk density
Φ	Wire mesh shape factor
ψ	Inlet temperature response time

Other Symbols

$!$	Factorial
∂	Partial derivative

Chapter 1. Introduction

Porous metal production and research has been gaining in popularity since the first efforts on the replication process came to light in the 60s [1], particularly in the last 15 years; research is summarised in reviews such as those of Banhart [2], Conde [3] or Goodall and Mortensen [4]. Notable development work in this area has been done in Professor Mortensen's group at the Ecole Polytechnique Federale de Lausanne in Switzerland.

Within the techniques for producing porous metals, replication is one of the most experimentally direct and simple, offering a significant level of structural control over the porous metal. In research, the materials produced by replication are commonly characterised as porous metals, sponges or microcellular metals.

The method involves the shaping of a metal by driving it in the liquid state into the free space of a “preform” made from particles of a solid space holder material that defines the form of the resulting porous metal [3], [5]. After cooling and solidifying the metal the elimination of the preform material takes place by dissolution or oxidation. A common space holder for aluminium [6]-[10] or aluminium alloy [11]-[14] porous samples is a group of NaCl particles. It has convenient characteristics such as being easily obtainable, non-toxic, dissolves in water, and has a relatively high melting point (801°C) so it can be used with metals that have a lower melting temperatures. If other types of materials are used as space holders it is possible to produce porous metals with even higher melting points [15].

In this study the equipment and experimental steps to be followed for the production of porous metals by the replication technique are presented. These steps are fairly simple to apply in a laboratory; in other research groups further variants of the same procedure can be found, using different machinery. For successful development however, a good grasp of the individual technique and equipment to be used is indispensable. The porous metals obtained will be tested for their heat transfer performance as regenerators.

The regenerator was developed in 1816, it was made as part of the Stirling engine, which operates on the basis of heat transfer, producing output energy from a difference in temperature [16], [17].

In Figure 1.1 a two piston Stirling engine can be seen, it should be noted that this is one of many configurations or arrangements for this type of engine. In this example a V type engine with both pistons connected to one crankshaft is shown. The spaces above the pistons are connected by a pipe in which the regenerator sits in the middle [17].

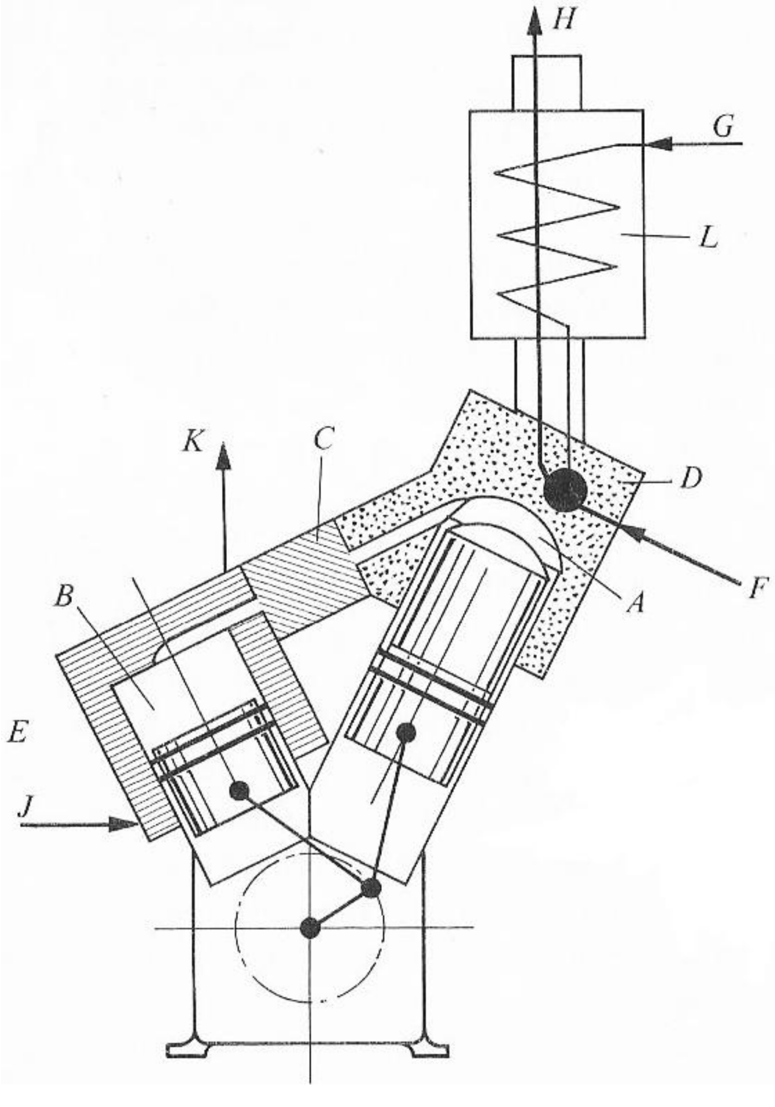

Figure 1.1 - Stirling engine diagram. A - Space for expansion, B - Space for compression, C - regenerator, D - heater, E - cooler, F - fuel inlet, G - air inlet, H - exhaust products of combustion, J - water inlet, K - water outlet, L - exhaust-gas inlet-air preheater [17].

Current manufacturing technology allows us to build regenerators that cooperate to obtain efficiencies that resemble the calculated ones. Porous metals are a relatively new option that helps achieve this objective. These porous metals have a significant amount of interconnected voids, which may allow fluid flow through it; having a large surface area, and in combination with specific metal characteristics such as heat capacity and thermal conductivity makes them a considerable element to transfer heat from and to fluids. The knowledge of the function the interconnected pore structure has on the fluid properties that passes through a porous material is essential for many industry processes involving different fields such as engineering, chemistry and/or geology. It is needed to model or predict the effect of the structure on the fluid flow reducing the full complexity of the structure to a reasonable number of parameters. Three of the most important structural characteristics of a porous material are surface area, porosity and pore size [18].

The purpose of a regenerator can be explained with reference to a Stirling engine. The essential role is to better the effectiveness of the cycle, to achieve this it employs a heat exchanger; many engines use them, however, a good heat exchanger cannot enhance an engine with other defects. The parts forming a Stirling engine are a heater, the regenerator, a cooler and an inlet air preheater [19].

The Stirling engine may work with a reversed cycle, acting as a refrigerator (a mode of operation where work is used to create a temperature difference), the terms then change since the engine is now working to reduce the temperature instead of increasing it; the previously mentioned "heater" is now a "freezer" and the "preheater" becomes the "precooler". If the engine is used as a heat pump the terms change once more; the heat pump increases the temperature of the received heat using work; the heater becomes the ‘absorber’ and the cooler is now the ‘heater’.

The regenerator acts as a simple heat exchanger; it receives the energy from the working fluid when it moves through it from the hot to the cold side; the regenerator precools the fluid; in the second half of the cycle the regenerator discharges the heat within to the working fluid passing the other way, from the cold to the hot side, the regenerator preheats the fluid.

Regenerators are also used in other applications such as in blast furnaces; in which the exhaust fumes at high temperature travel through ceramic bricks, capturing the heat, then when the cycle is inverted the fuel is preheated while passing the bricks; this furnace is known as the open hearth furnace or Siemens - Martin regenerative furnace, invented in the 1860's to produce steel [20].

At the moment there is no set of established rules for regenerator design, however, there are several conflicting requirements to answer for them to work effectively. In the Table 1.1 the ideal characteristics for a regenerator are shown, the relative importance between them is not known [19], [85], [115].

REQUIREMENT	REASON	HOW TO OBTAIN
Maximum heat capacity	The matrix needs to capture the largest amount of energy available to make the process more efficient.	There needs to be a large and solid element.
Minimum flow resistance	When the working fluid passes the matrix the opposition to the flow should be minimum.	There needs to be a small element with a high porosity.
Minimum dead space	The volume of working space should be as small as possible.	There needs to be a small element with low porosity
Maximum heat transfer	To obtain the maximum heat transfer the element must have a high surface area.	There needs to be a large matrix with very fine struts.
Minimum contamination build up	The working fluid must be free from any impurities, preventing blockage.	There needs to be a matrix that offers no obstruction to the flow.
Minimum thermal conductivity	The matrix needs to prevent energy travel through itself to make the process more efficient.	The element needs to be made from a material that does not conduct heat.

Table 1.1 - Ideal regenerator design requirements.

A typical regenerator is made from a porous matrix that allows the working fluid to pass through it, usually made from a material that is resistant to corrosion and high temperatures, wire meshes are currently used as regenerators, porous metals can also be used for this purpose; they have an advantage over wire meshes in that they can be tailored to many different shapes and a wide array of porosities, the challenge lies in producing the best structure for the purpose, it must have a high heat transfer area and provoke the less possible pressure drop when the fluid passes through it.

The main objective for this work is to compare the characteristics of replicated porous aluminium samples as regenerators with other alternative structures available, making it possible to select the best structure for this purpose, as well as evaluating the advantages and disadvantages of each. As different structures are not all available in the same metal or alloy, it was also necessary to explore the dependency of performance of the material in isolation of structural changes.

As the primary processing method used in the laboratory for porous aluminium production, the space holder or replication technique was examined, evaluated and upgraded. Three different pore sizes of porous aluminium samples were produced (controlled by the size of the space holder particles) and two packing methods of the space holder were used (random and vibrated). These were compared with existing and commercially-available regenerator structures or alternative porous metal candidates, such as; packed beds of ball bearings made from different materials (stainless steel, chrome steel, copper, aluminium and soda glass); felt-like samples made from pressed short wires of three different materials (stainless steel, copper and aluminium); stainless steel wire mesh samples of different pore apertures; and stainless steel and Ti6Al4V samples produced by additive manufacturing.

This thesis consists of 9 chapters, introduction in this present one, Chapters 2, 3 and 4 cover relevant parts of the literature and Chapter 5 gives the experimental procedures used. Since there were significant further developments of the porous aluminium processing technique during the work described in this thesis, relevant results are reported and discussed in Chapter 6, after that, the focus is on the performance of porous aluminium samples and comparable materials for regenerator purposes, Chapter 7 discusses the flow test results and Chapter 8 gives the heat transfer results, in both these chapters the performance results are discussed as well, conclusions are drawn about the relative performance of different porous structures and the metals from which they are made in Chapter 9.

Chapter 2. Processing of Porous Metals

2.1. Porous Materials

A porous material is a material that has many free spaces in its structure, they are called voids or pores. The pore sizes vary from a few nanometres to many millimetres, the size is dependent on the porous material's purpose. They can be made from organic materials, polymers, metals or ceramics. For example in the natural world they exist as trees, bone structures and beehives, to name a few. They permit an elevated strength to weight ratio, reducing localised stress, to prevent potential collapse in the structure. In engineering a homogeneous material is often preferred, however in the natural world the reverse effect happens, meaning that the pores are of different sizes in the same structure, this is defined as porosity gradation [3], [18], [21], [22].

The most common terms used in this particular area of porous materials are: true density, which is the density of a material not including pores or voids; bulk density is the density of a material including open pores and voids; pore volume is the addition of the volumes of the individual pores; pore size is the distance between the walls of the pore, its width or diameter; porosity is the relationship between the total pore volume to the apparent volume of the sample or particle and finally surface area, which is the area of solid surface of the material. The equations are presented in Table 2.1.

Term	**Equation (Units)**
True Density	$\rho_M = \frac{m_M}{V_M}$ (kg/m^3)
Bulk Density	$\rho_R = \frac{m_M}{V_R}$ (kg/m^3)
Pore Volume	$V_P = V_R - V_M$ (m^3)
Porosity	$\varepsilon = \frac{V_P}{V_R}$ (adimensional)
Surface Area (dependent on shape) (sphere as example) Or Heat Transfer Area (for this work)	$A_{HT} = 4\pi r^2$ (m^2)
Specific Surface Area	$A_{Sp} = \frac{A_{HT}}{V_R}$

Table 2.1 - Common equations used in the area of porous materials.

The characterisation of a porous material is dependent on the pore size according to IUPAC (International Union of Pure and Applied Chemistry); Roquerol and Liu mention three classifications: microporous, mesoporous and macroporous materials, their definitions follow [23], [24].

A *microporous material* has a pore size smaller than 2 nm; an example would be in the medical profession, making tapes for wound cover to prevent bacterial infection but still allowing air passage to provide a sterile environment [25].

A *mesoporous material* has a pore size in between 2 and 50 nm; example applications are in low bulk silica particles, zeolites, sieves, solar energy capture. They are used in catalysis, separation, adsorption and as hosts for certain molecules due to their uniform pore sizes [26].

A *macroporous material* has a pore size larger than 50 nm; commonly used for filters, anode material for fuel cells, stationary phases for different types of chromatography, bioreactors, microfluidic chips, filtering and heat transfer applications [27]. In this work, this type of material is used for a heat transfer application, the regenerator.

After defining the general characteristics of porous materials the focus in the next section is only for porous metals, which is the main interest of this work.

2.2. Porous Metals

The porous metals produced in this work are in the macroporous materials group. Previously a metal containing pores in its structure was considered to be defective, it was discarded since it was not acceptable for engineering applications. Currently the concept has changed due to the porous metals' specific mechanical and physical properties which cannot be obtained in other materials [27].

One of the key advantages of porous metals when compared to bulk and porous structures separately are that they can use certain properties from both groups, making a compound material with several properties of bulk metals, such as their heat capacity, malleability, ductility, thermal and / or electrical conductivity, and properties from porous structures, such as permeability, reduced weight and relatively high structural strength when the low density is accounted for.

These characteristics can be combined to produce a material with a high heat capacity and be permeable to a fluid, a heat exchanger; or a material with a high stress resistance with low weight, an automotive impact protector, to give two examples. The properties of the porous metal can be easily modified to accommodate both groups of properties from the solid and the porous structure.

A porous metal is generally considered as such when, apart from the solid, it includes another phase (liquid, gas) that is distributed throughout all its structure. These regions including the second phase are called cells, voids or pores. The structure surrounding the pore is the actual metal; this structure, depending on its shape is named a strut if its thickness is smaller than the pore, or wall if its larger, a micrograph can be seen in Figure 2.1.

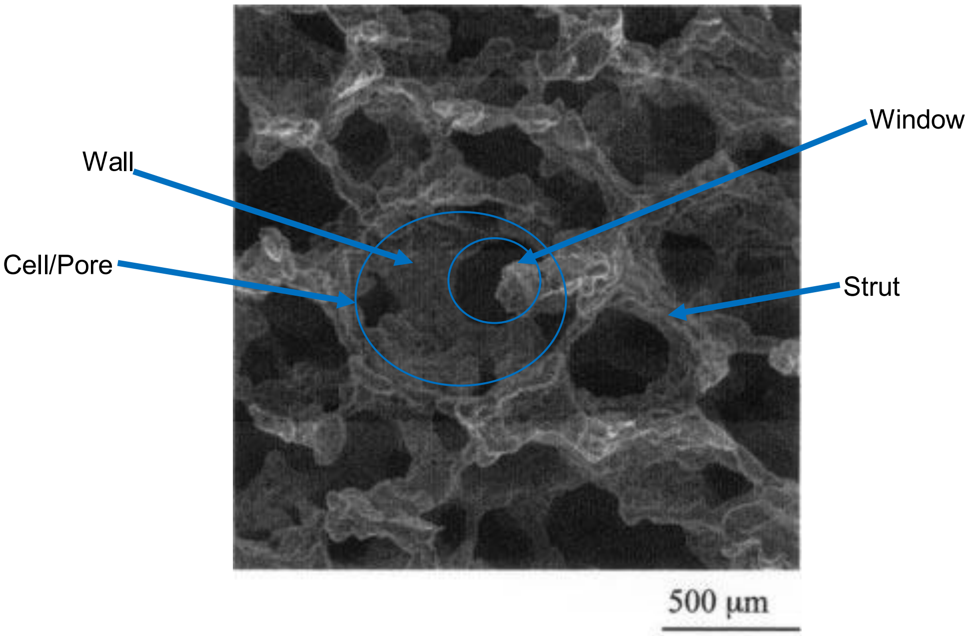

Figure 2.1 - Typical characteristics of a porous metal structure [28].

If there is a limited value of cells, most of them will be independent from one another and contained as pockets surrounded by metal, this is a closed cell structure aptly called a porous metal. If the pore fraction in the sample increases, there will be a time when they will converge with each other, producing a chain of free space that reaches the external surroundings; this is an open cell structure and may be called a metal sponge [18], [29].

In determining the properties of a porous metal the two most important factors are the solid metal it is made from and its structural shape. Within the structural shape a simple identification would be if the porous metal has open cells or closed cells.

To determine the volume fraction of the solid a measurement of the mass and volume has to be done, knowing the density of the metal the porosity can be obtained. To know the cell size, 2D image analysis may be done on images obtained from optical or electron microscopy [30] or for 3D images X-ray tomography is used [31]. The values obtained from these can be considered an average for the sample, though residual porosity may be present if the limit of the equipment is exceeded, for example, cells smaller than the minimum detection limit of the equipment will not be quantified in the results.

Porous metals can be manufactured with two different types of cells in the structure, open cell, closed cell or it can be a combination of the two types. In open cell porous metals there is a network of interconnected beams or columns permitting liquid or gas to flow through it [18], [21]. Its counterpart, the closed cell porous metal, is built by a network of interconnected neighbouring impenetrable pores. Their characteristics allow them to be employed in different situations; the open cell porous metal is used basically in heat transfer and filtering applications, while the closed cell porous metal is used in structural applications like impact absorption or the construction industry.

Their advantages compared to non metallic porous samples is their stiffness, ability to tolerate high temperatures and more resistant to certain environmental conditions. Compared to solid metals, porous metals can have an elevated specific stiffness (stiffness to weight ratio) especially for bending and their structure can be altered in a myriad of ways (size, shape, porosity, cell size) to meet the demands of a preferred application.

Next the focus will be on the different options available for porous metal manufacturing.

2.3. Porous Metal Production

In the development of porous metals a classification commonly used for processing techniques is by the state of matter in which the sample is built. For example when foaming a liquid metal by injecting gas or mixing it with gas releasing compounds such as titanium hydride, calcium carbonate or lithium borohydride, the product exits the manufacturing with mostly round pores usually due to the bubbles originated from the gas.

Other processes include investment casting, using a space holder to give the desired free space to the sample or the sintering of certain mixes that can include metal powders with polymers. To make porous metals with very high porosities electrochemical deposition may be used, as well as metal vapour deposition [2].

After reviewing their properties the different ways to produce porous metals are discussed. In Figure 2.2 a diagram of the different ways to produce a porous metal is shown [2]. In the following sections a detailed explanation of certain of these methods is presented.

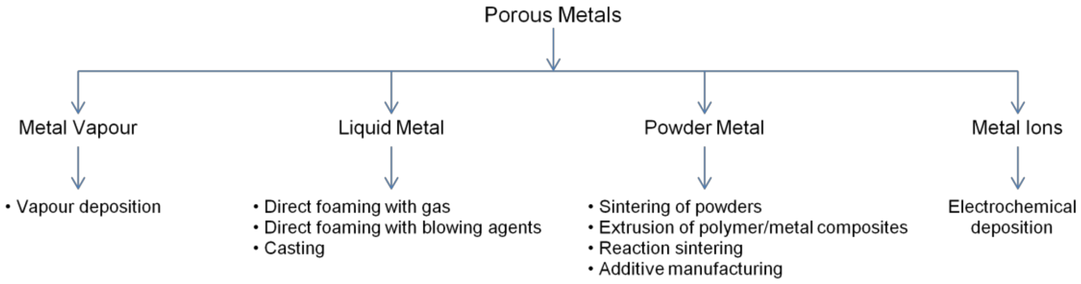

Figure 2.2 - An outline of several porous metal production techniques.

2.3.1. General Production Methods

2.3.1.1. Foaming

It takes place when a compound that reacts with heat is added to the molten metal, this material decomposes and produces gas which causes the metal to expand, the bubble created by the compound bursts, giving way to the pore. On occasion a mixer is used to reduce the processing time and to produce smaller bubbles. This technique makes closed cell porous metals with an elevated porosity.

A way to produce porous metals with blowing agents is by adding calcium metal to the molten aluminium at 680°C, agitating it to increase the viscosity through producing various compounds (calcium oxides, calcium-based intermetallics). After this, titanium hydride (the blowing agent) is added to the mix, releasing hydrogen gas to the liquid metal and causing expansion of the melt, before cooling to solidify the aluminium. The process can be made more effective if it is carried out in an enclosed volume as the material can be made to expand until this volume is filled. Then the sample may be removed and any final machining steps carried out [32].

Another alternative to adding a foaming compound is to inject gas into the molten metal; this technique is used by two companies, Hydro Aluminium in Norway (www.hydro.com) and Cymat Aluminium in Canada (www.cymat.com). Their process consists of first adding silicon carbide, aluminium oxide or magnesium oxide particles to increase the viscosity of the mixture. The liquid is then foamed in the next stage by directly injecting a gas into it (which could be air, nitrogen or argon) using appropriately built mixers to create the fine bubbles which are needed to produce a high quality porous metal. The combination of bubbles and melted aluminium rises to the surface of the liquid, turning into a dry porous structure as the metal solidifies and the molten metal drains from it. Then it is moved out of the surface by a conveyor belt permitting its solidification. The porous metal is then levelled out by a couple of rolls producing closed skins at the top and bottom. Aluminium alloys have also been used, such as AlSi10Mg and wrought alloys 1060, 3003, 6016 or 6061 [33], [34].

The reported porosity obtained for this type of porous metal can start at around 80% and be as high as 98% and the cell size can be from 3 mm up to 25 mm. The wall thickness and density are directly related, they both are inversely related to the extent of the voids. These parameters can be affected by the modification of the gas feed rate and the impeller velocity [34].

Some of the advantages of direct foaming are the low densities and the amount of porous metal that can be produced. Two disadvantages of direct foaming is that at some point the porous metal needs to be split (the production is continuous), damaging the cells locally and that it is quite brittle because of the addition of ceramic material required to stabilise the pores in the liquid.

2.3.1.2. Gas-Eutectic Transformation

Another option to create a porous metal is with a metal - hydrogen system; the molten metal is mixed with hydrogen gas until the objective composition is met then the liquid metal solidifies. The porosity obtained is similar to that provided by the infiltration method, which is approximately 70% [21].

2.3.1.3. ***Compacting with a Foaming Agent***

To make a sintered porous metal the heat needed for the operation does not have to be obtained from an external source, they can be formed using the energy released from the reaction of the mixing powders.

To compact the powders together there are several methods available, isostatic or uniaxial pressing, rod extrusion or powder rolling. When the heat treatment is due the time it is applied depends on the temperature reached; it ranges between a few seconds to several minutes; the heat causes the agent's reaction, inducing bubbling that gives way to the pores in the metal [42].

This technique is used when porous alloys and / or intermetallics are needed, usually to obtain a porous structure from materials with high melting points. The exothermic reaction speeds up as it progresses through the large surface area of the sample, this method is called Self - propagating High - temperature Synthesis or SHS [43], and has been used to produce NiAl and NiTi alloys.

2.3.1.4. ***Co-compaction of Powders of Two Materials, One Leachable***

in this method two powders (usually metal and NaCl) are mixed together and compacted. The NaCl is acting as a space holder. After the powders merge the NaCl is eliminated from the mixture using water. The range of densities obtained with this method is between 30 to 50% of the full density, and the cell size depends on the particle size used, which can vary from 10 µm to 10 mm [21].

2.3.1.5. Powder Sintering

To produce a porous metal sample from powder, it is pressed to form a tight compact and then sintered to join the particles together, diminishing the pore fraction. To achieve a porous metal by sintering the process needs to be stopped at a certain time before the sample is fully dense. This process has succeeded with copper [38], titanium [39] and steels [40]. Using porous titanium, samples have been made with large particles (from 0.18 mm to 2 mm) to increase the porosity [41] as the particle surface area, and driving force for sintering are reduced.

The sintered material is similar to expected shapes of solid materials, like castings, forgings and several manufactured forms. This method is used to create bonds between small granules of materials by applying heat. On occasion a preform can be used in conjunction to give a certain space between the particles, decomposing during the heat treatment, carbamide is commonly used. The difference with the previous method is that the preform is not leachable, it eliminates with the heat.

This process is a very complex one, due to the fact that it has many variables depending on the material that is to be sintered; changes with sintering can happen at the same time or one after the other. Some of these may be particular to porous materials, others may be common to any polycrystalline material exposed to high temperatures. The impact, economically speaking, of a powder metallurgy process is dependent on the inherent changes that the process produces, such as in the structure. It has to be considered that the material has two phases, porosity and solid material. Considering that each has its own characteristics, such as size, form, distribution and quantity.

Apart from the joining of grains, this procedure is useful to achieve different goals, including: creating alloys, giving a heat treatment to a metal, bonding materials and / or increasing their density, which happens with almost all of the different types of sintering. Even though the opposite can be achieved, growth or no dimensional change, this is particularly preferred in most commercial applications [42].

Within sintering two variants can be identified. The first one is hot pressing; this is a process in which the powder aggregate is affected by an elevated heat source and additional pressure; as with all sintering the heat source should not be as high to reach the powder's melting point. Sintering is a solid state process since no liquids are involved. It is most commonly used for ceramics and refractory metals.

In liquid phase sintering the heat applied is sufficient to melt one or more of the elements present in the powder composed of powders of multiple materials. This then flows into the pores of the powder and may alloy with the other compounds returning to a solid. This process is used to obtain high densities in a compound. In fibre metallurgy metal fibres are employed instead of powder, the porosity is highly variable as it depends on the amount of material used. The fibres can be made by machining or melt spinning, and then they are compacted and / or sintered; an additional coating could be included to improve attachment between them. If fibres are used the porosity in the powder compact can be greatly augmented, while liquid phase sintering ensures good bond strength between fibres [18], [24].

Stages in Sintering

A key characteristic of the sintering process is that it occurs at a fixed temperature; of course there is the option to change the times of the process to obtain different results. Considering this it would be helpful to explain the conditions in which sintering happens time wise. Since there are many variations in the whole process it will be handled in general terms. In Figure 2.3 the stages are shown.

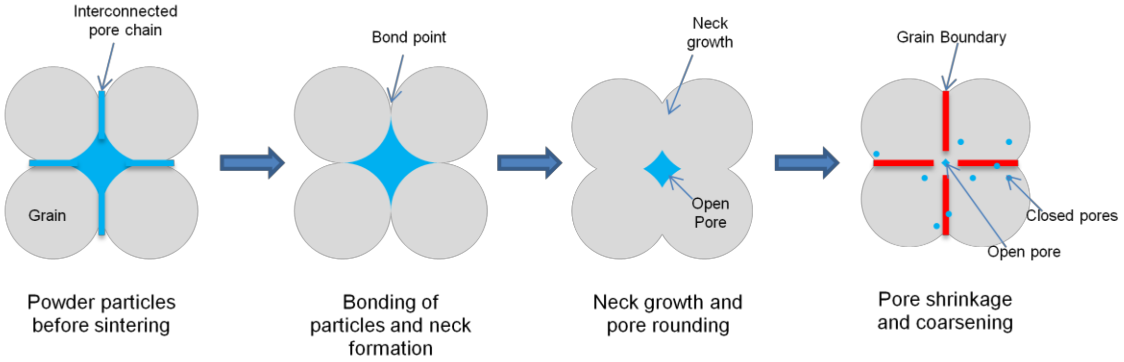

Figure 2.3 - Time lapse of powder particles during the sintering process.

1) *Bonding*

It happens as the thermal energy allows the material to create grain boundaries. This occurs in those places where there is close contact between particles. Most of the process occurs during heating before reaching the desired sintering temperature. In this stage there are no changes in the dimension of the sample but there are changes within it such as the consistency and inner connections [44].

2) *Neck Growth*

The new connecting areas are called necks; the necks get larger as the material is exposed to the high heat, meaning a higher amount of association between the material, it does not reduce the porosity as the size remains the same, nor does it affect the interconnectivity of the porosity [42].

3) *Pore Channel Closure*

This corresponds to a large change in the porosity of the sample, obstructing the interconnected pathways, producing closed and disconnected pores. This is an extremely significant change if the original interest is to have a fluid flow through the mass, such as in filtering [45].

4) *Pore Rounding*

This is a natural result of neck growth, it happens when material at the surface of the pore migrates to the neck regions, causing the pore to be remodelled into a more rounded version. This occurs to isolated and interconnecting pores alike, leaning more to the isolated ones [45].

5) *Pore Shrinkage*

This is considered the most significant stage out of the six; however it is encountered at long times. It depends mostly on the time that the powder is exposed to the high heat, making the sample denser. It includes movement from the solid portion of the material into the cavities and motion from the gas in the pore to the outside surfaces [46].

6) *Pore Coarsening*

If it occurs, it happens after all the other stages have finished. It consists of the decrease and removal of tiny separated pores and the increase in size of bigger ones. This causes a growth in size of the pores and a lesser number of them. There is no increase in density in this stage [44].

Variables in the Sintering Process [42], [47]

1) Particle Size

If the particle size is diminished the sintering rate is increased, due to the abundant surface in the whole mass.

2) *Particle Shape*

If more irregular shaped particles are used, the surface roughness increases, diminishing the performance of the sintering process.

3) *Particle Structure*

A sheer grain structure is needed to help the sintering process; it has a good result on various transport mechanisms. If there are more lattice imperfections, for example dislocations, there may be a benefit to the sintering process by enhancing the rate of certain diffusion processes.

4) *Particle Composition*

Sintering can be influenced by addition of alloys or contaminants in a metal, increasing or decreasing the rate. Surface impurities or oxidation are not advantageous to the process.

5) *Green Density*

If this characteristic decreases it means a higher quantity of internal surface area and a larger driving force, consequently better sintering. However high green density improves the ease of handling pre-sintering.

6) *Temperature*

Sintering is very dependent on this characteristic. If there is an increase in temperature the speed and degree of any changes happening also increases.

The transport mechanism controlling the sintering may change with different temperatures.

7) *Time*

It is not as meaningful when you compare this characteristic to the temperature. The sintering rate decreases with time. As time progresses the driving force from the process is reduced and it becomes harder to eliminate all of the porosity by sintering. One of the important parameters about time is the economics of the procedure; a lengthier time uses more energy, increasing the cost of finished product [18].

2.3.1.6. The Sintering Dissolution Process

When pressing and sintering does not achieve the desired porosity, the cell size is not large enough for a certain application or a better control over the procedure is required, one can resort to the space holder method. The use of a space holder, creating an extra stage in the process, includes using another type of material acting as a volume occupier that in the end, after removing it, will leave an empty space in the processed metal. The general process is shown in Figure 2.4, metal powder and space holder particles are mixed, pressed and eliminated before sintering takes place. This procedure increases green body strength and compaction making it viable to shape the part before sintering to avoid damaging the cell structure [48].

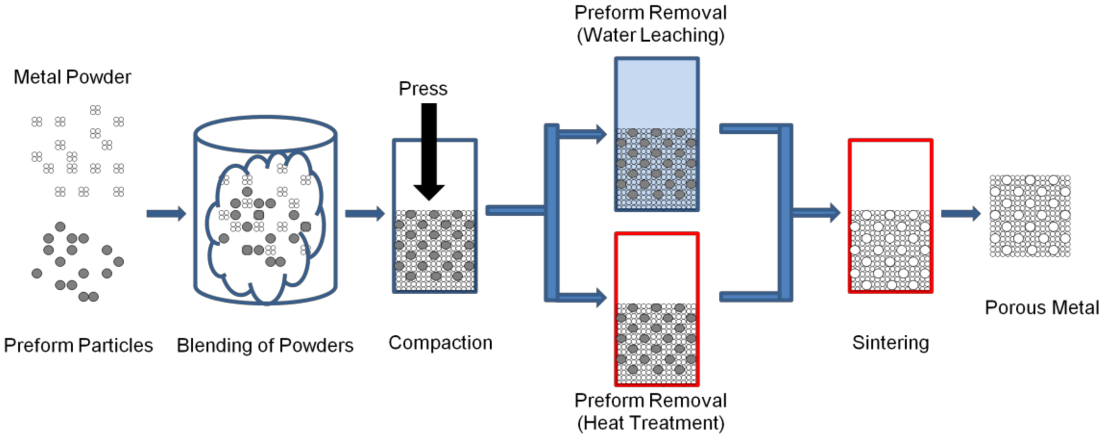

Figure 2.4 - The Sintering Dissolution Process.

This is one of the original techniques to produce a porous metal using aluminium powder and NaCl powder mixture as metal and space holder. In this method the mix temperature is elevated to work around the melting point of aluminium (660°C) and well under the melting point of the NaCl (801°C); the sintering time may vary from 2.5 to 50 hours, depending on the mixture type and sample size [49].

The operating temperature should be kept lower than 680°C to avoid the separation of the aluminium from the compound; the space holder is removed by water leaching, ending up with the porous aluminium [28]. In this work the porous metals have a range of porosities from 45 to 83% and a pore size range from 0.3 mm to 1.0 mm, taking up to six hours for the sintering process to complete.

In the space holder removal phase of the process, special care needs to be taken if the desired porosity of the porous metal will be under 60%, as it has been found by Zhao that NaCl particles may be almost completely surrounded by aluminium and remain, the water leaching time must be increased [28].

In some cases the addition of magnesium and tin to the compact can help the sintering step, reducing the oxide layer [50].

Titanium has been used [51], producing porous samples with low porosity range between 20 and 53%, higher porosities are achievable, however the pores are much larger and are difficult to vary in size. Steels have also been produced [52], achieving high porosities (≈ 70%), some samples include micro porosities, which is not desirable for many applications, by adding boron to them they aim to eliminate it.

2.3.1.7. Sintering with Other Space Holders

When using other space holders, they can be removed before or during the start of sintering. In some cases carbamide (in the form of spheres or flakes) is used as a space holder [18], like NaCl it may be leached before starting the sintering process [53]. Using ammonium hydrogen may require that the leaching stage in the previous process to be included in the sintering stage [54]. These space holders are used to make porous structures with materials of higher melting temperatures, certain steel alloys, titanium and copper porous samples have been produced.

For titanium and titanium alloy porous structures the space holder materials that are commonly used are NaCl [55], carbamide [31] and magnesium particles [56].

Other space holders apart from NaCl have been used, such as carbamide (CH_4N_2O) and ammonium bicarbonate (NH_5CO_3). In some processes these compounds are not removed from the compact by dissolving them, instead, they are eliminated by heat treatments at somewhat low temperatures (around 200°C) before the sintering step, or at its initial stage. The purpose of using these materials as space holders is to obtain porous metals with higher melting points, which require more support during sintering. Some of the samples produced with these space holders are made from titanium [31], stainless steel [57] and copper [58].

The use of carbamide is not exclusive to higher melting point metals, it has also been used as a space holder with lower melting point metals such as aluminium [59] and magnesium [60]. It can also be removed by washing it away with water in certain stainless steel porous samples [52]. The shape of the porous metals' pores depends on the shape of the space holder, most commonly they are available as spheres or irregular shapes [61].

Another material used as a space holder is potassium carbonate, K_2CO_3. This compound can be eliminated completely from the porous metal by heat treatment, leaching is not required. It breaks down when it reaches a temperature of 891°C. It is used to produce high melting point porous metals, like copper [62] or iron [63].

For high temperature applications porous metals have been produced out of Nickel - Titanium alloys using cold pressed powders only [64], the average porosity obtained was in the range of 40% and grain size range between 50 μm and 200 μm showing very good super elasticity and a symmetric pore distribution. By adding NaCl [65] and sintering the compound afterwards.

Another alloy used to make porous structures using an NaCl space holder is stainless steel - chrome - molybdenum [66]. The range of porosities obtained was from 40 to 58%, relatively low, with interconnected pores in a size range of 25 µm to 200 µm given by the space left by the NaCl particles after sintering; the powder grain size ranged from 18 µm to 22 µm, these porous metals have high mechanical energy absorption due to the material's high ductility.

When the powders are sintered without a space holder the porosity tends to be low, on average 35%. When the NaCl space holder is used the porosity may be increased by the size and abundance of the granules; however, this technique will introduce two pore sizes in the sample.

Polymers and binders have also been used as space holders. They are used to keep the shape of the powder (free space) until the sintering step, producing the desired part [67]. Nonetheless, this technique prevents precise control over the pore size and shape, since the polymers are significantly weaker than the metal. Metal Injection Moulding may be used to conform powders for sintering, making it a viable technique for porous metal manufacturing [68]. An alloy that is commonly used with this method is Ti6Al4V with poly methyl methacrylate (PMMA) acting as a space holder [69], stainless steel porous samples have also been made using PMMA space holders [70]. The PMMA space holder is removed from the porous metal while increasing the temperature during the sintering process.

2.3.1.8. Freeze Casting

An alternative to adding the preform to the powders while mixing or using PMMA is to make space holder particles in-situ, this is where freeze casting is used. This technique has been applied to titanium [71] and stainless steel [72]. A suspension of metal powder and water is made, then chilled uniaxially below freezing temperatures. When the water freezes, it pushes the powder particles away, joining them, thus acting as the space holder. The preform is then eliminated by sublimation, creating the voids in the porous metal, between the powder grains. Then sintering gives the grains the close-knit structural strength. This process creates a sample with high anisotropy [71].

2.3.1.9. Gas Entrapment

Another technique to produce porous metals is gas entrapment. Gas pressure is used to expand the frames composed by powder, one of the conditions is that the process occurs at very high temperatures; another, that the metal or alloy has to be highly deformed [73]. Titanium and nickel - titanium alloys are commonly used, the porosities achieved by this method are on average 57%. This is a relatively low porosity and initially pores were found to be closed, open pores were created by changing the pressure in the final stages of sintering, increasing the porosity due to the material's ductility.

The procedure happens as follows, the metal or alloy powder is compacted within an inert gas (usually argon), the gas accommodates itself within the voids, which become isolated voids. Vacuum sintering takes place making connections between the powder grains and broadening the cells due to the argon's pressure [74]. The diagram of the process can be seen in Figure 2.5.

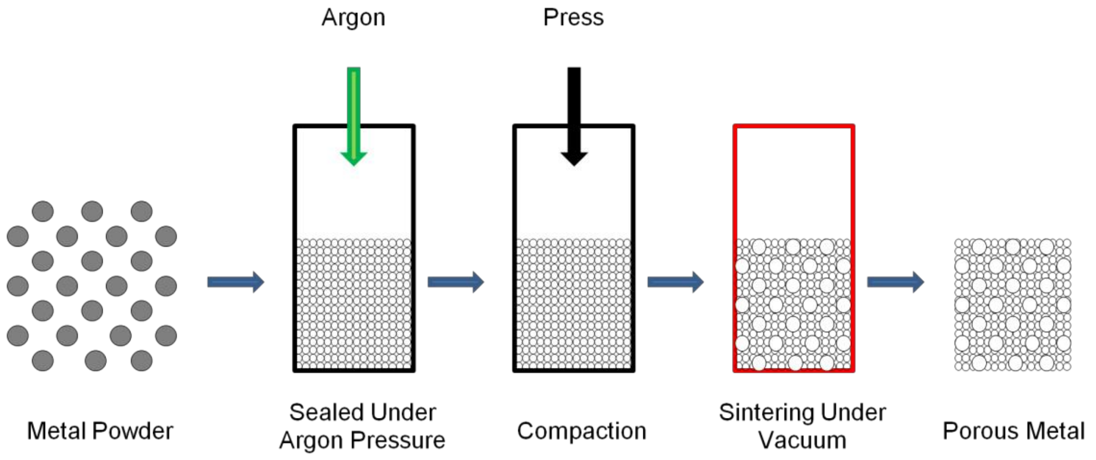

Figure 2.5 - The Gas Entrapment Process.

With this technique the shape of the porous metal can be modified. If a uniaxial force is applied to the sample during the pores' growth, it can hold it in place, causing the cells to be regulated [75]. If heating and cooling periods are applied the boundaries between the voids may disappear, increasing porosity [76].

2.3.1.10. Additive Layer Manufacturing

A newer porous metal producing technique is Additive Layer Manufacturing (ALM). The previous methods mentioned generate pores that are arbitrary, they are uncertain in size, pattern and region. With ALM it is completely different, since the sample outcome is based on a 3D image created by computer aided design (CAD) and produced into the desired part. Notable companies producing this type of equipment are Renishaw (www.renishaw.com) and Arcam (www.arcam.com). In the process the machine interprets the image file uploaded into layers. In Selective Laser Melting (SLM) metal powder is fed onto a manufacturing surface creating a layer.

According to the CAD file, a concentrated heat source, such as a laser beam, melts the granules of powder which are to be part of the final solid shape. The manufacturing surface is then moved downward and another powder layer is placed on top, repeating the process until the final sample is completed The schematic for the procedure can be seen in Figure 2.6. The unused powder is sieved and recycled. The materials that are commonly used in this process are titanium and stainless steel 316L [77].

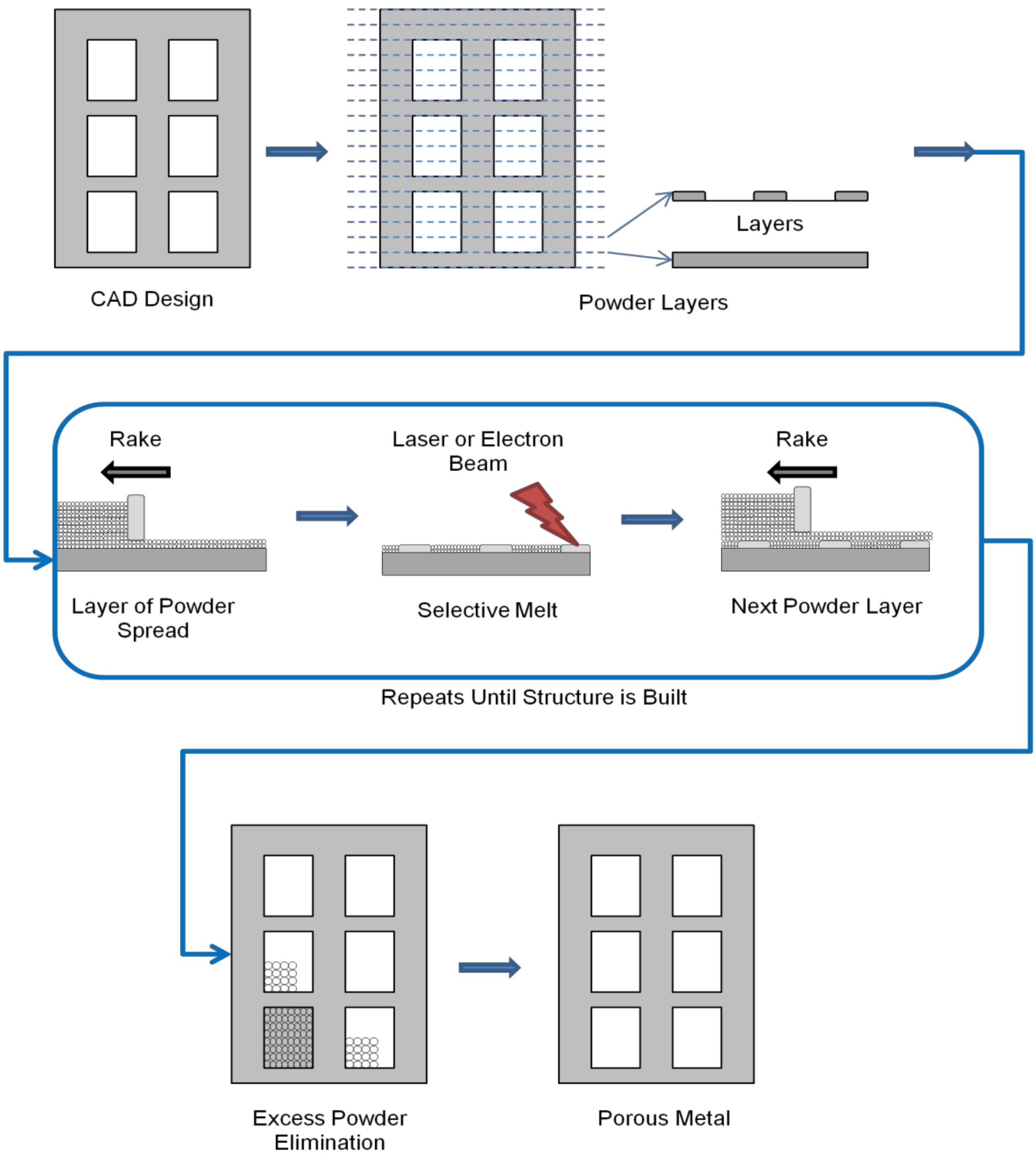

Figure 2.6 - Process followed to build a porous metal using Additive Layer Manufacturing.

Electron Beam Melting (EBM) (another ALM technique) has frequently been used to work with lattices made from titanium or titanium alloys such as Ti6Al4V, general structures are cubic based or diamond based [78]. EBM is a very adjustable procedure, to create more complex shapes, tomography pictures are often used as CAD files [79].

Other porous metals produced with EBM for biomedical usage are from cobalt and chrome alloys [79] and for operations using electricity or heat transfer, copper [80].

2.3.1.11. Spark Plasma Sintering

To produce a microstructure with fine grain size from powders, Spark Plasma Sintering (SPS) is used instead of regular sintering for the aluminium with NaCl space holder technique and for nickel - titanium alloys [81]. They have very low porosities of around 6% when compared to bulk TiNi, grain size being very small at around 50 nm creating nano sized pores, these porous metals promise biocompatibility due to the good attachment of cells.

2.3.2. Liquid Metal Replication Methods

2.3.2.1. Lost Foam Casting

This process is applied to obtain porous samples from metals and alloys that have relatively low melting points, such as copper, aluminium and lead. First a porous structure pattern is made, occasionally with polystyrene, it must include a sprue so the molten metal reaches the pattern; if several of these patterns are to be produced they can be joined using glue to form a cluster; the cluster is covered with a permeable refractory coating, leaving it to dry; then the cluster is placed in a foundry container; sand is added to cover the free space between the container and the cluster, being compacted to ensure a proper fit; the liquid metal is poured through the sprue and pattern, replacing the polystyrene, after cooling the porous metal is removed from the mould. This method produces a highly porous material as well [24].

2.3.2.2. Infiltration

In this technique liquid metal is forced into the free spaces of a preform or space holder, here there is usually a lower porosity when compared to the previous couple of methods [2]. The preform material most commonly used is NaCl [18], others used are clays [35], corundum [36] and porous alumina [37] for glass - alumina composite materials, although these latter are not removed. To introduce the metal a pressure system forces it to occupy the spaces between the preform particles. Another way is to mix the preform granules with the molten metal, in Figure 2.7 the infiltration method can be seen.

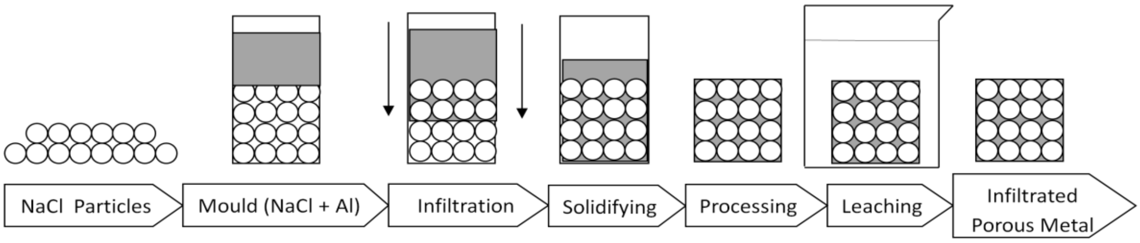

Figure 2.7 - Process followed to make a porous metal using infiltration.

To build porous metals of higher porosity, for example reaching 87% via the investment casting route, the space holder packing density when in the preform must be increased; this can be achieved by compacting it using Cold Isostatic Pressing, to maintain the same structure [82]; or by merging the NaCl particles together using sintering, however this reduces the particle surface area (the driving force for sintering to take place) and, as a direct consequence, the porous metal surface area; so here, when different densities were required, a vibration based route was followed.

The latter methods should be more effective when using NaCl particles smaller than 1 mm, since by reduction in size they are less prone to breaking and have an increased proportion of surface area to volume, increasing the driving force for sintering. Since the particle sizes in this study are larger and extra equipment would be needed to employ these routes, these techniques have not been used, keeping the method efficiently achievable.

Another method to control the size and shape of the space holder particles was applied by Goodall and Mortensen [14], modifying individual NaCl granules. Small powder particles of NaCl are blended with a binder, such as water and flour, giving the freedom to shape the paste into any desired form; after drying, the binder is removed by heating up the blend. This process is not difficult to follow to create a preform, the complexity rather arises when infiltrating; if the pressure is not controlled properly and precisely the small scale porosity inside the particles might get filled by molten metal, as well as the larger free space in between them.

NaCl is widely used as a preform due to its favourable characteristics like high melting point, high solubility in water, non toxic, low cost and readily available. However if one is aiming to produce porous samples out of higher melting point metals an alternative preform material would be sodium aluminate [15]. Its melting point is well above that of NaCl (≈ 1650°C) [83]. This and other alternative materials, while having advantages, also have downsides, frequently including a higher purchase cost and increased difficulty to dissolve.

To carry out replication processing with small particle size space holders a greater infiltration pressure is needed. The production rig for this study has been tested for pressures up to 7 bar, beyond which the risk of leaks from the graphite gaskets increases. To go beyond this pressure level an alternate design of infiltration chamber would be required. In one such design, the gasket areas are located apart from the high temperature part, with additional protection from circulation of low temperature water. This type of equipment (cold wall pressure chambers) is much more intricate and higher in expense than the one available.

The space holder manufacturing process or replication is one of the most straightforward and low-cost processes available to make porous metals. It gives a great advantage as part of a strategy to design, produce and test the effect of changing each porous metal structural characteristic or mix of characteristics to improve the regenerator performance. As of today, no tests have been published on replicated porous metals as regenerators.

The development phases to produce a porous aluminium sample by the replication method start with the preparation of the space holder. The preform is in essence the negative of the actual porous metal, it will be dissolved at the end leaving the shape of the porous metals' cells; as such, the size of the pores depends on it as well. The material for the preform must have a higher melting point than the porous material, it must not react with the it even with the increase in temperature and it must be capable of being eliminated smoothly from the porous metal once solidified.

NaCl complies with these characteristics. Its melting point is 801°C [18], well above the melting point of aluminium (660°C) and the operating temperature of the infiltration process (740°C) [149]. It is inactive when in contact with liquid aluminium or water and it does not pose the threat of reaction producing any dangerous compounds [3].

Porous metals processed by the replication method have a lower porosity range (from 65 to 75% on average) and therefore more consistent results than other techniques, culminating in less empty volume space and a larger capacity for heat absorption, being more suitable to be employed as a regenerator. Replication is one of the easiest and low cost methods to produce porous metals, it also provides a myriad of options for structure architecture [3].

There are many techniques in the area of porous metals which can be applied and modified for a particular goal; with our current manufacturing method, which is infiltration using NaCl as the preform, the aim is to create porous metals with different size, shape, structure, pore size and material in order to achieve a large amount of data from our test rigs to determine the best regenerator test samples that can be obtained.

In previous works [150], to improve contact between the NaCl particles sintering has been used, increasing the porosity up to 80%, this additional step takes some time. Another process [9] focuses on the melting of salt crystals to produce spheres, however this also takes more time and is costly. Cold Isostatic Pressing (CIP) has also been applied for this purpose, giving a superior stiffness and strength values when compared to the sintering process [8]. A simple way of increasing the contact between the particles of the sample holder is to vibrate the preform so the particles arrange themselves in a better way, this increases the porosity to around 76% [149].

There have been several variations of the basic method used to produce porous metals (using space holders) in this work. Previous research in the group had used induction heating and argon gas pressurisation of aluminium contained within a glass tube, also containing NaCl [3], [151], another was the vacuum - argon method [152], argon only (pressurisation) method [120], [149] and infiltration using a mechanical pressure. In particular the latter three of these methods were explored in the present work, with the greatest focus on the argon gas (pressurisation) method, the basic process of which was refined considerably for application here, in Table 2.2 some of the reported processing and structural characteristics are shown.

Material	**Infiltration Pres/Temp (bar/°C)**	**Preform Processing**	**Preform Packing density (%)**	**Porous Metal density (%)**	**Particle size (μm)**	**Particle shape**	**Ref.**
Al	5/750	Sintering (785°C)	≈ 75	20 - 27	500	Sphere	[201]
Al, Al12.6Si	5/750	Sintering (785°C)	≈ 75	20	400	Sphere	[11]
Al	5/750	CIP/Sintering (750°C)	70 - 90	13 - 30	40 - 400	Sphere	[202]
Al	2-80/710	CIP/Sintering	67 - 86	12 - 32	75 - 400	Sphere	[7]
Al, Al-Mg	4-80/710	CIP (10-60 MPa)/Sintering	64 - 93	5 - 35	75 - 400	Sphere, Angular	[12]
Al	80/710	CIP (5-60 MPa)/Sintering	64 - 90	10 - 35	75 - 400	Sphere	[8]
Al	0.96-2.48/760	CIP (32-50 MPa)/Sintering (730°C)	59 - 72	29 - 41	1400 - 2000	Sphere	[196]
Mg	1-4/750	None	64	22 - 33	1000 - 2000	Sphere	[169]

Table 2.2 - Processing and structural characteristics of replicated porous metals.

From the table above it can be seen that these techniques have certain limitations. For example, the random packing of equiaxed particles leads to around 64% of space being filled [203], so this represents an effective lower limit on the porosity that can be obtained with the basic method. There will be a certain limitation with regard to the pressure applied for non-wetting metals, which is discussed in more detail in section 6.2.

The inter-relation between processing and structure in great manner depends on the preform, from the table the range of its packing density will vary the amount of molten metal that is present in the final porous metal structure, another parameter is the infiltration pressure, if it increases, the amount of molten metal in the final structure is higher as well, reducing the porosity. The preform volume fraction will not be completely filled until a certain infiltration pressure is reached, infiltration is a gradual process [3].

The different shaped preform particles can be created using methods such as evaporation from brine, which creates cubes or antisolvent precipitation, which creates elongated parallelepipeds, hopper shaped as well as cubes.

Aluminium is commonly used to produce porous metals by replication due to its low cost, density and melting point. The research done on these elements as heat exchangers have included for use in airborne equipment and heat sinks for electronic equipment [143], having a large surface area, which is expected to be good for heat transfer; aluminium was thus the material chosen here to explore some of the structures that can be produced as a porous metal and test for regenerator properties.

In this chapter there has been an extensive view on the ways to produce porous metals, from general production to liquid replication methods, focusing on the various aspects of different techniques and the effects produced by changing certain parameters in the process, in Chapter 3 the regenerator, the Stirling engine and its cycle will be presented to associate porous metals with the regenerator application.

Chapter 3. Regenerators and Heat Transfer - Engineering and Theory

3.1. The Regenerator

A regenerator is a temporary heat storage unit for certain applications in which the thermal energy contained within a fluid is taken from it, only to be returned at a later stage of the process. It is used as an efficiency boost in a cycle in which a fluid is circulating in opposite directions between high and low temperature regions. It assists in restricting the exchange of heat between the two sides, which would narrow the temperature difference and reduce the efficiency of operation. In Figure 3.1 the configuration of an Alpha type Stirling engine and its regenerator can be seen.

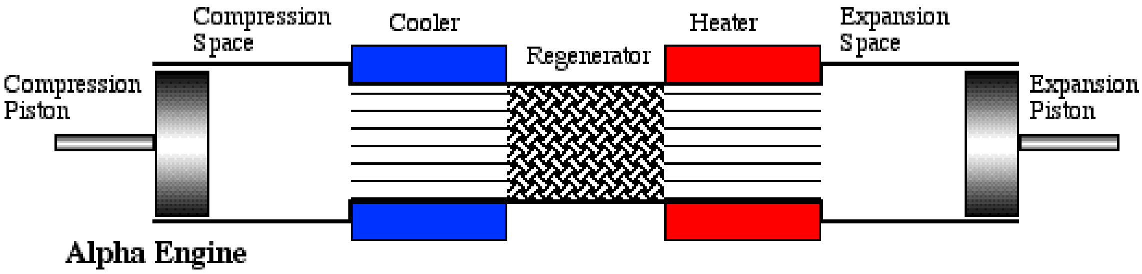

Figure 3.1 - Alpha type Stirling engine configuration [84].

Functionally there is a requirement for good heat exchange from the hot working fluid to the cold regenerator in the first half of the cycle and also heat exchange from the hot regenerator to the cold working fluid during the return phase of operation. As for heat exchangers, there is also the requirement for regenerators to set up as little opposition to the flow of gas as possible, as this would take energy away from the process. Nevertheless, despite these similarities regenerators differ fundamentally from heat exchangers, where the purpose is to move thermal energy only in a single direction, as the thermal energy must remain in the regenerator for subsequent return to the working fluid.

Both the regenerator and heat exchanger have the same exact relationship with the fluid, their efficiency and behaviour depend on the thermal conductivity and specific heat value of the material it is made out of [85]. A heat exchanger's efficiency will diminish if the heat is not transferred through the solid; this characteristic may be contrasted with a regenerator, since it has to return the captured heat to the fluid in the second half of the cycle, the movement of energy through the material must be low; if it is not, the temperature variation between the hot and cold side will be minimal causing the system to slow down and suffer energy losses to the surrounding environment.

A heat exchanger should ideally be made from a material with high thermal conductivity, such as aluminium, while for a regenerator a low thermal conductivity material element is needed, since at the start, the heat moves from the fluid to the solid and then, in the second half of the cycle, from the solid to the fluid. If the regenerator has a large value of thermal conductivity the energy would be transported through the porous metal, diminishing the energy change between the fluid and solid, lowering the efficiency of the element. For both types of component, a large specific heat value is required however [85].

One of the applications that uses regeneration is the Stirling engine, in the next section its operation will be addressed.

3.2. The Stirling Engine

A specific example of a case in which a regenerator is used is a Stirling engine. The Stirling engine is an external heat engine, meaning it can receive its input energy from a broad scope of sources via heat transfer. It has an elevated efficiency when compared to internal combustion engines, being an enticing option for power generation for the current and next generations of energy supply [86].

There are two containers (referred to as sides or chambers) within a Stirling engine; the expansion, or hot, side and the contraction, or cold, side. The heat enters the system on the hot side and causes the expansion of the working fluid. The regenerator often currently used in this type of engine is made out of a porous metal with an high surface area.

The effectiveness of the element depends on the type of material it is made out of. For example, in the General Motors (*www.gm.com*) Research Laboratories Ground Power Unit 3 Stirling engine and the Philips MP1002CA [87] the regenerator materials used are stainless steel meshes since they possess an elevated value of specific heat and a low value of thermal conductivity, as well as, importantly, the ability to withstand high temperature environments without melting or oxidising.

Other materials (aluminium, copper and brass) have been proven to be inferior in performance when compared against these stainless steel meshes [85]. However, no investigation of the effect of the structure (as distinct from the material) has been reported.

The Stirling engine has stages with different levels of temperatures and pressures affecting the working gas. It has no need for valves since the flow is restrained by volume expansion. The cycle can be reversed, meaning it can deliver heat if mechanical energy is introduced or deliver mechanical energy if heat is introduced; it can double as a heat pump or refrigerator if needed.

It is composed by a group of pistons, heat exchangers, the regenerator and the working gas. When absorbing heat from an external source, such as exhaust gases from another process, it generates the piston motion [19]. In Figure 3.2 the application of a Stirling engine is shown [88], to dissipate heat from an electronic system.

In the next section the operation of the engine's cycle is presented with fine detail.

Figure 3.2 - MSI ECOlution Chipset Cooler [88].

3.3. The Closed Regenerative Thermodynamic Cycle

The Stirling cycle operates in 4 steps, each one may be inverted. In the "ideal" (but not possible due to practical aspects) cycle there are 2 constant volume stages in which the fluid crosses the regenerator, becoming preheated or precooled. The 2 remaining stages occur at constant temperature in which the fluid comes in contact with a hot or cold source [89], [90]. In Figure 3.3 the cycle is shown with a pressure - volume diagram, and each of the key stages in the cycle will now be reviewed.

.

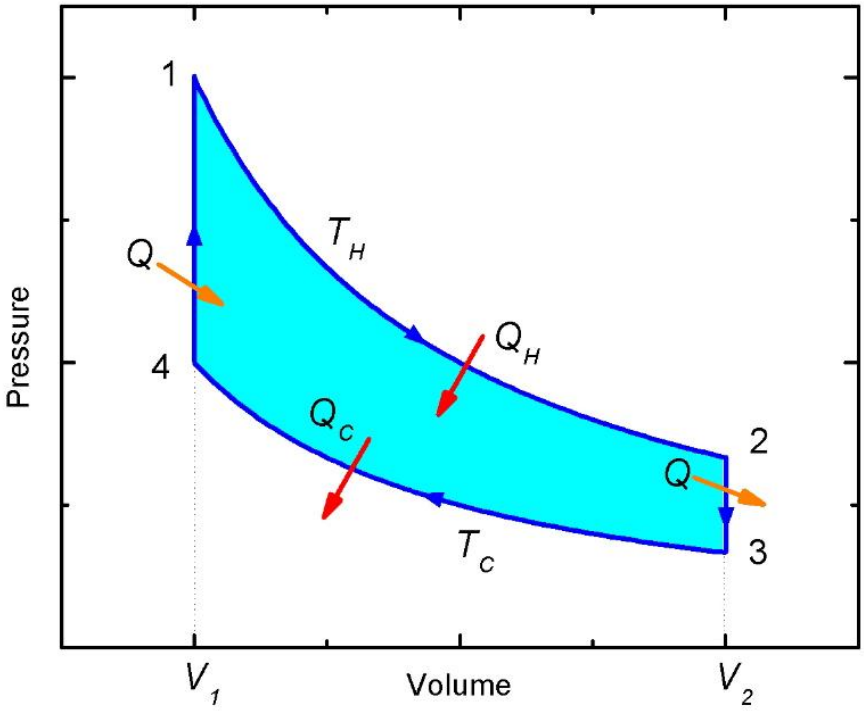

Figure 3.3 - Pressure - Volume diagram of the Stirling cycle [91].

1-2(a): The gas expands at a hot temperature T_H, the left piston travels down as the right one remains motionless. To stay at the same temperature, the gas absorbs heat energy Q_H from the supply.

2-3(b): At constant volume V_2 the gas at an elevated temperature moves from the left container through the regenerator to the right container, it leaves heat Q in the regenerator reducing the temperature T_H to T_C and operating both pistons during the process.

3-4(c): The gas compresses at a cold temperature T_C, the right piston shifts up as the left one remains motionless. To stay at the same temperature, the gas releases heat energy Q_C to the environment.

4-1(d): At constant volume V_1 the gas at a lower temperature travels from the right container through the regenerator to the left container, it absorbs heat Q stored in the regenerator from stage 2-3 having to absorb less heat from the supply to reach T_H, improving the cycle's efficiency.

In Figure 3.4 the schematic diagram of the Stirling cycle is shown.

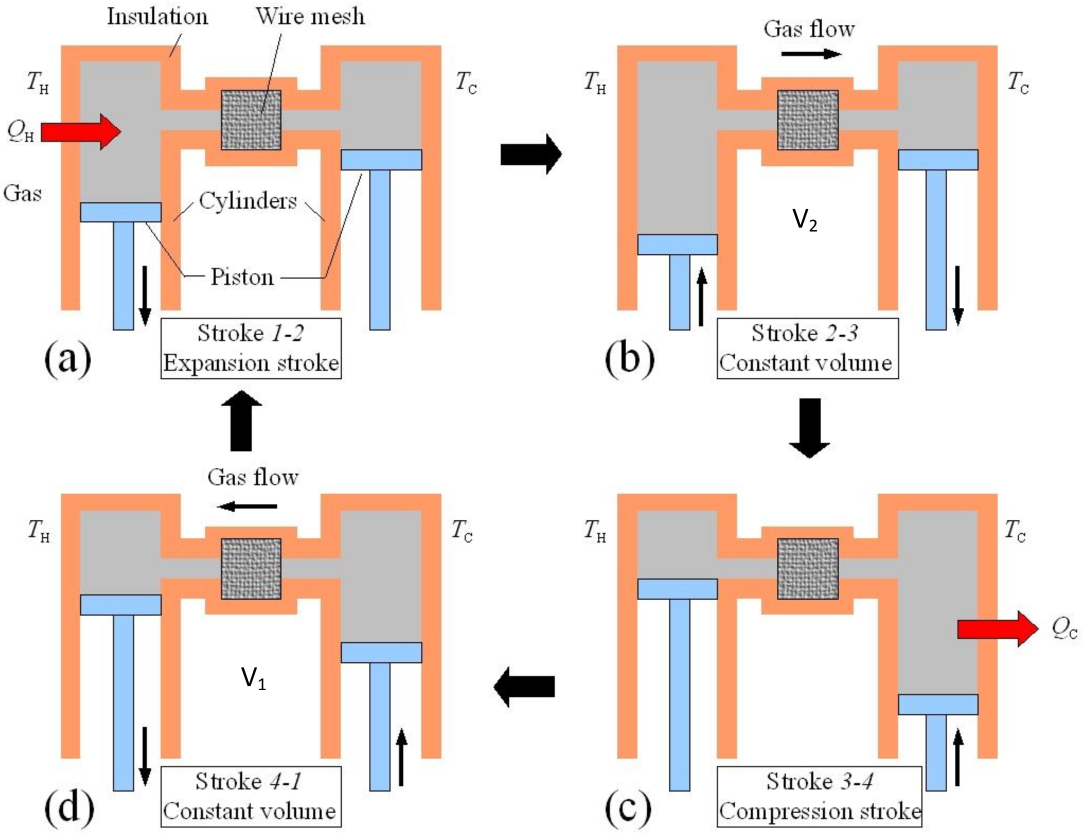

Figure 3.4 - Stirling cycle operation schematic diagram [92].

The regenerator is possibly the best innovation made by Robert Stirling in the development of the air engine; it is a component that permits recuperating energy. Stirling's idea was to recover the heat extracted in stage 2-3 and provide it back to the working fluid in stage 4-1. The regenerator's function is to preheat and precool the working fluid, greatly improving the cycle's efficiency [90].

A current acceptable regenerator structure is the stacked layers of wire mesh [94], packed beds of spheres [93] and another is the development of porous metal structures that allow a fluid to pass through the pores [94].

The main issue of regenerators is the resistance that opposes the flow of gas through it, which is the reason why low viscosity gasses such as hydrogen or helium are necessary to reduce friction losses. On occasion these losses are so elevated that make the engine deliver a better performance if the regenerator is removed, losing the possibility to recover the energy that can be stored in it.

From simple energy capture results it is not possible to determine if thermal conductivity is important for regenerator purposes, stainless steel has a low thermal conductivity and copper a high one, they both absorb similar amounts of energy when a hot fluid passes through them. Further tests are needed to prove this as Timoumi suggests that a regenerator needs to have a high heat capacity and a low conductivity to minimize internal heat loss [85].

The majority of the data on regenerators has been obtained using steady flow experiments, Tanaka focused his work on investigating the regenerator performance in an oscillating flow using different materials and structures, such as stainless steel in wire mesh structure, nickel in porous structure and bronze in a sintered structure and different porosities ranging from 37 to 96% [94].

One of the issues in their experiments was the thermocouples' temperature difference between the registered and the actual when using 50 μm thermocouples, having to correct the data. When using 25 μm thermocouples the problem is greatly reduced, that is why these are the ones used in the current work.

The relationship between the pressure drop and the piston speed was converted into the relationship between the friction factor and Reynolds number. Friction factor is a term related to the shear stress at the wall, which is a force that generates losses in the system, for the ideal performance it should be as low as possible.

The speed at which the piston worked was from 100 to 600 RPM and 0.1 to 1 MPa of pressure. In general, the friction factor values are different with different materials, determining that the mesh diameter was not convenient as the representative length for other porosities and regenerator shapes. On the other hand to establish the relationship between friction factor and Reynolds number the hydraulic diameter was used, as it depends on the porosity, mesh diameter and mesh shape. It was established that the shape factor was the ratio between the mesh surface area and the mesh volume [94].

It was stated [19] that the pressure drop in uniaxial flow is lower for a certain Reynolds number, suggesting that the friction factor in an oscillating flow is bigger; the regenerator efficiency (η) was calculated from the formula:

$$\eta = \frac{Q_{H,in} - Q_{C,out}}{Q_{H,in} - Q_{C,in}} \qquad \text{Eq. 3.1}$$

where $Q_{H,in}$ is the input heat from the supply, $Q_{C,out}$ is the output heat to the cooler and $Q_{C,in}$ is the input heat from the cooler; using the instantaneous temperatures at a certain given time; if the regenerator efficiency increases the heat transfer loss in the regenerator decreases this happens when the mesh number of wire went up (smaller pores).

When the relation between heat capacity in different materials to the working fluid is large, the Number of Transfer Units (NTU_R) and regenerator efficiency can be expressed as:

$$\eta = NTU_R/(NTU_R + 2) \qquad \text{Eq. 3.2}$$

Doing substitutions introducing heat in the equation:

$$NTU_R = \frac{2\left(Q_{H,in} - Q_{C,out}\right)}{Q_{C,out} - Q_{C,in}} \qquad \text{Eq. 3.3}$$

Next the mean heat transfer coefficient (h) is substituted:

$$h = \frac{A_{HT} NTU_R}{c_R \dot{\mathrm{m}}_{Air}} \qquad \text{Eq. 3.4}$$

where $\dot{\mathrm{m}}_{Air}$ is the average flow rate for a half cycle.

These are some of the basic equations to analyse the behaviour of a porous material acting as a regenerator, however certain ideas and equations need to be proven and adapted to different circumstances that can arise [19]. This occurred in this work while testing different types of wire meshes as stacked columns using three different sizes of wire mesh, confirming that in fact the pressure drop increases as the Reynolds number decreases.

3.4. Existing Regenerators

The regenerator is made from a porous matrix. Currently the most common Stirling engines use stainless steel mesh screens as their regenerator material, the size of the regenerator depending on the size of the engine, for example:

- Philips 400hp/cyl Stirling engine uses 6 regenerators that are 75 mm in length and 160 mm in diameter with its mesh number at 100 consisting of 89 screens and a porosity of 0.582.
- USS V-160 uses 1 regenerator of 30 mm in length and 65 mm in diameter with its mesh number at 200 consisting of 300 screens and a porosity of 0.69.
- Clapham 5.0CC uses 1 regenerator of 25 mm in length and 7.3 mm in diameter made from stainless steel locking wire and a porosity of 0.416, (this is an example that does not use the mesh configuration).

The Philips engine is at least five times larger than the USS engine. Performance wise it is proven that within Stirling engines the brake horsepower output has efficiencies of around 26% [16].

To choose or build a regenerator one must take into account the characteristics mentioned in Table 1.1, for maximum heat capacity a dense material with high specific heat is preferred, for minimum flow losses the element must be highly porous, based on the literature the range of porosities varies from 0.416 to 0.85 [17].

There needs to be a high surface area, translating into a matrix with many struts, the element must have a low thermal conductivity and it must not change its properties drastically in the range of operating temperatures which is between 300 and 1100 Kelvin [87]; in the literature there is not a structured material selection process or a study on the balance between pressure drop and heat transfer; pressure drop values through the regenerator vary from engine to engine, depending on its size and speed of operation, typical values for a 500W gamma type engine range from 10 to 14 kPa [206].

All reported regenerators use stainless steel, virtually all in the form of wire meshes except one. Exploration of alternative materials and structures has been extremely limited.

In this chapter the regenerator element has been discussed, looking at its characteristics to work in the Stirling engine application, exploring the way its cycle behaves and the considerations to take when designing one, existing regenerators have been mentioned and the materials that ideally would perform best, setting a baseline for design; in Chapter 4 the flow and thermal characteristics of porous metals will be addressed, this to understand the features to consider when manufacturing regenerators.

Chapter 4. Flow and Thermal Behaviour of Porous Metals

It has been shown that it is possible to make porous metals with a variety of characteristics which are interesting and have been explored for some heat management applications, in particular as regenerators. Thermal and flow behaviour of porous metals is complex however, and there has not yet been a systematic investigation over a wide range of structural types in the same test to truly say what is the best or optimal structure and optimal material for a porous metal for an application such as a regenerator. This is therefore the question that this thesis will attempt to answer. The first approach will be to understand the parameters that govern the flow properties of porous metals.

4.1. Fluid Flow in Porous Metals

The law that oversees the flow of fluids through a porous media is Darcy's law, defined by Henry Darcy in 1856 [95]. It came from his work analysing water seepage through packed beds made from sand, and is conceptually similar to other one dimensional transport laws. This law focuses on fluids moving at a certain velocity (superficial velocity = v_D) travelling a certain distance (L_R) generating a difference in pressure between two points or pressure drop (ΔP) through a porous element.

The fluid discharge ($\dot{m}_{Air}$) travelling through the porous element equals the product of its permeability (K) flow area (A_{CS}) and pressure drop (ΔP) divided by the absolute viscosity (⍰) of the fluid and the length of the regenerator (L_R):

$$\dot{m}_{Air} = \frac{K A_{CS} \Delta P}{\mu L_R} \qquad \text{Eq. 4.1}$$

Since the superficial fluid velocity (v_D) is obtained from the discharge ($\dot{m}_{Air}$) divided by the cross sectional area (A_{CS}):

$$v_D = \frac{\dot{m}_{Air}}{A_{CS}} \quad \rightarrow \quad \frac{\Delta P}{L_R} = \frac{\mu}{K} v_D \qquad \text{Eq. 4.2}$$

Eq. 4.2 is used for very small permeability-dependent Reynolds numbers (Re_K) of around 1, since Darcy's law is based on the velocity of water moving through sand (very low speeds) [96].

The value of fluid velocity (v_D) can also be substituted by the velocity through the porous metal. This velocity (v_ε) [97] considers the metal part of the porous element by dividing the superficial velocity (v_D) by the volumetric void fraction or porosity (ε) of the porous metal. Even if both velocities can be used, which of them is applied in a particular situation must be mentioned to avoid misunderstanding.

For faster velocities, a new term has to be included in the equation to calculate pressure drop [98], this effect adds the second term to the equation, known as the form drag coefficient (C) [99], Eq. 4.2 now turns into:

$$\frac{\Delta P}{L_R} = \frac{\mu}{K} v_D + \rho_{Air} C v_D^2 \qquad \text{Eq. 4.3}$$

This new quadratic term is applied for permeability dependent Reynolds number values between 5 and 80, as proven by Dybbs and Edwards [100] and Fand [101] with packed spheres and spheres of different sizes in one pack. This is known as the extended Darcy-Forchheimer equation, extensively used to calculate pressure drop in porous elements [102].

If the value of Re_K exceeds 80 a cubic term must be introduced to the equation, as demonstrated by Lage for correct pressure drop calculation in porous metals [103]. This is confirmed by Forchheimer as well [104]. The equation is as follows:

$$\frac{\Delta P}{L_R} = \frac{\mu v_D}{K} + \frac{\rho_{Air} C v_D^2}{\sqrt{K}} + c v_D^3 \qquad \text{Eq. 4.4}$$

K and C are obtained by fitting a curve using the pressure drop data, one way to do this is to apply a least squares quadratic curve fit [96] or a least squares cubic curve fit [103] if Re_K > 80. Another option is to divide equations 4.3 and 4.4 by v_D changing the equations into linear and quadratic forms:

$$\frac{\Delta P}{L_R v_D} = \frac{\mu}{K} + \rho_{Air} C v_D \qquad \text{Eq. 4.5}$$

$$\frac{\Delta P}{L_R v_D} = \frac{\mu}{K} + \frac{\rho_{Air} C v_D}{\sqrt{K}} + c v_D^2 \qquad \text{Eq. 4.6}$$

substituting coefficients a and b

$$\frac{\Delta P}{L_R v_D} = a + b v_D \qquad \text{Eq. 4.7}$$

$$\frac{\Delta P}{L_R v_D} = a + b v_D + c v_D^2 \qquad \text{Eq. 4.8}$$

To obtain the experimental values in this work, the quadratic turned into linear form (Eq. 4.7) was used since the values of Re_K are lower than 80 for all samples.

When the superficial velocity approaches zero the pressure drop / velocity rate becomes constant; the opposite effect occurs when the velocity increases to relatively high values, the first term then becoming trivial [105].

For flow investigations on porous metals Dukhan used the Forchheimer – extended Darcy equation (Eq. 4.3), which is widely accepted to accurately describe the pressure drop of a fluid passing through porous media [106].

From the previous equations it can be seen that there is a conflict between the pressure drop and the permeability, a high pressure drop through a porous element represents a low value of permeability giving way to low Reynolds numbers.

The porous metals in Dukhan's work are relatively large (5.08 cm x 10.16 cm x 24.13 cm) and the porosities high, from 92 to 94%. The flow speed ranged from 0.77 m/s to 2.73 m/s. The pressure drop was seen to increase in a quadratic way compared to the velocity, in compliance with the work from Boomsma, Lage and Bhattacharya [96], [103], [107].

Dukhan also found a good comparison with previous results obtained by a significant number of authors [106]. However, there is a need to analyse porous samples from different materials to see if there are different pressure drop results from them, as well as a larger range of flow rate (different Reynolds numbers).

There has been analysis of porous structures made from copper, nickel and a nickel – chromium alloy with pore sizes from 0.5 mm to 5 mm, velocities ranging from close to stationary to 20 m/s, others using water as a fluid at speeds from stationary to 0.1 m/s [108]. Testing Reynolds numbers from 10 to 5,000 found that the Forchheimer law was verified and that the permeability does not depend on the fluid nature, demonstrating that the pore size itself is enough to describe flow laws in porous metals, however, of course porosity and possibly pore shape would also be affecting factors.

It is important to point out that the variance in the pressure drop when comparing uniaxial and oscillatory flows is from four to six times higher than the steady flow at the same Reynolds number [109].

In Zhao's experiments [109] three different mesh size stainless steel meshes were used, three values of fluid displacement (controlled by the oscillations in his apparatus) and Reynolds numbers from 0.001 to 0.13. At higher Reynolds numbers the sinusoidal variation of the pressure drop phase presents lags but it remains independent from the oscillation in the fluid.

This paper [109] made a comparison with previous results obtained by a significant number of authors, however, there is a need to analyse porous samples from different materials to see if there are different pressure drop results from them, as well as a larger range of flow rate (Reynolds numbers).

4.2. Models for Permeability

4.2.1. Despois and Mortensen

This model is based on the microstructure of open pore microcellular materials it considers the obstacles presented by the "bottlenecks" in the path of the fluid as these control the flow rate. Replicated porous metals fall into this category of porous materials, where the bottlenecks are the windows that connect the pores. Assuming that there is a window through which all the fluid enters and another through which all the fluid exits, the area of the windows is estimated considering that the window to be circular in shape, another consideration is the random packing density of the spherical particles ε_0 = 0.64, the porosity ε and the particle/pore radius r.

The model considers a thick slab of porous metal of thickness 2r and a length of 1 m to calculate the number of pores, which is also the number of windows, giving the final equation for the model as:

$$K = \frac{\varepsilon r^2}{\pi \mu}\left[\frac{\varepsilon - \varepsilon_0}{3(1-\varepsilon_0)}\right]^{3/2} \qquad \text{Eq. 4.9}$$

showing that there is a strong dependence on porosity. This model also includes that the average window size starts to close when the porous metal passes the value of 0.36 of solid fraction [7].

4.2.2. Fourie and Du Plessis

This model was created to predict the pressure drop in a Newtonian fluid passing through a highly porous material with a uniformly distributed velocity. It is based on assuming a piece-wise plane Poiseuille flow and a simple geometric model to predict the Darcy and Forchheimer regimes.

It applies analytical concepts from volume averaging to the Navier-Stokes equation considering a representative elementary volume, porosity and a representative unit cell consisting of a geometrical distribution of rectangles with three axes (x, y and z), the cells are located in such a way that one of the axes is always parallel to the fluid velocity.

Another parameter considered in this model is the tortuosity (X) which is the total length of the pore within the length scale divided by the length scale of the sample. The porosity is considered as the ratio between the pore diameter and the cell dimension, the specific surface area is determined by the cell dimension porosity and cell size may be determined by optical microscopy, in this case a tetrakaidecahedral cell is used. The porous metals used to test this model are Duocel and the cross section of the struts considered is triangular. The permeability in this model is calculated as:

$$K = \frac{\varepsilon^2 d^2}{36(X-1)X} \qquad \text{Eq. 4.10}$$

in this equation there is a strong dependence on porosity, pore size and characteristic length of the sample, included to obtain the tortuosity [179].

4.2.3. Furman, Finkelstein and Cherny

In this model the NaCl particles are considered to be spherical, considering the lack of wettability of the NaCl by the molten metal, air pockets are formed between the particles called air collars, when solidification happens the pore sizes are defined by two dimensions, the maximum being the particle size and the minimum is the diameter of an air collar or two times the capillary radius.

The resulting permeability equation is:

$$K = \frac{\varepsilon N r_{min}^3}{6\pi r} \qquad \text{Eq. 4.11}$$

where N is the number of capillary radii for one NaCl particle, it is called the coordination number and it is calculated based on the solid fraction of the porous metal [198], this model applies the concept of bottleneck or window from the Despois and Mortensen model.

In all three models it is clearly seen that there is a dependency on the porosity at different power levels, the pore size is included directly in the first model as the radius, indirectly in the second model as part of the porosity calculation and in the third as a calculation of the minimum pore radius, the window size is considered in the first model to grow smaller up to when the volume fraction of material reaches 36%.

Having explored the terms required to describe the flow behaviour, the concepts surrounding the heat transfer part will now be addressed, the effects that the material, pore size, sample length, etc. have on the ability of the porous metals to capture and release energy will be investigated, as this is the main requirement for them to act as a regenerator.

4.3. Heat Transfer in Porous Metals

The study of heat transfer inside a regenerator is challenging because of the size of the voids and the complex structural characteristics. To record the speed of flow and quantity of thermal energy at specific points within the regenerator, the measuring equipment must be placed in the free space within the pores, leading to a complicated experimental setup which currently is not feasible, particularly not without having a significant impact on the behaviours it would be supposed to be measuring. For this reason the heat transfer coefficient of the regenerator is the usual characteristic parameter obtained [110]. This is calculated from the relationship between the regenerator and the fluid it is in contact with.

Some of the concepts to be analysed and determined are the effective thermal conductivity, permeability and the form drag coefficient of porous metal samples with different porosities and pore sizes. One of the ideas or ways to approach this challenge is by creating a theoretical model, like the one mentioned previously [107]; this model was made to determine the thermal conductivity k_R, representing the porous metal structure by a two dimensional hexagonal array where the fibres form the sides of the hexagons. The metal at the intersection of the two fibres was represented as an intersection of circular cross section. This analysis proved that the effective thermal conductivity of the porous metal depends strongly on the porosity and the relation between the cross sections of the fibre and the intersection. This theoretical model was validated experimentally, using high porosity ($0.85 \leq \varepsilon \leq 0.97$) porous aluminium and air and water as their working fluid [107].

These workers continued with another analysis to estimate this effective thermal conductivity, but now in terms of the porosity and the solid and fluid conductivities; additional models were made to predict the value of permeability, modified from the work of Du Plessis to include a wider range of porosities from 0.85 to 0.97 instead of the original model which was only acceptable for porosities above 0.97 [111].

Up to now the porous metals discussed have been tested with air, helium and water, there is another fluid used to test porous metals with which is 50% water – 50% ethylene glycol solution. Boomsma compares heat exchangers on the basis of required pumping power against thermal resistance [112]. The open cell porous aluminium heat exchangers generated thermal resistances two to three times lower than the best commercially available heat exchanger tested, while needing the same pumping power, this is due to the high surface area of porous metals and high conductivity of aluminium, indicating they perform well as heat exchangers.

The properties of a porous metal follow the combination of the particular metals or alloys that it is made from. For conductivity (both thermal and electrical) there are few evaluations in porous metals made from processed powders. As both use the same transport mechanism (free electrons) they are expected to be related. Electrical conductivity ranges in porous metals made by the space holder method are in Table 4.1 [18].

The general tendency is that the electrical and thermal conductivity of the porous metal decreases as porosity increases, data for different pore size and density of copper samples is available [113].

Metal	Pore Size (μm)	ε (%)	Conductivity (S/m) x 10^6	Reference
Cu	250->1000	70-85	0.26-6.26	[63]
	120-500	50-85	0.13-0.31	[145]
Ti	150-400	10-67	0.33-1.41	[114]
	136-403	31-64	0.13-0.69	[146]
Fe	425-1500	68-76	0.95-1.45	[63]
Al	452->2000	63-83	0.62-4.26	[144]

Table 4.1 - Electrical conduction characteristics of powder processed porous metals.

It has been found in copper and iron porous samples that the electrical conductivity increases proportionally with the pore size, the reason being the improved connection within the cell walls (more metal) [63]. Since the powder processed porous metals may contain oxides and other contaminants [12], their conductivity is lower when compared to samples made by other methods. Li found that the value of electrical conductivity for titanium was reduced by almost 30% when powder processed as compared to commercially available titanium [114]. All these trends would be expected to be reproduced for thermal conductivity. Processed powders are considered for this work since two of the methods used to produce the regenerator test samples in this work are made from them (SLM and EBM).

The global efficiency of the Stirling engine is affected by the amount of energy needed to push the working fluid through the porous metal. This can be identified as the pressure drop across the regenerator or the permeability of the element to gas flow (these two parameters are interlinked). It is understandable that for the regenerator to keep a high heat transfer efficiency more available material (the surface area) is needed. However, as the amount of material present increases, it will interfere more extensively with the working gas flow. Here is where the challenge arises, striking the correct balance between these two characteristics.

There are a variety of structures which can be used as the porous regenerator. Regenerators can be a bed of granular material, a wire coil, an irregularly shaped wire mesh, or stack of wire mesh layers. While placing the regenerator structure into an engine a common fault is that is does not form a full seal within the structure as the working fluid must not be able to bypass the regenerator, or the efficiency will be lowered; this type of defect is common with the wire mesh layers structure and so this was considered in the testing of the wire mesh regenerator samples, preventing the working fluid to pass around it.

The stainless steel wire nets that are used as regenerators for the Stirling engine have a large specific heat value, high surface area and low thermal conductivity, yet they are not ideal due to difficulty in getting good contact with the edge of the container and significant pressure drop. If the nets are oversized compared to the container the edge problem can be solved, however, it increases the pressure drop. As a third consideration, the arrangement of the wire meshes can be crucial to performance. Packing them in a certain way (random or deliberate) and the distance between each net will have a large effect on their efficiency [115].

One of the reasons for this study is that open cell metal samples have a particularly useful characteristic; their structure can be modified in several ways. If their density, pore size or pore shape is altered, the thermal performance and pressure drop through the finished regenerator changes as well, and such behaviour presents the opportunity of better control of properties through processing when compared to the alternative structures.

The measurement of the thermal behaviour in porous metals has been done in two ways, comparing the heat exchange between two solids (a surface and a porous metal) or between the gas and the solid (a porous metal and a fluid). The first method places the porous metal in contact with a heated surface, then the heat exchange between it and the passing fluid is registered and compared with the heat exchange between the hot surface and the passing fluid. This way is used to test them as heat exchangers.

A study for high porosity (> 85%) porous metals as heat exchangers was done by Zhao, analysing properties such as conduction and convection, showing that they are a promising element for heat dissipation in various applications due to their high surface area (1000 - 3000 m^2/m^3) and, if needed they can be compressed to obtain higher values of up to 8000 m^2/m^3 [116].

The other way to test porous metals monitors how heat is transferred from the gas to the porous metal. A gas flows constantly through the sample heating it until reaching the same temperature as the fluid (at which point heat transfer will stop under the second law of thermodynamics). The fluid flow entering the porous metal undergoes a temperature step change and the exiting temperature is recorded until it reaches the same value as the entering temperature (within experimental accuracy). The heat transfer coefficient is obtained by matching the exiting temperature curve with the curve provided by the Schumann and Hausen model, the equations are given in section 4.2.1 [117], [118]. This model is often named the *single blow method* [110], [119], [120], [121], a full explanation of one experimental embodiment of the approach is given later.

Most of the examinations using the latter approach to the testing of porous metals concentrated on packed beds of particles with porosities ranging from 40 to 50% [117], [122], [123], [124] or bundles of wire nets [94], [125], [126], although other studies have been carried out for ceramic porous structures [127], [128], giving insight of what can be analysed from these structures, even if the results obtained differ from what would be expected for porous metals due to their different base material properties.

Previous tests [94] have been carried out on porous aluminium produced by investment casting to obtain the pressure drop and the heat transfer coefficient. The pressure drop value obtained is much lower when compared to wire net layers, principally due to the elevated value of porosity (90%). This is, however, not a desirable feature, as it leads empty volume inside the engine which is effectively “dead” space, with a proportion of the gas which is not able to go through the full cycle (as would be required in the ideal case). It would also be anticipated that the heat absorption capacity of such a porous metal is low, reducing the efficiency when compared to the wire mesh layers.

To improve the heat transfer coefficient of high porosity porous aluminium, attempts have been made to compress the samples, lowering porosity (from 95 to 60%), leading to the materials performing better as heat exchangers; however, the pumping power of the fluid needs to increase as well, consuming more energy [112].

One experimental technique that can be applied to analyse both the behaviour of heat exchangers as well as regenerators is the single blow method [120], [126], [129]. Applied to regenerators, another technique used is analysis under oscillatory flow. This method more closely resembles the role of the regenerator, for example, in a Stirling engine, which is based on a closed regenerative thermodynamic cycle. When both methods are compared, the variation in the value of the heat transfer coefficient found is not significant. For a Reynolds number inside the voids of 60 or larger there is a maximum difference of 15% [94], [115]. The oscillatory flow test equipment design is not as straightforward to construct as the single blow test rig, since it operates at an elevated cycle rate (frequently multiple Hertz).

To obtain results from the single blow technique rig, three stages are to be completed [130]. These are the experiment itself, as explained in Chapter 5, modelling of the heat transfer and the pairing of the experimental data to the model. As the heat is being transferred in a dynamic situation, it is not possible to simply measure values and calculate the heat transfer, rather the response for particular values must be simulated and compared with the experiment to find a match.

The ideal single blow test proceeds as follows; a sample at a certain fixed temperature suddenly comes in contact with a steady flow of a fluid at a different (higher) temperature, causing a step change in the thermal environment; the heat moves from the fluid (since it is at a higher temperature) to the sample, generating an outlet temperature curve or hike curve; the test concludes when both temperatures (inlet and outlet) are stable within the precision of the equipment used. After this, the outlet curve is paired with the curve produced by the model and the heat transfer coefficient is estimated [94].

To estimate the hike curve of the outlet temperature, equations can be used to create a mathematical model resembling the regenerator form and fluid conditions. There are various categories of models that analyse the single blow method [131], the model used for this work will be approached in detail.

4.3.1. Dimensionless Groups

In the analysis of heat transfer, the complexity of a real situation can be reduced to allow the comparison of the behaviour of different materials by the use of particular parameters, referred to as dimensionless groups. The key values will now be explained.

4.3.1.1. Reynolds Number (Re)

The Reynolds number Re is a dimensionless number that represents the ratio of the inertial forces to viscous forces, it allows comparison of how a fluid flows through different structures; to calculate the Reynolds number through the porous metal samples the pore diameter (D_P) or the hydraulic diameter (D_H) was considered [96], [93], the resulting equations using these two parameters are:

$$Re = \frac{\dot{m}_{Air} D_P}{\mu A_{CS} \varepsilon} = \frac{\dot{m}_{Air} D_H}{A_{CS} \mu} \qquad \text{Eq. 4.12}$$

where $\dot{m}_{Air}$ is the mass flow rate, μ is the dynamic viscosity of the air at the test temperature, A_{CS} is the cross section area of the porous metal and ε is the porosity. D_P and D_H are commonly referred to as the characteristic length L_C of the porous sample [157], [171]. From the equation it can be seen that the number increases with the mass flow rate and the pore size (less obstruction), if there is less obstruction the pressure drop through the element is low, resulting in a high Reynolds number.

4.3.1.2. Prandtl Number (Pr)

The Prandtl number Pr is a dimensionless number depending solely on the working fluid's properties, it is the rate of heat transfer in different fluids, the ratio between the momentum diffusivity, also known as the kinematic viscosity to the thermal diffusivity of the fluid [93].

$$Pr = \frac{c_{Air}\mu}{k} \qquad \text{Eq. 4.13}$$

It is used to gauge the effectiveness of movement and heat transport by diffusion at a certain speed through the thermal boundary layers. If the number is low (much smaller than 1) it means that the conductivity produces a larger effect, if the number is high (much larger than 1) the viscosity dominates the effect [93].

For air and many gases the Prandtl number oscillates between 0.7 and 0.8; for these experiments the Prandtl number for air is considered to be 0.711 at 40°C [181].

4.3.1.3. Stanton Number (St)

The Stanton number (St) is a dimensionless number used to gauge convective heat transfer in fluids, it is the relationship between the convective heat transfer coefficient and the specific heat of the fluid [182], it can be calculated with Eq. 4.14.

$$St = \frac{hA_{CS}\varepsilon}{\dot{m}_{Air}c_{Air}} \qquad \text{Eq. 4.14}$$

This number directly depends on the relationship between the convective heat transfer coefficient of an element and the fluid it comes in contact with, considering the fluid to be the same (air) the properties of the material directly influence this value, a common value range for Stanton numbers in metals is from 0.03 - 0.3, if the value is low (≈ 0.03) it is less effective for heat convection, if the value is high (≈ 0.3) it is better suited for this purpose [93].

A common way to present the data obtained from these tests is using the Reynolds number vs. Stanton number multiplied by the Prandtl number raised to the power 2/3 (Re vs. $StPr^{2/3}$).

The power 2/3 is an approximation over a range of Prandtl numbers from 0.5 to 15 causing the least error in the 0.5 to 1 range, it is satisfactory for all gases in laminar flow, for a turbulent flow the analytical solution approximates the power value to 1/2, for laminar flow in long tubes the power value is near 1, for finite sized tubes (such as would be encountered in heat exchangers) the 2/3 power is near correct, thus being a reasonable arrangement [93].

4.3.2. Models to Analyse the Data Obtained from the Single Blow Method

As discussed, the regenerator sample in this test experiences a sudden change in the temperature of the fluid environment it is placed in. This difference is affected by the characteristics of the material it is made of, the particular properties of the fluid and the features of the testing equipment. To interpret the mix of these conditions equations constituting a mathematical model are applied to forecast the end data.

There are two main categories of mathematical models to consider based on the test characteristics [131]. The first is considering that the heat capacity of the fluid is limited (A.), the second is considering that the heat capacity of the fluid is limitless (B.).

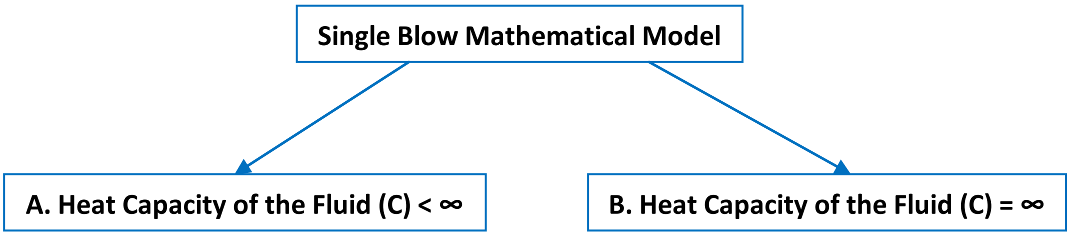

The first model group (A.) breaks down into two further categories (A1. and A2.); these consider the difference between the thermal resistance in the middle of the regenerator and the fluid. The first of these is the Schumann - Hausen model, which is applied if a thermal resistance exists between the fluid and the solid material, the second type is applied if the thermal resistance is insignificant (i.e. a value close to zero).

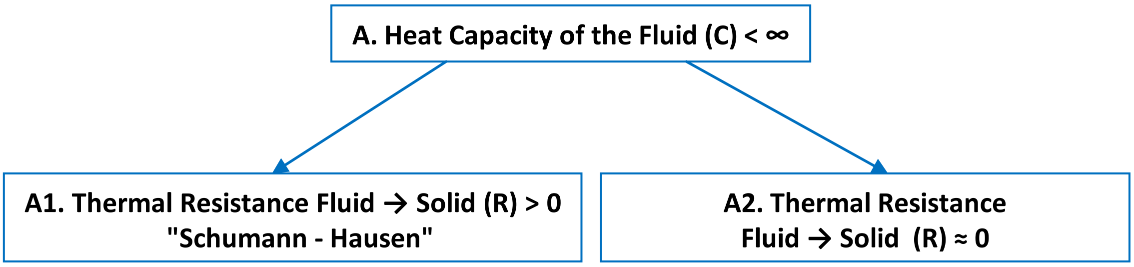

When the fluid is a gas with a small heat capacity it is recommended to presume the solid works under a defined fluid heat capacity. Within the fluid and the solid there is a temperature difference along the x axis, parallel to the fluid flow direction.

The Schumann - Hausen model had its origin in the late 1920's and was tested practically to learn the behaviour of heat transfer from a fluid to a group of ball bearings [117]. The exit experimental curve of temperature change with time was matched to the curve from the model to extract the heat transfer coefficient of the packed bed [122].

Other researchers applied Schumann's model to other structures to determine the effects produced by wire layer nets and a packed bed of ball bearings with varying void fraction volumes through several Reynolds number flow values, developing heat transfer and pressure drop equations [125].

The thermal conductivity of the solid is considered of high value in the Y axis (perpendicular to the flow) and nonexistent in the X axis (parallel to the flow), the temperature change will only happen in the X direction.

The assumptions of the model are:

1. The barrier surrounding the solid does not absorb heat.
2. A sudden change in temperature occurs at the entrance.

3. The solid has very high transversal thermal conductivity.

4. The solid has very low longitudinal thermal conductivity.

5. The fluid's speed does not change.

6. The heat transfer coefficient is consistent throughout the solid.

The expression of the energy balance for a volume that is increased by an incremental distance Δx is derived. The heat infiltrating the new volume is the addition of the heat leaving and the heat accumulated in the solid [131].

The equation is:

$$\dot{m}_{Air} c_{Air} T_{Air(x)} = \frac{h A_{HT} \Delta x}{L_R} (T_{Air} - T_R) + \dot{m}_{Air} c_{Air} T_{Air(x+\Delta x)} \qquad \text{Eq. 4.15}$$

where $\dot{m}_{Air}$ is the air mass flow rate, c_{Air} is the air heat capacity, T_{Air} is the air temperature, h is the heat transfer coefficient, A_{HT} is the heat transfer area, L_R is the length of the regenerator and T_R is the regenerator temperature.

The heat of the fluid leaving that distance is:

$$T_{Air(x+\Delta x)} = T_{Air(x)} + \frac{\partial T_{Air}}{\partial x} \Delta x \qquad \text{Eq. 4.16}$$

Consequently:

$$\frac{\dot{m}_{Air} c_{Air} L_R}{h A_{HT}} \frac{\partial T_{Air}}{\partial x} = (T_R - T_{Air}) \qquad \text{Eq. 4.17}$$

For the regenerator a similar analysis is made. The heat gained by the solid is the heat lost from the fluid. The equation is:

$$A_{CS}\Delta x\rho_R c_R\frac{\partial T_R}{\partial t}=\frac{hA_{HT}\Delta x}{L_R}(T_{Air}-T_R) \qquad \text{Eq. 4.18}$$

where A_{CS} is the cross section area of the regenerator.

Consequently:

$$\frac{L_R A_{CS}\rho_R c_R}{hA_{HT}}\frac{\partial T_R}{\partial t}=(T_{Air}-T_R) \qquad \text{Eq. 4.19}$$

The adimensional variables are:

$$x_a=\frac{hA_{HT}x}{\dot{m}_{Air}c_{Air}L_R}\quad,\qquad NTU_R=\frac{hA_{HT}}{\dot{m}_{Air}c_{Air}}\quad,\qquad t_a=\frac{hA_{HT}t}{A_{CS}L_R\rho_R c_R}\quad,$$
$$T_{aAir}=\frac{T_{Air}-T_0}{T_{Airi}-T_0}\quad,\qquad T_{aR}=\frac{T_R-T_0}{T_{Ri}-T_0} \qquad \text{Eq. 4.20}$$

Adimensional equations for the fluid and the solid:

$$\frac{\partial T_{aAir}}{\partial x_a}=T_{aR}-T_{aAir},\qquad \frac{\partial T_{aR}}{\partial t_a}=T_{aAir}-T_{aR} \qquad \text{Eq. 4.21}$$

Boundary conditions:

$$x_a=0,\qquad t_a=0,\qquad T_{aAir}=1,\qquad T_{aR}=1-e^{-t_a}=0 \qquad \text{Eq. 4.22}$$

To obtain the exit curve from the model, the analytical result of equations in Eq. 4.21 is presented as [132]:

$$T_{aAir} = e^{NTU_R}\left[1 + NTU_R t_a \sum_{i=0}^{\infty} \frac{t_a^l}{l+1}\left(\sum_{i=k}^{\infty} \frac{(-1)^{l-k} NTU_R^k}{k!\,(k+1)!\,(l-k)!}\right)\right] \qquad \text{Eq. 4.23}$$

The result from this equation is the exit flow temperature curve, depending on the NTU_R variation which was plotted against adimensional time t_a.

There are several considerations that the Schumann - Hausen model does not include:

1. *A perfect step change in temperature is unattainable* [130].

To solve this issue the way to interpret the step change temperature curve is to use an exponential change, producing a random value of entry temperature in place of a perfect step change in temperature [121,133,134], this produces an effective fix in the results.

2. *Assuming that the wall of the container does not absorb heat is unrealistic, the sample holder will gain some heat, affecting the exit temperature.*

If this amount of heat entering the wall is not considered the resulting heat transfer coefficient will be inaccurate. To prevent this, the effects caused by the thermal conductivity of the wall, number of transfer units of the wall and the capacitance relationship between the regenerator and the wall were included in the calculations. It was proved that they had a considerable effect as the results showed a difference of more than 30% when compared with the outcome of the straightforward Schumann - Hausen model [110].

3. *Since there is a pressure drop caused by the solid, the Joule - Thomson effect alters the exit temperature and must be included.*

It was established that the amount of heat in a fluid may decrease or increase when it reaches an obstacle in the flow direction [135]. Researchers demonstrated that this effect only happens when the pressure drop is considerably high (200 kPa produces a 3% temperature dip) [115].

4. *The longitudinal thermal conductivity impacts greatly on certain types of regenerators, mainly the ones used at very low temperatures.*

The absence of this effect in the calculations may cause a significant miscalculation in the assessment of the number of transfer units by a factor of 1.8 [130]. The effect has been shown to impact number of transfer units larger than 2 [136] and larger than 3 [121].

5. *The effect of radial thermal conduction within the regenerator is neglected.*

Researchers noted that for the single blow method studies assumed the temperature distribution inside the solid was uniform, however, irregular distribution does exist. From their results it was found that the radial conductivity had an effect on the number of transfer units of the regenerator close to a 9% decrease in value when compared to the results without considering this conductivity. This consideration must be applied to regenerators with an elevated number of transfer units, larger than 150; if the tested regenerator has a lower value of NTU_R this effect becomes trivial [126].

4.3.3. Single Blow Model Applied in This Work

Since the characteristics for this work include a set heat capacity of the fluid and a thermal resistance between the fluid and the regenerator the Schumann - Hausen route was followed, with some of the considerations that were applicable to the test samples that were produced.

The route followed for this study is based on the model proposed by Chang [126]. The Joule - Thomson effect was not included in the Schumann - Hausen model, since the pressure drop value produced by the samples are in the range of 5 to 15 kPa, an order of magnitude lower than the 200 kPa present in the literature experiment. The radial conductivity effect is not considered, based on the fact that the maximum NTU_R values obtained for these samples are around 80, considerably lower than the limit NTU_R value of 150.

The partial differential equations used to create the exit temperature curve are:

$$\frac{\partial T_{Air}}{\partial x} + NTU_R(T_{Air} - T_R) + NTU_w(T_{Air} - T_w) = 0 \quad \text{Eq. 4.24}$$

$$\frac{\partial T_R}{\partial \tau} - \lambda_R \frac{\partial^2 T_R}{\partial x^2} + NTU_R(T_R - T_{Air}) = 0 \quad \text{Eq. 4.25}$$

$$\frac{\partial T_w}{\partial \tau} - R_{tc}\lambda_w \frac{\partial^2 T_w}{\partial x^2} + R_{tc}NTU_w(T_w - T_{Air}) = 0 \quad \text{Eq. 4.26}$$

The adimensional variables are:

$$\begin{gathered} R_{tc} = \frac{m_R c_R}{m_w c_w}, \qquad \lambda_R = \frac{k_R A_{CS}}{\dot{m}_{Air} c_{Air} L_R}, \\ \lambda_w = \frac{k_w A_w}{\dot{m}_{Air} c_{Air} L_R}, \qquad t_a = \frac{\dot{m}_{Air} c_{Air} t}{m_R c_R} \end{gathered} \quad \text{Eq. 4.27}$$

The start and boundary conditions are:

$$\begin{gathered} t = 0, \qquad T_{Air}(x) = T_R(x) = T_w(x) = 0 \\ x = 0, \qquad T_{Air} = 1 - e^{(-t_a/\psi)}, \qquad \frac{\partial T_R}{\partial x} = 0, \qquad \frac{\partial T_w}{\partial x} = 0 \\ x = 1, \qquad \frac{\partial T_R}{\partial x} = 0, \qquad \frac{\partial T_w}{\partial x} = 0 \end{gathered} \quad \text{Eq. 4.28}$$

This arrangement consists of three partial differential equations, for the fluid, for the regenerator and for the wall. Distance and time are independent, and the temperatures of the fluid, regenerator and wall are to be obtained. These equations are of the second order, forming parabolas affected by the boundary conditions [137].

4.3.4. Numerical Scheme

An explicit finite difference scheme is used to solve the parent equations for this single blow model. It has an accuracy of the second order in distance and time. Afterwards a correction method was applied, the Crank - Nicolson scheme, to refine the results. Then the results were compared with those obtained by the Kohlmayr analytical solution [132].

To solve the equations of the fluid, solid and wall a discretisation process took place to define the positions of each in distance and time. Considering that the radial conductivity was not taken into account, since the samples had lower NTU_R values than 150, discretisation was performed only in the direction parallel to the movement of the fluid.

To near each component of the partial differential equations, the following approximations were applied:

Second Order Centre Space

$$\frac{\partial^2 T}{\partial x^2} = \frac{T_{i+1}^{l} - 2T_i^l + T_{i-1}^{l}}{\Delta x^2} \qquad \text{Eq. 4.29}$$

First Order Forward Time

$$\frac{\partial T}{\partial t} = \frac{T_i^{l+1} - T_i^l}{\Delta t} \qquad \text{Eq. 4.30}$$

First Order Forward Space

$$\frac{\partial T}{\partial x} = \frac{T_{i+1}^{l} - T_i^l}{\Delta x} \qquad \text{Eq. 4.31}$$

These equations were introduced to the partial differential equations of the fluid, solid and wall, obtaining:

$$\begin{gathered}
\frac{T_{Airi+1}^{l}-T_{Airi}^{l}}{\Delta x}+NTU_R(T_{Airi}^{l}-T_{Ri}^{l})+NTU_w(T_{Airi}^{l}-T_{wi}^{l})=0\\
\frac{T_{Ri}^{l+1}-T_{Ri}^{l}}{\Delta\tau}-\lambda_R\frac{T_{Ri+1}^{l}-2T_{Ri}^{l}+T_{Ri-1}^{l}}{\Delta x^2}+NTU_R(T_{Ri}^{l}-T_{Airi}^{l})=0\\
\frac{T_{wi}^{l+1}-T_{wi}^{l}}{\Delta\tau}-R_{tc}\lambda_w\frac{T_{wi+1}^{l}-2T_{wi}^{l}+T_{wi-1}^{l}}{\Delta x^2}+R_{tc}NTU_w(T_{wi}^{l}-T_{Airi}^{l})=0
\end{gathered}\qquad \text{Eq. 4.32}$$

From these equations it can be noted that the solution of each point depends on the solution of the previous point in time (*l, l+1*) and distance (*i, i+1)* [137].

Consideration has to be taken in the number of calculations the equations will entail. If the difference between time points (Δt) and distance points (Δx) are close to zero the data will reach the actual value of the solution but it will increase the computation time. If the difference between time points (Δt) and distance points (Δx) is substantial the computation time is short but the solution may not be balanced or it may have poor convergence.

To obtain an acceptable solution, which is stable and will converge, the value of the diffusion number ($\delta i = \lambda_R(\Delta\tau/\Delta x^2)$ [138] will be a maximum of 0.5. It is recommended for this value to be lower than 0.17 to minimise the inaccuracy of the solution. For the samples tested in this study, the diffusion number was maintained lower than 0.5. Since this value is dependent on λ_R for each sample, the difference in time and distance was obtained to guarantee a balance between having convergence and stability while considering computing time for the solution.

For fine tuning of the results the Crank - Nicolson method was applied to the equations of the regenerator and the wall (Eq. 4.25 and Eq. 4.26). Several repetitions were performed until the temperatures of the regenerator, wall and fluid converged. To apply this method the value of *l+1* must be known, if the value is nonexistent, or it has not been found, the solution cannot be achieved. This is the reason why the method is applied as a correction method after the explicit method to improve the results, reaching towards the actual solution [115], [129].

The equations for the Crank - Nicolson method are:

$$\begin{aligned}T_{Ri}^{l+1} = T_{Ri}^{l} &- \left(\frac{2\lambda_R \Delta t_a}{\Delta x^2} + NTU_R \Delta t_a\right)\left(\frac{\overline{T_{Rl}^{l+1}} + T_{Ri}^{l}}{2}\right) \\ &+ \frac{\lambda_R \Delta t_a}{\Delta x^2}\left(\frac{\overline{T_{Rl+1}^{l+1}} + \overline{T_{Rl-1}^{l+1}} + T_{Ri+1}^{l} + T_{Ri-1}^{l}}{2}\right) \\ &+ NTU_R \Delta t_a \left(\frac{T_{Airi}^{l+1} - T_{Airi}^{l}}{2}\right) = 0\end{aligned} \qquad \text{Eq. 4.33}$$

$$\begin{aligned}T_{wi}^{l+1} = T_{wi}^{l} &- R_{tc}\left[\left(\frac{2\lambda_w \Delta t_a}{\Delta x^2}\right)\left(\frac{\overline{T_{wl}^{l+1}} + T_{wi}^{l}}{2}\right)\right. \\ &\left. + \frac{\lambda_w \Delta t_a}{\Delta x^2}\left(\frac{\overline{T_{wl+1}^{l+1}} + \overline{T_{wl-1}^{l+1}} + T_{wi+1}^{l} + T_{wi-1}^{l}}{2}\right)\right] \\ &+ NTU_R \Delta t_a R_{tc}\left(\frac{T_{Airi}^{l+1} - T_{Airi}^{l}}{2}\right) = 0\end{aligned} \qquad \text{Eq. 4.34}$$

This numerical solution value was evaluated against the original value (without correction scheme), the difference between them in the exit temperature was 0.6%, with the numerical solution value being lower by this percentage.

4.3.5. Effect of the Regenerator Characteristics on Exit Temperature

To interpret the effect of the regenerators' properties the curves are defined by the relation between the NTU_R value and the maximum gradient of the exit temperature curve [132]. The ideal regenerators will have a high value of maximum gradient, if the NTU_R value of the sample is larger the exit curve gradient will increase.

To increase the NTU_R value of a regenerator the surface area value must be higher, or the flow rate of the fluid passing through must be lower. Both of these characteristics will increase the maximum gradient.

When searching for the NTU_R value the effect of the wall must be considered. This is obtained by estimating the values of the number of transfer units on the wall, the heat capacity relationship between the regenerator and the wall and the thermal conductivity of the wall [132].

The heat in the fluid will transfer towards two elements, the regenerator sample or the wall. If the heat crosses through the wall it will not pass through the regenerator, diminishing its thermal performance.

The longitudinal heat transfer through the regenerator depends on the type of material the regenerator is made of and the structure it possesses. The effect can be changed by altering the thermal conductivity, which has an inverse effect on the maximum gradient of the exit temperature curve.

The regenerator prevents contact between the low and high temperature sides of the system. If its longitudinal thermal conductivity value is small it fulfils the isolation role, increasing the efficiency of the cycle.

The relationship between the heat capacity of the regenerator and the heat capacity of the wall (R_{tc}) indicates that if the regenerator's heat capacity value increases and the heat capacity value of the wall decreases, the efficiency of the regenerator will be higher, which is observed as an increase of the maximum gradient. If this effect is not considered when obtaining the results the NTU_R value of the regenerator will be falsely enhanced [132].

The inlet temperature response time (ψ) is the time it takes the inlet temperature to achieve stability, it depends on the equipment efficiency. If the response time is reduced the results will be less reliable. The NTU_R may be undervalued if this effect is not considered [132].

In Chapter 5 an explanation of how these factors affect the exit temperature curve is given in more detail.

4.3.6. Curve Matching Methods

After applying and solving the model for the exit fluid temperature curve the predicted curve needs to be matched with the curve obtained from the experimental data. Duplicating the curve exactly is somewhat ambitious, considering experimental errors and discrepancies from the model's results. There are a few techniques that can be applied to solve these issues in the single blow method by simplifying the part of the data where fitting is sought.

a) Maximum Slope Method

There is an intricate relationship between the NTU_R of a regenerator and the maximum slope value of the outlet curve, and a method using this was developed by Locke [123]. The data from the experimental exit curve is derived once and matched with the predicted model. The matching is done over a single point, the maximum gradient value. The technique has been used extensively [124], [125], it can be applied to regenerators with an NTU_R value larger than 2 [132].

b) Selected Point Matching Technique

For this technique only a certain number of points are used to predict the NTU_R value of a regenerator. Since matching the entire curve is practically impossible only part of the curve is matched. Some researchers considered a perfect response time (ψ) and matched the curve only in a certain area [139], however, this technique was only valid for NTU_R values up to 20.

For the selected points matching technique different points in the experimental curve are chosen, which then are matched with the predicted value from the model for that time, obtaining a tentative theoretical NTU_R value. This is done with other points in different times, to obtain the actual NTU_R the mean of all these values is considered [121], [133].

c) Differential Fluid Enthalpy Method

This is a slightly more complicated technique since it involves the specification of the testing equipment's NTU_R value from the fluid to the wall, the time constant of the thermocouples, regenerator specific heat and time constant of the temperature signal at the entrance. For this technique the temperature values from the inlet and outlet were integrated considering time as a reference. The values are multiplied by the ratio of fluid capacity then deducted from each other to have the enthalpy difference between those two points [140].

d) Least Squares Method

In this technique the matching takes place over all of the data using the least square error, it is also known as direct curve matching. In previous experiments [141] the comparison between experimental and model predicted data was made using several techniques. The NTU_R value obtained with the differential fluid enthalpy method and the least squares method was overestimated, considering that the step change in these experiments was not fast enough, allowing the temperature at the entrance to escalate progressively and affecting the exit temperature curve. However small this variation in the exit temperature is, the maximum gradient will be affected, which is the reason why the response time at the entrance should be minimal.

4.4. Summary of the State of the Art

Regenerators used for Stirling engines are commonly stainless steel wire meshes of several sizes, mesh 100 (150 μm) and mesh 200 (75 μm) are common, their dimensions vary, their length ranges from 20 to 75 mm and diameters from 14 to 160 mm, depending on the engine that holds them.

Research has explored the use of porous metals in general, and examples have been tested in a varied array of configurations such as in experiments performed by Du Plessis [111], Bhattacharya [107] and Boomsma [96]. However these tests were all done on different rigs in different ways (air or water as the working fluid for example), and there is no comparison across an array of different structures and materials through the same tests measuring both pressure drop and heat transfer through the regenerator matrix.

Therefore, it would be of great value to make a systematic assessment of parameters relating to heat transfer and flow behaviour for a wider variety of porous structures made from different materials, under conditions of potential relevance to the Stirling engine. This is the focus of the work described here, and this, along with the assessment of many types of porous material not previously analysed, is the main original contribution of the work.

Chapter 5. Experimental Methods: Apparatus, Processing and Data Interpretation

The goal of this work is to understand the capabilities of different materials and structures as regenerators, and to find potential new candidate materials for regenerators. For the latter goal, the requirements for a regenerator are set out in Table 1.1. The material and structure that is currently used as a regenerator is the 200 stainless steel mesh, and this is the baseline regenerator for this work.

From the requirements of a regenerator a broad array of samples were tested for heat transfer and flow behaviour.

For many of these samples aluminium was used for its ease of structure tailoring with the replication process and its high specific heat, copper was chosen for its high thermal conductivity and density; chrome steel was chosen to compare against stainless steel, having similar values except for the thermal conductivity, which is higher; soda glass was chosen to compare its low thermal conductivity value against stainless steel and Ti6Al4V was chosen to compare against the stainless steel porous structure made by additive manufacturing.

After collecting the data, identification of the best materials, and the ranking of the remainder, is done by considering a summation of the performance relative to the key attributers defined in Table 1.1. While this method does not take into account different emphasis that may be placed on different attributes (for example heat capacity may have a greater effect on efficiency), it provides a basis for comparison of materials.

Considering the properties of stainless steel, which is the material most commonly used for regenerators and basing the selection on a high density, high specific heat a material selection chart considering these properties can be developed and is shown in Figure 5.1.

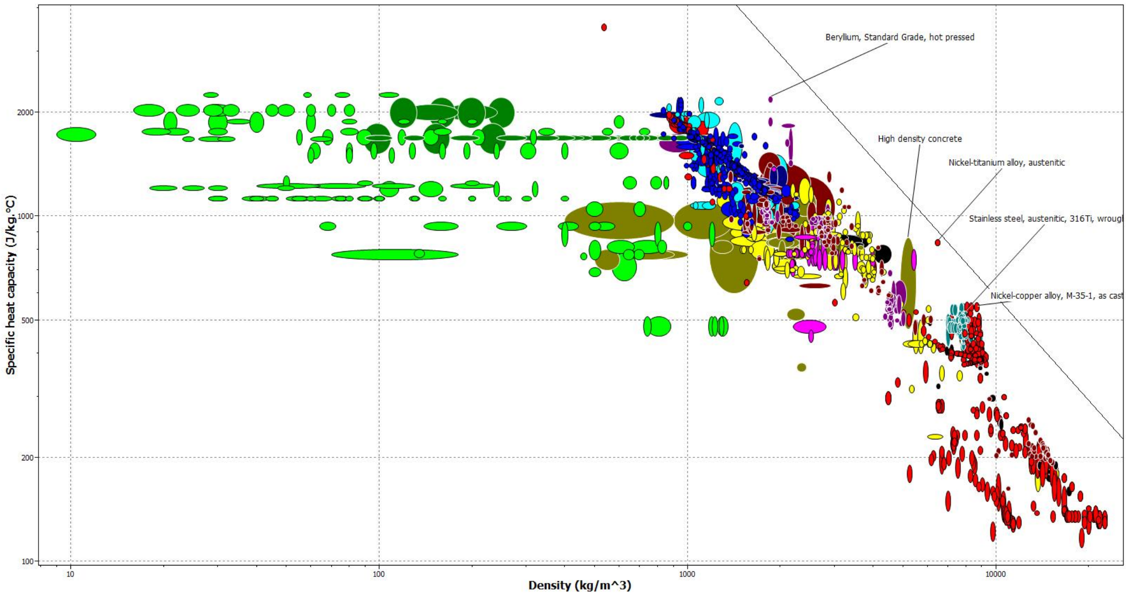

Figure 5.1 - Tentative regenerator material selection chart based on density and specific heat.

From this chart it can be seen that when considering these two properties stainless steels are close to the limit of what is available, the others being nickel-copper alloys and the closest material to this limit nickel-titanium alloys (Nitinol), however, now cost would come into consideration as comparing it to steel it is 400 times more expensive [197]; for this work out of the materials from the chart only the stainless steels 304L, 316L, 420 and chrome steel were available, aluminium was chosen since it was the easiest material to work with for creating the replicated porous metals, copper and soda glass were chosen to compare the others against a material with a very high and very low thermal conductivity. Initially the experimental methods used to create and test samples will be described.

5.1. Replication Process

The space holder technique or replication method [3] is one method used to produce porous metals. The molten metal is infiltrated around a space holder or preform which has the purpose of keeping the pore space free of metal until it is eliminated by a chemical method (such as dissolution) or by increasing the heat (causing chemical breakdown and evaporation). NaCl was first used to produce porous aluminium, and has since been a frequent choice for the space holder material [8], [147]. This method was first attempted in 1965 [148], it was seen as cheap and safe, since NaCl is non-toxic and can be dissolved with water. In the method the cell diameter can be modified by the space holder's particle size and the porosity changed by the density of the preform packing, pressure applied to infiltrate and precise technique used [8].

In this investigation porous metals were made by implementing the space holder technique, using 99.7% pure aluminium (*William Rowland Ltd, Sheffield*) and NaCl as the preform material. To obtain an array of samples, three different preform particle sizes were used (1.09 mm, 1.55 mm and 2.18 mm). For these porous metals the packing method was at random, meaning that the NaCl particles were simply poured into the infiltration mould. Another batch of replicated porous metals was made to analyse the packing method, using only one size (1.55 mm) of NaCl particles; this time the space holder was vibrated for 1 minute to ensure the NaCl particles were closer between them than the ones from the non-vibrated preforms leaving less free space. When the mould was prepared and sealed with an ingot of aluminium placed above and melted, the molten aluminium is pushed into the preform by argon gas pressure.

The infiltration method was modified, improved and developed during this investigation (discussed in detail in Chapter 6). In this chapter the equipment used in the space holder arrangement, metal infiltration, the outcome of different infiltration pressures and sample extraction, the production of the other types of samples (meshes, felts, ball bearings and ALM porous metals) and the flow and heat transfer equipment to measure and analyse all the produced specimens will be discussed.

The preforms are made with Hydrosoft water softening NaCl granules (http://www.aquadition.co.uk/shop/granular-water-softener-salt-25kg/). The granules are separated into different size ranges using six stacked sieves, the NaCl particles collected are from the green coloured sieves (2.00 mm, 1.40 mm and 1.00 mm) for the respective preform range, this is explained in Figure 5.2.

Figure 5.2 - Stacked sieves diagram to obtain the three preform sizes used in this work.

The granules left in the 2 mm sieve are smaller than 2.36 mm and larger than 2 mm, their average is 2.18 mm, they are used as the preform for the "C" samples. The granules left in the 1.4 mm sieve are smaller than 1.7 mm and larger than 1.4 mm, their average is 1.55 mm, they are used as the preform for the "B" samples. The granules left in the 1 mm sieve are smaller than 1.18 mm and larger than 1 mm, their average is 1.09 mm, they are used as the preform for the "A" samples.

Additionally, three sets of samples were made to observe the effect of the packing density of the preform. This characteristic varies in an inverse way to the porous metal porosity. If the space holder particles are simply randomly loaded into the infiltration container the highest porosities that can be obtained are around 70%.

In addition, other porous metal samples were produced using different methods to have a wide array for comparison with the porous aluminium samples.

In the following section the equipment and techniques used to produce porous metal samples by replication is presented.

5.2. Replicated Porous Metal Manufacturing Equipment

5.2.1. Apparatus

For producing porous metals by replication with the vacuum - argon or the argon only methods the apparatus needed is composed of a top loading electrical resistance furnace, an airtight stainless steel infiltration chamber, a vacuum pump, valves and pipe system, supply of argon gas and a copper block for longitudinal cooling from bottom to top. In Figure 5.3 the porous metal production equipment is shown.

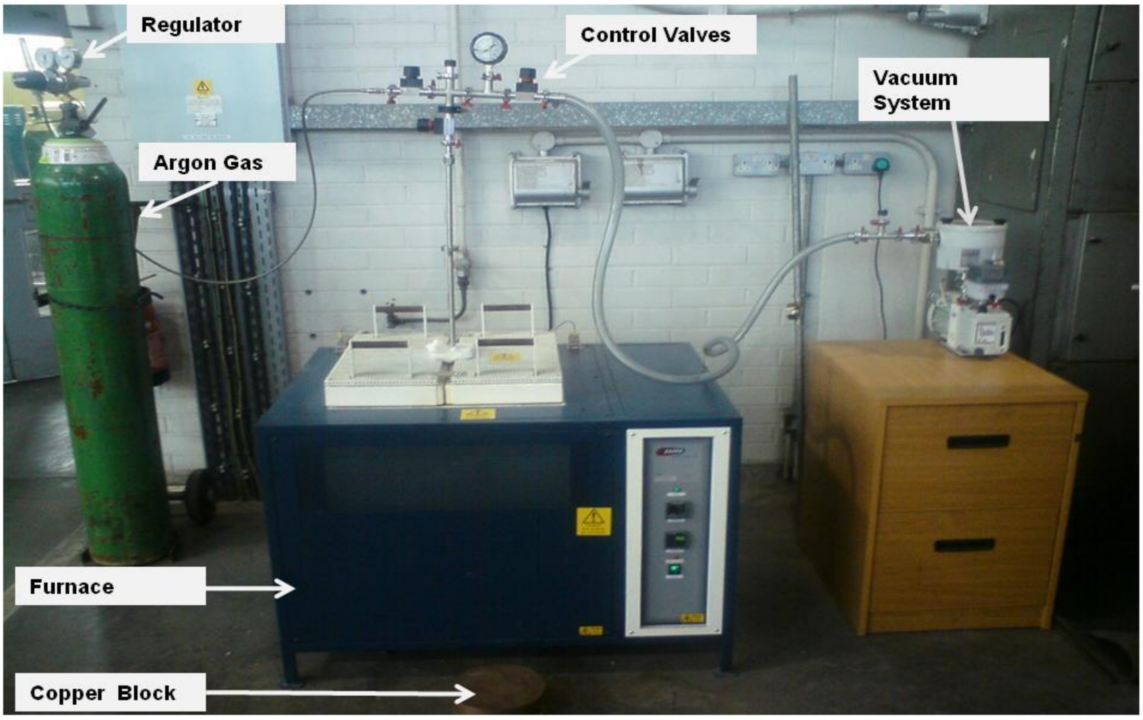

Figure 5.3 - Porous metal infiltration equipment.

The infiltration mould and the connecting part of the pipe system are made from stainless steel, and they are attached to the argon gas tank and the vacuum pump via two hoses and the pertinent accessories. The argon gas has a 10 bar regulator installed and the vacuum pump a manometer to measure the vacuum level.

There are four valves and a vacuum manometer in the pipe system, valve A is used to allow the argon gas to pass towards the "+" fitting, valve B allows the vacuum to do the same and valve C controls the connection between the + fitting and the replication chamber, the relief valve sits at the top; in Figure 5.4 the valve system can be seen.

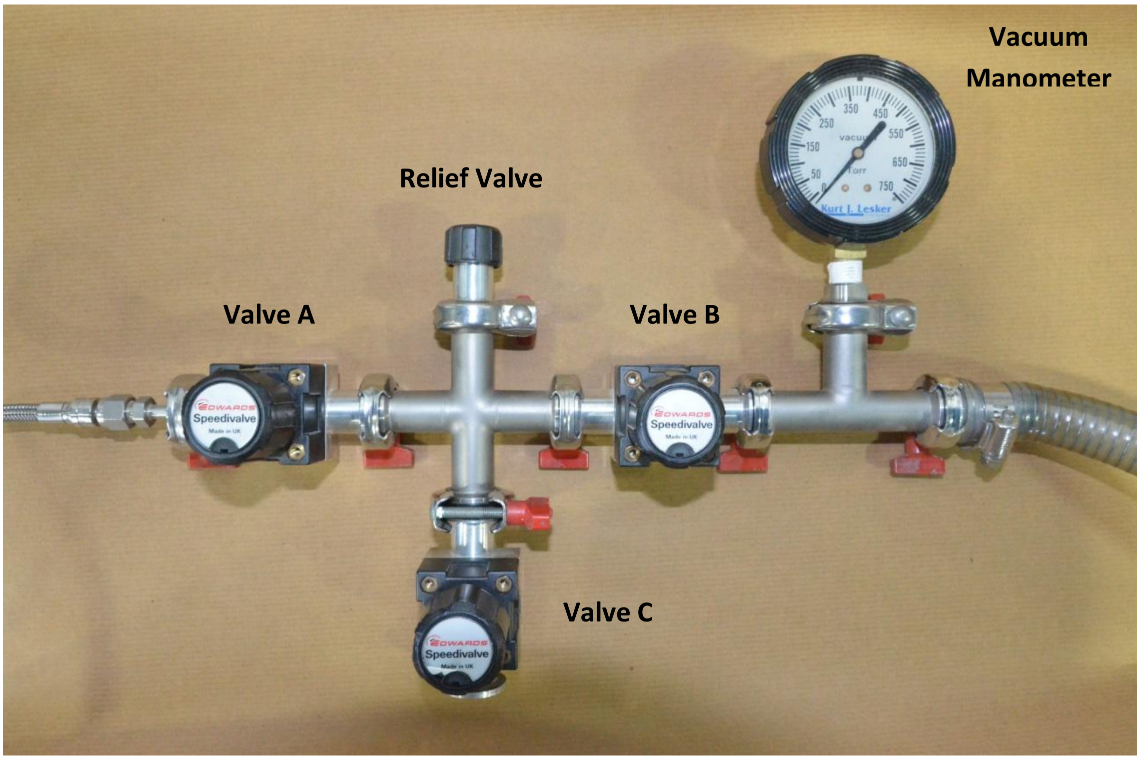

Figure 5.4 - Infiltration valve system.

The infiltration mould is shown in Figure 5.5, and is composed of a chamber wall, a base and a lid which has a welded stainless steel pipe leading up to the valve system. The parts are kept together by four stainless steel threaded rods attached to the base with four 13 mm M8 chrome steel nuts. The chamber wall is placed in a groove machined into the base, and the lid, which also has a groove matching the chamber wall machined into it, is placed on top; the rods go through the lid to be attached by another group of four chrome steel nuts. Graphite paper is cut to discs fitting into the machined grooves on the top and the bottom of the chamber wall, and as the nuts are tightened the force causes the graphite paper to be sandwiched between the chamber wall and the top and bottom plate, forming a seal. Initially stainless steel nuts were used for durability, however, after some tests it was found that the nuts harmed the rods' threads, leading to a decision to use chrome steel nuts instead. Nevertheless, these lasted for a maximum of a small number of runs, and were usually discarded after one cycle for consistency in the results and preventing leaks of the vacuum or gas pressure.

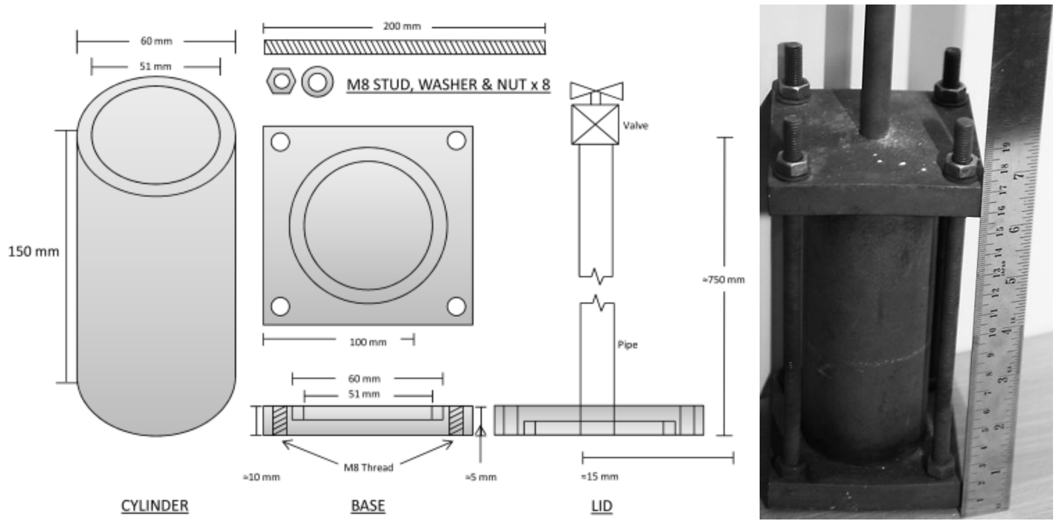

Figure 5.5 - Infiltration mould schematics and image [149].

5.2.2. Processing

The procedure to make a porous aluminium sample is as follows. Initially it was discovered that by placing irregular aluminium pieces in the infiltration mould the samples produced were different from one another. To have more consistent results it was observed that the interior edge of the mould should be close to the aluminium block at all points. For this reason and after several trials, it was decided to recast the aluminium bar feedstock into sizes slightly smaller than the interior diameter of the infiltration mould, which is 51 mm. For efficiency, four steel moulds were made for this purpose with an interior diameter of 50 mm. 99.7% pure aluminium ingot was placed in a crucible in a furnace at 800°C for an hour, and was then poured into the four steel moulds to produce the bars. These bars were cut into four pieces each, providing cylindrical ingots of roughly 200 g for each run.

The infiltration mould was prepared by first taking the separate parts (the chamber wall, lid and base) and sanding away any impurities or build up from previous experiments. Special care was taken with the top and bottom edges of the chamber wall since they make the seal which holds the gas pressure or vacuum depending on the infiltration method. The inside of the mould was sprayed with a thin coat of boron nitride powder in aerosol form to prevent the bonding of the molten aluminium with the stainless steel wall; care was taken to get full coverage of the inside of the chamber. The top and bottom edges of the chamber wall were kept free from boron nitride spray to avoid leaks. Graphite gasket rings were used as a seal between the mould cylinder and the base and the lid.

To prepare the space holder the NaCl particles must be sieved to the chosen size range; the size of the particles used has an almost exact relationship with the size of the pores in the porous metal. For this operation two sieves are needed, and a container and lid as well to contain the material while sieving takes place. After pouring a sufficient quantity (around 500 g) of NaCl in the top, larger mesh size sieve, the lid was placed on top, with the finer mesh size sieve below and the container to collect fines below that. The stack was then agitated manually or in a sieve shaker for 1 minute. Depending on the porous metal sample height required, the amount of NaCl that needs to be placed in the mould, can vary between 100 g and 300 g.

After the boron nitride coat was dry, the NaCl was poured into the mould and the pre-cast aluminium bar added on top. The height of the chamber was 15 cm, and it was found that after placing the NaCl to be infiltrated at the bottom and the aluminium bar on top, if there was a considerable (more than about 1 cm) gap remaining between the aluminium bar and the mould lid, irregular samples were common. This issue was solved by adding more aluminium on top of the bar, which could be another piece of the pre-cast aluminium bar or irregular pieces of aluminium ingot, just sufficient to fill the empty space; the shape of the extra piece (or pieces) were not found to have an effect. It was also important for more consistent successful infiltrations that the whole bottom face of the pre-cast aluminium bar was in contact with the top face of the NaCl particles to be infiltrated.

5.2.2.1. Vacuum - Argon Infiltration

This technique was used initially, following the same procedure for mould preparation, with the 51 mm diameter mould and another mould of 100 mm diameter. After adding the NaCl particles of the space holder and the aluminium bar on top the graphite gasket was placed in the groove and the lid placed on top of the chamber. The chamber was then closed by tightening the nuts on the rods. Valve A was closed, valves B and C were opened, and the vacuum pump was activated to remove the air from the infiltration cylinder and pipes. If the system had a good seal, the pressure in the vacuum gauge would read around 50 Torr, which was used as a confirmation check before the chamber and pipe system were put in the furnace.

The heating pattern for this method had two heating ramps with a dwell time in between and another after reaching infiltration temperature. Both ramps have a heating rate of 10°C per minute. The first dwell time is for 30 minutes at 400°C, and is to reduce thermal gradients and ensure that all components are at the same temperature before reaching the infiltration temperature, which is set at 740°C. The second dwell time was set at two hours, to ensure the aluminium is fully melted before infiltration. Ten minutes before infiltration, valves B and C are closed and valve A is opened to allow the argon gas to pass into the cylinder.

Too little gas entering the chamber will not provide sufficient pressure to drive the aluminium into the NaCl (aluminium does not wet NaCl and so will not spontaneously flow in between the NaCl particles), causing limited infiltration. This was found to occur for pressures somewhat below 1 bar. If the pressure is very high (above around 3 bar), the flow rate of gas into the mould will be great, and will hit the molten aluminium with force, producing a jet of gas which can penetrate through the aluminium, and disturb the NaCl particle packing, leading to poor infiltration and defects. It was found that the best range of regulator pressure for good infiltration results was between 1.5 and 2 bar. However the results obtained were not always consistent, and a contributing factor to this is the vacuum seal, which was not always of consistent quality.

After letting the gas into the chamber, the chamber was left in the furnace for ten minutes under the same pressure, then taken out and set down on top of a cylinder shaped copper slab at room temperature, to promote longitudinal cooling (from bottom to top) over inward cooling (from the edges to the centre), such that shrinkage in the metal on final solidification took place outside the NaCl particles. It was essential for valve A to remain open to maintain the gas pressure constant in the chamber until the porous metal was fully solidified (around 5 minutes), preventing possible sudden changes in the sample structure. This technique was reported not to be satisfactory (Figure 5.6) when porous space holders were used [14], and the pressure was too high; as the liquid metal was found to have crept into the miniature cracks of the space holder due to the differential pressure between the vacuum they contained and the pressure applied.

Figure 5.6 - Unsuccessful porous metal samples due to porous space holders and overpressure.

5.2.2.2. Mechanical Pressure Infiltration

As discussed previously, to cause infiltration, the molten metal requires a force to act upon it and move it in the required direction, overcoming its natural tendency not to wet the NaCl. A new method was trialled using a manually-displaced piston rather than a gas pressure to achieve this. The piston was accommodated into an extra lid for the 51 mm mould, and a new mould was designed to test production of a smaller size of porous metals at 20 mm in diameter. In Figure 5.7 the 51 mm and 20 mm mechanical infiltration moulds are shown. The intention was that applying pressure in this way would allow greater sensitivity and control at the low pressure end of infiltration; with gas pressure the difference between the pressure required to cause infiltration and a pressure which would lead to almost isolated pores might be low compared to the precision of the regulator.

Figure 5.7 - Mechanical infiltration moulds, 51 mm (left) and 20 mm (right).

Another basic difference of this technique when compared with the gas and vacuum method is that instead of pushing the molten aluminium around the space holder, the manual piston pushes the preform into the molten aluminium. The reason for this was that if the piston was pushed into the liquid metal a very good seal would be required around the piston to prevent the metal flowing back out past it (liquid aluminium being very fluid), and not all of the preform would then be infiltrated (in addition the piston would become blocked in the cylinder on solidification). Having a good seal would require high forces to move the piston, and the good control that was sought would have been lost.

The key characteristic of the samples made using this method was that the porosity was found to be not uniform throughout the volume. The porosity at the edge of the sample is irregular (Figure 5.8), this is caused by the fact that the aluminium is not directly pressurised, the pressure is coming through the bed of NaCl particles, producing a higher pressure gradient through the bed when compared to the other methods.

Figure 5.8 - Unsuccessful samples produced with the mechanical infiltration method.

To try and obtain more homogeneous samples, the infiltrating temperature was changed to alter the viscosity of the molten aluminium. The initial operating temperature was set at 740°C, obtaining the results discussed above. At 760°C the molten metal flowed better, however, a greater quantity accumulated at the bottom of the sample, producing a greater difference in porosity between the bottom and top parts, without solving the porosity issue at the edge of the cylinder; also, the NaCl particles in the preform started to merge together due to the temperature being closer to its melting point (801°C) under the force received from the piston.

An explanation for this phenomena may be the solidification shrinkage of the aluminium [153], this effect may be pulling the aluminium towards the bottom of the sample where it first solidifies; this effect is routinely encountered in casting, for example when producing the aluminium bars for infiltration. When pouring the liquid aluminium into the 50 mm steel mould, care had to be taken when the change in temperature created a void in the bar, prompting the addition of more liquid metal to compensate for this effect.

At 720°C the results seemed to improve, with little difference between the porosities of the bottom and the top and less difference from the porosities at the edge compared with the centre, the downside of this temperature was that since the viscosity of the aluminium is lower, greater force is needed to move the piston, possibly with the assistance of a press the procedure would have been achievable for a larger quantity of samples but this once again may limit the precision and, if higher pressures are applied, the risk of failure of the chamber increases with repeated use. The successful porous metals made by the method had a porosity of roughly 70% and samples with the three pore sizes were achievable. In Figure 5.9 a successfully produced sample can be seen.

Figure 5.9 - Successful sample produced by the mechanical infiltration method.

These samples were made with the intention of finding an alternative manufacturing method to the vacuum - argon and argon only techniques, yet the smaller size mould was not suitable for making samples of a large enough sample size to pore size ratio to reproducible results on testing. The same technique was run with the 51 mm chamber, but with the increase in cross sectional area, it needed a greater force to push the preform into the molten metal, magnifying the concern of damaging the mould. A small number of samples were made at 760°C, with the same defects as the 20 mm samples.

5.2.2.3. Argon Only Infiltration

The defects noted in the techniques described before meant that an improved technique was required for the work presented here. The main method used for the samples discussed was argon only infiltration. Using spherical granular NaCl, the mould and chamber are prepared in an identical manner to the vacuum - argon method. The closing and opening of the valves and the infiltration procedure is however different. When the mould has been joined to the valve system the chamber undergoes a seal test, initially all valves are closed then valves B and C are opened, the vacuum pump is turned on to withdraw the air from the infiltration chamber and ducts, and the vacuum pressure gauge should read around 50 Torr if the arrangement has an acceptable seal.

However there is in addition a second part of this check; the vacuum pump is turned off and the pressure in the chamber monitored. The vacuum value of 50 Torr should hold for at least 5 seconds before it starts to climb slowly (at a rate of less than 50 Torr per second). Indication of failure in this test would be if by turning off the vacuum the gauge needle jumped quickly or the value started to climb rapidly. The most common issue for this was fund to be an incorrect torquing of the nuts closing the lid, although other instances occurred from time to time such as a damaged base or lid gasket or an incorrect positioning of the base or lid in their respective grooves. If the test is passed, valve B is closed and the relief valve of the system is opened to allow atmospheric air in, the chamber is placed in the preheated furnace.

Initially the heating pattern for this method was the same as for the vacuum - argon method. However, after many trials it was found that the time could be reduced considerably per sample. The previous profile had been developed for a chamber under vacuum where heat transfer would be low. The presence of air however allows convection to operate and speeds up the rate at which the aluminium becomes heated and melted. The new pattern has only one heating ramp with a dwell time after reaching infiltration temperature of at least fifty minutes, sufficient time to melt the aluminium bar piece and ensure homogeneity. The heating rate for the ramp is 20°C per minute, the infiltration temperature is set at 740°C. A minute before infiltration, valve C and the relief valve are closed. The infiltration pressure is set using the cylinder's regulator, and valve A is opened swiftly to allow the argon gas to pass into the cylinder.

Infiltration with this approach presents the same concern as with the vacuum - argon method, valve A has to be opened rapidly as, if the gas flowing into the chamber is slow, it may be able to find its way through the small crevices in the boron nitride layer between the mould wall and the aluminium, filling up the free space between the preform particles and so preventing the aluminium from occupying those parts on infiltration. For each particle size of the preform, the infiltration pressure had to be varied slightly, smaller particle size, larger infiltration pressure, although not by much. In Table 5.1 the pressure values for each particle size used are given.

Particle Size (mm)	**Infiltration Pressure (bar)**
1.09	3.5
1.55	3.0
2.18	2.5

Table 5.1 - Initial infiltration pressures applied to obtain a replicated porous metal.

This infiltration pressure has a great effect on the porosity and by consequence the pressure drop required to cause air to travel through the structure. The void space between the NaCl particles remaining unfilled by aluminium decreases as the infiltration pressure increases, which reduces the aperture between the pores in the structure.

After infiltration, the cylinder is left under the argon gas pressure in the furnace for one minute, then taken out and set on the copper slab at room temperature for longitudinal cooling. Valve A was left open for five minutes to keep the pressure until solidification of the metal. This technique may be applied to porous space holders [14], with less risk of the metal getting into the pace holder internal pores. In Chapter 6 an evaluation of the different infiltration pressures used is shown and the effects produced on the samples. As well as a more detailed explanation of the replication process development.

The general technique for porous metal processing described in this work has been applied by other investigators in many ways. While making these samples the porosity targeted is on average 70%, except for the ones produced with the vibration method, which have on average 76% porosity.

To compare the regeneration performance of the porous metal samples made by the replication method other porous metal samples were created; the first structure is the wire mesh, which is a structure that is commonly used to make regenerators.

5.3. Wire Mesh Sample Manufacturing

Four sheets of different size 10 (10 wires per inch, 2 mm holes), 20 (20 wires per inch, 1 mm holes), 30 (30 wires per inch, 0.5 mm holes), 200 (200 wires per inch, 75 μm holes) stainless steel 304L woven wire mesh were obtained from Inoxia (*www.inoxia.co.uk*) as raw material to produce the stacked wire mesh samples to test as regenerators.

To reach the target diameter of 51 mm a Norton 6DB Fly Press was used. The mesh sheets were cut into 60 mm squares and were stacked in sets of 5 sheets per operation round of the fly press. The sheet set was placed between two slabs of thin (1.5 mm) aluminium to ensure even cutting of the stainless steel sheets by the fly press.

After the amount of layers were processed the stacked sheets were kept together by threading them with a thin (0.025 mm) stainless steel wire on 8 points of the cross section forming a knot at one end; this procedure was applied to the 10, 20 and 30 meshes. For the 200 mesh since the pores were considerably smaller than the other meshes the sheets were joined by surrounding them with the wire twice, instead of threading. In Figure 5.10 the fly press, mesh sheets, aluminium plates and a finished sample can be seen.

The next structure to produce is the wire felt, these samples can be interpreted structure wise as an in between structure of the replicated and the mesh samples, since these are made using wires (like the mesh) but with an irregular pattern of pores (like the replicated porous metals).

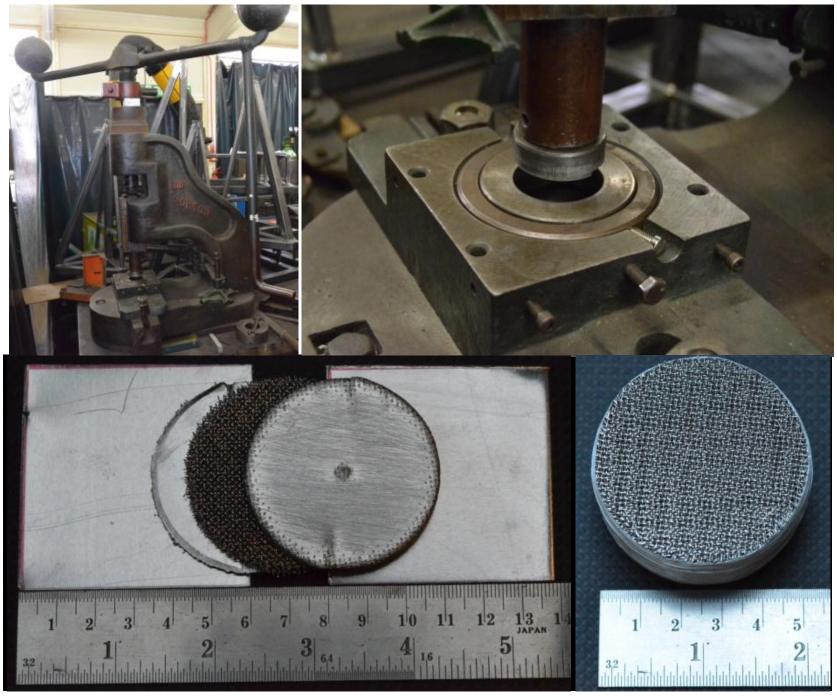

Figure 5.10 - Equipment used for the production of the wire mesh samples.

5.4. Pressed Wire Felt Sample Manufacturing

Three 500 m rolls of the same size diameter wire (0.25 mm) made from three different materials (commercially pure 99.5% aluminium, commercially pure 99.9% Copper and AISI 304L stainless steel) were obtained from Advent Research Materials (*www.advent-rm.com*) as raw product to manufacture the regenerator wire felt samples.

Initial trials to produce a pressed wire felt sample showed that a variation in the wire length was necessary. If the wires were of the sample were on average 100 mm in length, while pressing the wires certain patterns emerged which was undesirable for the aim of achieving a random pressing of the wires. To avoid the patterns, in the next trial, the wires were cut to an average length of 25 mm; this produced a sample without obvious patterns but it proved too brittle, it could not be handled properly.

The suitable option was a mix of lengths, 80% of the wires were 100 mm in length on average and 20% of the wires were cut to a length of 25 mm. This technique proved best, the short wires reduced the pattern formation and the long wires prevented the sample from breaking into pieces.

Once the wires were cut they were placed in a 51 mm diameter steel mould and a plunger placed on top. A manual hydraulic press was used at a pressure of 2 metric tons to produce the samples. Aiming for a sample of 51 mm in diameter and 25.4 mm in length with a porosity of roughly 70%; a length of between 300 and 310 metres of wire was cut for each sample in pieces at the stated lengths. In Figure 5.11 the cut wires, mould, manual hydraulic press and finished sample can be seen. The next section explains the production of the packed spheres samples, this structure is used in flow and heat transfer applications as well.

Figure 5.11 - Equipment used for the production of the wire felt samples.

5.5. Packed Spheres Sample Manufacturing

Five packs containing 10,000 spheres with a nominal diameter of 2 mm made from different materials (commercially pure 99.5% aluminium, AISI 52100 Chrome Steel, commercially pure 99.9% copper, AISI 420 Stainless steel and Soda Lime Silica Glass) were obtained from three different companies, GMS Ball Company Limited (*www.gmsball.co.uk*), Dejay Distribution Limited (*www.dejaydistribution.co.uk*) and VWR (*uk.vwr.com*) as raw material to assemble the packed spheres samples for regenerator testing.

To contain the packed spheres cages made from a circumference of acetate sheet and two stainless steel 304L wire mesh (1.5mm pore size) lids were built. The lids were threaded to each other on the exterior part of the circumference at 8 points after placing the spheres inside the cage. Porosities from 38 to 42% were achieved, in packing range comparable to previous experiments [93]. In Figure 5.12 the spheres, cage and finished sample can be seen.

Currently there are other techniques available to produce porous metals via CAD design, taking advantage of this, the following section explores the Selective Laser Melting production technique.

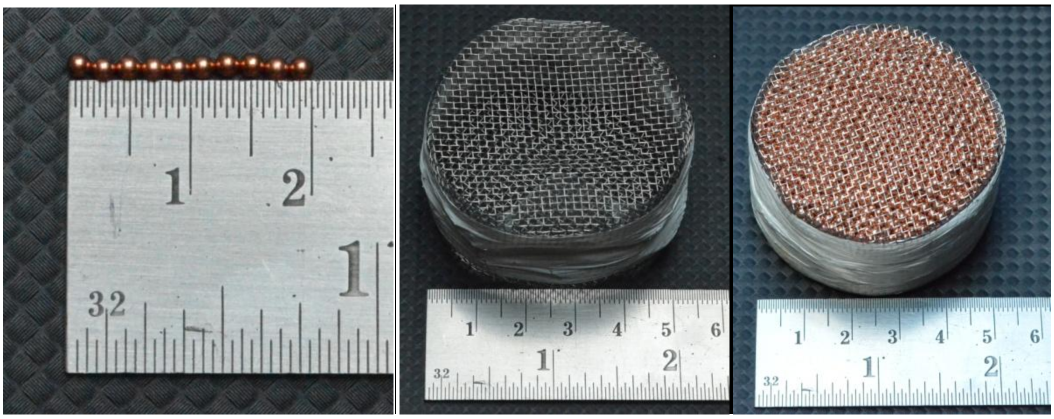

Figure 5.12 - Equipment used for the production of the packed spheres samples.

5.6. Selective Laser Melting (SLM) Sample Manufacturing

Five samples made by multiple runs of Selective Laser Melting were produced using the same CAD file used to produce the Ti6Al4V porous samples [154] in section 5.7.

The scans were exported to an STL file, in which for the SLM process the sample requires support bars to sustain the weight while it is being made.

The samples were made from SS316L powder with a size range of 15 µm to 45 µm. The chemical composition provided by the manufacturer can be seen in Table 5.2.

Element	Fe	Cr	Ni	Mo	Mn	Si	N	Cu	O	C	P	S
%	BAL	17.8	12.9	2.35	1.25	0.06	0.04	0.03	0.0185	0.012	0.012	0.005

Table 5.2 - Chemical composition of SS316L powder used for sample production.

The powder was spread in layers of 40 µm. When the machine finished the sample was freed from the base and the supports were removed, the remaining powder inside the porous metal was blown away using high pressurised air.

A sketch of support placing can be seen in Figure 5.13 as well as the building cycle being run. In Figure 5.14 three finished samples are shown. The next section is focused on the Electron Beam Melting process, using the same CAD design as with the SLM samples the following ones are made from Ti6Al4V to compare with the stainless steel 316 porous samples.

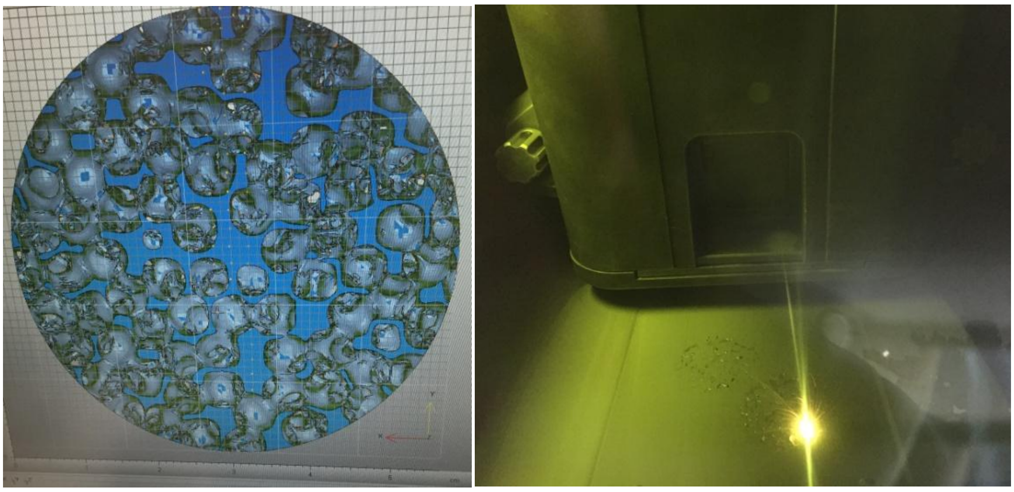

Figure 5.13 - Supports placing structure scan (l*eft*) and SLM cycle run (*right*).

Figure 5.14 - SLM SS316L porous samples, SS316L(5) (*left*), SS316L (3) (*centre*) and SS316L (1) (*right*).

5.7. Electron Beam Melting (EBM) Sample Manufacturing

To understand the effect of metal properties on porous structure behaviour, it was also desired to make the same forms from another metal. Five samples made by multiple runs of Electron Beam Melting (EBM) of Ti6Al4V powder were produced using a porous geometry extracted from an X-ray computerised tomography scan of packed spheres made from glass [154].

The solid to void relation was obtained by applying certain limit values during the solid creating procedure. This process is called segmentation, to produce rigorous images this process is of the utmost importance [155]. These samples were built using a specific limit value for each one giving a specific volume of void fraction, respecting the regions of the voids.

The scans were exported to an STL file, where extra design changes took place, such as expansion or contraction of surfaces to attain the different void fraction volumes and setting the diameter of the sample at 51 mm and the length of 25.5 mm. In Figure 5.15 the five different sample scans are shown.

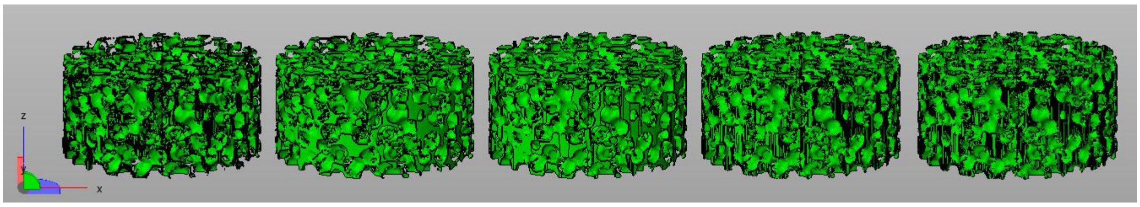

Figure 5.15 - Computer aided design porous metal sample structures for EBM processing.

The sphere size of 3.9 mm is the size of the pore, this was altered by the change in surface quantity due to the scaling for each sample while keeping the spherical shape. The critical point of note about these samples is not that this is likely to be a suitable processing route for regenerator materials (the method is not likely to be suitable for large volume of production), but rather that the series of operations produces samples where the density changes while the relative positions of the pores remains fixed; this should permit the variations in behaviour with density to be clearly understood, in isolation from the changes due to the random structure of a porous metal.

The samples were made from Ti6Al4V powder with a size range of 40 µm to 100 µm. The chemical composition provided by the manufacturer can be seen in Table 5.3.

Element	**Ti**	**Al**	**V**	**Fe**	**O**	**N**	**C**	**H**
%	BAL	6.1	4.1	0.16	0.13	0.011	0.005	0.002

Table 5.3 - Chemical composition of Ti6Al4V powder used for sample production.

The production happened under a controlled vacuum atmosphere, at a pressure of 0.0013 mbar using a voltage of 60 kV and a current within a range of 1.9 mA to 3 mA for the melting beam. The energy use in these machines is modified while the manufacture is occurring. The reason for this is to make up for certain points in the process in which the beam requires more or less intensity [156].

The powder is spread in layers of 70 μm, the electron beam worked in a continuous pattern in single beam fashion. When the machine finished the remaining powder in the porous structure was swept from its inside using high pressurised air. In Figure 5.16 three of the finished samples can be seen. After explaining all production processes some example images of all produced samples are shown in the next section.

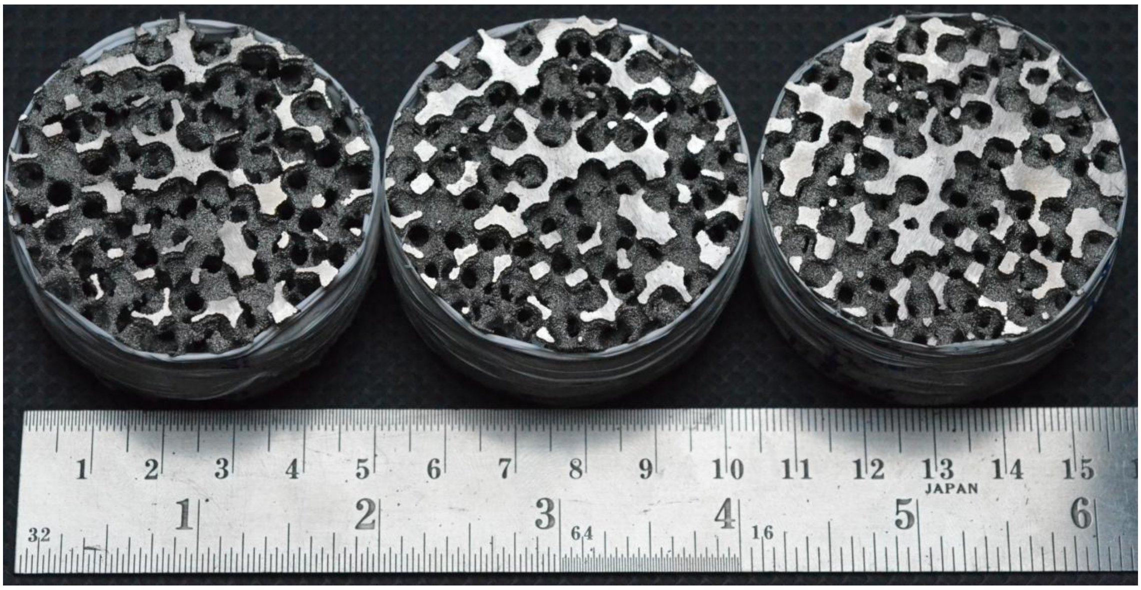

Figure 5.16 - EBM Ti6Al4V porous samples, Ti6Al4V(5) (*left*), Ti6Al4V(3) (*centre*) and Ti6Al4V(1) (*right*).

5.8. Example Images and Structure Characterisation of the Produced Samples

In the following figures the images of all structures available for this work are shown, the quantitative results of the structure characterisation are shown in Table 5.4. The pore size is determined by the salt particle size range in the replicated samples and for the ball bearing structure the pore size is determined to be in the same order of magnitude as the ball bearing size, for window size in our 2D scan there is a rough measurement taken for the samples, the strut geometry in the replicated porous metals considering that they were made with spherical particles are mostly triangular in shape [8].

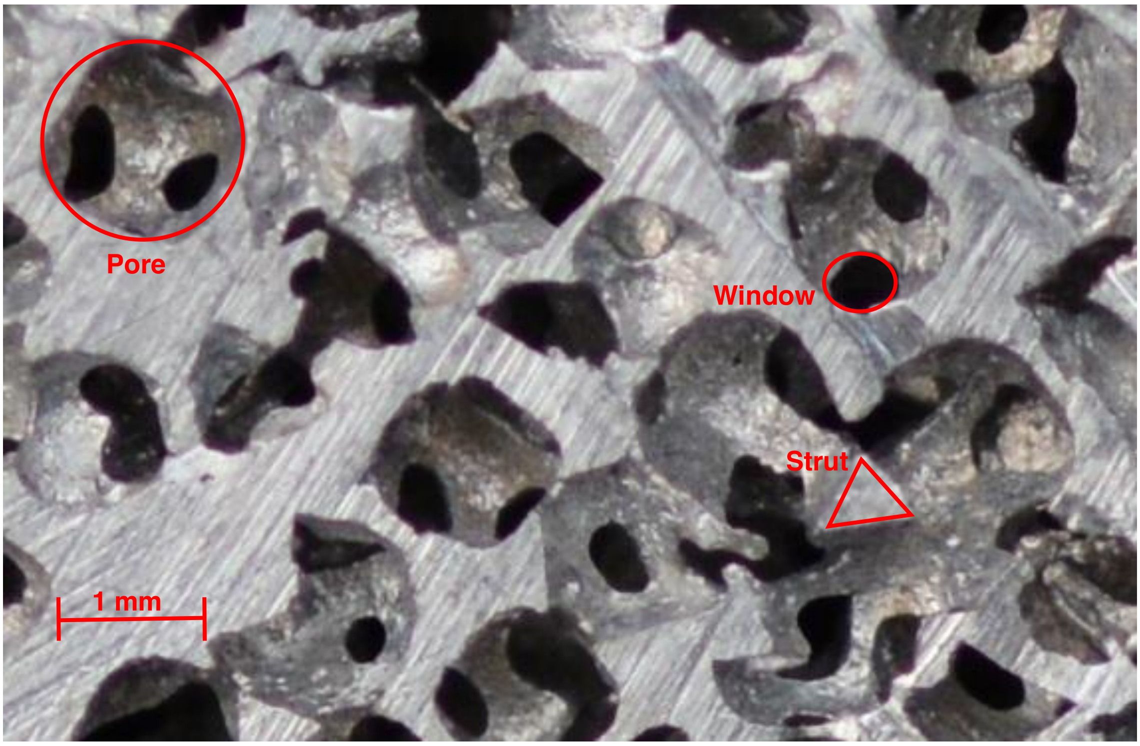

Figure 5.17 - Example image of the replicated porous aluminium sample A1 structure.

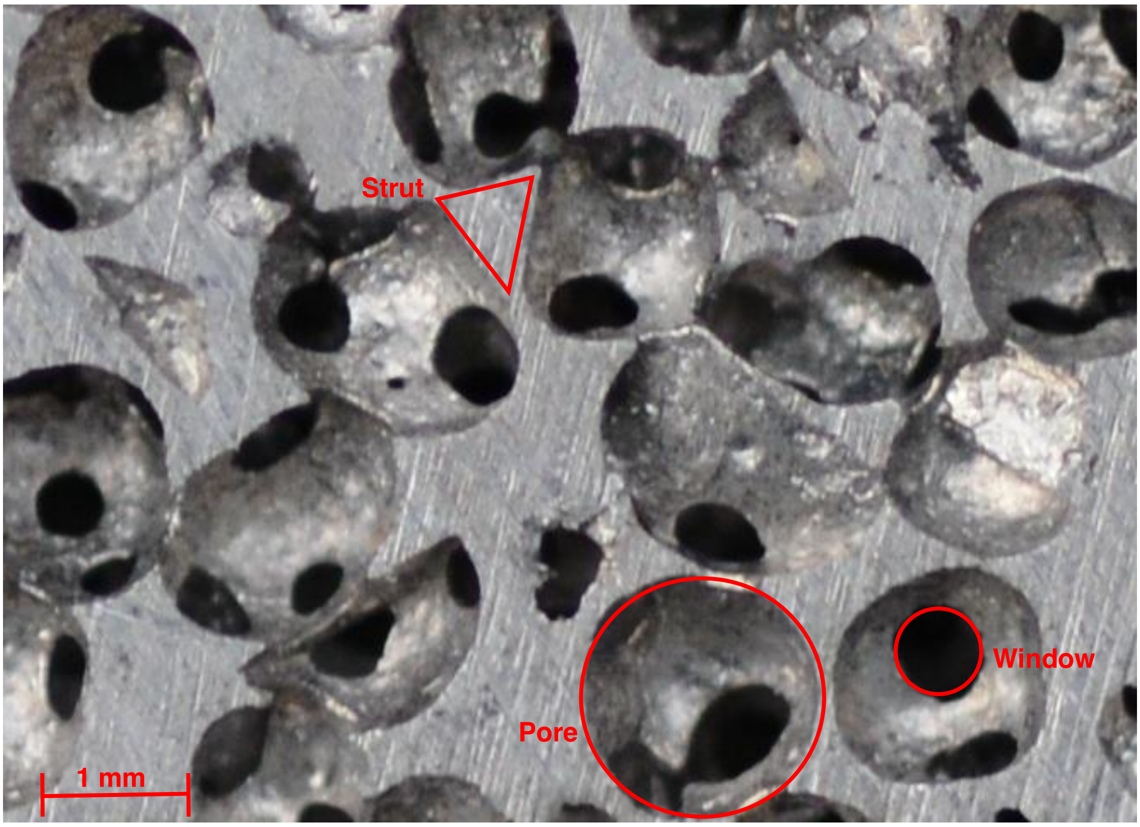

Figure 5.18 - Example image of the replicated porous aluminium sample B1 structure.

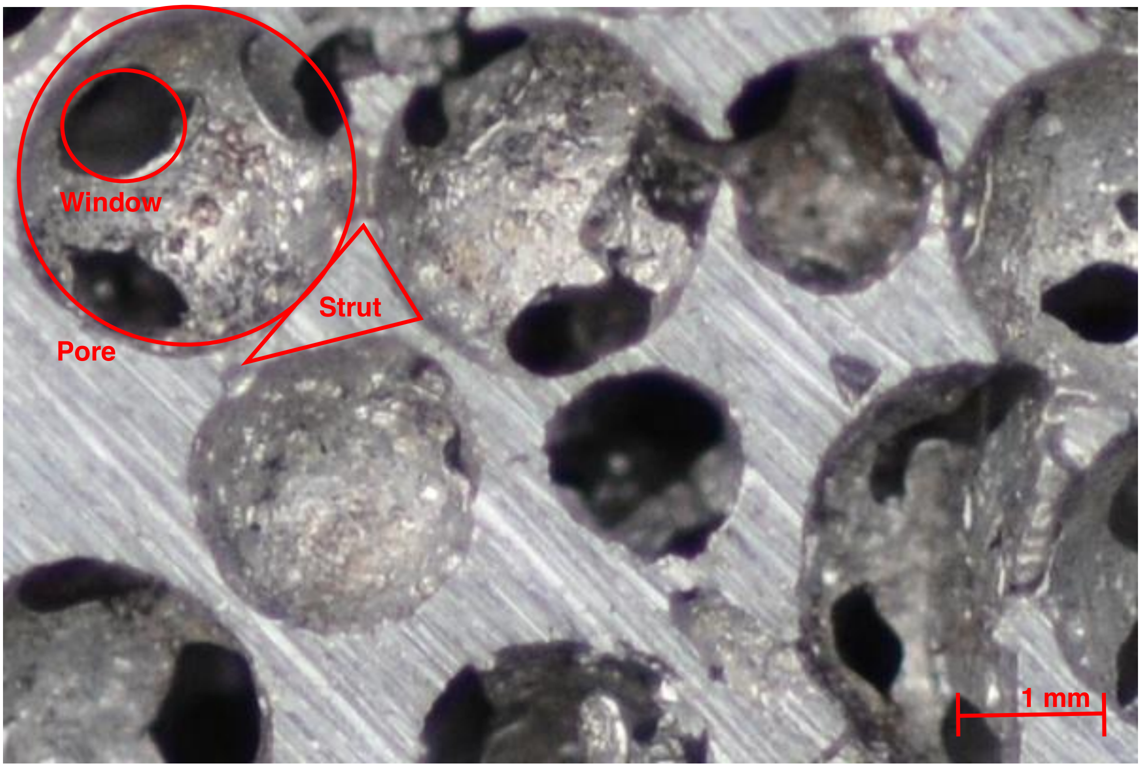

Figure 5.19 - Example image of the replicated porous aluminium sample C1 structure.

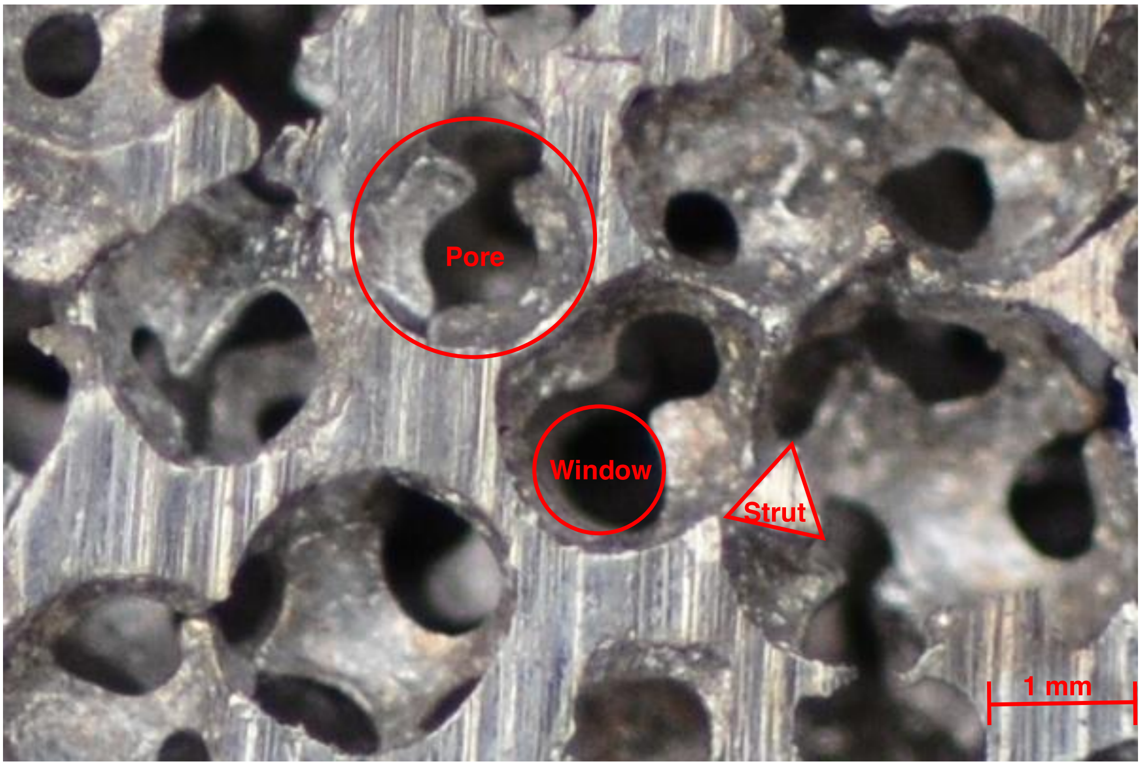

Figure 5.20 - Example image of the replicated porous aluminium sample V1 structure.

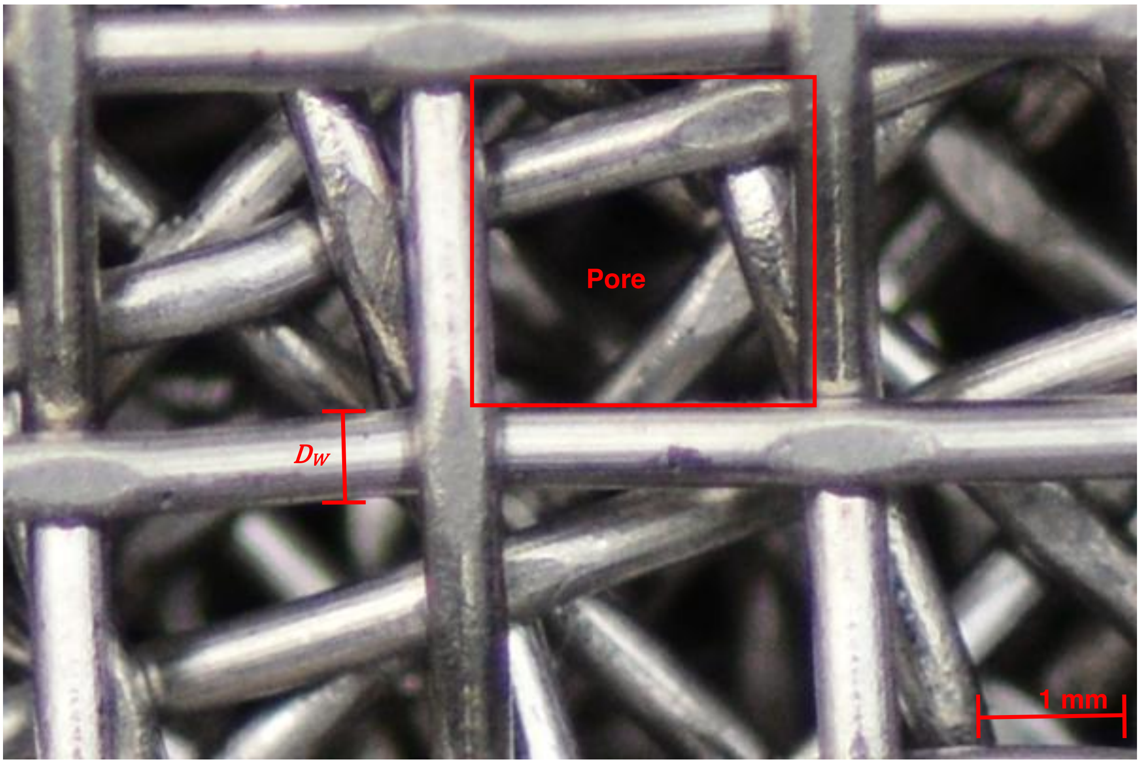

Figure 5.21 - Example image of the wire mesh sample 10 Mesh structure.

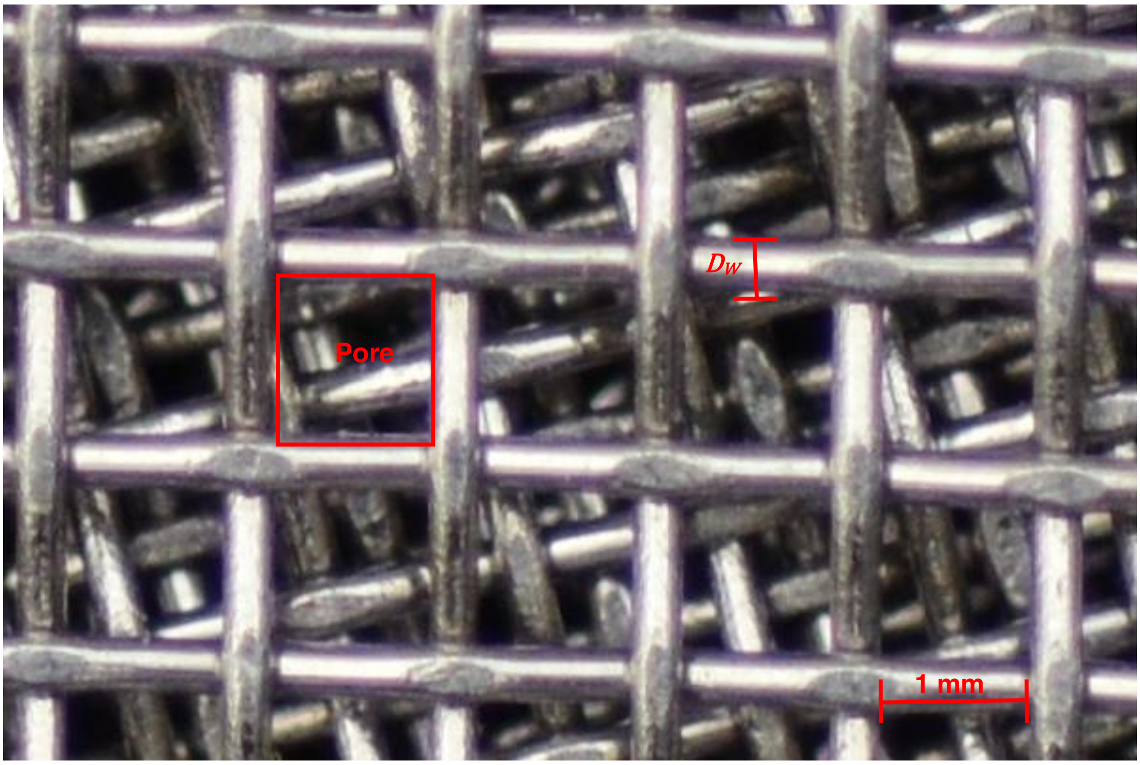

Figure 5.22 - Example image of the wire mesh sample 20 Mesh structure.

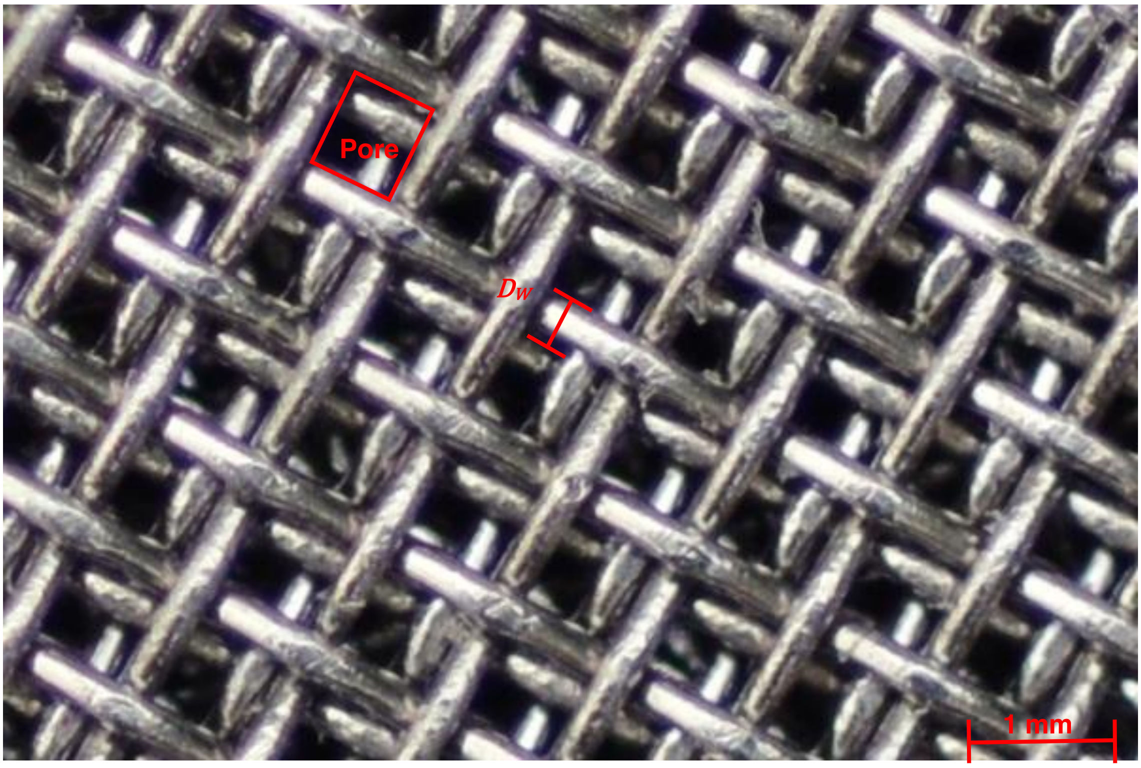

Figure 5.23 - Example image of the wire mesh sample 30 Mesh structure.

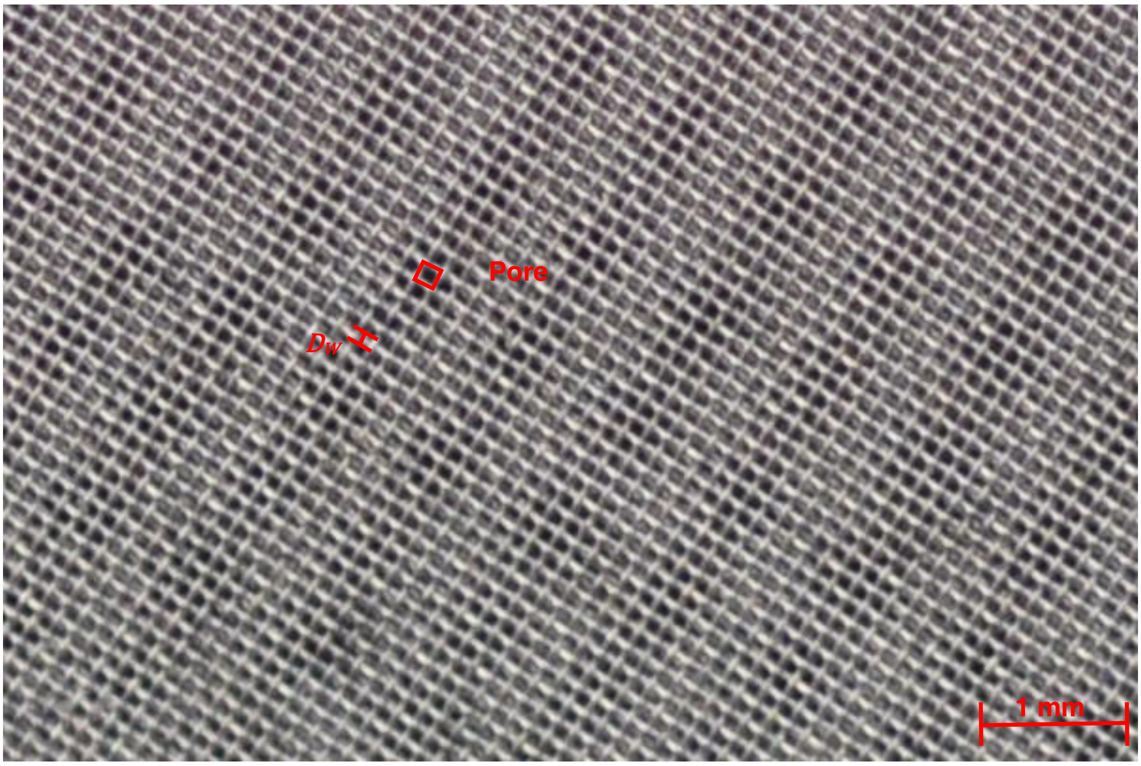

Figure 5.24 - Example image of the wire mesh sample 200 Mesh structure.

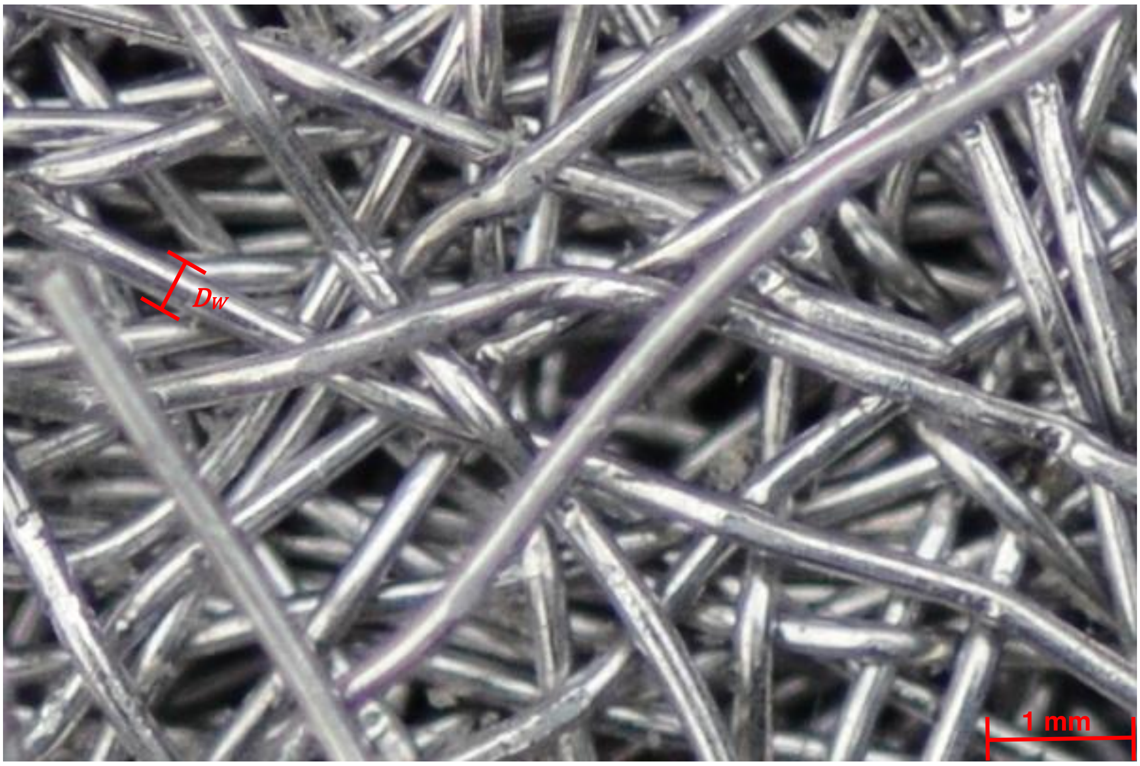

Figure 5.25 - Example image of the wire felt sample Al Felt structure.

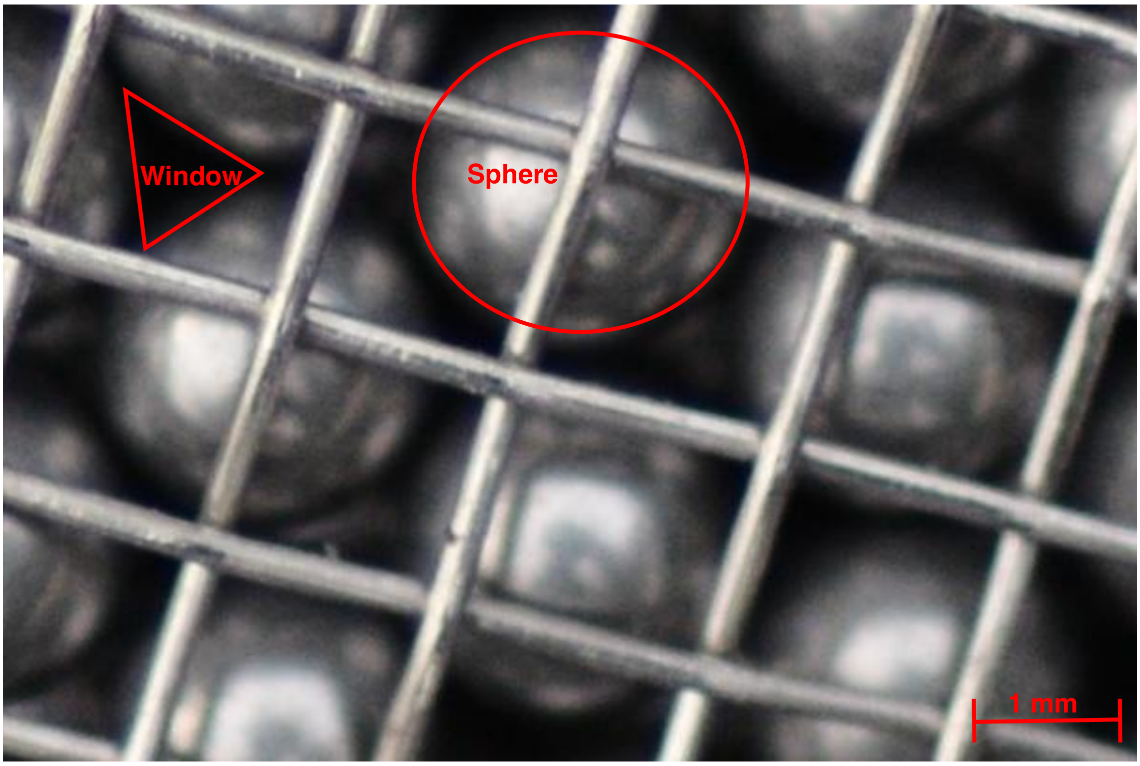

Figure 5.26 - Example image of the packed spheres sample Al Sph structure.

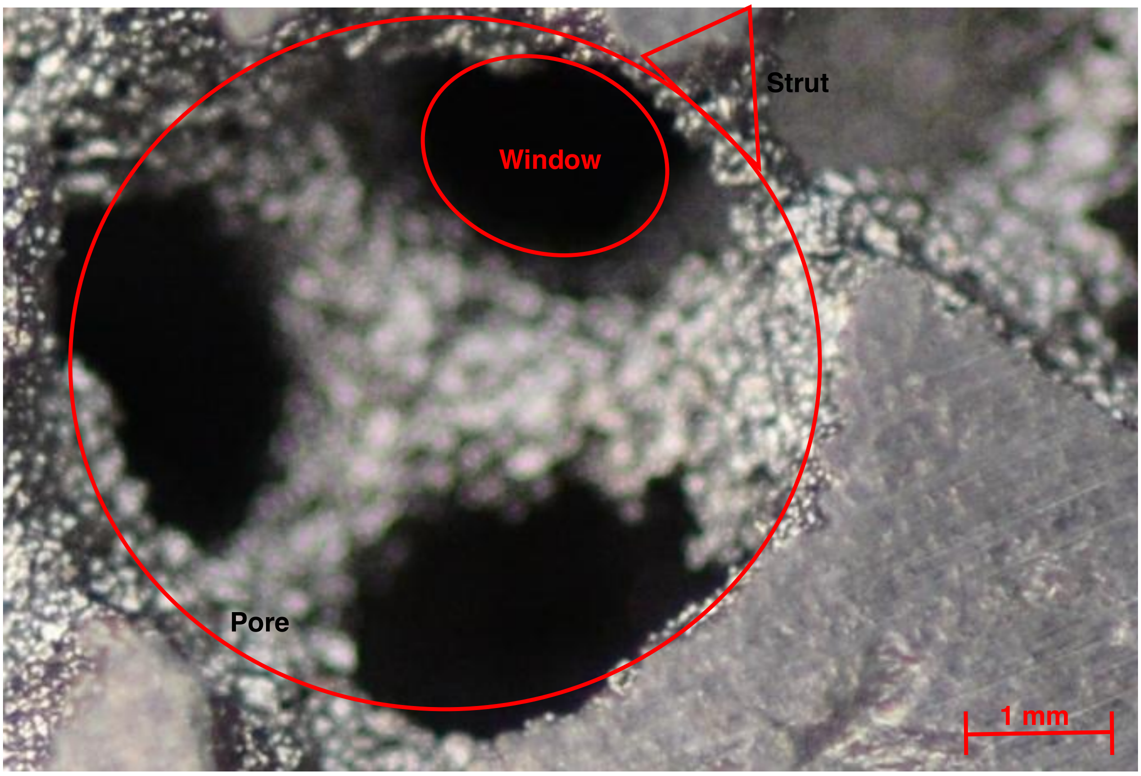

Figure 5.27 - Example image of the Additive Layer Manufactured sample Ti6Al4V (3) structure.

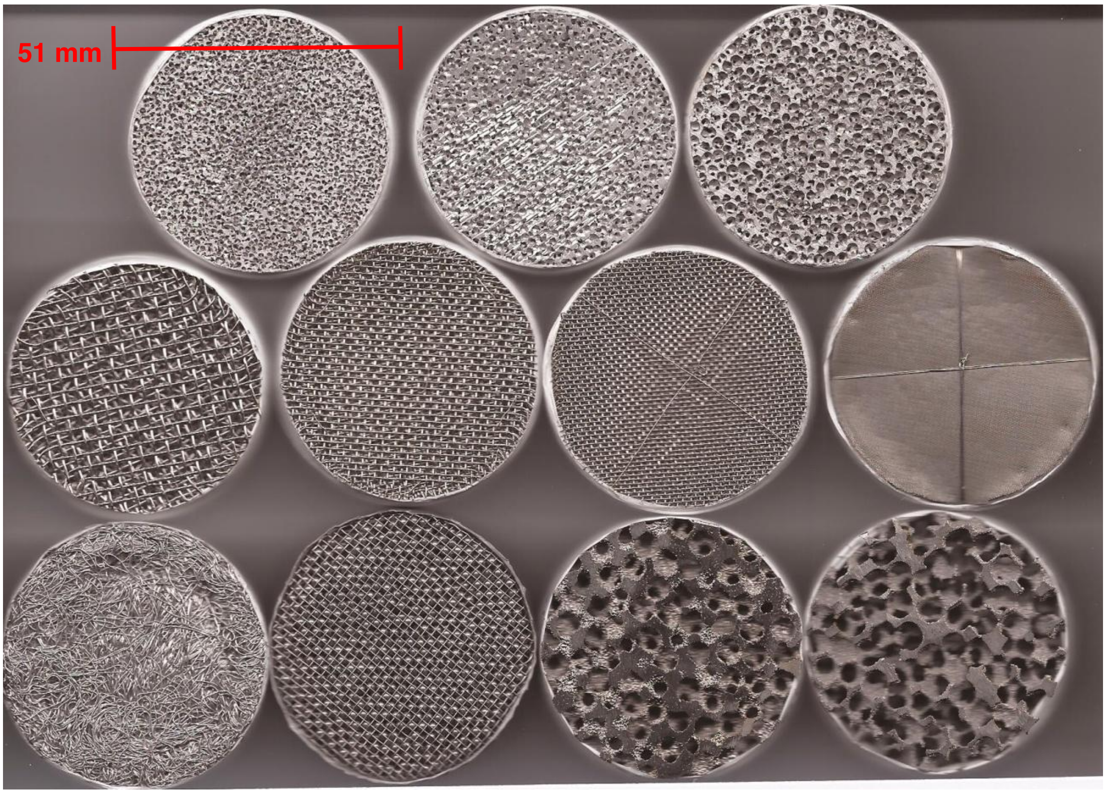

Figure 5.28 - Example image of all structures available for this study (Top: Replicated porous metals, Middle: Wire meshes, Bottom: Wire felt, Packed bed of spheres and ALM porous samples).

Samples	Porosity (%)	Pore/Particle Size (mm)	Measured Window (mm)	Calculated Window Size (mm)	Wire Size (mm)
A	70 - 73	1.00 - 1.18	0.33	0.26	-
B	69 - 70	1.40 - 1.70	0.44	0.37	-
C	70 - 72	2.00 - 2.36	0.62	0.51	-
V	75 - 78	1.40 - 1.70	0.64	0.52	-
10 Mesh	78 - 81	2.00	-	-	0.56
20 Mesh	75	1.00	-	-	0.36
30 Mesh	73	0.50	-	-	0.28
200 Mesh	75	0.075	-	-	0.052
Felts	69 - 70	-	0.13	0.09 (smallest)	0.25
Sphere Beds	38 - 42	2.00	0.85	0.73 (smallest)	-
ALM	61 - 83	3.90	1.08	0.84	-

Table 5.4 - Structure characterisation of the porous metal samples used for this study.

The measurement of the replicated, packed spheres and ALM porous metal samples' window size was taken by averaging 10 window sizes and the calculation was made using Eq. 5.1 [7].

$$d_w = \sqrt{\frac{D_P^2}{3}\left(\frac{\varepsilon - \varepsilon_0}{1 - \varepsilon_0}\right)} \qquad \text{Eq. 5.1}$$

For the calculation of the felt and packed spheres smallest window size a diagram created in AutoCAD to measure the smallest possible space in between the three circular sections was considered creating an equilateral triangle in the middle which is the window as can be seen in Figure 5.29.

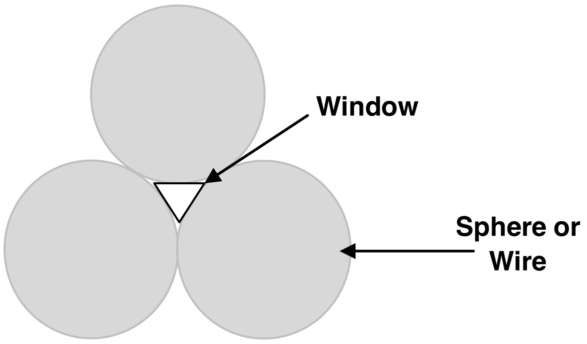

Figure 5.29 - Window in between spheres or wires.

5.9. Apparatus for Pressure Drop Measurement in Porous Materials

The equipment used to measure pressure drop across porous metals developed by Barari [157] consists of two fans, a sample holder with a pressure transducer, an orifice plate with a pressure transducer, an autotransformer and CPU with a data acquisition card (DAQ) to register the information. The two 1 kW fans, specified for use at high velocity, are placed in a sealed square wooden container, intaking atmospheric air and forcing it through the pipe and porous metal sample holder system. The fan velocity is regulated by the manually controlled 8 ampere autotransformer and an exit valve attached to the wooden container. The schematic diagram is shown in Figure 5.30.

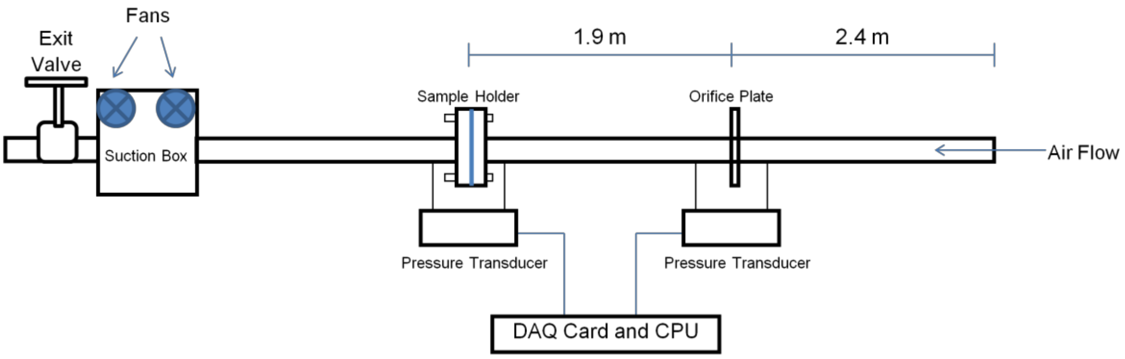

Figure 5.30 - Pressure test rig schematic diagram.

An issue appeared with the fans at low speeds; a great deal of fluctuation occurred, which was solved with the combination of using both the exit valve and the fans at high speed, the valve was used for regular, coarse tuning of the speed and the manual control of the autotransformer for focused tuning of the speed.

The intake system consists of an ABS pipe 52.9 mm in diameter with a wall thickness of 3.5 mm; the pipe length before meeting the orifice plate was 1.5 m, this to guarantee a fully developed flow. The flange type orifice plate is calibrated against an Original Equipment Manufacturer (OEM)-calibrated laminar flow meter (Cussons Technology, model P7250) with a discharge coefficient of 0.632 and a maximum inaccuracy of ± 0.5%. For the pressure drop measurements across the orifice plate a Furness Controls differential pressure transducer type 332-4W with a maximum inaccuracy of ± 0.25% was used. The locations of the pressure tapping points were specified following BS EN ISO 5167-1:1997 [158]. When fully assembled, the fittings and pipe system were set under an absolute pressure of 1.3 bar for a short time span, and were covered in soap and water, searching for cracks in the polymer which would be evident by the formation of bubbles. None were observed.

For flow rate measure corrections involving room temperature, pressure and humidity a wall mounted psychrometric thermometer was used and cross referenced with a digital thermometer (VelociCalc type 8347 A). For measurements across the regenerator samples a differential pressure transducer (Omega model DPGM409DIFF-350HDWU) with a maximum inaccuracy including linearity, hysteresis and reproducibility of ± 0.08% was employed.

The sample holder is made from two flanges and a 200 mm piece of pipe, on the pipe three 5 mm screws were arranged uniformly around it to hold the sample in place, 3.5 mm of their length is embedded in the wall and only 1.5 mm in the pipe; the effect of this on the pressure drop measurements was found to be imperceptible. To prevent sample movement and air flow around the sample inside the holder, thread seal tape was applied to the circumference of the samples [157].

The data acquisition card connected to the CPU is from National Instruments model PCI - 6221; LabView software was used to receive and interpret the information received from the pressure transducers.

After the flow equipment details have been shown next is the explanation of the testing procedure to obtain the pressure drop results.

5.10. Pressure Drop Testing Procedure

After placing the samples in the 200 mm holder and locking the four nuts and bolts on each side the fans were activated. Regular tuning was controlled by the exit valve and the fine tuning with the voltage selector controlling the autotransformer. Sample pressure drop readings were taken at 24 different flow rates and repeated 20 times at each point to ensure a correct value. In Figure 5.31 an example is shown of the readings, average values are registered for each sample to plot the following figures for each sample.

The data obtained from the pressure drop tests was plotted on graphs using the velocity obtained by dividing the air mass flow rate by the cross sectional area, called superficial velocity. For the first set of graphs the pressure drop was divided by the length of each sample (allowing variations in this length to be accounted for) and the superficial velocity for comparison.

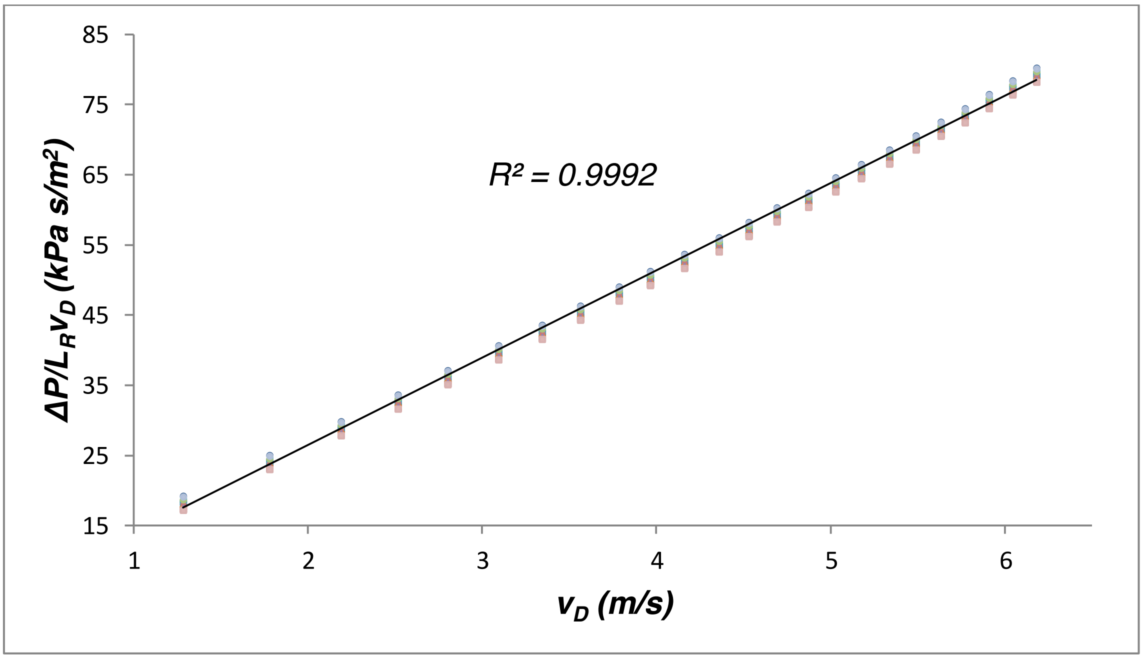

Figure 5.31 - Average linear pressure drop values for sample A1 taken from 20 runs.

The pressure drop (ΔP) does not show simple linear behaviour with velocity, so to calculate the form drag and the permeability of each sample a curve fitting process was applied using Eq. 4.6. Linear regression was implemented to calculate coefficients *a* and *b* present in Eq. 4.8. To ensure an acceptable fit the coefficient of determination (R^2) was calculated as well, and found to have a range from 0.9964 to 0.9999 for all samples.

The range of superficial velocities spans from 1.25 m/s to 6.25 m/s, the latter value obtained from the maximum allowed velocity when testing the sample with the highest pressure drop without exceeding the limits of the test equipment.

After looking at the flow testing equipment in the next section the equipment to test the samples' heat transfer properties is presented.

5.11. Apparatus for Heat Transfer Measurement in Porous Materials

This equipment is arranged to work in conjunction with the pressure drop apparatus described previously. It is constructed based on the single - blow method for the interpretation of heat transfer data. It consists of two fans, a sample holder with thermocouples installed on the ABS pipe on each side, an orifice plate with its pressure transducer, an autotransformer and CPU with a data acquisition card (DAQ) to register the information. The two 1 kW fans, specified for use at high velocity, are placed in a sealed square wooden container, intaking atmospheric air and forcing it through the pipe and porous metal sample holder system. The fan velocity is regulated by the manually controlled 8 ampere autotransformer and an exit valve attached to the wooden container [157]. The schematic diagram is shown in Figure 5.32.

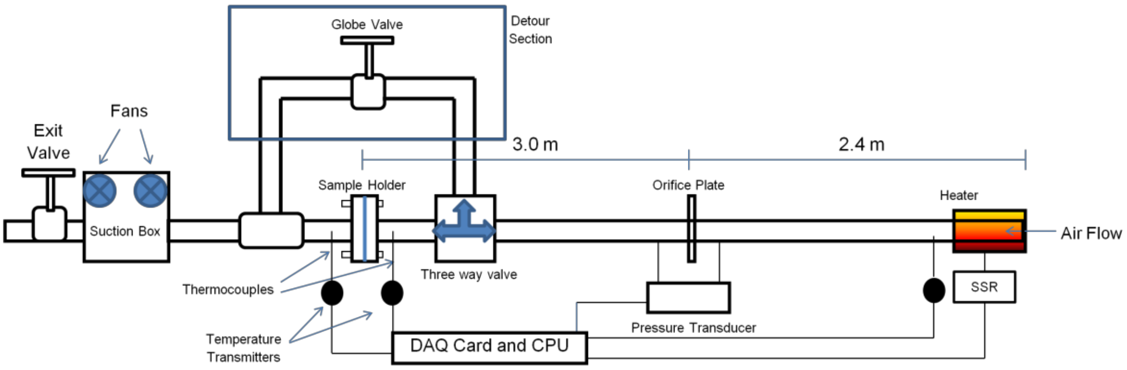

Figure 5.32 - Heat transfer test rig schematic diagram.

To obtain reliable results using the single - blow method the flowing heated air must remain steady in terms of temperature variations. An Omega AHF - 14240 inline heater powered and controlled by a 240 VAC was positioned at the end of the pipe system to heat up the air arriving at room temperature. The fans drew air through the heater and made it flow into the pipe system. A two position electronic switch regulates the status of the heater to off or on, while a proportional integral derivative (PID) controller connected to LabView software managed the operating period of the device.

To harmonize the heater operation with the input voltage a synchronous solid-state relay (SSR) was employed. The heater cycle was fixed at seven hertz, working from PID to DAQ to SSR to a K type thermocouple positioned next to the heater giving temperature readings back to the PID, closing the information circuit.

The heater was internally fitted with 10 sheets of stainless steel wire mesh to help straighten any variation in air flow caused by the heating coils, before passing through the 1.5 m of ABS pipe before reaching the orifice plate, guaranteeing a fully developed flow. For the pressure drop measurements across the orifice plate a Furness Controls differential pressure transducer (type 332-4W) with a maximum inaccuracy of ± 0.25% was used. The location of the pressure tapping points was determined following BS EN ISO 5167-1:1997 [158].

A detour section was installed on the main pipe to produce a reproducible pressure as in the test section by keeping it at the same level of pressure drop.

The detour section is accessed by a three way ball valve operated by a 90 degree pneumatic mini - rotary vane actuator (Norgren M/60284/90) for reduction in actuation time (0.15 s) and to automatise the system.

A globe valve was placed on the detour section to compensate for the sudden change in pressure from a free flow pipe to the pressure drop created by the sample. This sudden change prevented the heater from rapidly adjusting the temperature before the sample, taking a short time before reaching equilibrium. Before running the actual test, the detour section valve was set to resemble the same pressure drop as given by the sample, eliminating the jump in pressure, and the resulting change in incoming air temperature on switching.

The sample holder is made from two flanges and a 100 mm piece of pipe, on the pipe three 5 mm screws were arranged uniformly around it to hold the sample in place, 3.5 mm of their length is embedded in the wall and only 1.5 mm in the pipe. To prevent sample movement and air flow around the sample inside the holder, thread seal tape was applied to the circumference of the samples.

To ensure a fast thermal response of the inlet and outlet (before and after the sample) temperature differences, two Omega K type 0.25 mm thermocouples were placed in the middle of the pipe, with an assisting cord to stabilise their movement. These thermocouples are calibrated to respond in 3 milliseconds at an air speed of 20 m/s; registering the signals were two Farnell 300TX transmitters with an inaccuracy of ± 0.2%. The data acquisition card connected to the CPU is from National Instruments model PCI - 6221; LabView software was used to receive and interpret the information received from the temperature transmitters [157].

Another property that is needed in the regenerator analysis is the thermal conductivity, the testing rig to obtain this value is explained in the following section.

5.12. Effective Thermal Conductivity

To include thermal conductivity in the model calculations one must take into account the material of the regenerator and the structure it has. Since the porous metals are not a solid block of material, this value is lower than the thermal conductivity of the bulk metal. The samples have a variable structure, which is the reason why their individual thermal conductivity was challenging to assess.

To calculate a prediction for the precise effective thermal conductivity in porous media is problematic since it involves two phases, solid and fluid; it depends on the location of the solid, fluid and the boundary between them [159]. This parameter may on the other hand be estimated or obtained from tests.

In previous studies the thermal conductivity of porous media has been obtained for packed beds built with sintered powders. Their equations are based on the porosity and thermal conductivity of the material making up the porous structure. Numerous equations to predict their thermal conductivity have been suggested, often very specific to a particular type of material. A representative structural design to calculate the thermal conductivity of a porous metal of high porosity has been introduced, which is based on the cell geometry shape [160] and was expressed by Eq. 5.2 [107]:

$$k_R = 0.35[\varepsilon k_{Air} + (1-\varepsilon)k_M] + \frac{0.65}{\dfrac{\varepsilon}{k_{Air}} + \dfrac{1-\varepsilon}{k_M}} \qquad \text{Eq. 5.2}$$

where k_R is the effective thermal conductivity of the regenerator and k_M is the thermal conductivity of the material. The values obtained were consistent with the experimental values from another researcher [161].

To measure the effective thermal conductivity of the samples another experimental rig was employed (developed by Mr Ahmed Abuserwal, Dept. Mechanical Engineering, University of Sheffield). This equipment consists of a 100 Watt heater, two heat flux aluminium pieces, a container in which cold water flows, polyisocyanurate foam as insulation material and twelve thermocouples to register the temperature differences. The test rig diagram can be seen in Figure 5.33.

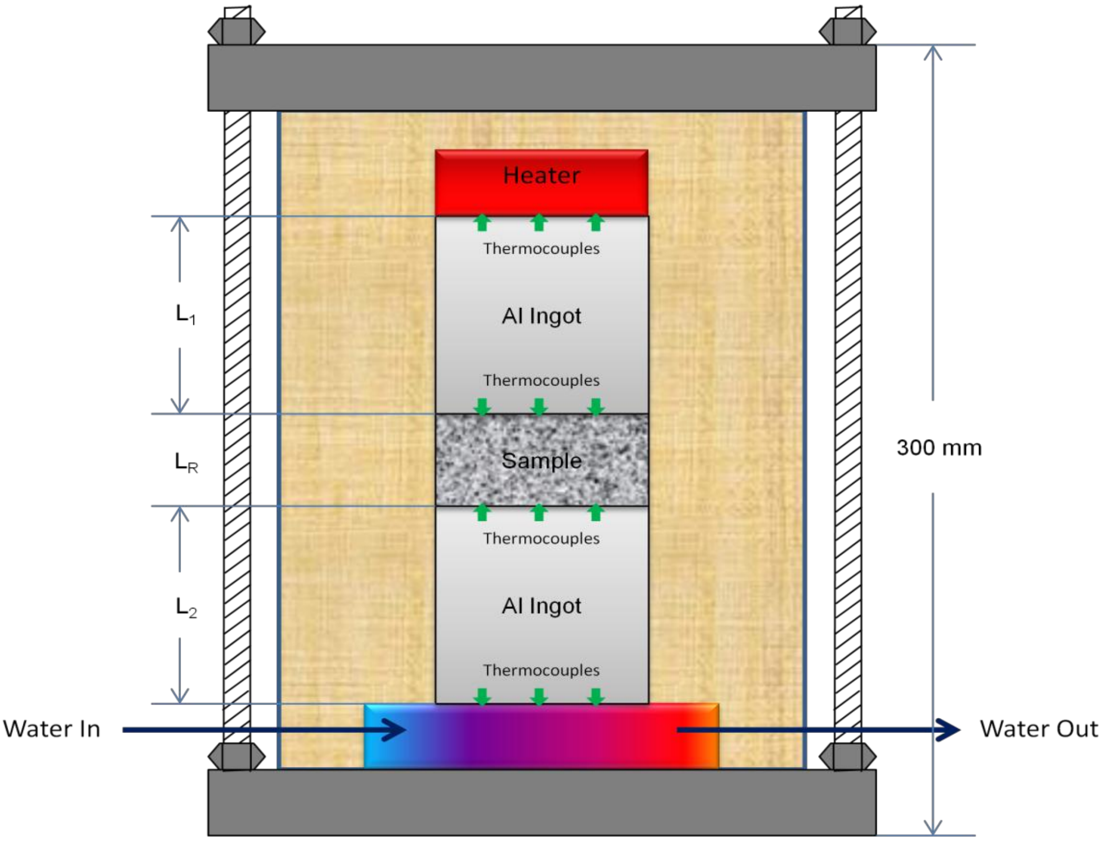

Figure 5.33 - Thermal conductivity test rig.

The heater was set to 80°C, and the flowing cold water, which is used to remove heat from the experimental rig and create a balance in the heat flow, was set at 5°C. To transport the heat between them and the specimen efficiently, both heat flux pieces were made from commercially pure (99.7%) aluminium.

The regenerator sample is placed in the middle of the two aluminium blocks, and for precise contact with the flux meters both surfaces of the regenerator were treated by sanding the surface for optimal contact. Three K-type thermocouples of 1.5 mm in diameter were installed at different points around a spiral in the four joints between components; they were calibrated against both a mercury and a digital thermometer using the freezing and boiling points of water as reference. The maximum error was set at ± 0.2°C. The heat loss by radiation between the layers was found to be less than 1.5% [162]. To achieve this, the temperature of the external insulation surface at three different points was measured (T_{ex}). To ensure the authenticity of the obtained thermal conductivity values the equipment was tested with three different materials of which their thermal conductivity is well known: common brass (CuZn37), chrome steel and commercially pure (99.7%) aluminium. The results varied only within 5% of the established amounts [191].

All components were kept in place by locking two aluminium plates at the top and bottom using four sets of nuts and bolts. After the experiment reaches stabilisation the temperature differences were registered and the average taken for calculation.

The heat transport by radiation and convection is considered to be insignificant. Convection is suppressed by having the heater on top, and radiation is less significant at lower temperatures. The flux of heat was therefore principally by conduction and was assumed to be directional from the heater to the water container. The equations for heat flow through the aluminium pieces are:

$$Q_{Al_1} = A_{CS} k_{Al} \frac{(T_{avg_1} - T_{avg_2})}{L_1} \quad \text{Eq. 5.3}$$

$$Q_{Al_2} = A_{CS} k_{Al} \frac{\left(T_{avg_3} - T_{avg_4}\right)}{L_2} \quad \text{Eq. 5.4}$$

A_{CS} is the area of the sample and aluminium piece, k_{Al} is the thermal conductivity of aluminium, L_1 is the length of the upper aluminium piece and L_2 is the length of the lower aluminium piece.

To obtain the loss of energy to the surroundings (Q_{ex}) the heat equation was applied to the insulation material. The temperature T_{ex} was the average of the external temperature of the insulation material at all heights and sides.

$$Q_{ex} = \frac{2\pi L_R k_{In} (T_{ex} - T_0)}{ln\left(\frac{D_0}{D_R}\right)} \quad \text{Eq. 5.5}$$

k_{In} is the thermal conductivity of the insulation material polyisocyanurate, L_R is the length of the regenerator, D_0 is the transversal length of the insulation and D_R is the diameter of the regenerator.

To calculate the heat flow through the regenerator one must average the heat flow through the upper and lower aluminium pieces minus the heat loss to the environment. The equation is:

$$Q_R = \frac{Q_{Al_1} + Q_{Al_2}}{2} - Q_{ex} \qquad \text{Eq. 5.6}$$

To obtain the effective thermal conductivity of the regenerator the energy equilibrium equation is:

$$k_R = \frac{Q_R L_R}{A_{CS}(T_{avg_2} - T_{avg_3})} \qquad \text{Eq. 5.7}$$

To ensure accurate measurement every sample was measured on both positions, face up and face down, the result is the average of these two values.

Following the calculation of the thermal conductivity values for the regenerator samples the adimensional value of thermal conductivity needs to be known, it is calculated with Eq. 4.24:

$$\lambda_R = \frac{k_R A_{cs}}{\dot{m}_{Air} c_{Air} L_R}$$

After focusing on the heat transfer testing equipment the next section contains the explanation on how to test the samples and the considerations that need to be taken.

5.13. Heat Transfer Test Procedure

For the heat transfer tests thread seal tape (EAGLE, www.wickes.co.uk) was used for wrapping the circumference of each sample to prevent the passing of heated air between the outer circumference and the pipe wall. The wrapped sample was placed in the holder and the holder in turn placed between the flanges of the rig with the two corresponding gaskets in place to prevent leakage, with the whole assembly held in place by eight sets of nuts and bolts.

The fans were then started and afterwards the heater was set; the heater was programmed to run only when the fans are active to prevent damaging the heater and / or causing a risk of fire. Before starting the tests the system needed to reach a stable temperature to prevent the heating up of the cold rig itself from affecting inlet and outlet temperatures. Initially the warm up time for the rig was 30 minutes; after a few trials it was found that 15 minutes was sufficient time to prepare the equipment.

Most of the time the three way valve remains on the position directing the air towards the detour section. After the rig is preheated the air passes through the orifice plate and then reaches the three way ball valve, which is activated, changing the flow of air to go through the sample. At this time the flow rate is set at the highest flow rate to be tested, at around 6.25 m/s. Before switching, with the three way valve is directed towards the detour section, the globe valve is adjusted to provide a resistance to flow and only allow the same flow rate to pass through it (this, as explained before, is to prevent the jump in pressure on changing the gas flow path from one route to the other and thereby inhibiting the adjustment of the heater to a new temperature if the flow rate is changed).

When room temperature is reached the nuts and bolts are fastened and the test is ready to start. The LabView software to record data is activated at the same time as the solenoid that operates the three way ball valve to cause hot air to pass through the sample. Each test lasts until well after (approximately 50 seconds) the outlet temperature is constant when compared to the inlet temperature.

After testing and recording the required data, the nuts and bolts of the sample holder with the inlet flange are loosened and the sample is cooled down to room temperature by the flow of unheated air through the gap between the flange and the sample holder. To accelerate this cool down a moist cloth is placed on top of the gap, reaching the target temperature in approximately three minutes. The process is then repeated for the next flow rate. A total of six flow rates are registered per sample and the whole assessment is repeated three times for a more accurate result.

The next section explains how to interpret the information and values obtained from the heat transfer tests, it shows data for illustrative purposes only, the results are in Chapters 7 and 8.

5.14. Data Interpretation

In this work the methods chosen to calculate the heat transfer coefficient were the maximum slope method and the least squares method, as other researchers did [115], [126], [127], [142]. The effects for the heat transfer towards the wall, the response time at the entrance and the thermal conductivity in direction of the flow were considered. The Joule - Thomson effect and radial conductivity were not considered.

In Figure 5.34 a chart showing three runs (green, yellow and red) made for the replicated porous aluminium sample A1 can be seen; from these three runs an average value curve is registered to calculate the subsequent coefficients, seen in Figure 5.35. It can also be noted that by changing temperature within the runs the difference between each inlet - outlet run stays practically the same, indicating that the behaviour of the sample does not change.

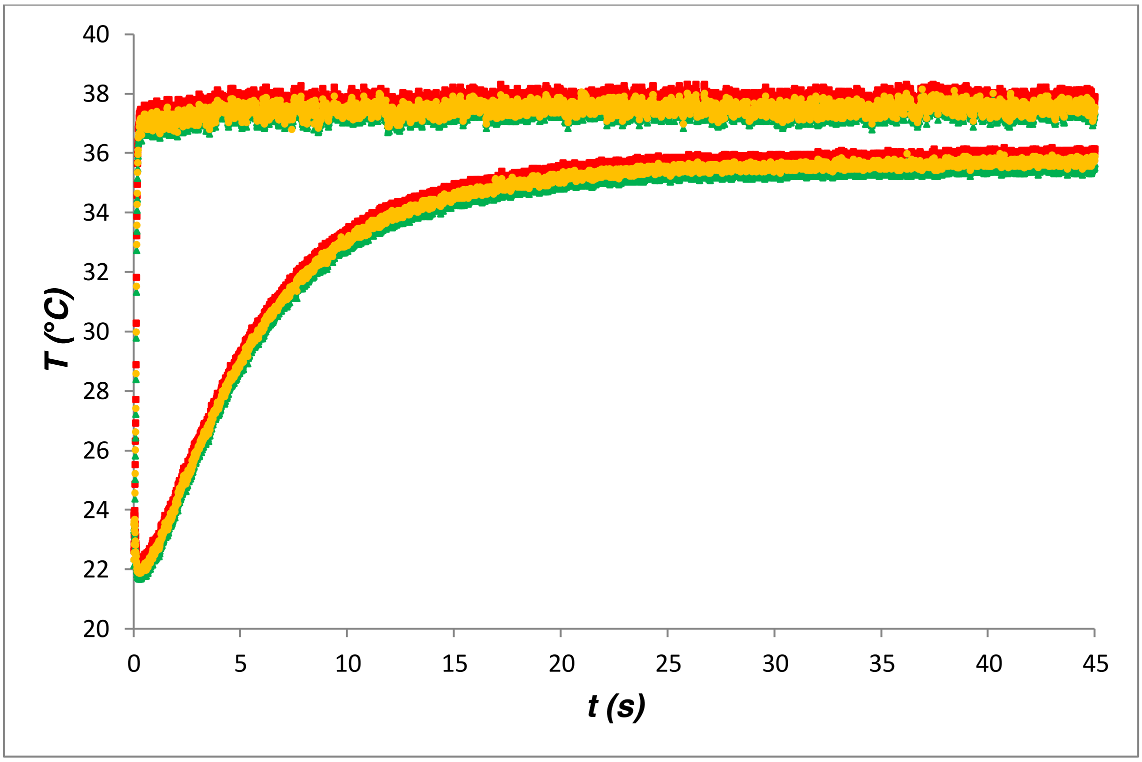

Figure 5.34 - Three thermal test runs for sample A1 at 2.55 m/s (each colour indicates a different run).

5.14.1. Thermal Data

In the typical temperature-time data obtained from the test rig a step change is visible for the inlet temperature as a gradual increase of the outlet temperature takes place. Both lines show fluctuation with the inlet temperature having more than the outlet, this is due to the turbulence in the fluid before entering the sample caused by its velocity. When the air passes through the sample, it acts as a flow straightener [163], lowering the air speed and generating a pressure drop, which is the reason why the outlet temperature line is smoother.

It can be seen that the outlet temperature does not reach the same value as the inlet temperature, and in fact this will never happen, even if the duration of the test is increased. This is because there is heat loss from the regenerator through the wall of the system. (This heat loss through the wall is included in the calculation model used for the analysis as explained in section 4.2.2).

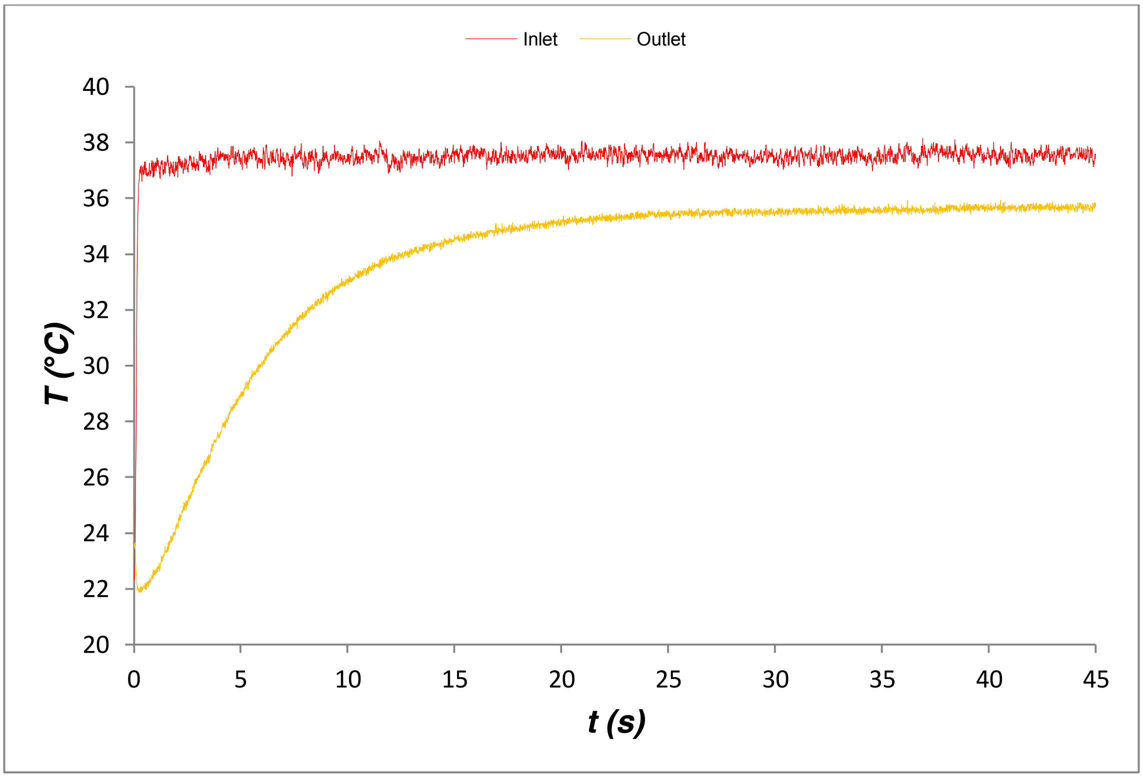

Figure 5.35 - Resulting average curve from a thermal test run for sample A1 at 2.55 m/s.

When experimental data were examined, a slight variation was found in the time it took the three way globe valve to open when compared to the start of the test. Preheating the system causes the elements to expand, and this affected the globe valve by increasing the response time after it is activated by the switch.

Initially when building the test rig the opening of the globe valve was driven by the laboratory compressed air feed, which had a maximum pressure of 6 bar. This somewhat limited the speed of the response due to the expansion of the valve, which led on occasion to it not working at all. This was solved by installing a compressed air tank feeding the valve; the regulator on the tank allowed for higher pressures to be used, up to 10 bar. Currently for this study the regulator is set at 8 bar, more than enough pressure to overcome the expansion effect of the valve.

The obtained experimental data from the test rig should be changed into adimensional data before applying the curve matching technique.

The time was converted to an adimensional value using Eq. 4.24:

$$t_a = \frac{\dot{m}_{Air} c_{Air} t}{m_R c_R}$$

In which t_a is the adimensional time, $\dot{m}_{Air}$ is the air mass flow rate, c_{Air} the heat capacity, t the time at that point, m_R the mass of the regenerator and c_R the specific heat of the regenerator's material.

The temperature was converted to an adimensional value using Eq. 4.20:

$$T_{aAir} = \frac{T_{Air} - T_0}{T_{Airi} - T_0}$$

In which T_{aAir} is the adimensional temperature, T_{Air} is the temperature at that point, T_0 is the minimum outlet temperature and T_{Airi} is the maximum inlet temperature.

5.14.2. Smoothing Process

To dispense with the unwanted noise that may alter the results of the experimental data points a smoothing process was applied, as described below. Periodically, outliers were present in the data set, possibly caused by electrical noise or equipment signal error. If the smoothing process was applied considering these outliers, the result would be distorted and not display behaviour representative of the real data, for which reason they were eliminated. For this purpose an outlier was defined as a point in a data set which is an exceptional indication of the irregular instability within the data, which can be caused by an unusual change in the experimental method, calculation or recording inaccuracy [164] Such points were identified and manually removed from the data.

From here the smoothing process was started using the Curve Fitting Tool from MathWorks MATLAB software. The procedure chosen was the Moving Average method. This technique builds a series of points which are the averages of a few sequential values of the original series. The equation applied was:

$$z_t = \frac{1}{2k+1}\sum_{j=-k}^{k} y_{t+j}\,, \qquad t = k+1, k+2, \ldots, n-k \qquad \text{Eq. 5.8}$$

From here $z_{k+1}, \ldots, z_{n-k}$ builds a new series of points based on the averages of the original set of points; it is also known as running mean or rolling averages approach [165]. In the equation z_t is the average value for a certain point, k is the number of points surrounding z_t and $2k+1$ is the interval [166]. In Figure 5.36 a chart of the values that emerge from the Moving Average method.

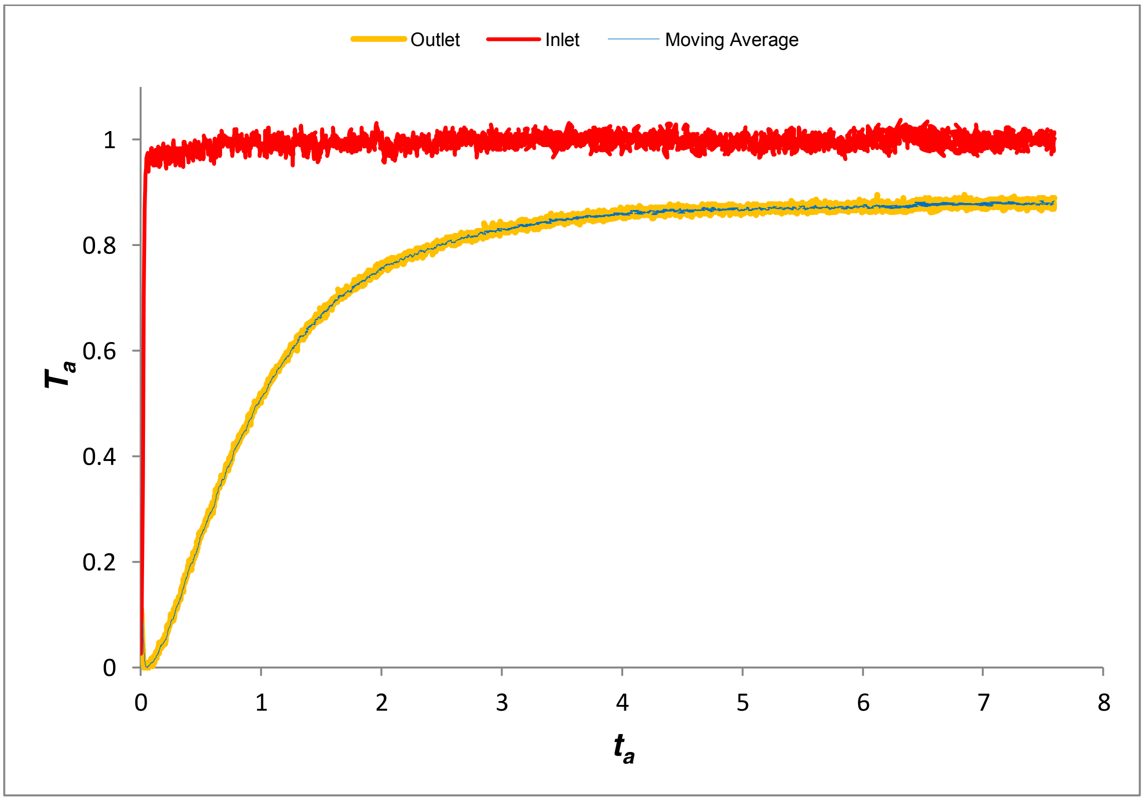

Figure 5.36 - Point series created by the Moving Average method for the A1 sample at 2.55 m/s.

5.14.3. Curve Fit Process

After applying the Moving Average to the data a curve fitting method was performed, to ensure that the points of the first derivative curve from the data follow one another. The curve fitting method uses splines, which are numeric functions defined by polynomial functions, giving a certain smoothness to the links between them.

There are different degrees of polynomials, a linear spline is made from first order polynomials. To ensure that the derived curve points follow one another the polynomial function should be at least of the second order or quadratic level. If the polynomial functions are of the third order or cubic it gives a better guarantee of the accuracy of the curves. For this work these are the ones used [138].

The equation applied to the data by the MATLAB software is:

$$p\sum_{n}[y_n - s(x_n)]^2 + (1-p)\int\left(\frac{d^2s}{dx^2}\right)^2 dx \qquad \text{Eq. 5.9}$$

In this equation p is the order of the spline, x_n and y_n are the coordinates of a specific point and s is the spline used. After this the program applies numerical solutions and it shows the fitted curve in a chart which the user evaluates and decides if the fit is correct.

In Figure 5.37 the data points, smoothed data and fitted curve can be seen, the R squared value is higher than 0.9962 for all samples.

To understand if the curve fits, the residual values must be taken into account. A residual value is the discrepancy between the experimental data and the fitted curve. If the residual value is similar or lower in magnitude when compared to the random variation of the experimental data points it signifies that the fitted curve may be considered to be correct.

The difference between the residuals and the random variation are shown in Figure 5.38, from these values it is clear that the curve is a good fit.

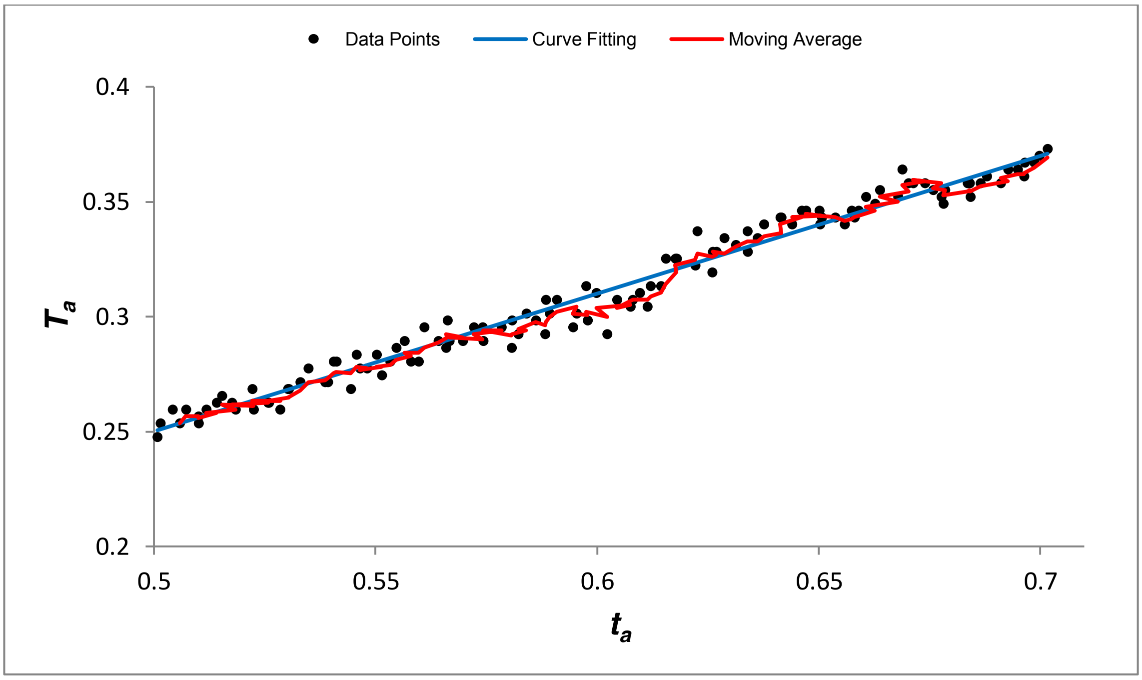

Figure 5.37 - Magnified view of a range of the adimensional outlet temperature values. Data points, smoothed data and fitted curve for the A1 sample at 2.55 m/s.

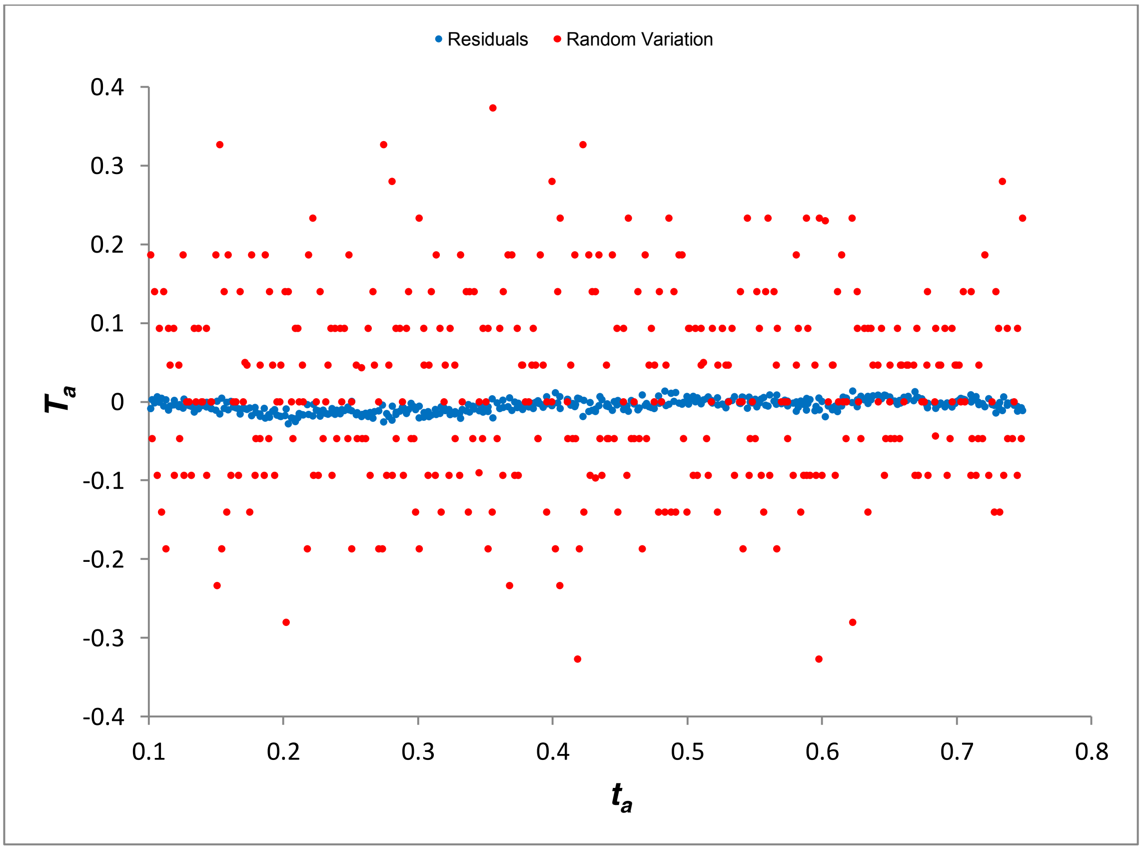

Figure 5.38 - Magnified view of the random temperature variation compared to the residual values obtained from the curve fitting for the A1 sample at 2.55 m/s.

The numerical values are an intrinsic operation of the software, giving the error evaluation using the sum of squared residuals (SSR) which measures the difference between the experimental and the predicted data [167].

$$SSR = \sum_{i=1}^{n} [y_i - f(x_i)]^2 \qquad \text{Eq. 5.10}$$

The variable y_i is the set value of the original variable, x_i is the independent variable and $f(x_i)$ is the new value of y_i.

The coefficient of determination was also used, this value expresses how adequately the data fits a statistical model [168].

It is also named the R squared value, and has a range between zero and one. If the value is closer to 1 it means that the fit is better. It may be interpreted as a percentage, for example if the R squared value is 0.96 it signifies that the fitted curve is 96% in agreement with the data.

The equation incorporates two values, the regression sum of squares:

$$RSS = \sum_{i}^{n} (f_i - \bar{y})^2 \qquad \text{Eq. 5.11}$$

and the total sum of squares:

$$TSS = \sum_{i}^{n} (y_i - \bar{y})^2 \qquad \text{Eq. 5.12}$$

Coefficient of determination:

$$R^2 = \frac{RSS}{TSS} = \frac{\sum_i^n (f_i - \bar{y})^2}{\sum_i^n (y_i - \bar{y})^2} \qquad \text{Eq. 5.13}$$

5.14.4. Derived Curve

After performing the smoothing and curve fitting the experimental data, to determine the maximum gradient the curve is differentiated. This gives rise to a second curve of which its highest value is the maximum gradient.

To obtain this curve the command "differentiate" was introduced in the code as bx=differentiate(cf_,X), which applies the following equation in the program:

$$\frac{db}{dx} = \frac{b(x + \Delta x) - b(x - \Delta \mathrm{x})}{2\Delta x} \qquad \text{Eq. 5.14}$$

5.14.5. Exit Temperature Forecast Curve

To successfully forecast the exit temperature curve with the model the characteristics and natural properties of the porous metals to be tested must be imputed as meticulously as possible.

5.14.5.1. Entrance Temperature

One of the parameters is the air temperature at the entrance, as mentioned in Chapter 4, to register a perfect step change in the temperature is practically implausible; however, the approximation to this generated by the equipment is sufficient. The function that governs the temperature at the entrance is in Eq. 4.28:

$$T_{Air} = 1 - e^{(-t_a/\psi)}$$

meaning that the temperature increase depends on the time raised at an exponential rate. This equation makes up for the difference in value from an ideal step change to the actual step change. This equation is applied to the experimental data in order to calculate the value of the temperature response ψ. This value was obtained for each run of each sample and was included in the calculations.

There is a small drop in temperature after the moment the test is started, which was caused by a small quantity of air trapped between the ball valve and the sample, which was colder is because it is not in contact with the incoming hot air until the start of the test (up to that moment the air is passing through the detour section) and from the other side it is blocked by the sample, allowing extra cooling to take place in the meantime before starting the test. Since the fitted curve does not consider this event, this instant is discarded ahead of any smoothing alteration. In Figure 5.39 The typical exit temperature fitted curve for a replicated aluminium porous structure can be seen.

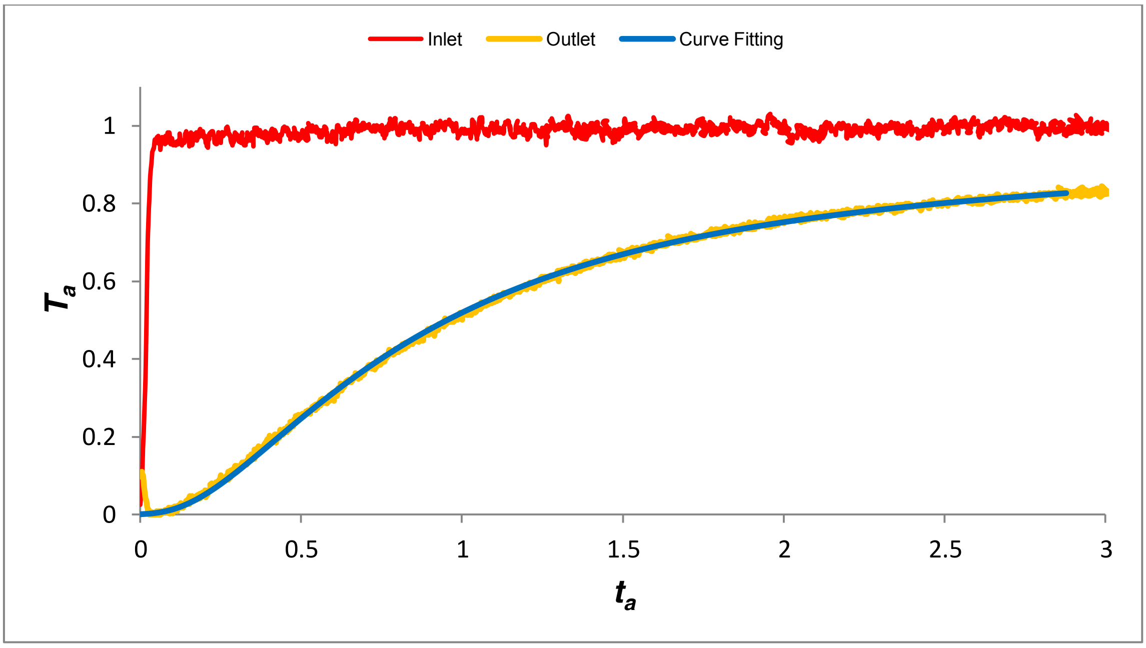

Figure 5.39 - Exit temperature fitted curve for the A1 sample at 2.55 m/s.

5.14.5.2. Specific Heat Proportion R_{tc}

The relationship between the heat capacity of the sample and the heat capacity of the wall was calculated based on the length of the sample and the length of the wall, from here the mass of the wall is obtained from the wall's volume. The mass of the thread seal tape used to prevent the hot air passing through the space between the wall and the sample was insignificantly small (≈ 1.3 g) when compared to the wall mass (≈ 70 g). The equation is present in Eq. 4.27:

$$R_{tc} = \frac{m_R c_R}{m_W c_W}$$

5.14.5.3. Regenerator Thermal Conductivity k_R*,* NTU_R **and** NTU_W **Values**

The measured k_R values for the replicated porous metals, wire felts and additive manufactured samples are in Table 5.5. The effective thermal conductivity for the wire meshes and packed spheres was less than 0.1 W/mK (lowest possible value to register with the test rig) due to the poor contact between its layers or particles, the thermal conductivity test rig was not able to determine the values for these samples, they were estimated as were the NTU_R and NTU_W.

Sample	**Material**	**k_M (W/mK)**	**k_R (W/mK)**
A1	Aluminium	205.0	26.4
A2	Aluminium	205.0	25.7
A3	Aluminium	205.0	18.8
B1	Aluminium	205.0	27.3
B2	Aluminium	205.0	28.9
B3	Aluminium	205.0	28.2
C1	Aluminium	205.0	25.0
C2	Aluminium	205.0	24.7
C3	Aluminium	205.0	26.0
V1	Aluminium	205.0	19.9
V2	Aluminium	205.0	16.6
V3	Aluminium	205.0	20.0
Al Felt	Aluminium	205.0	6.5
Cu Felt	Copper	385.0	9.4
SS304L Felt	Stainless Steel 304L	16.2	1.1
SS316L (1)	Stainless Steel 316L	16.2	2.2
SS316L (2)	Stainless Steel 316L	16.2	2.0
SS316L (3)	Stainless Steel 316L	16.2	1.6
SS316L (4)	Stainless Steel 316L	16.2	1.3
SS316L (5)	Stainless Steel 316L	16.2	1.1
Ti6Al4V (1)	Titanium Alloy Ti6Al4V	6.7	0.8
Ti6Al4V (2)	Titanium Alloy Ti6Al4V	6.7	0.7
Ti6Al4V (3)	Titanium Alloy Ti6Al4V	6.7	0.6
Ti6Al4V (4)	Titanium Alloy Ti6Al4V	6.7	0.5
Ti6Al4V (5)	Titanium Alloy Ti6Al4V	6.7	0.4

Table 5.5 - Measured thermal conductivities for the porous metal samples with a value higher than 0.1 W/mK.

Now that all the criteria are available the exit temperature curve may be calculated by the model. The estimated values of NTU_R, NTU_W and the measured value for k_R are introduced to run the program. The code produces the fitted curve and places it on the same graph as the experimental data. If one curve is placed on top of the other then these estimated values of NTU_R and NTU_W are correct; if this is not the case, the process is repeated iteratively until this occurs.

5.14.5.4. Matching Data (Replicated Sample)

As discussed earlier, matching the data is a procedure that needs special care, included in the following figures are the changes in various parameters to study the effect they have on the results.

To equalise the predicted to the experimental data, two methods were explained earlier, the maximum gradient was more direct when compared to matching all the points of the curve. To achieve this the values of the specific heat capacity of the regenerator in proportion to the wall, and effective thermal conductivity must be known to estimate correctly the number of transfer units of the wall and the sample.

If the regenerator has an inconsequential value for the number of transfer units compared to the wall and effective thermal conductivity, estimating the number of transfer units for the regenerator becomes simpler; this is applicable to the regenerators made from wire screens.

The wire net screens have small contact points with the sample holder; also, they are made from stainless steel, which has a very low thermal conductivity (16.2 W/mK) compared to other metals. This makes the number of transfer units through the wall and the effective thermal conductivity value to be negligible when predicting the number of transfer units through the regenerator.

In comparison, the porous metals have a generous contact surface with the holder, increasing the number of transfer units travelling through the wall due to the high thermal conductivity of aluminium (205.0 W/mK), more than an order of magnitude larger than stainless steel (16.2 W/mK). These two parameters must be specified accurately to predict the number of transfer units of the regenerator.

The reliability and accuracy of the method used were investigated. To demonstrate this in Figures 5.40, 5.41 and 5.42 the effect of incorrectly estimating the values of NTU_R, k_R and NTU_W for sample A1 at 2.55 m/s is shown to provoke a considerable variation in the exit temperature curve, symbolising the physical effect they have on the sample.

Before the exit temperature curve reaches stabilisation it may be divided into "reaction regions" to describe the physical meaning of what occurs in the test sample. These regions are introduced for illustration purposes only, they do not have a set range value and are independent for each porous sample.

The Start Region is primarily affected by the heat absorbed by the sample caused by convection between the fluid and the porous metal; the number of transfer units (NTU_R) of the regenerator dominates the behaviour in this region. An effect is present in the End Region as well, however it is negligible when compared to the Start Region.

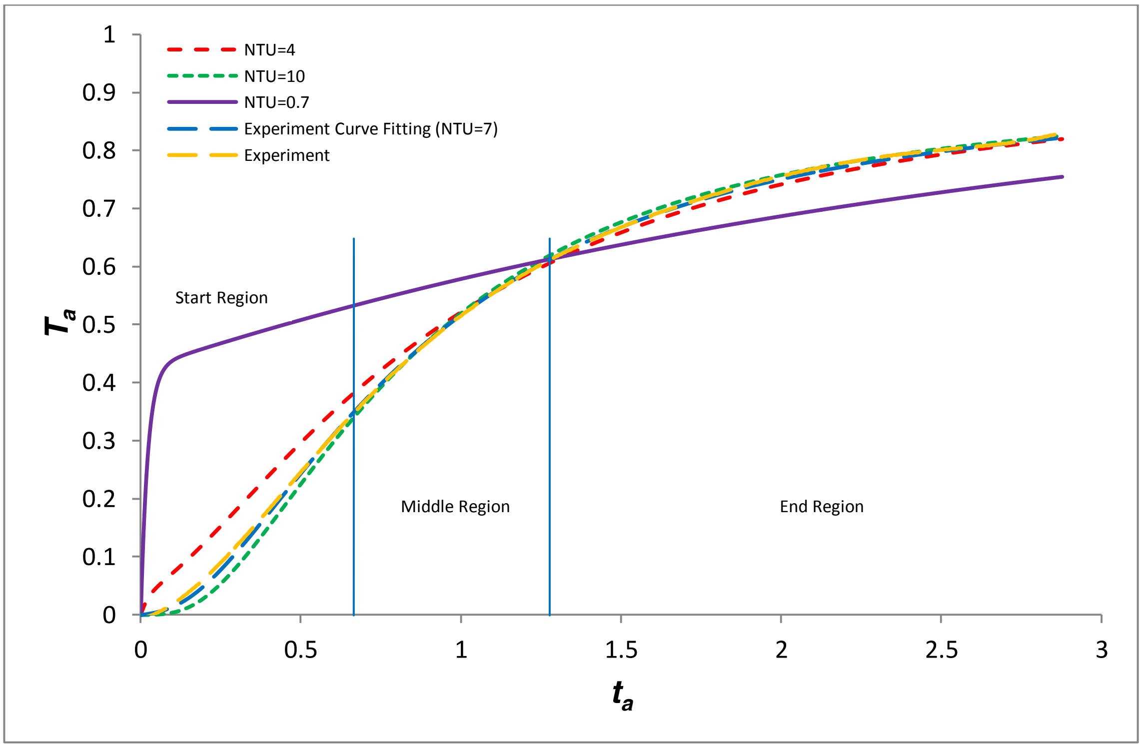

Figure 5.40 - The effect of changing the NTU_R value on the fit to experimental data for replicated porous aluminium samples.

In Figure 5.40 the difference between imputing correct and incorrect values for the number of transfer units (NTU_R) of the samples is clearly observed. All other values in the program were correct.

The orange line represents the experimental values for the A1 sample at an air speed of 2.55 m/s. The blue line represents the model's fitted curve with what was determined to be the correct value for the number of transfer units of the porous metal (NTU_R = 7). The red and green lines represent the fitted curve with incorrect values for the number of transfer units of the sample at 4 and 10 respectively. The purple line is set at NTU_R = 0.7, an order of magnitude lower than the correct amount, indicating that the sample would absorb a very small amount of heat before the system reaches stabilisation. The Start Region was used as the beginning of the curve matching process, since the NTU_R is seldom affected by the other variables.

After the convection process fills the porous metal with a certain amount of heat conduction within the sample takes charge of the effect. In Figure 5.41 it can be seen that by changing the value of the effective thermal conductivity the most significant movement in the data occurs in the Middle Region. If the conductivity in the regenerator is lower it takes longer for the temperature to reach stabilisation since a higher amount is escaping through the wall.

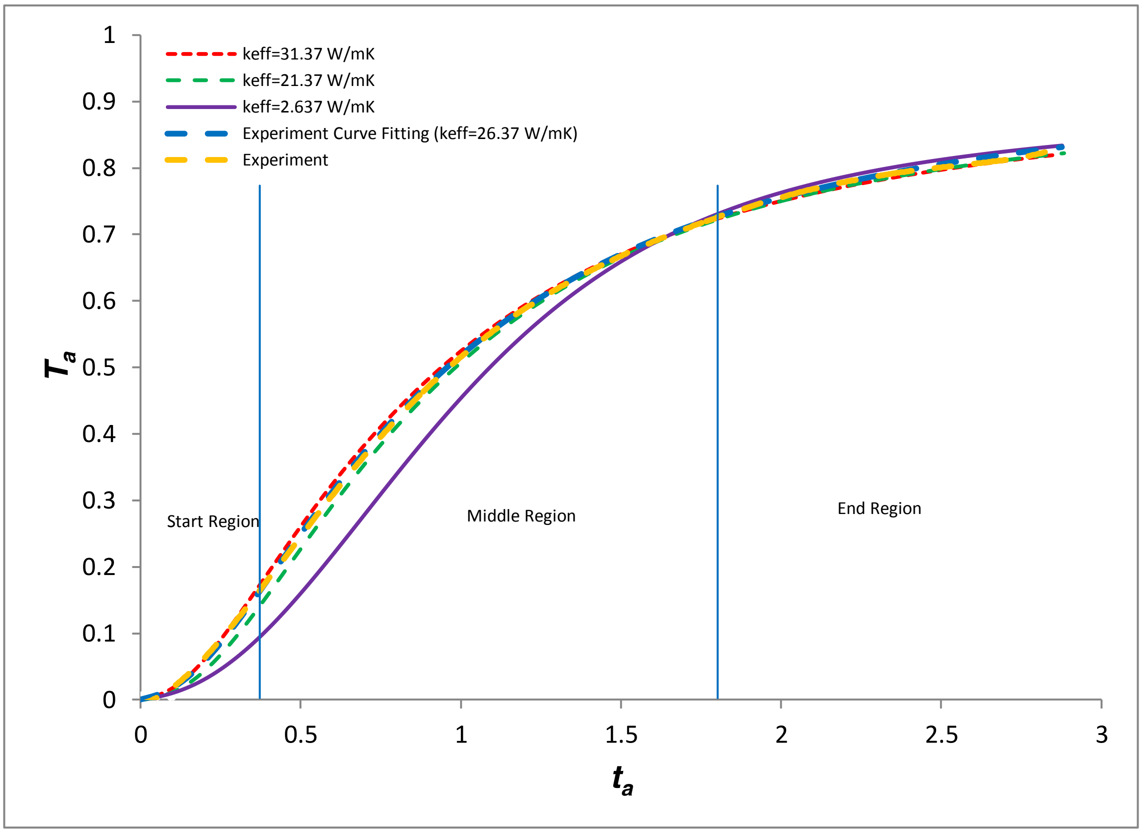

Figure 5.41 - The effect of changing the k_R value on the fit to experimental data for replicated porous aluminium samples.

In Figure 5.41 the difference between imputing correct and incorrect values for the effective thermal conductivity on the porous aluminium samples is noted. All other values in the program were correct.

The orange line represents the experimental values for the A1 sample at an air speed of 2.55 m/s. The blue line represents the model's fitted curve with the correct value for the effective thermal conductivity (k_R = 26.37 W/mK). The red and green lines represent the fitted curve with incorrect values for the effective thermal conductivity at 31.37 W/mK and 21.37 W/mK respectively, this variation is small, but noticeable. The purple line is set at 2.637 W/mK, an order of magnitude lower than the correct amount.

After both convection and conduction fill the sample with heat the air and porous metal start to transfer heat to the lowest conductivity material in the equation, which is the sample holder or wall (effectively leaving the system); this is the reason why changing the value of the number of transfer units through the wall (NTU_W) has the effect in the End Region.

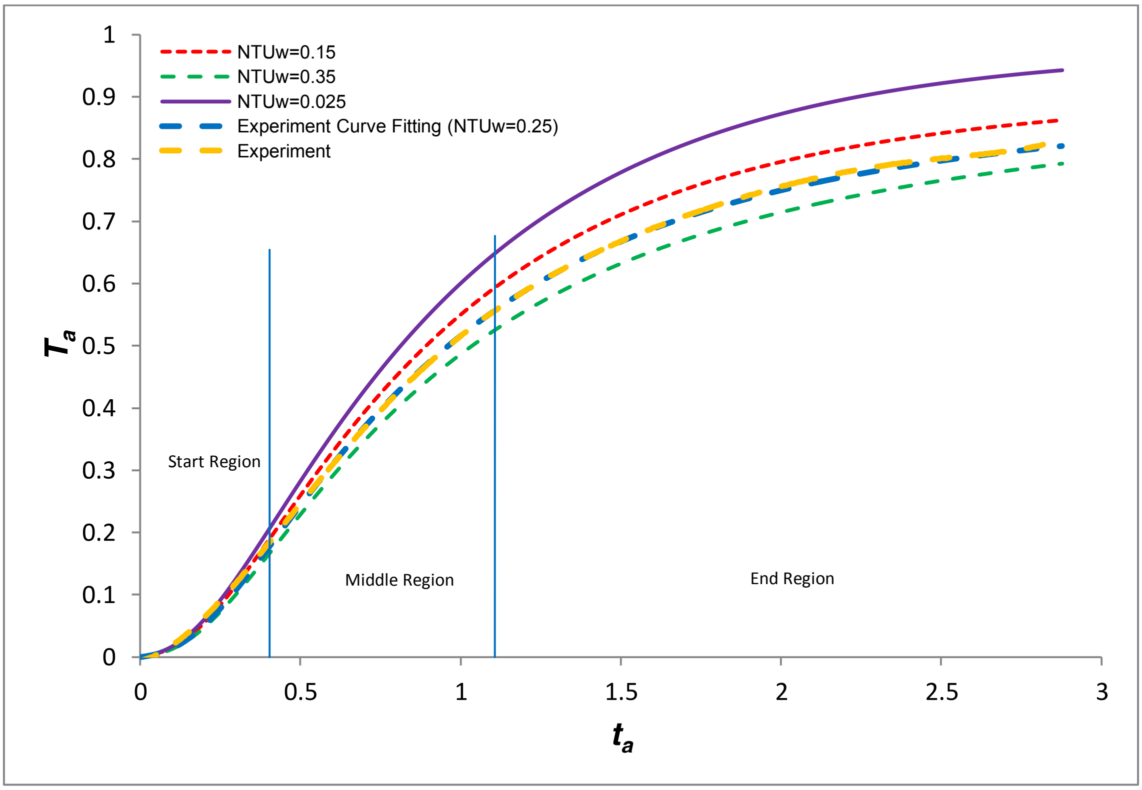

Figure 5.42 - The effect of changing the NTU_W value on the fit to experimental data for replicated porous aluminium samples.

In Figure 5.42 the difference between imputing correct and incorrect values for the number of transfer units of the wall (NTU_W) is noted. All other values in the program were correct.

The orange line represents the experimental values for the A1 sample at an air speed of 2.55 m/s. The blue line represents the model's fitted curve with the correct value for the number of transfer units of the wall ($NTU_W = 0.25$). The red and green lines represent the fitted curve with incorrect values for the number of transfer units at 0.15 and 0.35 respectively. The purple line is set at $NTU_W = 0.025$, an order of magnitude lower than the correct amount, indicating that the wall would absorb a very small amount of heat before the system reaches stabilisation. The effect of the NTU_W on the Start Region is very small since the heat transfer follows the easiest route possible, a material with a high heat capacity first and so on.

5.14.5.5. Matching Data (Mesh Sample)

A comparison with the previous graphs of the curve matching behaviour while changing the different curve matching parameters (NTU_R, k_R and NTU_W) for the 30 mesh sample is made; this is done to examine the difference if the sample is made from a different structure (replicated porous aluminium against mesh).

When comparing the behaviour of the replicated porous metals to the wire meshes while changing the values of NTU_R, k_R and NTU_W a similar behaviour can be seen. In Figure 5.43 the NTU_R change graph for the 30 mesh sample is presented.

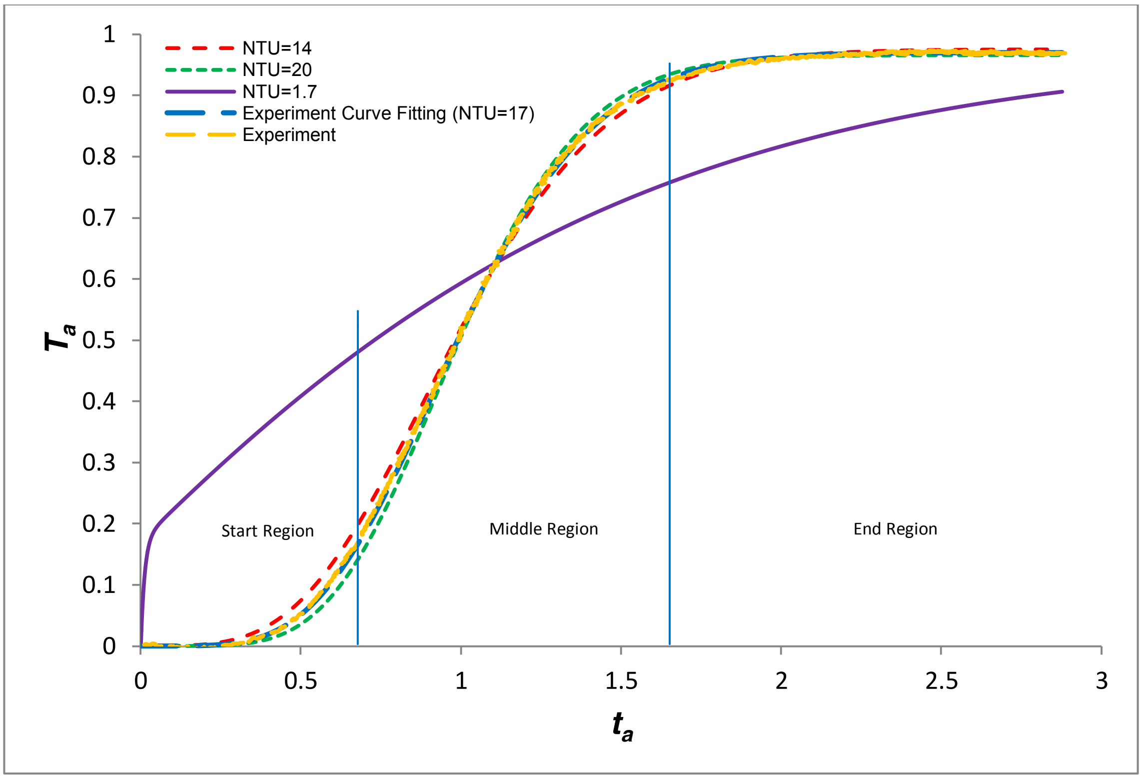

Figure 5.43 - The effect of changing the NTU_R value on the fit to experimental data for wire meshes.

In this graph the difference between imputing correct and incorrect values for the number of transfer units (NTU_R) of the mesh is noted. All other values in the program were correct.

The orange line represents the experimental values for the 30 Mesh sample at an air speed of 2.55 m/s. The blue line represents the model's fitted curve with the correct value for the number of transfer units of the porous aluminium (NTU_R = 17). The red and green lines represent the fitted curve with incorrect values for the number of transfer units of the porous aluminium at 14 and 20 respectively. The purple line is set at NTU_R = 1.7, an order of magnitude lower than the correct amount, again indicating that the sample would absorb a very small amount of heat before the system reaches stabilisation. The change in the Start Region for the mesh is not as significant when compared to the Start Region of the A1 porous sample (Figure 5.40); this occurs due to the difference in structure between the samples and the material (Al vs. SS304L) it can be noticed that the plateau at the beginning of the graph from the mesh sample is longer when compared to the mesh, this translates to the difference in NTU_R values from 7 for the replicated porous aluminium to 17 for the mesh. In Figure 5.44 the k_R change graph for the mesh can be seen.

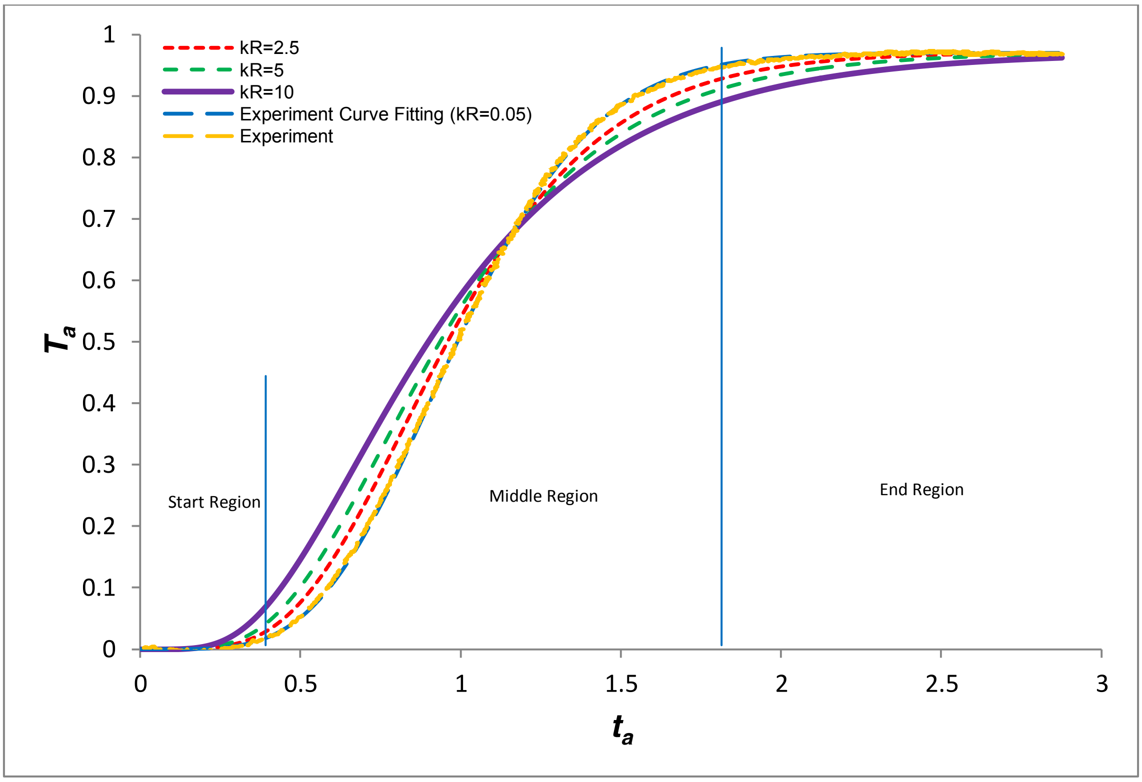

Figure 5.44 - The effect of changing the k_R value on the fit to experimental data for wire meshes.

In this graph the difference between imputing correct and incorrect values for the effective thermal conductivity on the aluminium porous samples is noted. All other values in the program were correct. As with the A1 sample, the significant change when altering the thermal conductivity value happens in the Middle Region.

The orange line represents the experimental values for the 30 Mesh sample at an air speed of 2.55 m/s. The blue line represents the model's fitted curve with the correct value for the effective thermal conductivity (k_R = 0.05 W/mK). The red and green lines represent the fitted curve with incorrect values for the effective thermal conductivity at 2.5 W/mK and 5 W/mK respectively. The purple line is set at 10 W/mK, higher than two orders of magnitude than the correct amount. The difference in the behaviour of the lines when compared to the k_R graph (Figure 5.41) of the A1 sample is due to the structure and material, in Figure 5.45 the 30 Mesh NTU_W change graph can be seen.

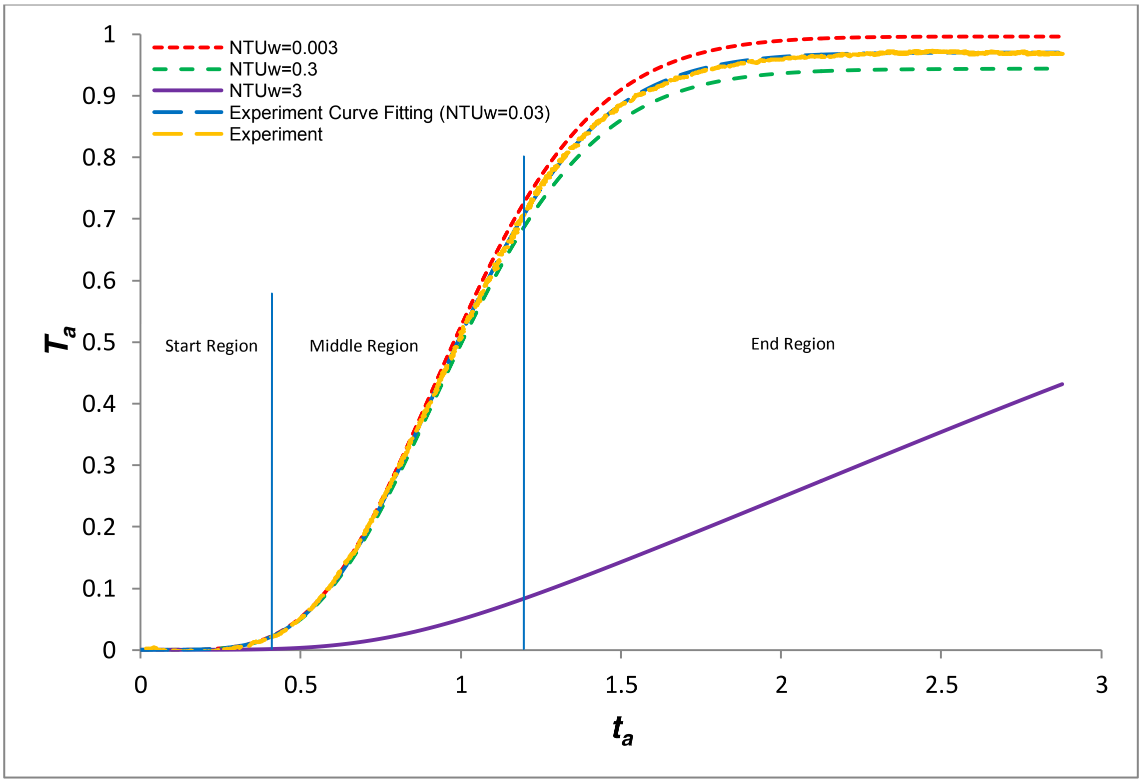

Figure 5.45 - The effect of changing the NTU_W value on the fit to experimental data for wire meshes.

In this graph the difference between imputing correct and incorrect values for the number of transfer units of the wall (NTU_W) is noted. All other values in the program were correct.

The orange line represents the experimental values for the 30 Mesh at an air speed of 2.55 m/s. The blue line represents the model's fitted curve with the correct value for the number of transfer units of the wall ($NTU_W = 0.03$). The red and green lines represent the fitted curve with incorrect values for the number of transfer units of the wall at 0.003 and 0.3 respectively. The purple line is set at $NTU_W = 3$, three orders of magnitude higher than the correct amount. When compared to the A1 sample NTU_W Change graph (Figure 5.42) the behaviour is very similar.

5.15. Summary of Steps to Obtain an NTU_R Graph

1. Perform the run on the heat transfer test rig.
2. From the output data change time and temperature to adimensional values, and calculate the constants needed to obtain the exit temperature curve (average mass flow rate, air density based on the temperature of the test, entrance temperature constant pressure, minimum and maximum temperature values to set the upper and lower limits of the graph, specific heat proportion).
3. Estimate the values of NTU_R and NTU_W (and k_R if it was not measured), input the physical characteristics of the sample and the data from the test to the MATLAB code to calculate the exit temperature curve (smoothing, curve fitting, plotting).
4. If the curve does not fit the experimental data step 3 is repeated until this occurs.
5. The correct values for that sample at that flow rate are registered, this translates to one point for one sample in the NTU_R graph.
6. If the NTU_R value is correct the MATLAB code repeats the process for the next flow rate.

In this chapter the experimental methods for porous metal production are shown, it includes the description of the equipment and the three different ways to produce porous metals by the replication technique, out of the three, the argon only technique was selected to produce the samples for this work.

Apart from these samples others were created with the purpose of comparing different structures (mesh, felt, packed spheres and ALM samples) to determine the best for regenerator purposes and to evaluate if the replicated samples have the opportunity to challenge the wire meshes that are currently used as regenerators in Stirling engines.

In the second part of the chapter the testing procedure for flow and heat transfer is addressed and finally the manner in which the results are to be interpreted is presented in detail with a short summary in the final subsection; in Chapter 6 the replication process developments are explained in detail.

Chapter 6. Replication Technique Developments

From a general understanding and specific applications, porous metals create interest within the materials community. Their applications have been suggested and tested experimentally, they have been used in impact absorption producing low weight structures, as heat exchanger units due to their large heat transfer area, as bone substitution implants in the body, just to name a few. Even though an advanced knowledge concerning their structure, properties and production methods is available; there is still left to complete the information on the particular characteristics and outcomes that the different building processes create.

The porous metal production process known as replication, entails a molten metal being forced into the free spaces between granules of a disposable preform element; this process permits an elevated level of control. However, the procedure depends on personal knowledge. The objective of these protocol alternatives is to create porous metals in a simple and direct manner, allowing to adjust their properties by certain modifications in the procedure. Open cell porous aluminium samples with a porosity range of 61 to 78% and a pore size range of 1.00 mm to 2.36 mm were made.

First to discuss are the assessments done prior to choosing the replication production technique parameters to produce all regenerator samples.

6.1. Initial Tests

For aluminium infiltration gravity is not enough force the molten metal to enter into the NaCl space holder particles, due to the elevated value of the metal surface tension. This is the reason why assistance is needed for the three methods explored here. The vacuum - argon process was applied previously in the laboratory at Sheffield, yet when running the cycle, the rate of quality sample production was low and sample variation remained high. After the challenges presented by the mechanical pressure method (as discussed earlier) for this work the option of the argon only method appeared to be the most viable, and when compared to the other two methods it seemed the most suitable approach for further development.

When performing the argon only method initially the rate of fully successful infiltrations with no observable defects (Section 6.2) was low (around 1 out of 10), although this was still advantageous compared to the vacuum - argon method where the rate of defect-free specimen production was around 1 out of 15. This, and the many drawbacks of the mechanical pressure method, meant that test trials were started with the argon only method.

It was found that the process was significantly affected by very small variations in the operating protocol. For example, initially irregular pieces of aluminium ingot were placed directly on top of the preform without considering their arrangement or the free space between them, giving rise to poor infiltrations even when raising the pressure to elevated values (5 - 6 bar); this problem was corrected with the manufacturing of the aluminium bars which fitted closely in the chamber. After this, the infiltration pressure which needed to be applied was much lower (3 - 4 bar) and the rate of defect-free samples produced increased to around 3 out of 10.

Another change was filling the infiltration mould almost to the top by adding more NaCl or a larger piece of the aluminium bar, this produced much better results, with the rate of defect-free samples increased to around 8 in 10. There were additional advantages to productivity.

Following the heating pattern of the furnace used with the vacuum - argon method the rate of sample production only allowed two samples per day, with the new method, up to five samples a day could be produced. This was achieved by reducing the dwell time from two hours to 50 minutes per sample. The infiltration pressure used was 3.5 bar. 15 samples were produced for the purpose of establishing the shortest acceptable dwell time.

6.2. Sample Defects

Visual assessment of the samples took place, evaluating the infiltration of the NaCl preform from a range of 1 (worst) to 5 (best) at different dwell times, in Table 6.1 the results are shown. The assessment was based on the uniformity of the structure from the outside, this type of defect has been caused in other experiments [199] by the preheating temperature of the mould, indicating that at a lower preheating temperature (500°C) the molten metal solidifies faster than when using a higher value (550°C), however in these experiments the mould is not preheated and the defects can be attributed to the dwell time and infiltration temperature; additionally the samples were split in half to observe the internal structure, these defects are of the macroscopic nature.

Dwell Time (min)	Al Sample	Assessment
120	1	4
120	2	5
120	3	5
60	4	5
60	5	5
60	6	4
30	7	2
30	8	2
30	9	1
40	10	4
40	11	4
40	12	3
50	13	4
50	14	5
50	15	5

Table 6.1 - Dwell time assessment for the replication process of aluminium samples.

The optimal operation temperature for infiltration was also evaluated. Parting from the 740°C from the vacuum - argon method, two additional temperatures were tested, nine porous aluminium samples were produced for this purpose.

The infiltration pressure used was 3.5 bar. Visual assessment of the samples took place, evaluating the infiltration of the NaCl preform from a range of 1 (worst) to 5 (best) at different temperatures, in Table 6.2 the results are shown.

Temperature (°C)	Al Sample	Assessment
740	16	5
740	17	5
740	18	5
720	19	4
720	20	3
720	21	4
760	22	4
760	23	4
760	24	3

Table 6.2 - Temperature assessment for the replication process of aluminium samples.

In Figure 6.1 sample 20 can be seen, made with the furnace set at 720°C. The sample has noticeable defects on the side, in this case the liquid metal's viscosity is higher, improperly filling all the crevices between the NaCl preform.

Figure 6.1 - Sample 20, infiltrated at 720°C with noticeable defects on the outer wall.

In Figure 6.2 sample 24 can be seen, made with the furnace set at 760°C. The aluminium's viscosity is lower (2%) [200] due to the higher temperature, in this case causing it to encase and infiltrate some of the NaCl particles, this prevents their leaching. This type of defect is of the microscopic kind, it has been seen by other researchers and is attributed to the high infiltration pressure pushing the molten aluminium into the salt particles, not just around them [9].

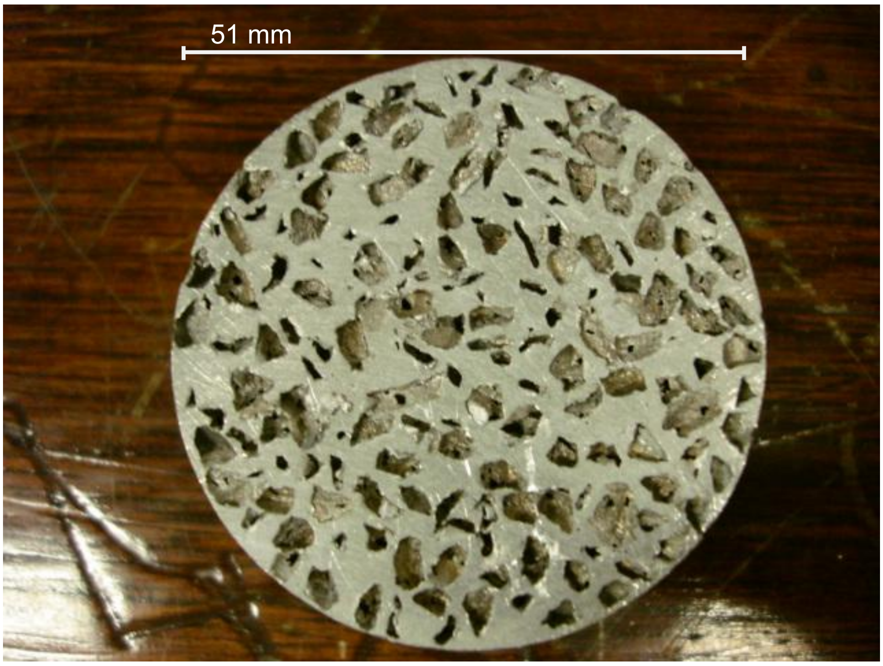

Figure 6.2 - Sample 24, infiltrated at 760°C with noticeable defects in its interior structure.

In Figure 6.3 sample 16 can be seen, made with the furnace set at 740°C. The sample structure looks uniform when compared to the others, in the end confirming that 740°C was a suitable temperature for these processes.

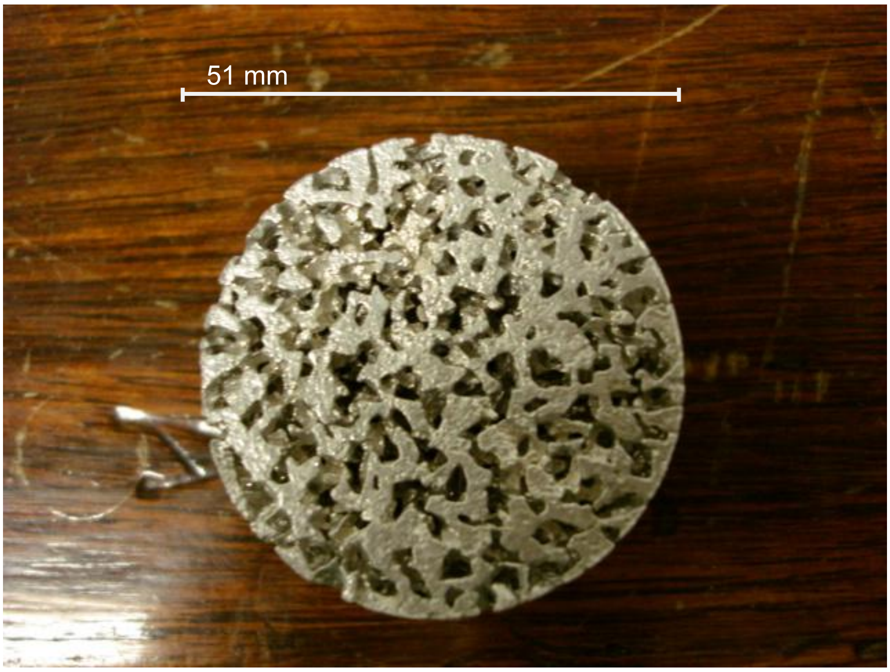

Figure 6.3 - Sample 16, infiltrated at 740°C with a uniform structure.

The defects present in Figures 6.1 and 6.2 were similar to the defects present in the samples produced to evaluate the dwell time, this to illustrate the assessment values 3, 4 and 5; for values 1 and 2 the defects were more noticeable.

The infiltration pressure is related to the capillary radius directly by using the Young-Laplace equation.

$$p_c = \frac{2\gamma cos\theta}{r} \qquad \text{Eq. 6.1}$$

This depends on γ the surface tension of the molten aluminium (0.89 Nm [195]) and θ the contact angle between the molten aluminium and the NaCl particles (139° [196]).

With an infiltration pressure of around 3 bar for a sealed chamber under vacuum the molten metal would be predicted by the equation above to be able to infiltrate preform particles with spaces of 9 μm, so the infiltration of particles of 100 μm diameter should not have been a challenge, however, for the type of experimental setup in this work it was not found to be possible due to the fact that the system is not under vacuum, and in addition to this there may be possible leaks at the top of the mould, reducing the actual infiltration pressure applied.

During the melting process the chamber is open to the atmosphere, leaving air to flow freely inside it, once the aluminium melts it captures the air present in the free spaces of the preform, when the argon pressure is applied to the liquid metal it compresses the air toward the bottom of the chamber, which is the reason why the preform with these particle sizes (1 - 2.36 mm) is infiltrated at these pressure levels.

The addition of boron nitride spray to the mould prevented the bonding between the molten aluminium and the stainless steel after cooling down, making it easier for the samples to be removed. Taking special consideration for the bottom and top edges of the mould to be free from any impurities and in perfect contact with the graphite gaskets was also found to be critical in obtaining a good seal.

The drying time of the boron nitride coat was found to also play a small but important part of the process; after a few trials of the coating not being dried properly before adding the preform it was found that when pouring the NaCl particles and then shaking the mould slightly to position the top layer of the particles as a flat surface, the movement of the particles removed the layer of boron nitride, preventing it from being effective. It was noted that heating the mould for some time at a relatively low temperature (100°C) helped with the drying, however, it was not compulsory as the coating will dry naturally if left for sufficient time.

Originally the mould was assembled with the pipes and valves system and introduced in the furnace directly, however, this caused uncertainty in the outcome of processing. When repeating the process exactly with each trial the result could still be positive or negative. For some of the unsuccessful cases, the fault was traced to the moment of infiltration or in the cooling period. The indicator of a fault was a leak of the molten metal at the bottom of the mould while infiltrating, or a leak of argon while cooling down the mould on the copper slab, and therefore the fault was attributed to improper sealing of the chamber. To prevent this occurring, the vacuum seal test step was developed.

The end result after making all these changes to the original argon only (or gas only) method is that, if following the process steps precisely, the rate of uniform to non uniform porous metal structures improved from approximately 1 out of 10 to approximately 9 out of 10 samples, further attention to the fine details could possibly achieve 10 out of 10 uniform samples in the near future. The production rate was increased from a maximum of 2 a day to 5 a day. The procedure has been adopted by other workers and applied successfully, for example to magnesium, by using a protective atmosphere of sulphur hexafluoride [169] during the infiltration procedure; it can also be used for different size moulds.

After determining the correct parameters for infiltration the alternatives in the replication technique to produce samples with different characteristics are presented, these are named infiltration protocols.

6.3. Infiltration Protocols

The infiltration protocols were developed from the need to produce quality samples by replication, exploring different options of pressures, preform density and accessories or extra materials to be used as aides in the technique. For all protocols the same procedure for the aluminium bar preparation, the furnace temperature and heating rate and sample extraction remain the same. The difference lies in the preform preparation, mould preparation and infiltration pressure used. All protocols are for the 51 mm diameter infiltration mould. In these techniques efforts have been made to minimise the use of complicated machinery so the method is easily applicable and as rapid as possible.

Originally the preform was made from Hydrosoft water softening NaCl tablets, these tablets were square shaped 20 mm pieces and had to be broken down and refined manually to fit the particle size of the desired preform. At the start of the study a production run of 6 samples was made to find out if the shape of the NaCl particle had an effect on the porosity of the resulting porous metal, the results are given in Table 6.3.

NaCl Particle Shape	ε (%)
Irregular	63.5
Irregular	63.0
Irregular	63.1
Spherical	63.1
Spherical	62.6
Spherical	63.3

Table 6.3 - Porosity differences between samples with irregular and spherical preform particle shape.

It was found that, the shape of the NaCl particles (irregular and spherical) had no major effect on the porosity of the samples when compared to the change in production protocol [149]. The porosity was measured using the sample volume and bulk weight. In Figure 6.4 the two shapes of the NaCl particles are shown, as well as two of the produced samples, to illustrate the visible differences among them. To save time and energy the Hydrosoft tablets were substituted by Hydrosoft granules.

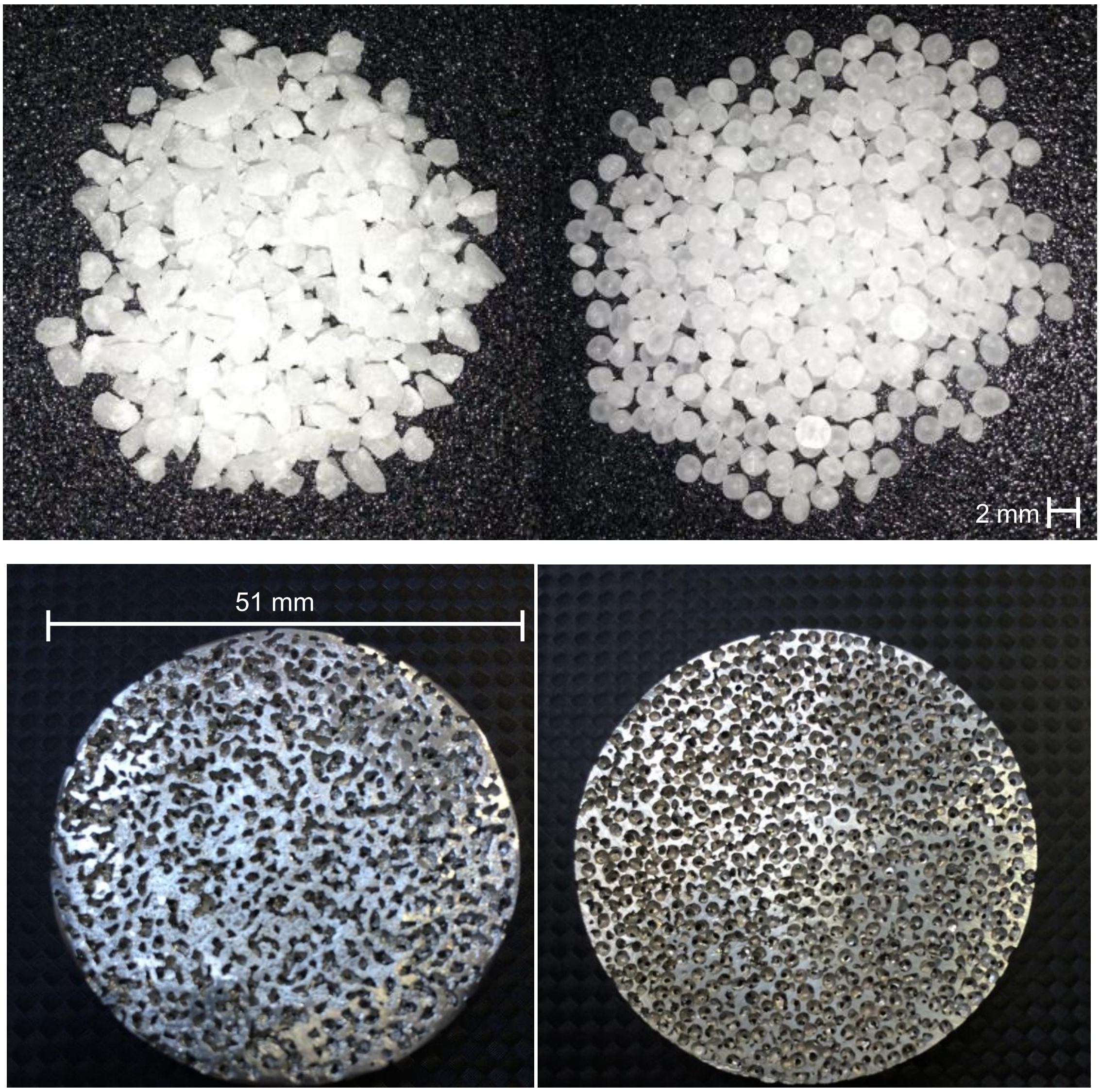

Figure 6.4 - Shape of the NaCl particles and the porous metal produced (Left: Broken Hydrosoft tablets produce irregular shaped pores; Right: Hydrosoft granules produce spherical shaped pores).

6.3.1. Protocol W

Protocol W can be called the modified technique to process porous metals using the replication method; it is the technique emerging with all the changes and improvements over the original argon only technique, the description of this protocol is in Section 5.2.2.3.

As mentioned before, the methods for aluminium bar production, furnace and sample extraction remain unchanged. At the preform preparation stage, considering an average size of NaCl particles of 1.55 mm, and depending on the height of the porous metal required, the amount of NaCl used varies from 100 g to 300 g; consequently the amount of aluminium should be between 200 g and 400 g on average.

Images of samples produced by this protocol are in Figure 6.5, these were produced with the irregular preform particles.

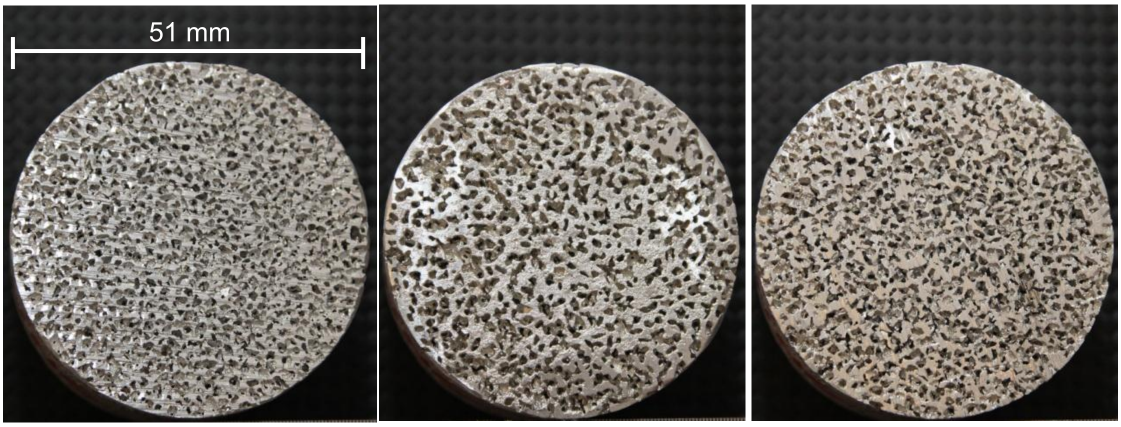

Figure 6.5 - Protocol W porous metals are made of 99.7% aluminium in an open cell configuration with irregular shape preform particles, a pore size average of 1.55 mm, an average porosity of 63%, measuring 51 mm in diameter and 25.4 mm in height.

6.3.2. Protocol X

Protocol X was devised as a means to reduce the infiltration pressure applied and so to boost the porosity of the porous metal created. Higher pressures were needed to cause infiltration than were expected purely from considerations of the surface tension of the liquid aluminium, suggesting that some gas or vapour existed in the preform, requiring an additional pressure to be overcome. The difference of this protocol from protocol W is that in the preform preparation, an additional step is present.

This step is the addition of fine NaCl particles to the infiltration mould, before pouring in the NaCl particles which make up the preform. The schematic diagram can be seen in Figure 6.6.

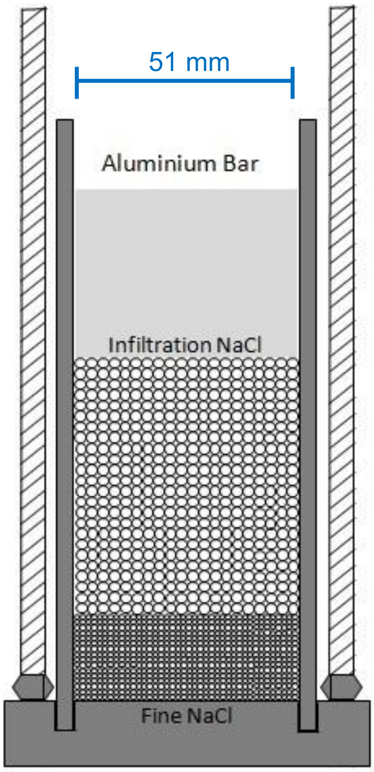

Figure 6.6 - Protocol X schematic diagram.

The size of these particles is roughly one fourth the size of the infiltration NaCl, it was determined from previous infiltration tests in which was noted that the molten aluminium did not creep into the particles, creating an effective stop for the liquid metal, the size recommended for each particle size of NaCl used in preforms here can be seen in Table 6.4. The amount of fine NaCl added per infiltration round was 100 g.

Infiltration NaCl Particles	Fine NaCl Particles
1.09 mm	< 250 μm
1.55 mm	< 400 μm
2.18 mm	< 500 μm

Table 6.4 - Fine NaCl particle size recommended for each infiltration NaCl particle size.

The purpose of these fine NaCl particles is to create a pocket of free space at the bottom of the mould, allowing that the air contained inside it to be moved from the preform intended to be infiltrated into this space. This permits the molten aluminium to occupy the space between the infiltration NaCl particles. Overall this change manifests itself in a reduced requirement for pressure, 3 bar compared to 3.5 bar for protocol W. With this pressure the molten metal will not infiltrate the fine NaCl particles also preventing the aluminium from reaching the bottom of the mould, this way avoiding a leak. To this extent, the control of infiltration with the use of fine NaCl is self-regulating; there will be no infiltration of the fine NaCl unless the sizes greater than the fine NaCl are fully infiltrated.

Another effect is that by reducing the infiltration pressure a uniform yet more porous sample can be produced. When compared to samples made by protocol W, protocol X samples have an increase of 5% in porosity, moving from an average of 63 to 66%, while still keeping uniformity in its structure. Images of samples produced by this protocol are in Figure 6.7.

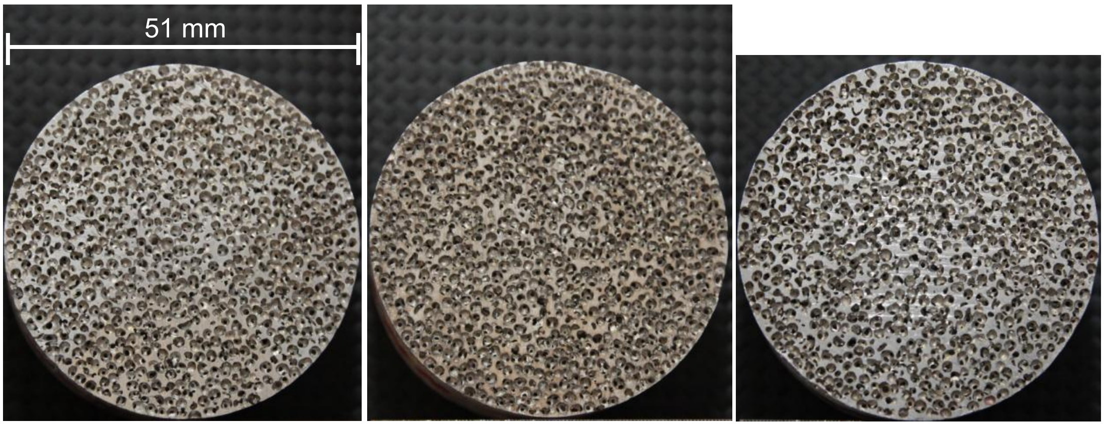

Figure 6.7 - Protocol X porous metals are made of 99.7% aluminium in an open cell configuration with spherical shape preform particles, a pore size average of 1.55 mm, an average porosity of 66%, measuring 51 mm in diameter and 25.4 mm in height.

6.3.3. Protocol Y

The objective of protocol Y is, like protocol X, to reduce the infiltration pressure and to increase the porosity of the porous metals. Like protocol X, protocol Y uses the fine NaCl at the bottom of the mould. Here the difference lies in the removal of the bottom gasket of the mould, located in the base groove, to provide a path for gas from the fine NaCl to be evacuated from the chamber.

By removing this gasket, the infiltration pressure applied falls greatly from 3 bar in protocol X to 1 bar in protocol Y. As with protocol X this amount of pressure is enough to infiltrate the preform but not the fine NaCl particles, meaning that the absence of the gasket does not introduce the risk of leaks.

Additionally, by this reduction of infiltration pressure, a porous metal with a higher porosity than one made using protocol X can be produced. When compared to samples made by protocol X, protocol Y samples have a further increase of around 5% in porosity, moving from an average 66 to 70% while still keeping uniformity in its structure. Images of samples produced by this protocol are in Figure 6.8.

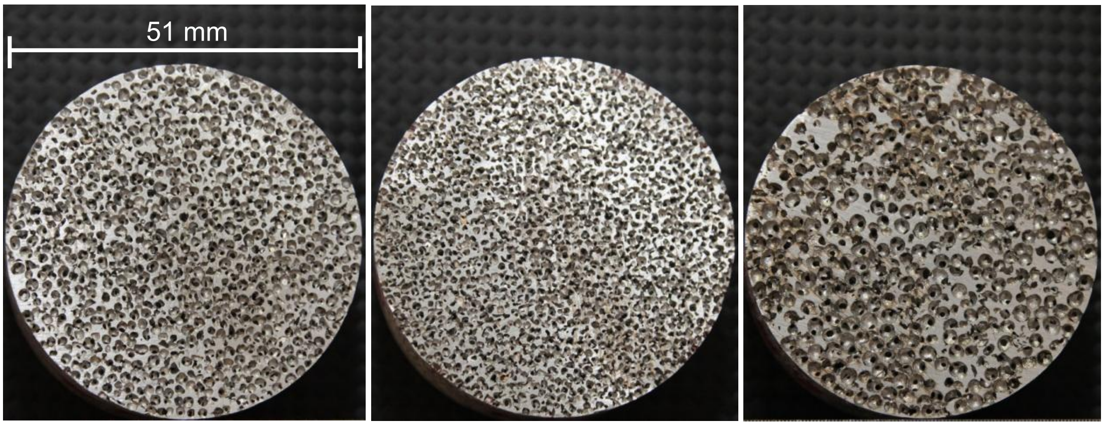

Figure 6.8 - Protocol Y porous metals are made of 99.7% aluminium in an open cell configuration with spherical shape preform particles, a pore size average of 1.09 mm, 1.55 mm and 2.18 mm respectively, an average porosity of 70%, measuring 51 mm in diameter and 25.4 mm in height.

To demonstrate the effect of preform particle size at a relatively low infiltration pressure of 1 bar, these three samples made with protocol Y have very similar porosities. The change of the NaCl particle size has no noticeable effect compared to the protocol used. This is only valid for low infiltration pressures. As mentioned before, with higher infiltration pressures (> 1 bar) when changing the NaCl particle size of the preform, the infiltration pressure does increase if the NaCl particle is smaller.

6.3.4. Protocol Z

For protocol Z, as before, the idea was to further increase the porosity of the porous metal, this time keeping the same infiltration pressure as with protocol Y of 1 bar. As with protocol Y a layer of fine particle size NaCl is used and the bottom gasket is absent from the base groove.

The key step of protocol Z is to vibrate the space holder NaCl particles once they have been introduced into the mould, so that they are accommodated more efficiently, eliminating a larger amount of free space where the molten metal could pass, increasing the density of the space holder, and decreasing that of the porous metal.

To meet this objective, after adding the fine NaCl particles at the bottom of the infiltration mould, two circles made from 2 mm thick Kaowool sheet of 51 mm in diameter are added on top of the fine NaCl particles before pouring the infiltration NaCl particles (this layer prevents mixing of the two different particle sizes). After doing so, the mould and base are attached to a vibrating table, the set was shaken for one minute at 50 Hz and a 0.01 m amplitude.

After the mould and base were vibrated, the regular steps of the protocol (identical to Protocol Y) are followed. The increase in porosity was a considerable rise from the 70% of protocol Y, reaching 76% on average. Images of samples produced by this protocol are in Figure 6.9.

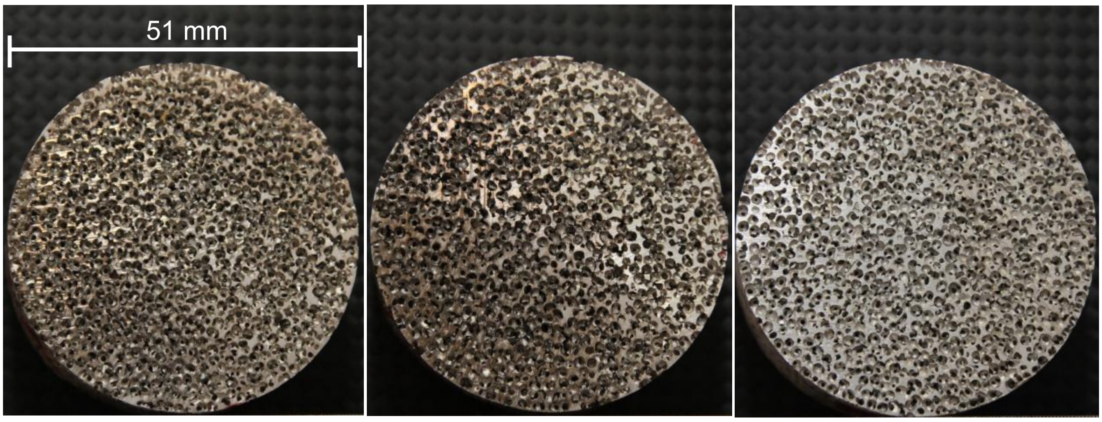

Figure 6.9 - Protocol Z porous metals are made of 99.7% aluminium in an open cell configuration with spherical shape preform particles, a pore size average of 1.55 mm, an average porosity of 76%, measuring 51 mm in diameter and 25.4 mm in height.

In summary these four protocols were developed to increase the porosity of replicated open cell porous aluminium samples, the porosity change overall was from 63 to 76% on average with a reduction in infiltration pressure from 3.5 bar to 1 bar. In protocols X, Y and Z the addition of the fine NaCl particles provide a place for air contained in the space holder while infiltrating and acting as a stop for the molten metal as well. In Table 6.5 the characteristics of the protocols are summarised.

Protocol	ε (%)	Infiltration NaCl Particle Size (mm)	Infiltration Pressure (bar)	Fine NaCl Particle Size (μm)	Bottom Gasket Removal	Preform Vibration
W	63.5	1.55	3.5	x	x	x
W	63.0	1.55	3.5	x	x	x
W	63.1	1.55	3.5	x	x	x
X	66.3	1.55	3.0	< 400	x	x
X	66.2	1.55	3.0	< 400	x	x
X	66.1	1.55	3.0	< 400	x	x
Y	70.0	1.09	1.0	< 250	✓	x
Y	70.0	1.55	1.0	< 400	✓	x
Y	70.8	2.18	1.0	< 500	✓	x
Z	76.2	1.55	1.0	< 400	✓	✓
Z	75.7	1.55	1.0	< 400	✓	✓
Z	76.6	1.55	1.0	< 400	✓	✓

Table 6.5 - Four different infiltration protocols and their characteristics.

Protocols Y and Z use a much lower infiltration pressure of 1 bar, while still producing a uniform structure. The removal of the graphite gasket at the bottom enables a minute flow of air to escape from the infiltration mould, allowing for a higher difference in pressure, preventing the compression of the air present in the space holder, allowing for a much smoother infiltration. If this process were to be done without the fine NaCl particles the aluminium would have been likely to be able to escape from the chamber, but the fine NaCl layer is not infiltrated at 1 bar, keeping the aluminium inside the mould.

Frequently, the region of poor infiltration is found at the base of the porous metal, likely to be as the molten aluminium has the longest distance to travel to reach here. This is the reason why the mould is left in the furnace under pressure for a minute after infiltration, before placing it on the copper slab. On rare occasions there is also another poorly-infiltrated region found at the top, where the top of the preform NaCl meets the molten metal. To avoid influence of either of these areas, which may not pre representative of the material as a whole the top and bottom parts of the porous metal are removed with a band saw after infiltration.

The mechanical cutting of the sample must be done before leaching the NaCl out. If the porous metal is cut after leaching the internal structure will be damaged and may create a blockage, preventing a fluid from being able to pass through it. If the cuts have to be made after leaching a favourable technique is Electro Discharge Machining (EDM) since it is a non-contact cutting method that does not load the sample; it is also known as spark erosion.

After discussing the alternatives of porous metal production by replication, in the next section the amount of pressure used to infiltrate is discussed in more detail.

6.4. Effect of Infiltration Pressure on the Replicated Porous Metals

Several tests using Protocol X were done to evaluate the effect of the infiltration pressure on the porous metals produced. A 3 bar infiltration pressure was used to make samples with a pore size (from the particle size of the NaCl used) of 1.55 mm on average, obtaining a uniform structure all around and a porosity of 66%. If the NaCl particle size was increased to 2.18 mm the pressure needed to infiltrate and obtain good infiltration with similar density was 2.75 bar. If the NaCl particle size was decreased 1.09 mm the infiltration pressure needed for a uniform structure rose to 3.25 bar. This means that if the surface area of the preform increases (smaller NaCl particles) the liquid metal needs a larger force to act upon it to produce infiltration [170].

Depending on the method used, the difference between the values of infiltration pressure when changing the space holder particle size decreases as the infiltration pressure value decreases. In Table 6.6 the pressure applied to infiltrate the different preform particle sizes depending on the protocol used are shown.

Protocol	Particle Size (mm)	Infiltration Pressure (bar)
W	1.09	4.00
W	1.55	3.50
W	2.18	3.00
X	1.09	3.25
X	1.55	3.00
X	2.18	2.75
Y & Z	1.09 - 2.18	1.00

Table 6.6 - Infiltration pressures applied depending on the protocol used.

When using Protocol Y or Z, 1 bar is used for the three preform particle sizes, at lower pressures the change in particle size is less significant when considering infiltration pressure.

Using a fixed 1.55 mm NaCl particle size and Protocol X (nominally 3 bar infiltration pressure), tests were done varying the pressures to observe the effect on the porosity of the produced samples, yielding the results shown in Table 6.7.

Infiltration Pressure (bar)	ε (%)
2.5	69
3	67
3.5	66
4	65
5	63
6	62
7	61

Table 6.7 - Protocol X infiltration pressure increase test results.

It has to be noted that using a lower infiltration pressure increases the porosity of the sample, however, visible structural defects start to appear. When using a higher infiltration pressure some of the NaCl particles became enclosed by the metal, making the sample impractical for regenerator purposes. In Figure 6.10 the differences between the surface appearance of samples after infiltration and before dissolution of the NaCl are shown. The left image is of a test using an infiltration pressure of 1 bar, and it can be seen that the outer surface of the preform contains only a few traces of the metal. The middle image is of a test using an infiltration pressure of 3 bar, a uniform infiltration. The last image is of a test using an infiltration pressure of 7 bar, where few of the NaCl particles are visible, being enclosed within the metal. These are surface images, from experience it was found that they are representative of the bulk condition as well, in the next section, the samples that were produce for this work are detailed.

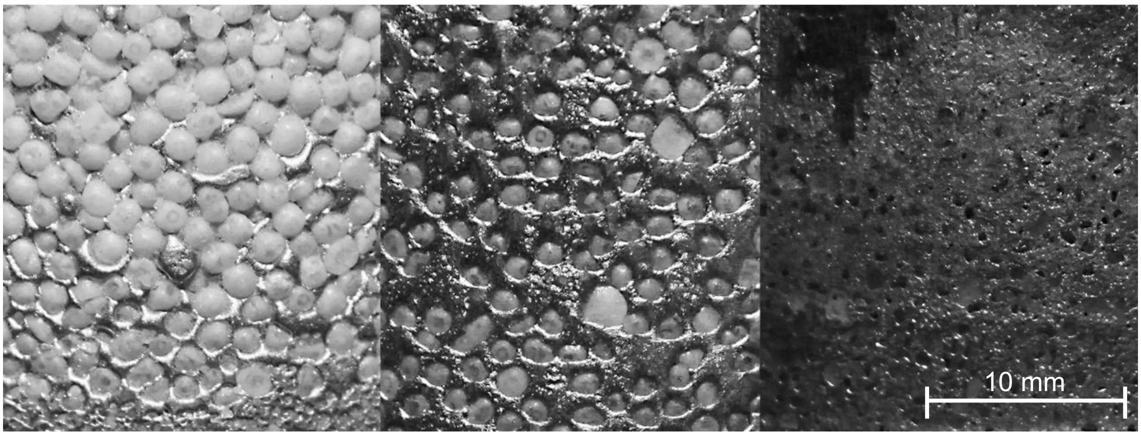

Figure 6.10 - Infiltration pressure effect on porous metals, under (left), correct (middle) and over infiltration (right).

6.5. Replicated Porous Aluminium Samples Produced for this Work

The argon only method was the infiltration method selected for porous metal production after evaluating the other existing techniques in the department. 12 replicated porous metal samples were made using Protocols Y and Z to test for their performance as regenerators, using the argon only protocols newly developed for this work, applying low infiltration pressure to obtain the highest porosity samples available with these protocols. Their characteristics are in Table 6.8.

Sample	Preform Particle size (mm)	Length (mm)	ε (%)
A1	1.09	25.1	69.6
A2	1.09	25.3	69.9
A3	1.09	25.6	73.0
B1	1.55	25.0	69.0
B2	1.55	26.1	69.2
B3	1.55	25.2	70.2
C1	2.18	25.0	69.7
C2	2.18	23.9	70.8
C3	2.18	25.6	72.2
V1	1.55	26.7	76.3
V2	1.55	25.8	78.0
V3	1.55	25.2	75.3

Table 6.8 - Measured Characteristics of the replicated porous metal samples.

6.6. Processing Developments Made

The need to develop porous metals by replication with a consistent uniform structure and to obtain higher porosities than the ones available (≈ 63%) with the argon only method (called Protocol W) required an exploration of alternative techniques.

One way to obtain higher porosities is to compact or densify the salt bed [196], or alternatively to lower the infiltration pressure [149]. The first development made was adding the fine NaCl particles at the bottom of the mould to provide a refuge space for gas present in between the infiltration NaCl particles. This permitted reducing the infiltration pressure from 3.5 to 3 bar and the porosity of the resulting samples increased from 63 to 66%; this development was called Protocol X.

Further into the investigation it was noted that the fine NaCl particles acted as a stop for the liquid aluminium preventing it from reaching the bottom of the mould, this allowed for the bottom gasket to be removed permitting the air located in between the NaCl particles to escape, allowing a further reduction of the infiltration pressure from 3 to 1 bar and a porosity increase from 66 to 70%; this development was called Protocol Y.

The final development in the replication process was made with the sole purpose of increasing the porosity of the samples, it consisted of vibrating the preform for one minute before assembling the mould, this step allows for the NaCl particles to achieve higher packing densities than in the previous protocols, applying this condition increases the sample porosity from 70 to 76%; this development was called Protocol Z.

In this chapter the developments to the argon only replication process are presented, the chapter starts with the explanation of the initial tests done to improve the available technique to increase the rate of suitable quality (uniform structure) samples produced and the speed at which they can be obtained, when these parameters were known (furnace temperature and production cycle length).

The next step was to develop a way to increase the porosity and reduce the infiltration pressure while keeping the uniform structure, four protocols were created (W, X, Y and Z), where different parameters may be selected, depending on the porosity level needed from a replicated porous metal (61 to 76%), finally the 12 replicated porous metal samples produced for this work were made applying the last two protocols only (Y and Z) to have two different porosity levels for testing (70 and 76%); following in Chapter 7 the results, analysis and discussion of the flow tests.

Chapter 7. Flow Tests - Results, Analysis and Discussion

7.1. Replicated Porous Aluminium Samples

The outcome of the values indicates that the permeability increases proportionally to the pore size and the form drag decreases inversely to the pore size; however, if the size difference between pores is narrow the random structure has a larger effect, which is the reason why in the replicated porous metals' case the K and C values are random.

The sample characteristics and the calculated values for permeability K and form drag C for this group are in Table 7.1. In Figure 7.1 the pressure drop values for the replicated porous aluminium samples can be seen.

Sample	**D_R (mm)**	**L_R (mm)**	**m_R (g)**	**D_P (mm)**	**ε (%)**	**$K \times 10^{-8}$ (m^2)**	**$C \times 10^{-3}$ (m^{-1})**
A1	51.0	25.1	42.22	1.09	69.6	1.40	10.0
A2	50.8	25.3	41.71	1.09	69.9	3.80	10.0
A3	50.9	25.6	38.02	1.09	73.0	0.48	8.7
B1	50.9	25.0	42.53	1.55	69.0	2.80	10.1
B2	50.8	26.1	44.03	1.55	69.2	3.70	10.0
B3	50.9	25.2	41.29	1.55	70.2	0.70	14.0
C1	51.0	25.0	41.66	2.18	69.7	1.70	8.9
C2	51.1	23.9	38.79	2.18	70.8	2.80	12.0
C3	50.9	25.6	38.95	2.18	72.2	1.26	12.0
V1	50.4	26.7	34.10	1.55	76.3	1.80	2.7
V2	50.7	25.8	30.96	1.55	78.0	1.50	2.4
V3	50.7	25.2	33.89	1.55	75.3	2.50	2.2

Table 7.1 - Sample characteristics, permeability and form drag values for the replicated porous metals.

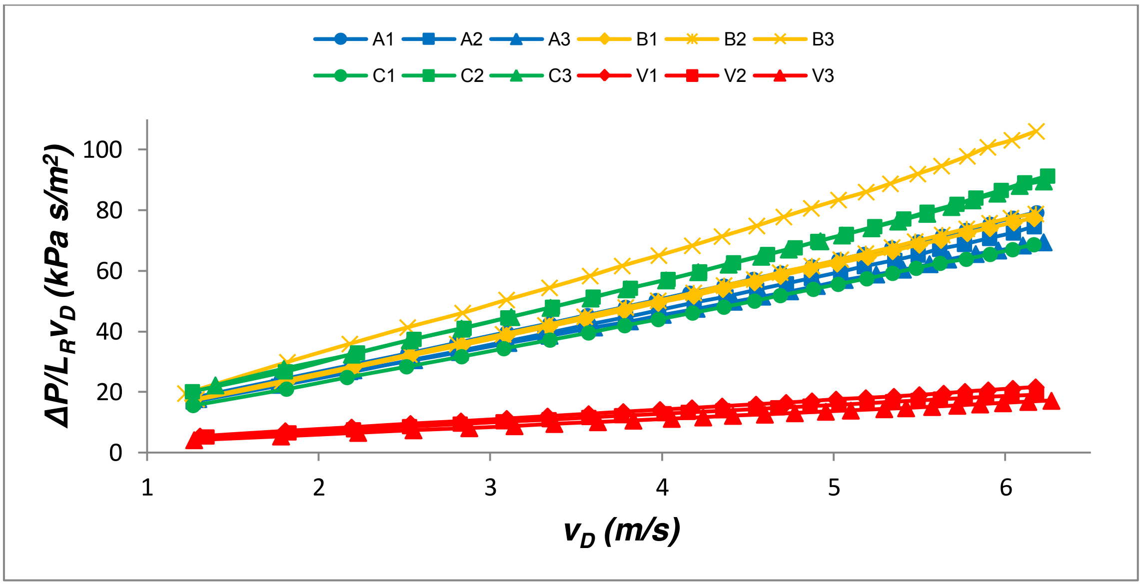

Figure 7.1 - Replicated porous metals' linear pressure drop against superficial velocity.

The group of porous metals with the lowest pressure drop is the one containing the vibrated samples (V). These have a considerably higher porosity on average by 9%, when compared to the non vibrated samples (A, B and C). The effect is evident in the form drag values as well.

For the non vibrated samples with different pore size, the difference between the pressure drop, permeability and form drag values does not appear to be systematic with these variables. This is caused by variation in several factors; the empty space within the sample, the location, form, surface and size of the particles composing the space holder. Sample B3 is an example of the irregularity in the flow properties that may occur in these porous metals.

In a series of experiments it was demonstrated previously that for a group of particles these previous characteristics may affect the result by 20 to 30% due to the effect of random packing when compared to a tight packing [105]. For example a perfectly packed space holder of 50 mm in height could be increased between 60 mm and 65 mm at random packing.

The tightness of fit for the space holder is also likely to be affected by the friction of the particles between themselves and the container, their density, the size proportion of the particles to the container and other factors that were outside the scope of this research. Next are the pressure drop results for the wire mesh samples are presented.

7.2. Wire Mesh Samples

The sample characteristics and the calculated values for permeability *K* and form drag *C* for this group are in Table 7.2. In Figure 7.2a the pressure drop values for the wire mesh samples can be seen. An additional graph is present in Figure 7.2b, the "Y" axis is in the logarithmic base 10 scale to better discern the samples' pressure drop behaviour.

Sample	**D_R (mm)**	**L_R (mm)**	**m_R (g)**	**D_P (mm)**	**ε (%)**	**K x 10^{-8} (m^2)**	**C x 10^{-3} (m^{-1})**
10 Mesh 10	51	9	29.00	2.000	81	1.5000	0.70
10 Mesh 20	51	18	57.33	2.000	81	1.6700	0.79
10 Mesh 30	51	24	86.09	2.000	78	1.5000	1.00
10 Mesh 40	51	33	115.32	2.000	78	1.5200	0.94
20 Mesh	51	26	110.35	1.000	75	0.5300	1.90
30 Mesh	51	26	115.20	0.500	73	0.2660	3.00
200 Mesh	51	12	50.49	0.075	75	0.0216	15.00

Table 7.2 - Sample characteristics, permeability and form drag values for the wire mesh samples.

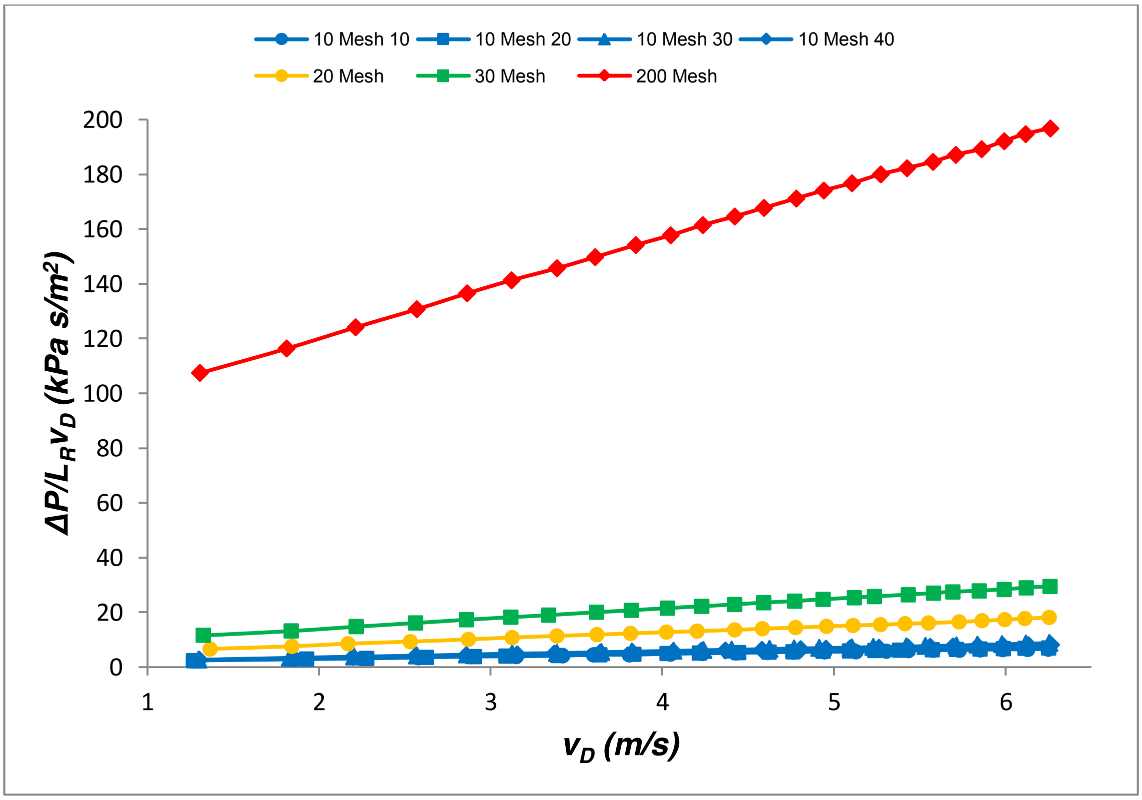

Figure 7.2a - Wire meshes' linear pressure drop against superficial velocity.

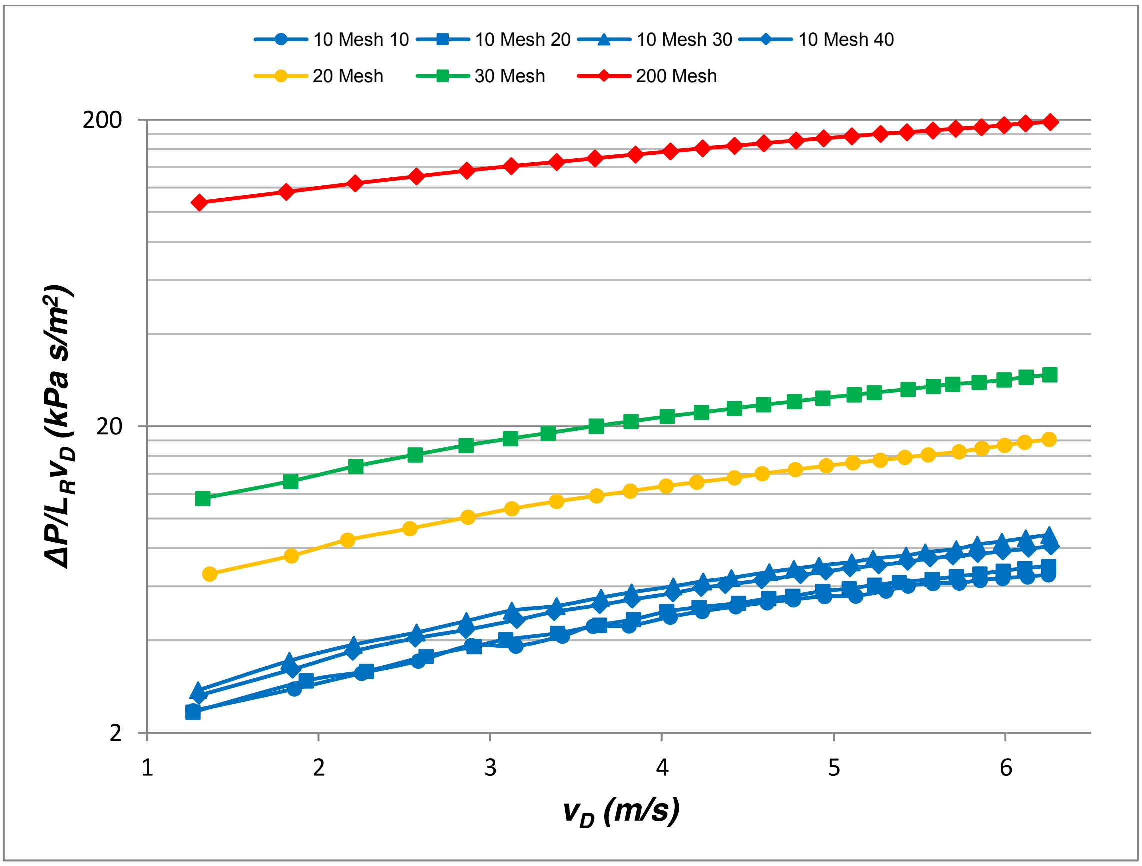

Figure 7.2b - Wire meshes' linear pressure drop (log scale) against superficial velocity.

From these charts the sample that creates the highest pressure drop is the 200 Mesh, which has the smallest pore size, 30 times smaller than the 10 Mesh samples and a form drag 15 times higher.

Between the 10 Mesh samples the variation in permeability and form drag is due to the random positioning of the mesh layers, for example considering the 10 Mesh 30 vs. 10 Mesh 40, more layers means more obstruction for the air to pass through, however, the random arrangement causes the form drag to be 0.94 for the 10 Mesh 40 but 1.00 for the 10 Mesh 30 when, logically, it should be the other way around. This indicates the level to which the random arrangements of the porous metal structure can affect the results in these tests.

From these samples it is clear that by reducing the pore size the permeability diminishes and the form drag increases. In the following section the pressure drop results for the wire felt samples are presented.

7.3. Wire Felt Samples

The sample characteristics and the calculated values for permeability *K* and form drag *C* for this group are in Table 7.3. In Figure 7.3 the pressure drop values for the wire felt samples can be seen.

Sample	D_R (mm)	L_R (mm)	m_R (g)	ε (%)	K x 10^{-8} (m^2)	C x 10^{-3} (m^{-1})
Al Felt	51	24	40.21	69	0.190	4.3
Cu Felt	51	24	132.71	70	0.182	4.1
SS304L Felt	51	25	121.83	70	0.190	4.0

Table 7.3 - Sample characteristics, permeability and form drag values for the wire felt samples.

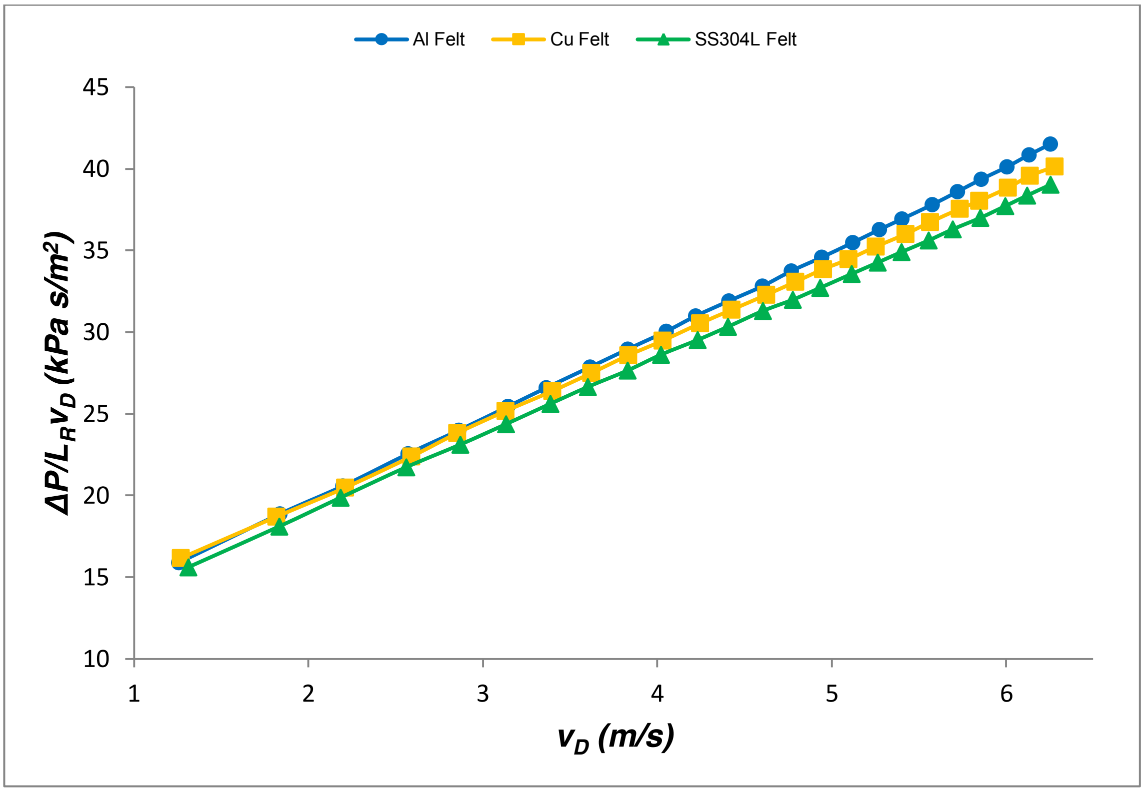

Figure 7.3 - Wire felts' linear pressure drop against superficial velocity.

From the graph it can be determined that the pressure drop difference between the samples is around 10%. The lowest pressure drop was produced by the stainless steel felt and the highest by the aluminium felt. The permeability value for the aluminium felt is slightly higher than the others, however the difference falls within the expected margin of error of the measurements. In the following section the pressure drop results for the packed spheres samples are presented.

7.4. Packed Spheres Samples

The sample characteristics and the calculated values for permeability *K* and form drag *C* for this group are in Table 7.4. In Figure 7.4 the pressure drop values for the packed spheres samples can be seen.

Sample	D_R (mm)	L_R (mm)	m_R (g)	D_P (mm)	N_{Sph}	ε (%)	K x 10^{-8} (m^2)	C x 10^{-3} (m^{-1})
Al Sph	51	30	94.40	2.03	7700	42	0.27	11.0
Cr Steel Sph	51	27	265.28	1.99	8100	39	0.42	10.4
Cu Sph	51	30	311.94	2.03	7900	43	0.52	12.6
Soda Glass Sph	51	30	95.05	2.00	8100	38	0.22	13.8
SS420 Sph	51	29	271.42	2.00	8400	40	0.48	12.0

Table 7.4 - Sample characteristics, permeability and form drag values for the packed spheres samples.

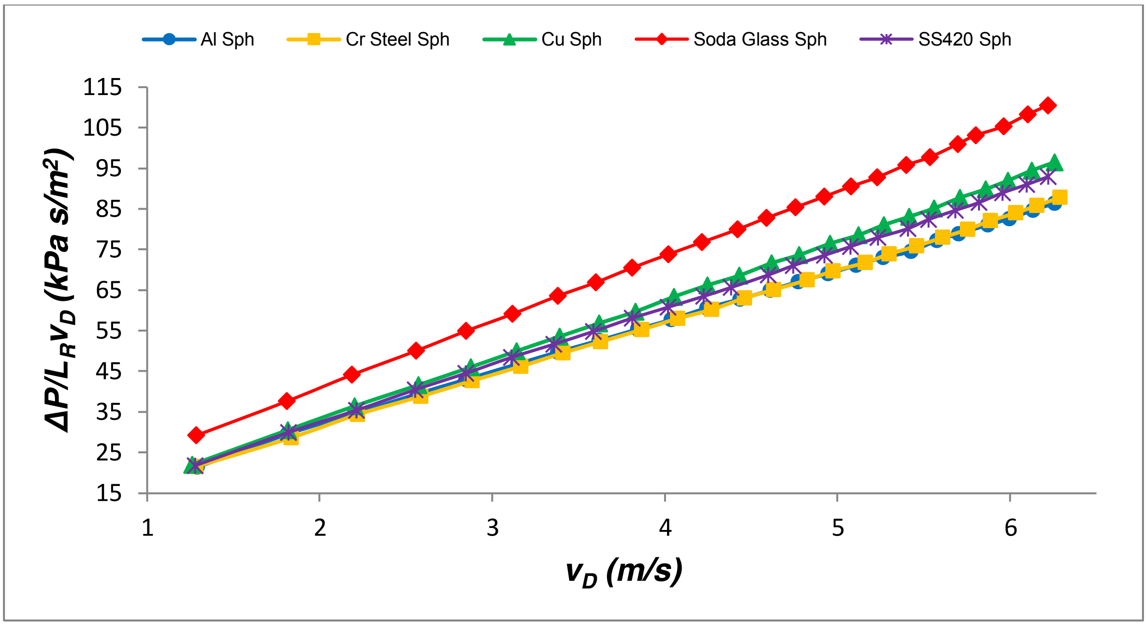

Figure 7.4 - Packed spheres' linear pressure drop against superficial velocity.

The chart shows that the soda glass spheres sample produces the highest pressure drop, approximately 30% higher than the chrome steel spheres, they also have the highest form drag and the lowest permeability value; this could be due to the soda glass's tighter packing. In the following section the pressure drop results for the SLM produced porous samples are presented.

7.5. SLM SS316L Porous Samples

The sample characteristics and the calculated values for permeability K and form drag C for this group are in Table 7.5. In Figure 7.5 the pressure drop values for the SS316L porous samples can be seen.

Sample	D_R (mm)	L_R (mm)	m_R (g)	D_P (mm)	ε (%)	K x 10^{-8} (m^2)	C x 10^{-3} (m^{-1})
SS316L (1)	51.1	25.6	159.94	3.9	61.8	2.0	2.20
SS316L (2)	51.0	25.5	142.24	3.9	65.7	2.7	1.47
SS316L (3)	50.8	25.3	116.41	3.9	71.5	3.7	1.08
SS316L (4)	51.0	25.3	93.32	3.9	77.3	3.9	0.68
SS316L (5)	51.0	25.2	73.72	3.9	82.0	3.8	0.45

Table 7.5 - Sample characteristics, permeability and form drag values for the SLM SS316L porous samples.

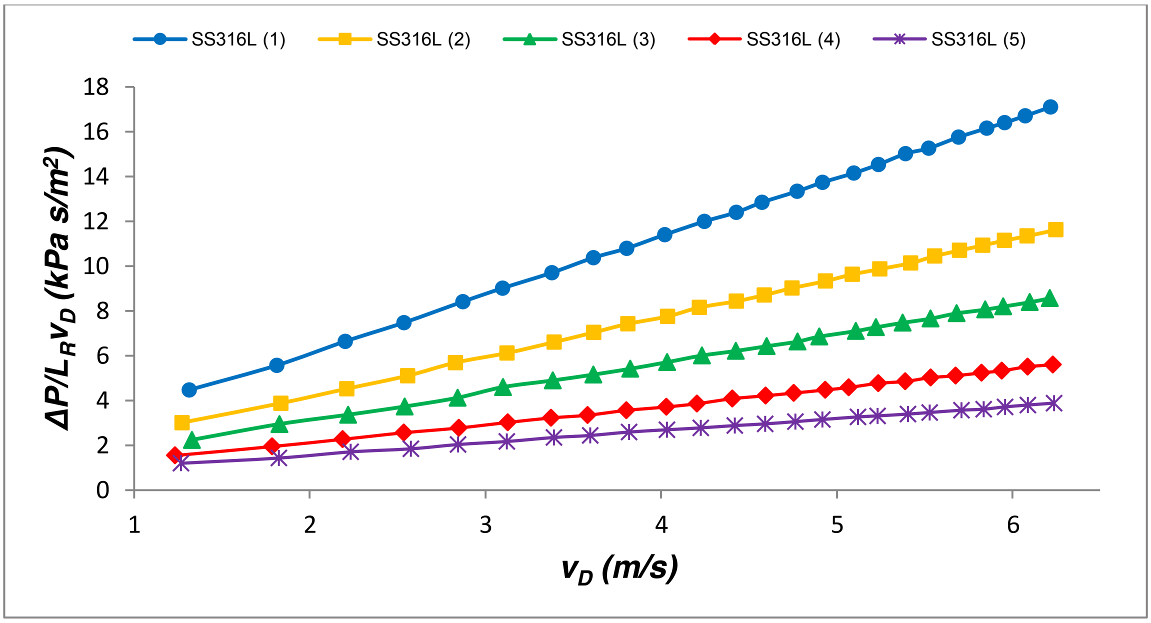

Figure 7.5 - SLM SS316L porous samples' linear pressure drop against superficial velocity.

This chart demonstrates that sample SS316L (1) with the highest pressure drop has the lowest porosity of 62%, on average 3.5 times higher than SS316L (5), the form drag follows this pattern as well. In the permeability values the discrepancy is between samples SS316L (4) and SS316L (5) which theoretically their values should be higher for SS316L (5) and lower than SS316L (4), however, it falls within experimental error. In the following section the pressure drop results for the EBM produced porous samples are presented.

7.6. EBM Ti6Al4V Porous Samples

The sample characteristics and the calculated values for permeability *K* and form drag *C* for this group are in Table 7.6. In Figure 7.6 the pressure drop values for the EBM Ti6Al4V porous samples can be seen.

Sample	D_R (mm)	L_R (mm)	m_R (g)	D_P (mm)	ε (%)	$K \times 10^{-8}$ (m^2)	$C \times 10^{-3}$ (m^{-1})
Ti6Al4V (1)	51.5	25.6	74.16	3.9	66.4	2.0	1.96
Ti6Al4V (2)	51.3	25.6	67.64	3.9	70.9	2.6	1.37
Ti6Al4V (3)	51.0	25.4	56.31	3.9	75.3	3.1	0.90
Ti6Al4V (4)	51.2	25.4	43.08	3.9	81.3	3.7	0.55
Ti6Al4V (5)	51.0	25.4	39.89	3.9	82.5	3.8	0.42

Table 7.6 - Sample characteristics, permeability and form drag values for the EBM Ti6Al4V porous metal samples.

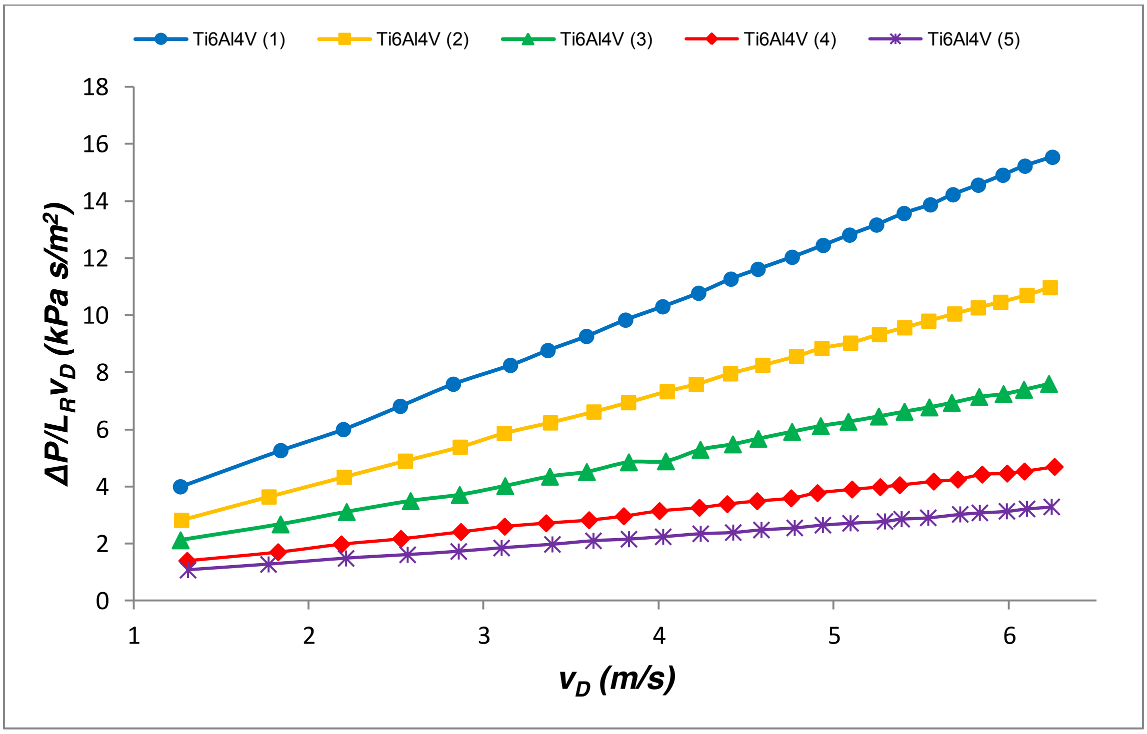

Figure 7.6 - EBM Ti6Al4V porous samples' linear pressure drop against superficial velocity.

The titanium alloy samples produced have a similar behaviour to the porous stainless steel samples with the ranges of pressure drop, permeability and form drag within similar values. The sample with the highest pressure drop is the less porous Ti6Al4V (1) being between 3.5 to 4 times higher than the Ti6Al4V (5) porous metal.

7.7. Pore Size Change Effect on Flow Through Porous Structures

In a porous metal the effect that the pore size has on pressure drop (Table and Figure 7.7) can be seen clearly in the wire mesh sample group while keeping a similar structure and material.

Sample	Pore Size (mm)	$\Delta P/L_R v_D$ (kPa s/m^2)
10 Mesh 10	2.000	3.43
10 Mesh 20	2.000	3.55
10 Mesh 40	2.000	4.06
20 Mesh	1.000	9.27
30 Mesh	0.500	16.13
200 Mesh	0.075	130.73

Table 7.7 - Pore size effect on pressure drop on the wire mesh samples at 2.55 m/s.

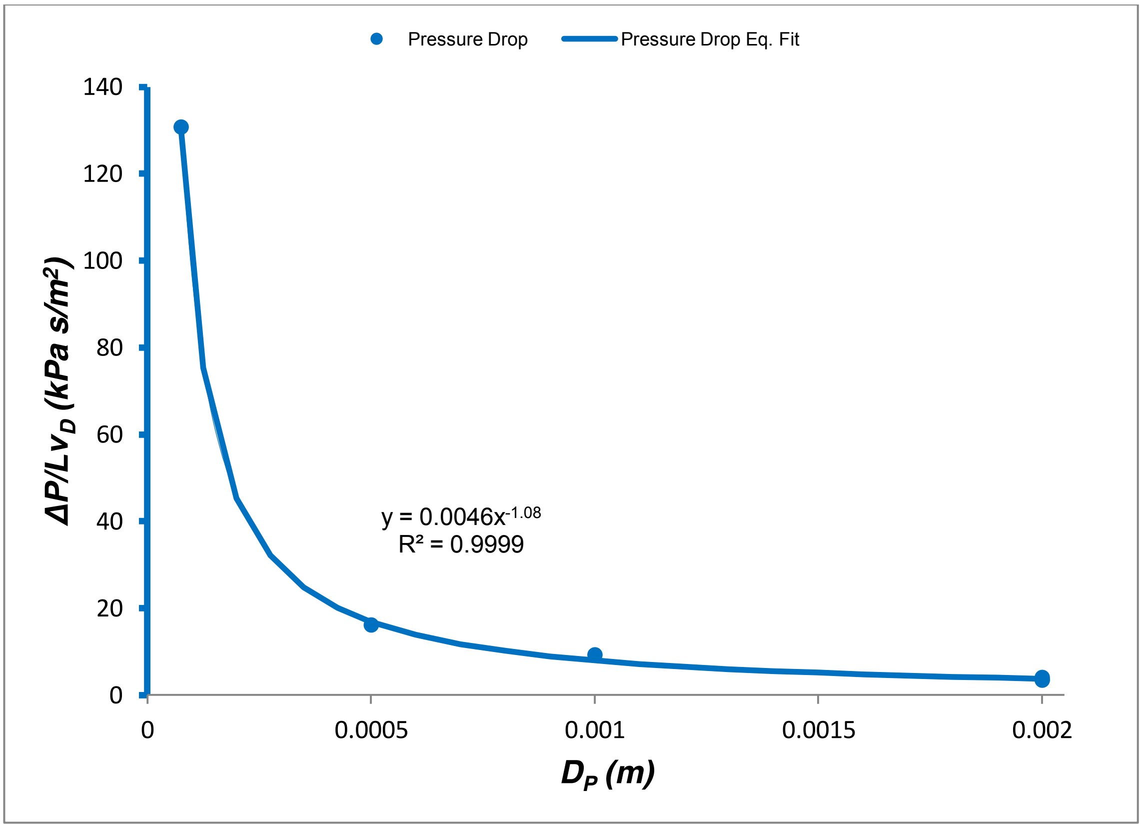

Figure 7.7 - Pore size effect on pressure drop of the wire mesh samples at 2.55 m/s.

From Table 7.7 it can be seen that the pressure drop increases steadily with the reduction of pore size. In Figure 7.2 the pore size effect can be seen for all velocities.

With layer quantity the pressure drop increases slightly, from 10 to 20 layers the increase is 3.5%, from 20 to 40 layers the increase is 14.4%; however, when the pore size is halved (20 Mesh) the increase in pressure drop is 122%, much more significant. If the pore size is halved again (30 Mesh) the pressure drop increases another 74%. The difference between 3.5% - 14% and 122% - 74% is due to the random positioning of the mesh sheets. An empirical correlation relating pore size and pressure drop using these four points for the wire mesh samples would be:

$$\frac{\Delta P}{L v_D} = a * (0.0046 d_P^{-1.08}) \approx a * (\frac{0.0046}{d_P}) \qquad \text{Eq. 7.1}$$

This equation indicates that, within the range of mesh pore sizes tested, there is possibly an inverse proportionality between pore diameter and normalised pressure drop.

When comparing 30 Mesh to 200 Mesh the pore size difference has a factor of 6.67, the pressure drop difference has a factor of 8.1. With this information it can be established that the relationship between pore size and pressure drop is of a higher order than a linear behaviour.

7.8. Porosity Change Effect on Flow Through Porous Structures

In a porous metal the effect that the porosity has on pressure drop (Table and Figure 7.8) can be seen clearly in the SLM SS316L sample group while keeping a similar structure and material.

Sample	ε (%)	$\Delta P/L_R v_D$ (kPa s/m^2)
SS316L (1)	61.8	7.47
SS316L (2)	65.7	5.10
SS316L (3)	71.5	3.72
SS316L (4)	77.3	2.56
SS316L (5)	82.0	1.84

Table 7.8 - Porosity effect on pressure drop on the SLM SS316L samples at 2.55 m/s.

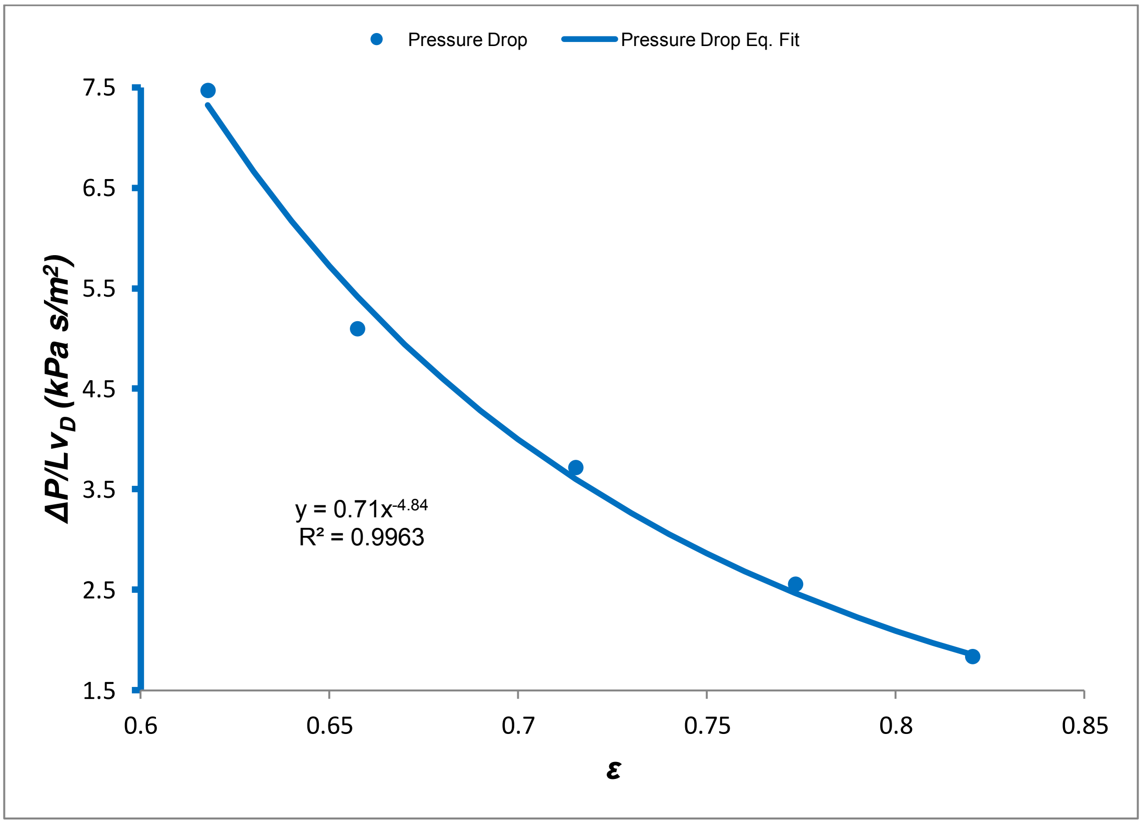

Figure 7.8 - Porosity effect on pressure drop for the SLM SS316L samples at 2.55 m/s.

From Table 7.8 it can be seen that the pressure drop decreases steadily with the increase of porosity. In Figure 7.5 the porosity effect can be seen for all velocities.

With increase in porosity the pressure drop decreases slightly, from SS316L (1) to SS316L (2) the increase is in porosity is 6.4% and the decrease in pressure drop is 31.7 %. From SS316L (3) to SS316L (4) the increase in porosity is 8.1% and the decrease in pressure drop is 31.2%, the ratios get lower as porosity increases. An empirical correlation relating porosity and pressure drop using these five points for the SLM SS316L samples would be:

$$\frac{\Delta P}{L v_D} = a * (0.71\varepsilon^{-4.84}) \qquad \text{Eq. 7.2}$$

When comparing both equations (Mesh Eq. 7.1 vs. ALM sample Eq. 7.2), the fact that they are a completely different fit shows evidence that the relationship between the mesh structure and the ALM structure to pressure drop does not behave in the same way.

7.9. Permeability Data Comparison

In Figure 7.9 the comparison between the replicated samples with results provided by Despois and Mortensen and Fourie and Du Plessis is shown. In this graph [7] the evolution of the permeability (K) normalized by the square of the pore size (D_P^2) in function of the regenerator density (ρ_R) can be seen.

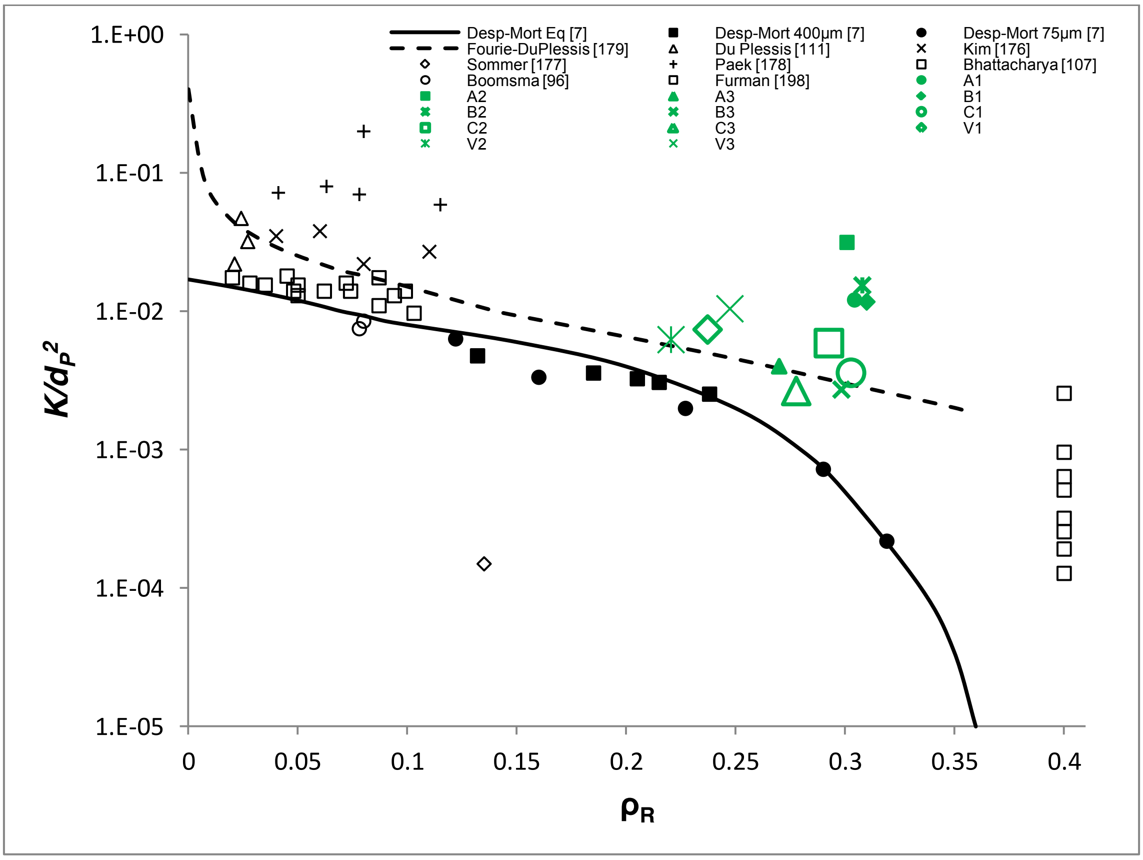

Figure 7.9 - Replicated porous metal density vs. normalised permeability.

The difference between the two equations [7] represented by the straight and segmented lines is that in the Despois and Mortensen equation the effect of the pores being closed off is considered. The difference between Despois and our production process is that Despois uses an increase in the infiltration pressure to change the density and in our process the particles are rearranged keeping the same infiltration pressure.

The location of the four samples in the upper right corner of the graph (A1, A2, B1, B2) is due to the variations in the structure that cannot be perfectly controlled by this infiltration process, such as strut thickness or window size. For regenerator purposes these four perform better than the rest, having a higher permeability value, allowing the fluid to pass through them with less energy. The samples from the Furman equation are infiltrated at different pressures while maintaining a porosity of about 60%.

In Figure 7.10 and Figure 7.11 a comparison between porosity, pore size and permeability can be seen. The range of porosities for the Bhattacharya and Du Plessis samples ranges from 0.899 to 0.972 and from 0.973 to 0.978 respectively, the permeability values changes greatly in the Du Plessis batch due to the pore size of their samples (250 μm, 400 μm and 600 μm).

In Figure 7.10 there is a slight trend in which by increasing the porosity the permeability increases and in the second graph the trend is more noticeable, this indicates that the pore size has a larger impact in the regenerator's permeability than the porosity. The uncertainty analysis is explained in Appendix 3.

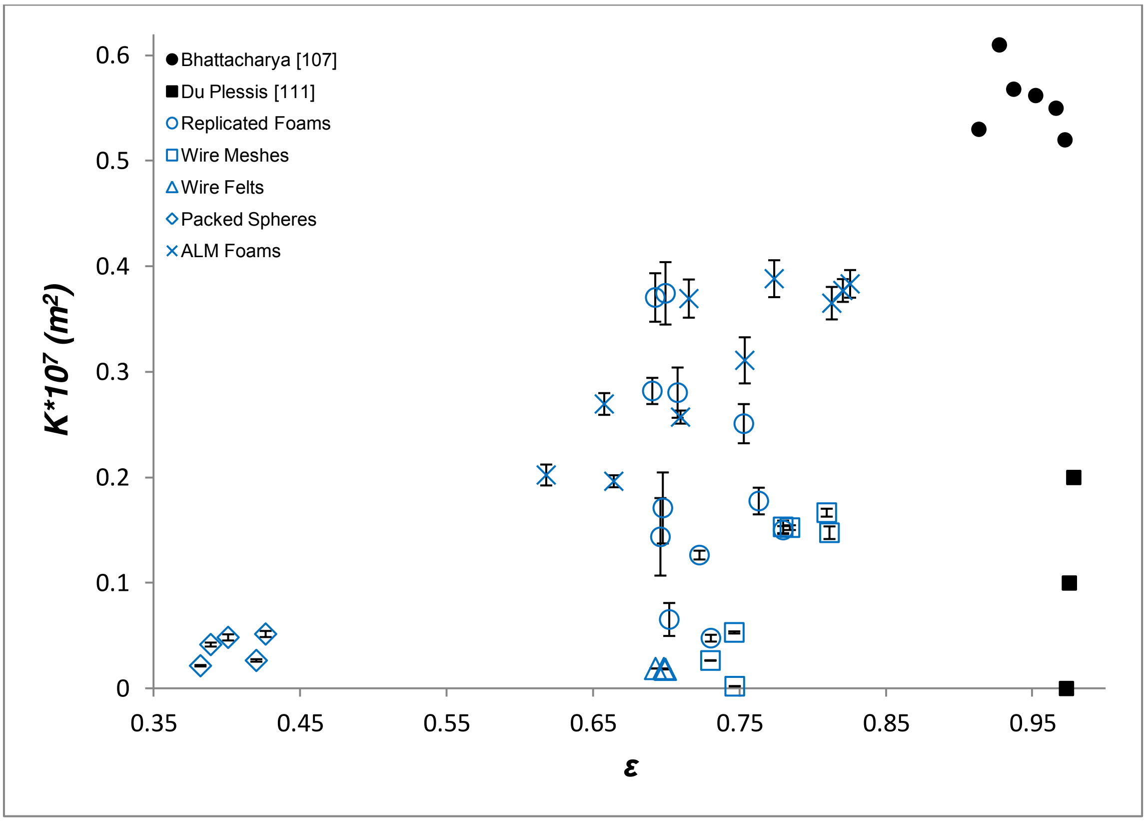

Figure 7.10 - Permeability comparison, Porosity vs. Permeability.

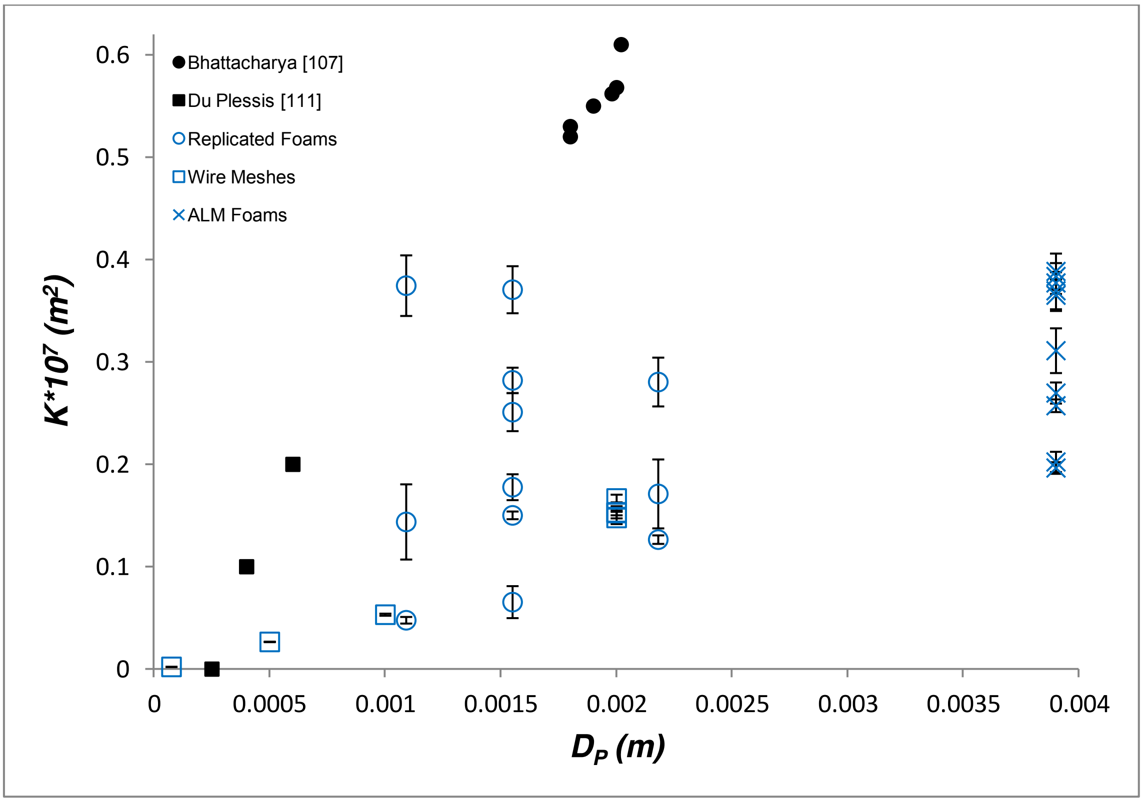

Figure 7.11 - Permeability comparison, Pore size vs. Permeability.

It is clear that the porosity and pore size have a substantial effect on pressure drop agreeing with the work of Dukhan [102] in which 8 different samples are tested, 4 of a high porosity value (91.5 to 92.4%) and 4 of a low porosity value (67.9 to 79.4%), and two different pore sizes. The study considers the reciprocal of the permeability value against the first surface area based parameter and considering the Ergun parameter:

$$\frac{1}{K} = \propto \frac{(1-\varepsilon)^2 A_{Sp}^2}{\varepsilon^3} \qquad \text{Eq. 7.3}$$

giving values that well agree with the power equation of the curve for all the samples in this work, agreeing with previous researchers:

$$y = 205234x^{0.4898} \qquad \text{Eq. 7.4}$$

With the flow tests on the regenerator samples it can be clearly seen that the pressure drop through them increases as the pore size (by consequence window size) decreases as shown in the work done by Despois in which to calculate the pressure drop in the replicated porous aluminium samples the diameter of the window or "bottlenecks" is inversely proportional to the value [7].

For the porosity it is a similar case, the pressure drop is affected by the level of porosity in the sample, if the porosity increases the air flow passing through it has less obstruction in its path, generating a lower pressure drop, such effect has been investigated by other researchers as well [96], [107], [204]; the work done by Dietrich relates the porosity of the sponge as inversely proportional to the pressure drop, an effect that is seen in the samples of this work.

In this chapter the results for flow tests on the porous metal samples are presented, each section contains the experimental data given by the test rig and analysed in the terms which are of interest for the regenerator application, this being the amount of pressure drop produced by the sample at a certain velocity, next was to analyse the effect of pore size and porosity on pressure drop, concluding with a permeability comparison with several models available in the literature by different authors; following in Chapter 8 the determination and analysis of the number of transfer units NTU_R and heat transfer coefficient h for all samples will be made.

Chapter 8. Heat Transfer Tests - Results, Analysis and Discussion

8.1. NTU_R Values of Each Structure Group of Porous Metals

8.1.1. Replicated Porous Aluminium Samples

In Figure 8.1 the NTU_R values obtained for the porous aluminium samples at six different flow rates are shown; as mentioned in section 4.1 the Reynolds number was obtained for the flow in each sample using Eq. 4.12, the characteristic length considered was the average pore size for each sample [157], [171].

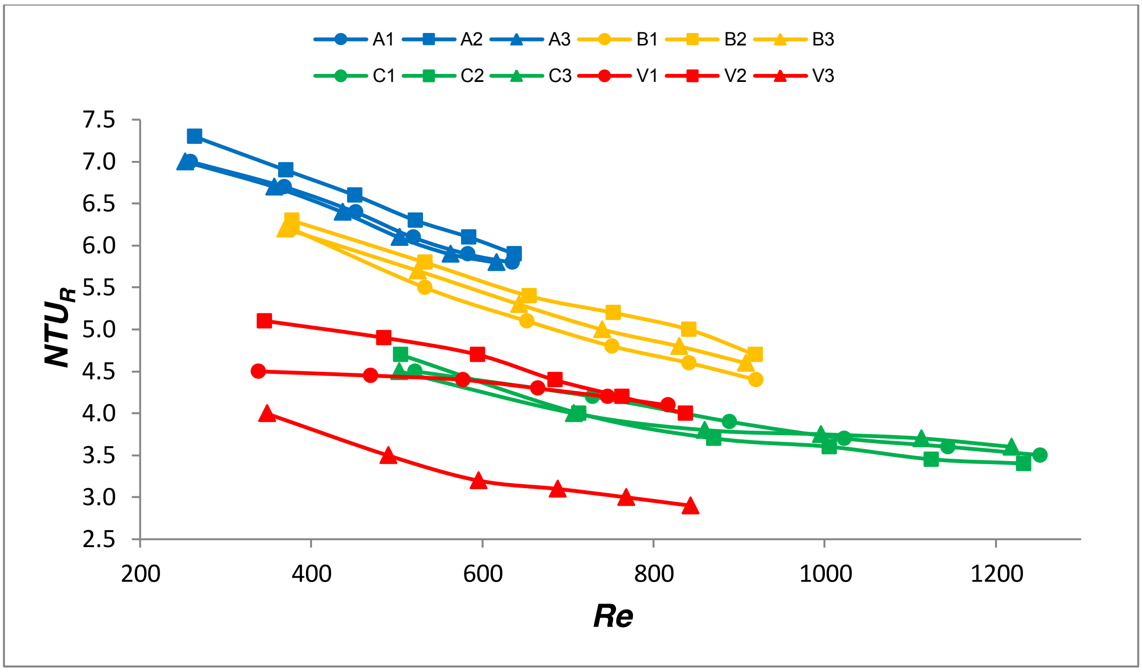

Figure 8.1 - NTU_R values for the replicated porous metal samples.

Out of the replicated porous metal samples the group with the highest NTU_R value was that shown in blue in the figure, those having the smallest average pore size of 1.09 mm; they were followed by the group shown in yellow with a 1.55 mm pore size and last those shown in green with the pore size of 2.18 mm.

The group shown in red was composed by the vibrated samples having a pore size of 1.55 mm as well but made with a higher porosity of around 76% compared to 70% for the other three groups. The vibrated samples have a lower NTU_R than the samples from the yellow group having the same pore size with only a 22% loss in NTU_R.

8.1.2. Wire Mesh Samples

In Figure 8.2a the NTU_R values obtained for the wire mesh samples at six different flow rates are shown; the characteristic length used was the hydraulic diameter D_H calculated with Eq. 8.1 [94] and the Reynolds number was obtained for the flow in each sample using Eq. 8.2 [94]. An additional graph is present in Figure 8.2b, the "Y" axis is in the logarithmic base 10 scale to better discern the samples' NTU_R values.

$$D_H = \frac{4\varepsilon D_W}{\Phi(1-\varepsilon)} \qquad \text{Eq. 8.1}$$

$$Re = \frac{\rho_{Air} v_D D_H}{\mu} = \frac{\dot{m}_{Air} D_H}{A_{CS}\mu} \qquad \text{Eq. 8.2}$$

where D_W is the wire diameter of the mesh, Φ is the shape factor which for a wire screen is 4 [115], ρ_{Air} is the density of the air and v_D is the superficial velocity of the air.

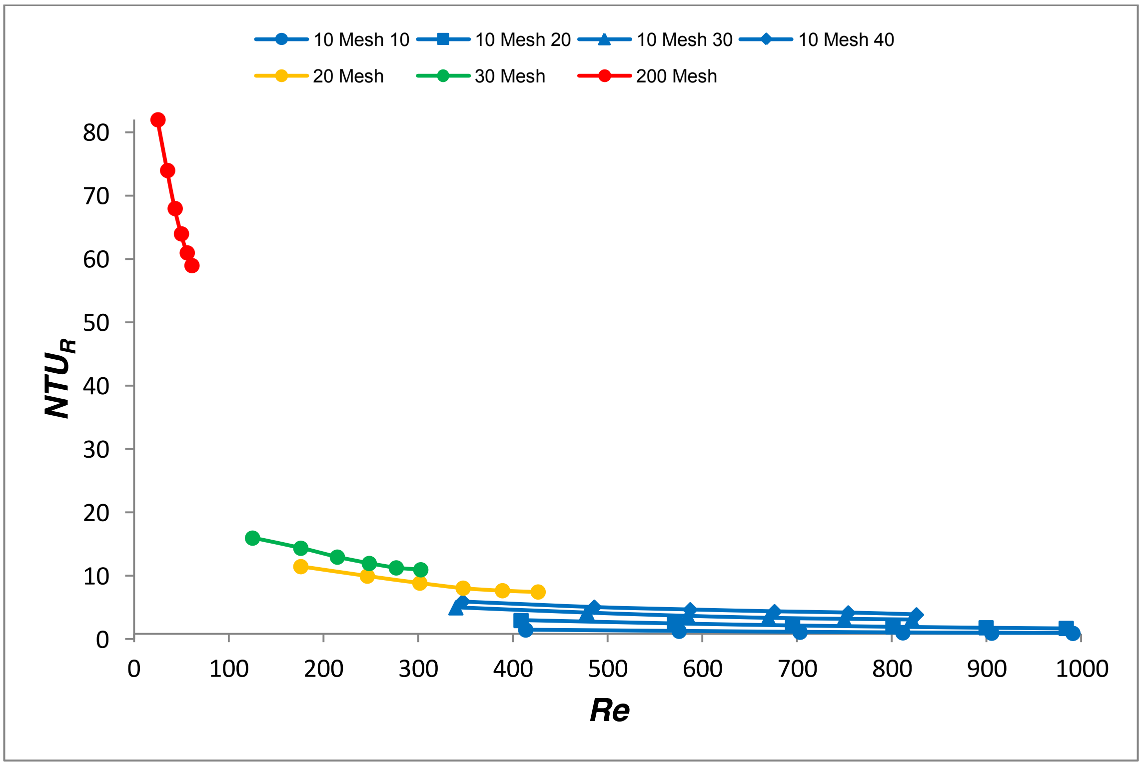

Figure 8.2a - NTU_R values for the wire mesh samples.

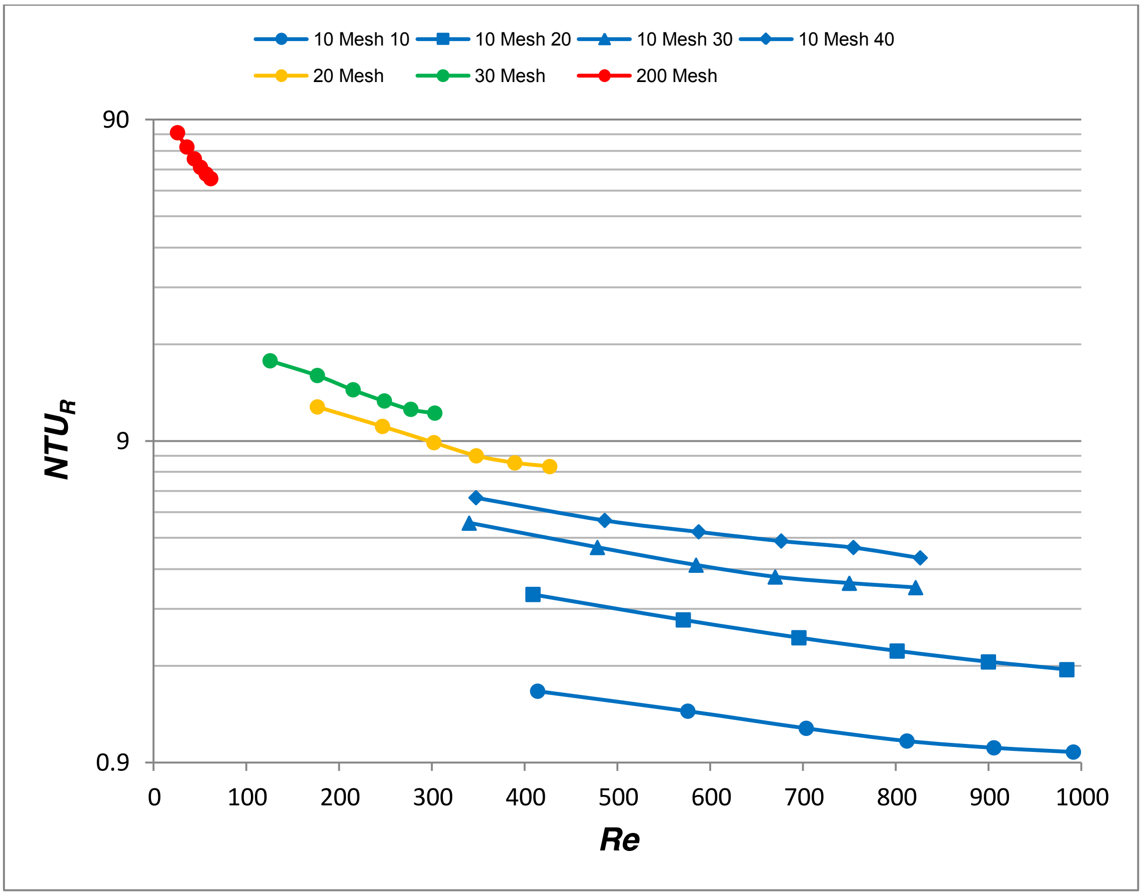

Figure 8.2b - NTU_R values (log scale) for the wire mesh samples.

Out of the wire net samples the one with the highest NTU_R value was the 200 Mesh, having the smallest pore size and highest surface area, this mesh number is in fact commonly used as a regenerator [94]. It was followed by the other meshes (in decreasing order 30, 20 and 10).

The group shown in the figure in blue was composed by 10 Mesh with different numbers of layers, their change over a wide range of Reynolds numbers is limited and the actual values are small when compared to other nets.

8.1.3. Wire Felt Samples

In Figure 8.3 the NTU_R values obtained for the felt samples at six different flow rates are shown; the characteristic length used was the hydraulic diameter calculated with Eq. 8.1 and the Reynolds number was obtained for the flow in each sample using Eq. 8.2.

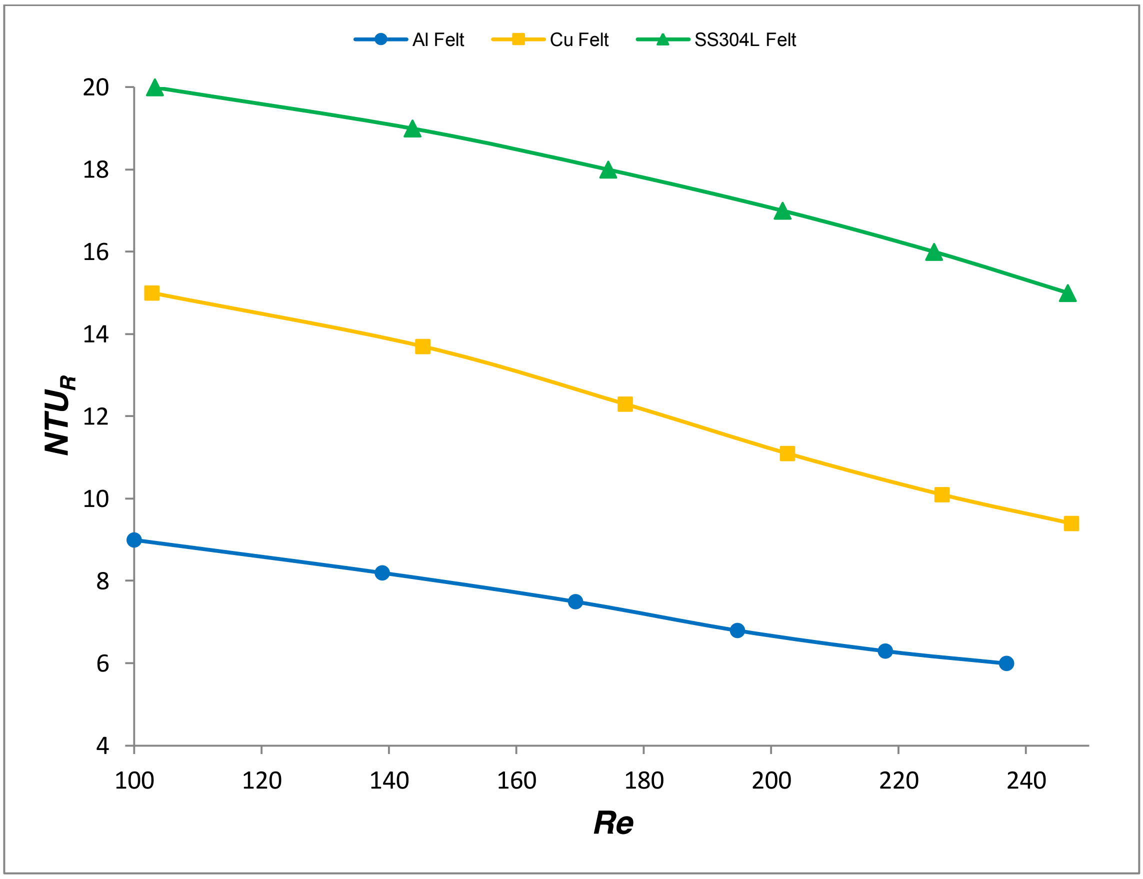

Figure 8.3 - NTU_R values for the wire felt samples.

These samples show the best type of material to be used as a regenerator. The stainless steel sample has the highest number of transfer units, which is likely to be the main reason why it is one of the most common materials used in regenerator applications, in comparison the copper and aluminium felts did not perform as well.

8.1.4. Packed Spheres Samples

In Figure 8.4 the NTU_R values obtained for the packed spheres samples at six different flow rates are shown. The Reynolds number was obtained for the flow in each sample using Eq. 8.1, the characteristic length considered was the sphere diameter for each sample [157], [172].

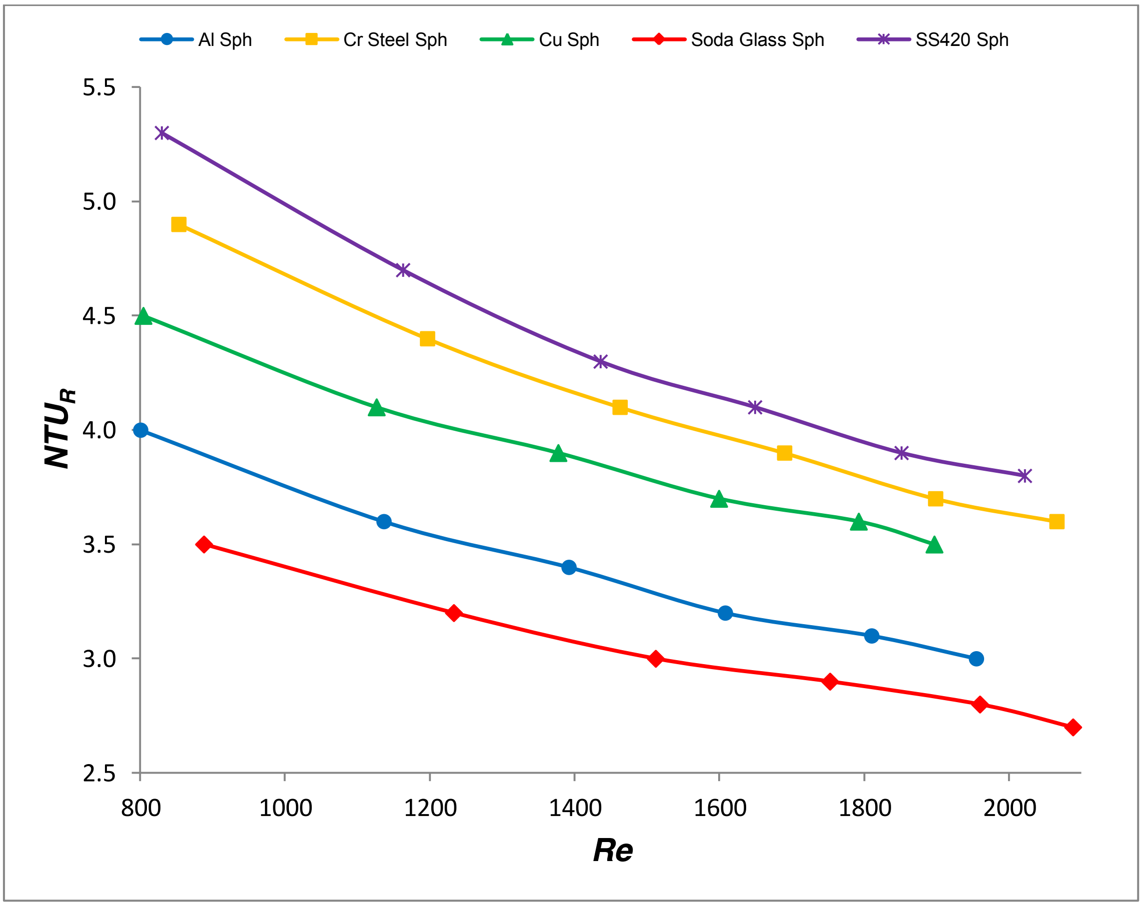

Figure 8.4 - NTU_R values for the packed spheres samples.

As with the felt samples, the packed spheres show the behaviour of the different materials used, allowing them to be compared for an equivalent structure in a way that is not possible for porous metals, because of the specific nature of different processing methods to different materials. The stainless steel sample again has the highest NTU_R values among the others, chrome steel and copper performed very similar, soda glass is the worst performing one of the group.

8.1.5. SLM SS316L Porous Samples

In Figure 8.5 the NTU_R values obtained for the stainless steel porous samples made through selective laser melting are shown. Since the pore size is considerably larger than the replicated porous metals (3.9 mm as opposed to 1.09 mm - 2.18 mm) the NTU_R values are much lower. The Reynolds number was obtained for the flow in each sample using Eq. 4.12, the characteristic length considered was the pore diameter.

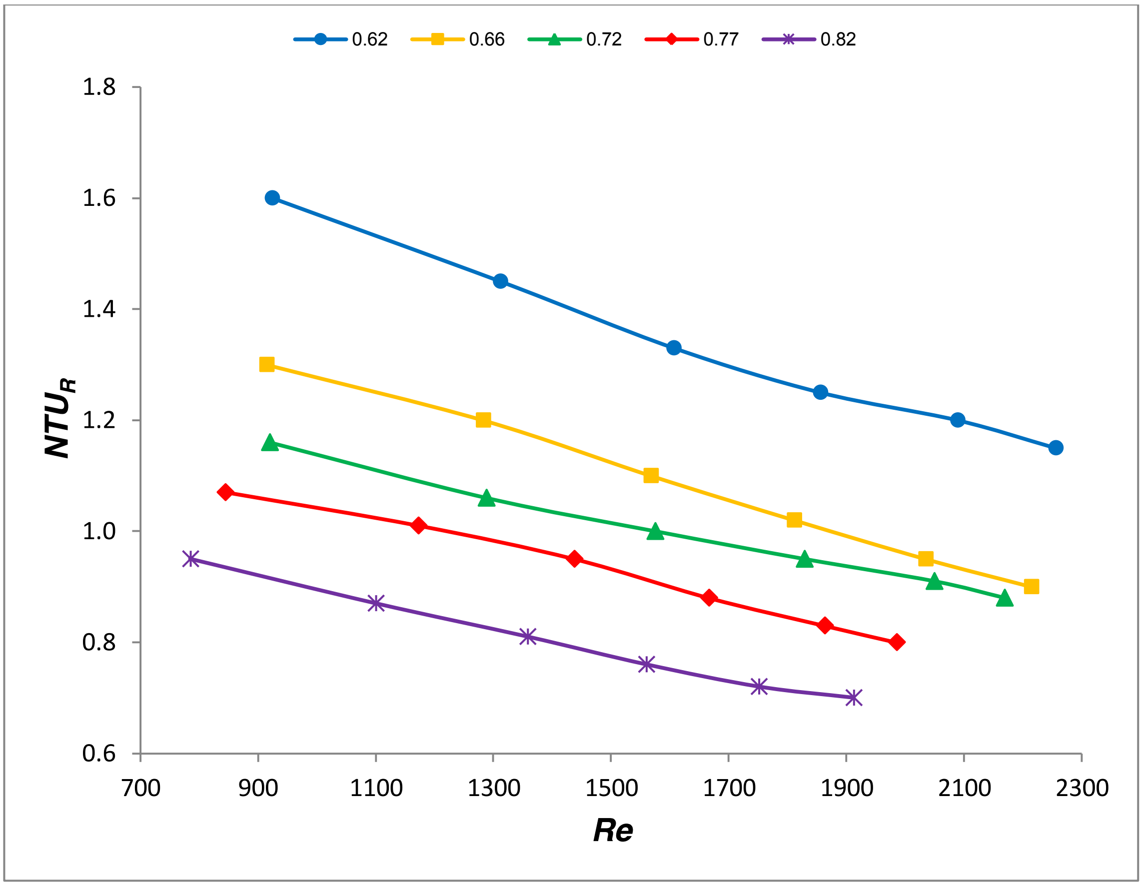

Figure 8.5 - NTU_R values for the SLM SS316L porous samples.

Out of the stainless steel porous samples the best performing was number 1, having the lowest porosity of the group (61.8%), by consequence the highest mass. It can be seen that the NTU_R value for higher porosity porous metals changes less (15% of sample 0.82 vs. 30% of sample 0.62) with different flow rates which is a desirable quality, however, their NTU_R values are low compared to other porous material types.

8.1.6. EBM Ti6Al4V Porous Samples

In Figure 8.6 the NTU_R values obtained for the Ti6Al4V porous samples made through Electron Beam Melting are shown. As for the previous stainless steel porous samples the pore size is considerably larger than the replicated porous metals (3.9 mm as compared to 1.09 mm - 2.18 mm), by consequence, the NTU_R values are lower. While it should be remembered that smaller pore size structures are possible with such methods, the intention here is to create samples where the effect of density can be examined systematically, so these are not realistic candidates for applications. The Reynolds number was obtained for the flow in each sample using Eq. 4.12, the characteristic length considered was the pore size diameter.

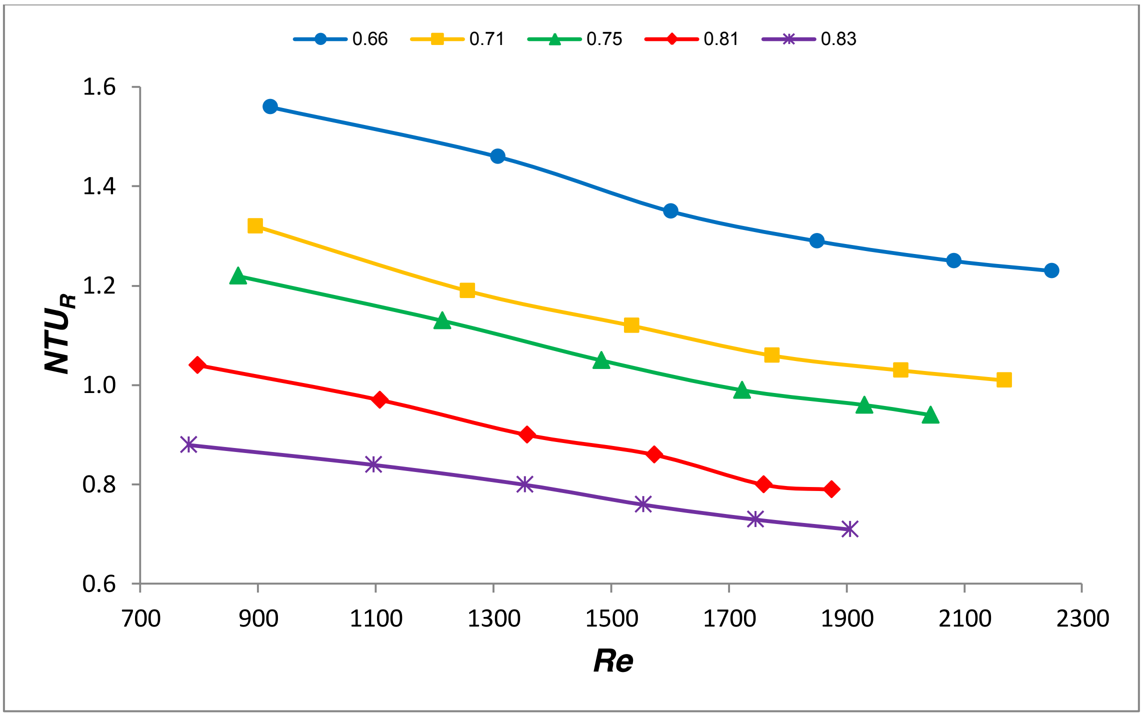

Figure 8.6 - NTU_R values for the EBM Ti6Al4V porous samples.

This group of Ti6Al4V porous samples has a strong similarity with the previous batch; since the CAD design is very similar; the sample with the highest mass and lowest porosity has the highest NTU_R values Ti6Al4V (1). In the following section the heat transfer coefficient h results for all porous metal samples are presented.

8.2. h Values of Each Structure Group of Porous Metals

After knowing the number of transfer units within each sample the heat transfer coefficient (h) may be obtained using Eq. 8.3.

$$h = \frac{NTU_R \dot{m}_{Air} c_{Air}}{A_{HT}} \qquad \text{Eq. 8.3}$$

For the replicated porous aluminium samples the calculation of the heat transfer area (A_{HT}) is done using Eq. 8.4 [173], it equals the product of the regenerator's volume (V_R), calculated using sample measurements, by the specific surface area (A_{Sp}).

$$A_{HT} = V_R A_{Sp} \qquad \text{Eq. 8.4}$$

For the calculation of the specific surface area (A_{Sp}) Eq. 8.5 is used [174].

$$A_{Sp} = \frac{6\varepsilon}{L_C} \qquad \text{Eq. 8.5}$$

This equation is derived from the one used to calculate the specific surface area of the packed spheres samples, the difference is that for the porous metals the equation includes the term "ε" instead of "$1- \varepsilon$", reason for this is that the pore space is in place of the solid sphere.

8.2.1. Replicated Porous Aluminium Samples

In Figure 8.7 the h values obtained for the replicated porous aluminium samples at six different flow rates are shown.

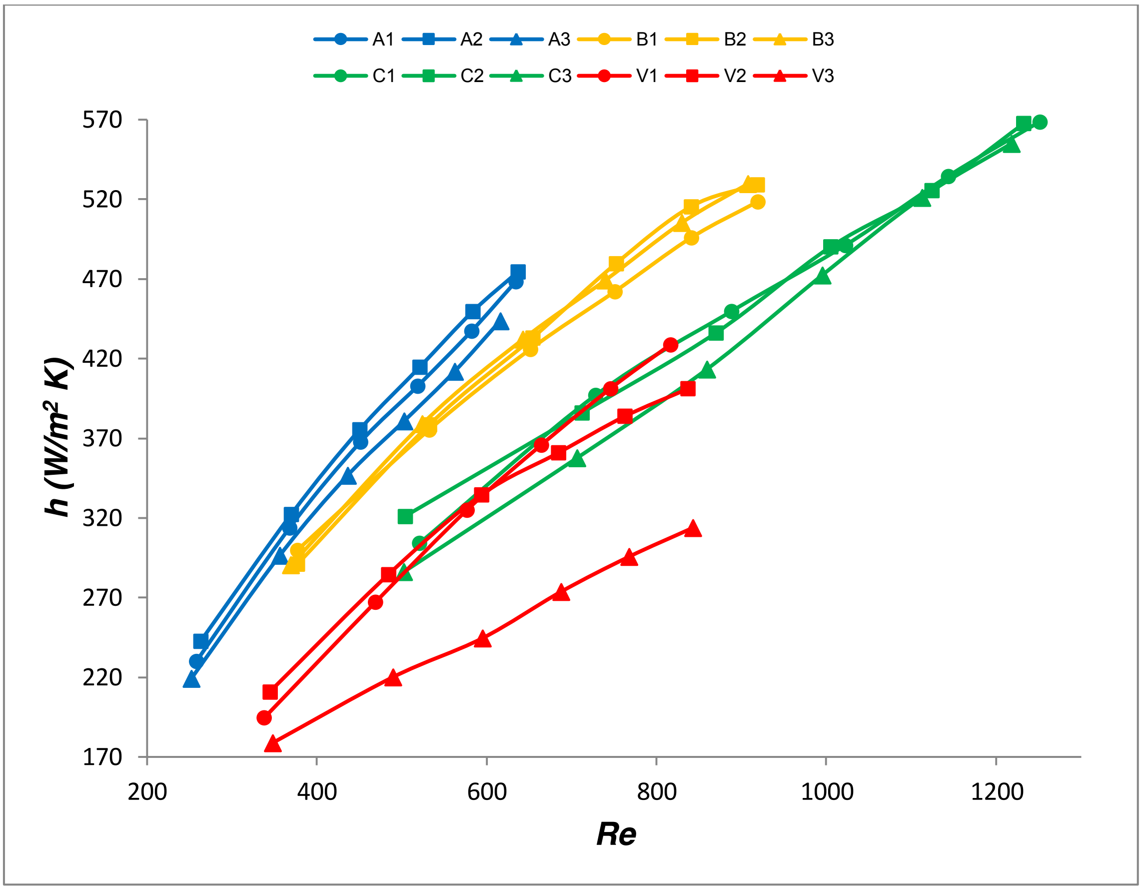

Figure 8.7 - h values for the replicated porous aluminium samples.

It can be noted that the group shown in green (samples with a 2.18 mm pore diameter) have the highest values of heat transfer coefficient, especially sample C1. However to achieve this value the Reynolds number is approximately double the value of the A2 sample. In this case A2 achieves 70% of the h value compared to the C1 sample at half the Reynolds number, making it a more efficient regenerator.

8.2.2. Wire Mesh Samples

For the wire meshes the calculation of the heat transfer area (A_{HT}) is done using Eq. 8.6 [115], it includes the net wire diameter (D_W):

$$A_{HT} = \frac{4(1-\varepsilon)V_R}{D_W} \qquad \text{Eq. 8.6}$$

In Figure 8.8 the h values obtained for the mesh samples at six different flow rates are shown; the Reynolds number was obtained for the flow in each sample using Eq. 8.2, the characteristic length considered was the hydraulic diameter.

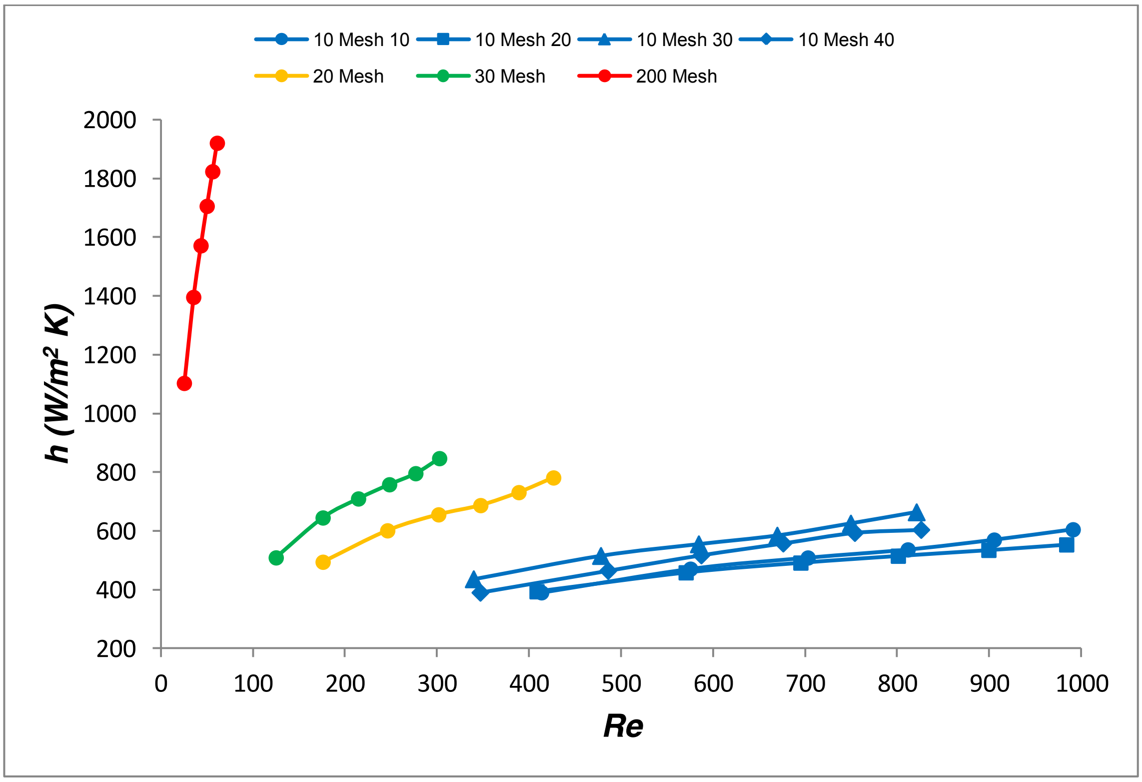

Figure 8.8 - h values for the wire mesh samples.

In this batch of samples the best performing one was the 200 mesh, considering only heat transfer coefficient, ideally it would be best if the Reynolds number was higher; the other samples have lower h values at higher Reynolds numbers.

8.2.3. Wire Felt Samples

For the wire felts the calculation of the heat transfer area (A_{HT}) is done using Eq. 8.6.

In Figure 8.9 the h values obtained for the felt samples at six different flow rates are shown; the Reynolds number was obtained for the flow in each sample using Eq. 8.2, the characteristic length considered was the hydraulic diameter.

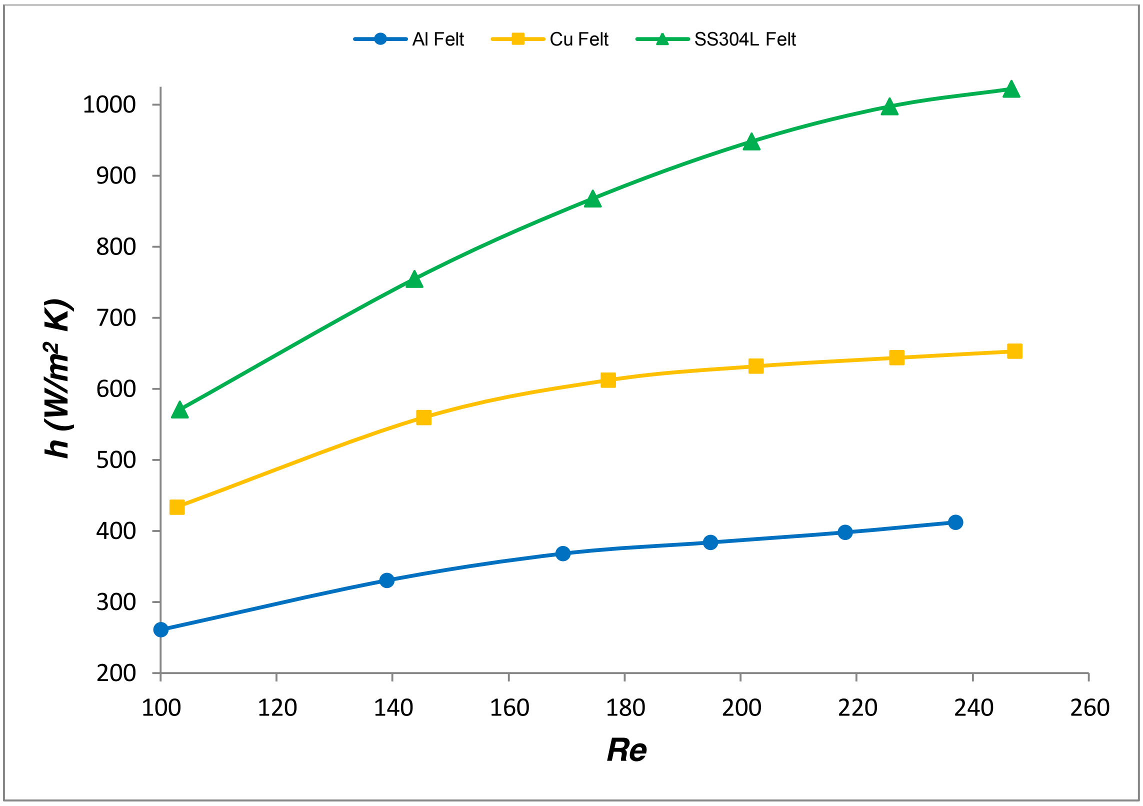

Figure 8.9 - h values for the wire felt samples.

For the wire felts the best performing sample was the stainless steel felt. Their structure also provides for high heat transfer coefficients at relatively low Reynolds numbers, making them a viable option as regenerators.

8.2.4. Packed Spheres Samples

For the packed spheres samples the calculation of the heat transfer area (A_{HT}) is done using Eq. 8.7 [175].

$$A_{HT} = \pi D_{Sph}^2 N_{Sph} = \pi L_C^2 N_{Sph} \qquad \text{Eq. 8.7}$$

This equation is to calculate the surface area of a sphere (πD_{Sph}^2) and then multiplied by the total number of spheres (N_{Sph}) that form the packed bed. The characteristic length used is the sphere diameter. For the calculation of the specific surface area (A_{Sp}) Eq. 8.8 [174].

$$A_{Sp} = \frac{6(1-\varepsilon)}{L_C} \qquad \text{Eq. 8.8}$$

In Figure 8.10 the h values obtained for the packed spheres samples at six different flow rates are shown; the Reynolds number was obtained for the flow in each sample using Eq. 4.12, the characteristic length considered was the sphere diameter for each sample.

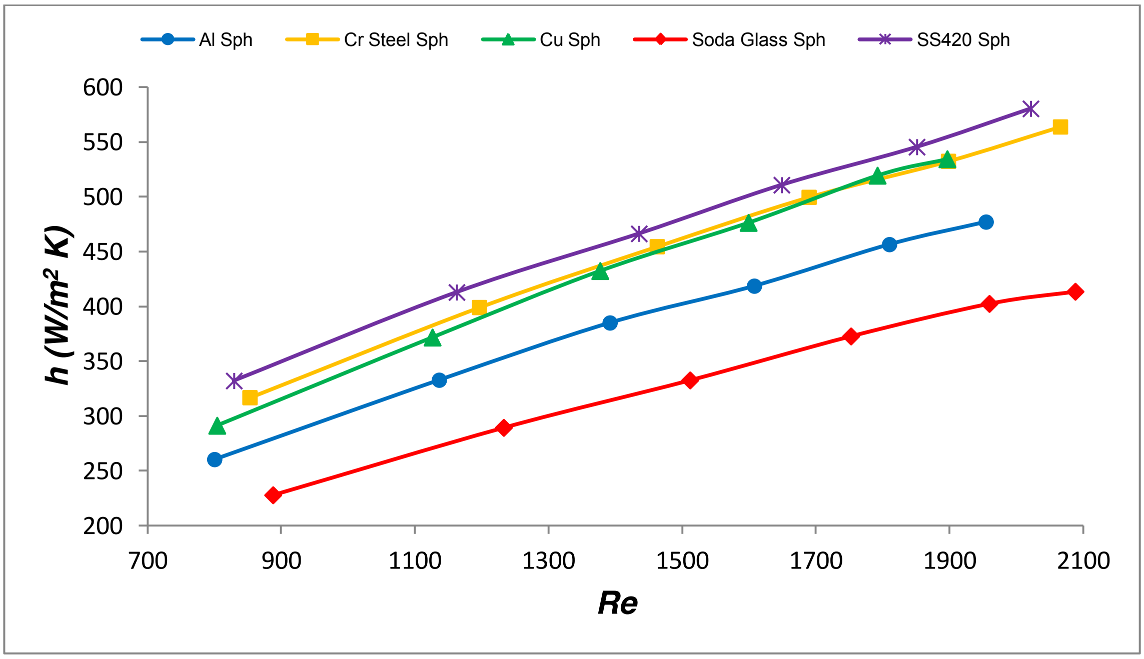

Figure 8.10 - h values for the packed spheres samples.

The best performing packed bed of this group was the stainless steel sample, with very similar behaviour between the chrome steel and copper samples. In general the heat transfer coefficients have a high value, however the Reynolds numbers are also elevated. Soda glass is the worst material out of this group followed by aluminium.

8.2.5. SLM SS316L Porous Samples

For the SLM stainless steel porous samples the calculation of the heat transfer area (A_{HT}) is done using Eq. 8.4.

In Figure 8.11 the h values obtained for the stainless steel porous samples at six different flow rates are shown; the Reynolds number was obtained for the flow in each sample using Eq. 4.12, the characteristic length considered was the pore size of each sample.

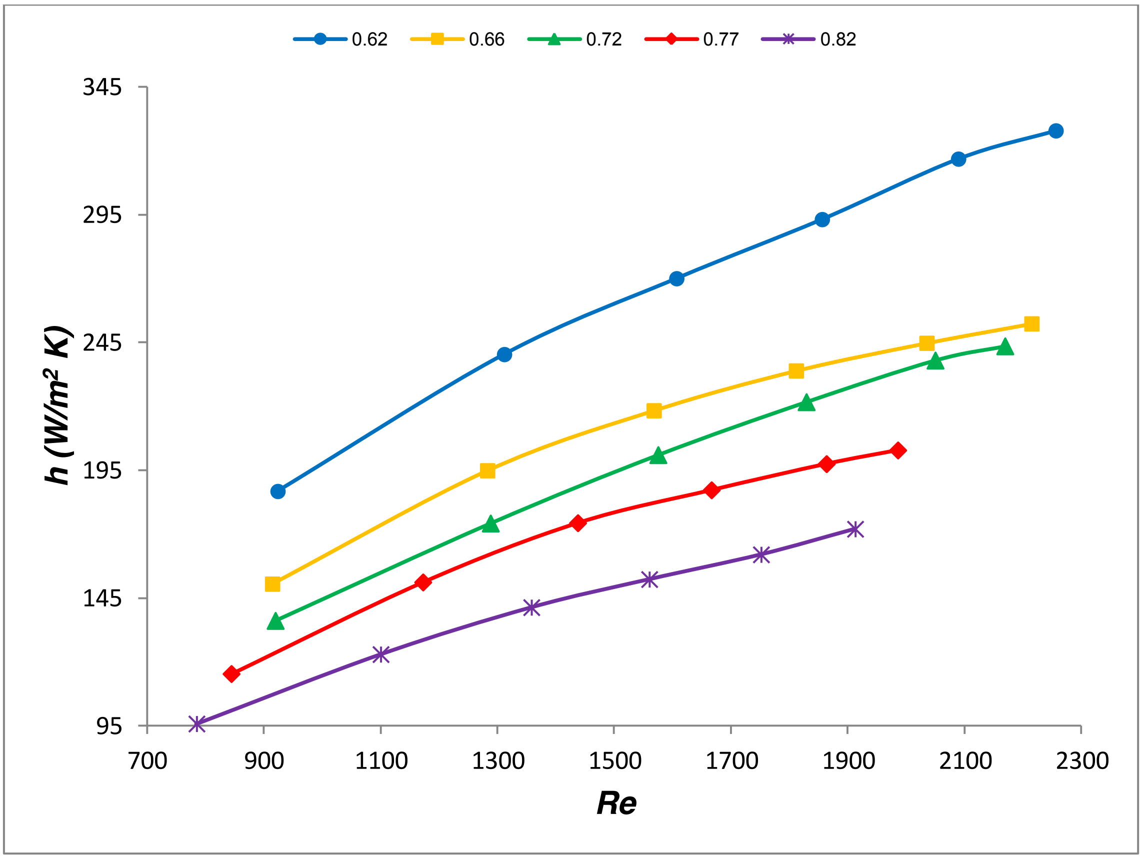

Figure 8.11 - h values for the SLM SS316L porous samples.

The best performing sample out of this group is the SS316L (1) due to its higher mass, capturing more heat than the others. For the rest of the samples as the porosity increases the heat transfer coefficient decreases.

8.2.6. EBM Ti6Al4V Porous Samples

For the EBM Ti6Al4V porous samples the calculation of the heat transfer area (A_{HT}) is done using Eq. 8.4.

In Figure 8.12 the h values obtained for the EBM Ti6Al4V porous samples at six different flow rates are shown; the Reynolds number was obtained for the flow in each sample using Eq. 4.12, the characteristic length considered was the pore size of each sample.

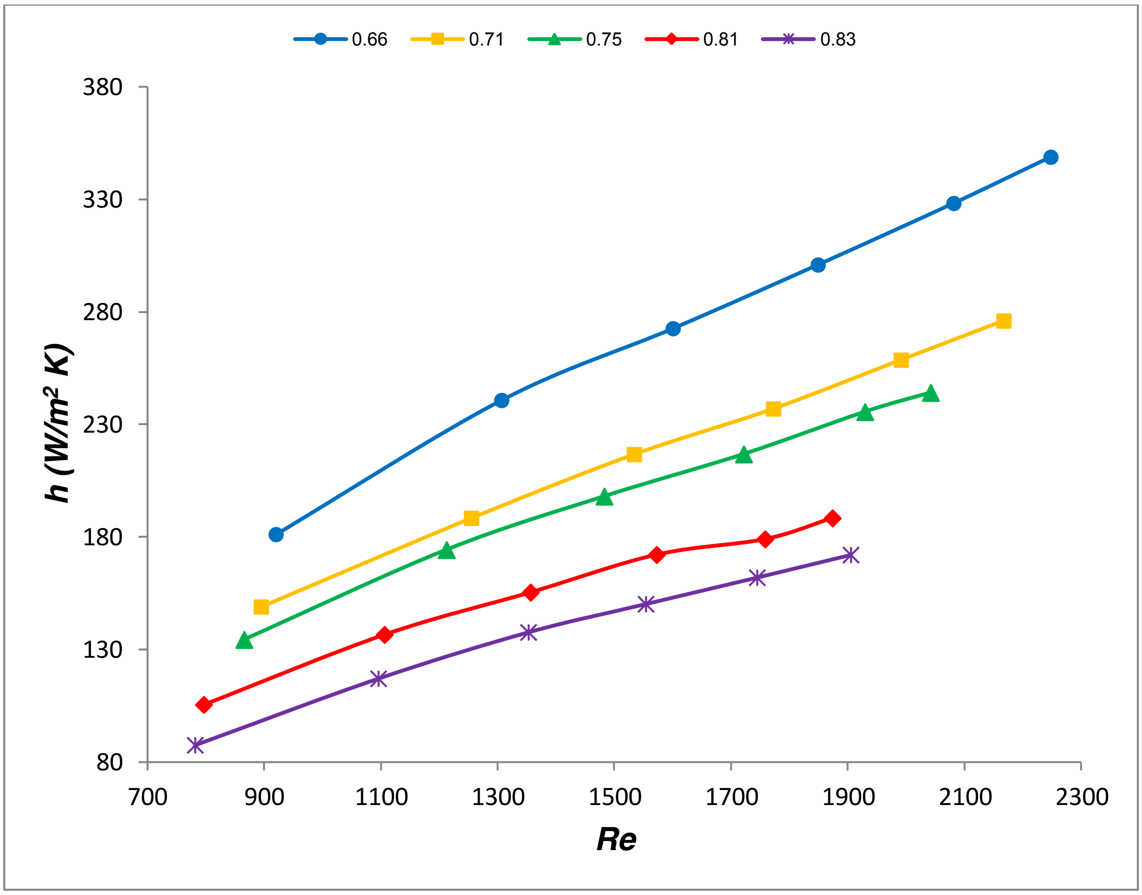

Figure 8.12 - h values for the EBM Ti6Al4Vporous samples.

As with the stainless steel porous samples the best performing one out of this group is the Ti6Al4V (1) due to its higher mass, as mentioned before, the CAD design for these two groups is very similar, it can be seen that the difference between the first sample and the rest of the group is comparable in both figures.

8.3. Pore Size Change Effect on the Heat Transfer Coefficient

In a porous metal the effect that the pore size has on the heat transfer coefficient (Table 8.1 and Figure 8.13) can be seen clearly in the wire mesh sample group while keeping a similar structure and material.

Sample	**Pore Size (mm)**	**h (W/m^{2}K)**
10 Mesh 10	2.000	390
10 Mesh 20	2.000	394
10 Mesh 40	2.000	391
20 Mesh	1.000	494
30 Mesh	0.500	509
200 Mesh	0.075	1103

Table 8.1 - Pore size effect on heat transfer coefficient of the wire mesh samples at 2.55 m/s.

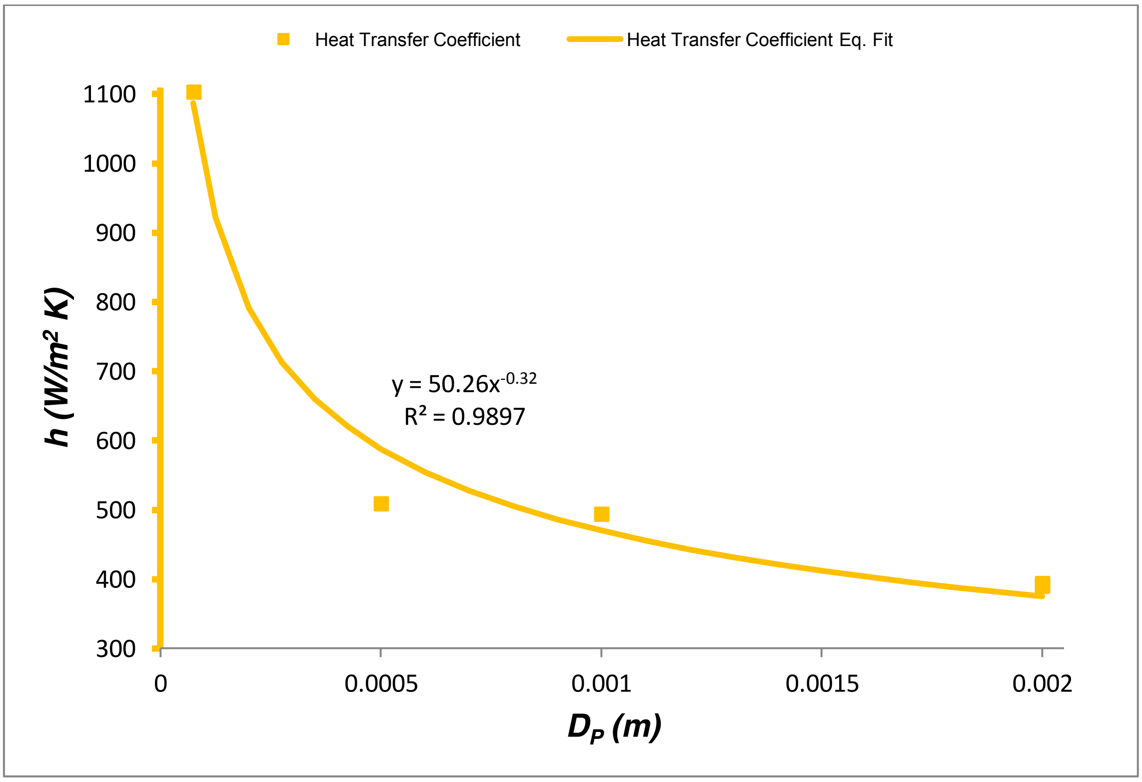

Figure 8.13 - Pore size effect on heat transfer coefficient of the wire mesh samples at 2.55 m/s.

An empirical correlation relating pore size and heat transfer coefficient using these four points for the wire mesh samples would be:

$$h = a * (50.26 d_P^{-0.32}) \qquad \text{Eq. 8.9}$$

From Table 8.1 it can be seen that the heat transfer coefficient increases steadily with the reduction of pore size, from Figure 8.14 the similar trends of the velocity against heat transfer coefficient can be seen, if another velocity is chosen similar results are produced.

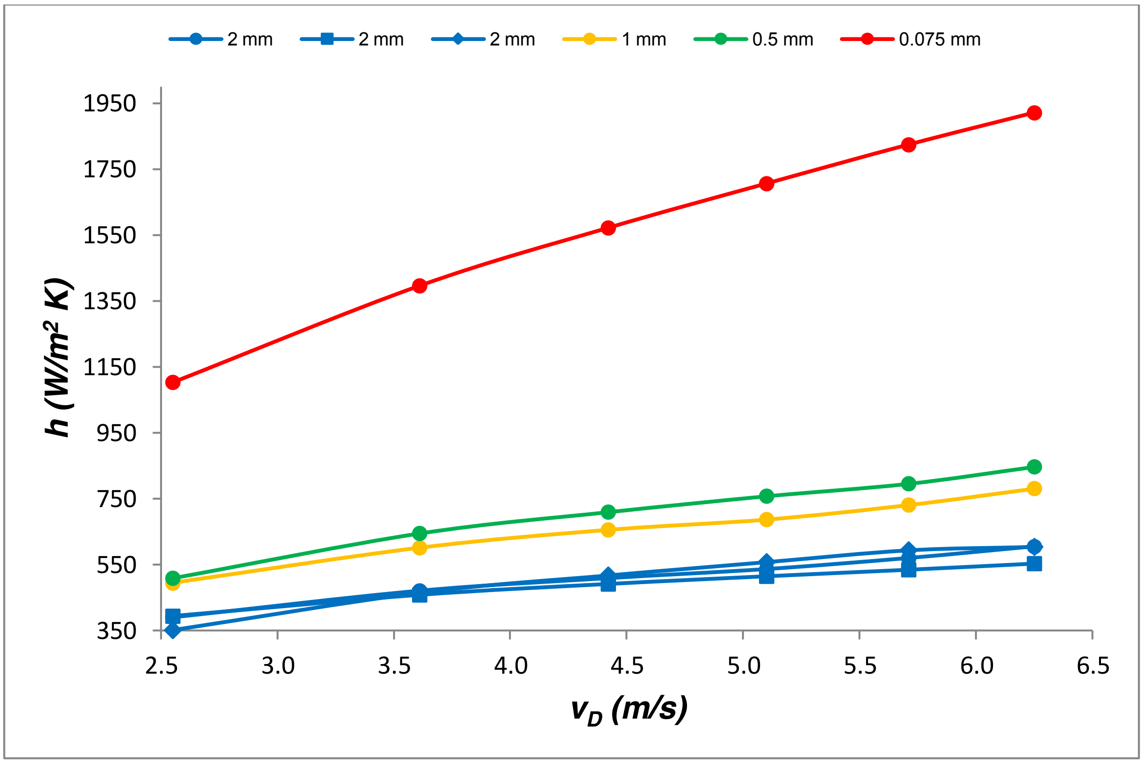

Figure 8.14 - Pore size effect on heat transfer coefficient for the wire mesh samples at different velocities.

With layer quantity the heat transfer coefficient changes slightly, however, this is due to the random positioning of the mesh sheets not the layer increase; for example, to obtain the heat transfer coefficient the NTU_R value is needed, if the number of layers is doubled the heat transfer area is doubled, when calculating the heat transfer coefficient with Eq. 8.3 these two values cancel each other out, leaving the same value for h.

When the pore size is halved (20 Mesh) the increase in the heat transfer coefficient is 26% on average. When comparing 30 Mesh to 200 Mesh the pore size difference has a factor of 6.67, the heat transfer coefficient difference has a factor of 2.17.

8.4. Porosity Change Effect on the Heat Transfer Coefficient

In a porous metal the effect that the porosity has heat transfer coefficient (Table 8.2 and Figure 8.15) can be seen clearly in the SLM SS316L sample group while keeping a similar structure and material.

Sample	**ε (%)**	**h (W/m^{2}K)**
SS316L (1)	61.8	190
SS316L (2)	65.7	151
SS316L (3)	71.5	136
SS316L (4)	77.3	115
SS316L (5)	82.0	96

Table 8.2 - Porosity effect heat transfer coefficient on the SLM SS316L samples at 2.55 m/s.

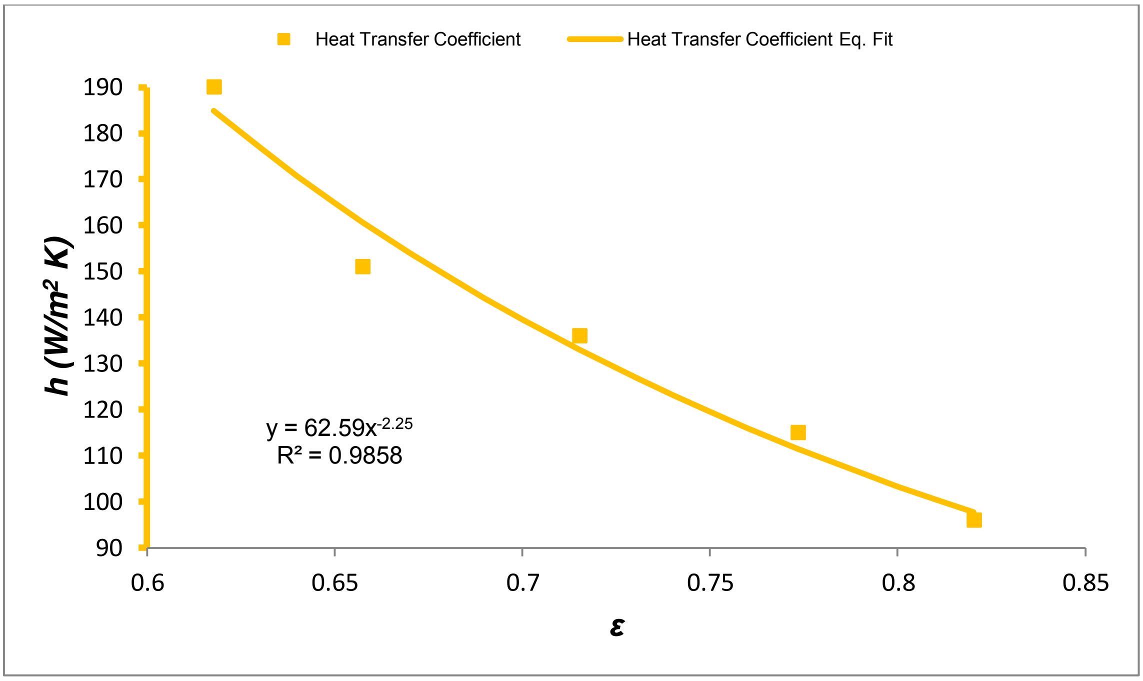

Figure 8.15 - Porosity effect on heat transfer coefficient for the SLM SS316L samples at 2.55 m/s.

An empirical correlation relating porosity and heat transfer coefficient using these five points for the SLM SS316L samples would be:

$$h = a * (62.59\varepsilon^{-2.25}) \qquad \text{Eq. 8.10}$$

When comparing both sets of equations (Mesh Eq. 8.9 vs. ALM sample Eq.8.10), the fact that they are a completely different fit shows evidence that the relationship between the mesh structure and the replicated structure to heat transfer coefficient does not behave in the same way. In Figure 8.16 the porosity effect can be seen for all velocities.

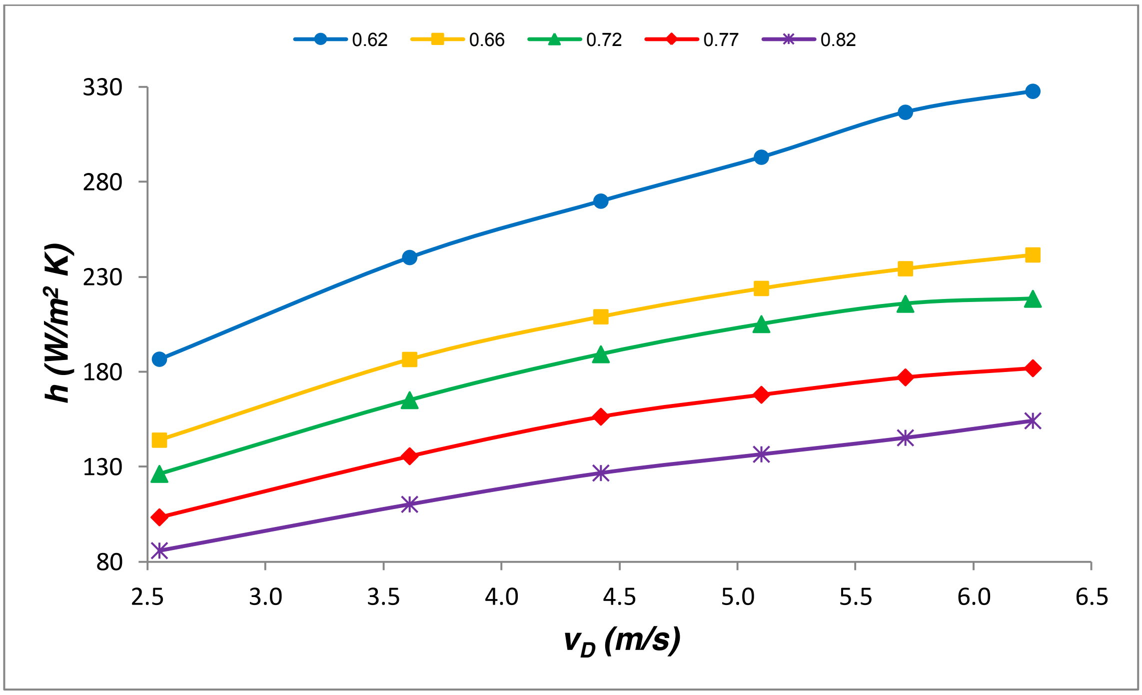

Figure 8.16 - Porosity effect on heat transfer coefficient for the SLM SS316L samples at different velocities.

From Table 8.2 it can be seen that the heat transfer coefficient decreases steadily with the increase of porosity.

With increase in porosity the heat transfer coefficient decreases slightly, from SS316L (1) to SS316L (2) the increase is in porosity is 6.4% and the decrease in heat transfer coefficient is 20.5%. From SS316L (3) to SS316L (4) the increase in porosity is 8.1% and the decrease in heat transfer coefficient is 15.4%, the ratios become lower as porosity increases.

8.5. Material Change Effect on the Heat Transfer Coefficient

In a porous structure the effect that the material has on the heat transfer coefficient (Table 8.3 and Figure 8.17) can be seen in the packed spheres sample group while keeping a similar structure, porosity range and longitudinal thermal conductivity close to 0, due to the lack of contact between the spheres.

Sample	**Material**	**$Q/V=c_R\rho_R(1\text{-}\varepsilon)$ (kJ/m^{3}K)**	**h (W/m^{2}K)**
Al Sph	Aluminium	1413	260
Cr Steel Sph	Chrome Steel	2292	317
Cu Sph	Copper	1980	291
Glass Sph	Glass	1298	228
SS420 Sph	Stainless Steel 420	2137	332
Ni-Ti45 Sph	Nitinol	≈ 3254	≈ 414

Table 8.3 - Material effect on heat transfer coefficient on the packed spheres samples at 2.55 m/s.

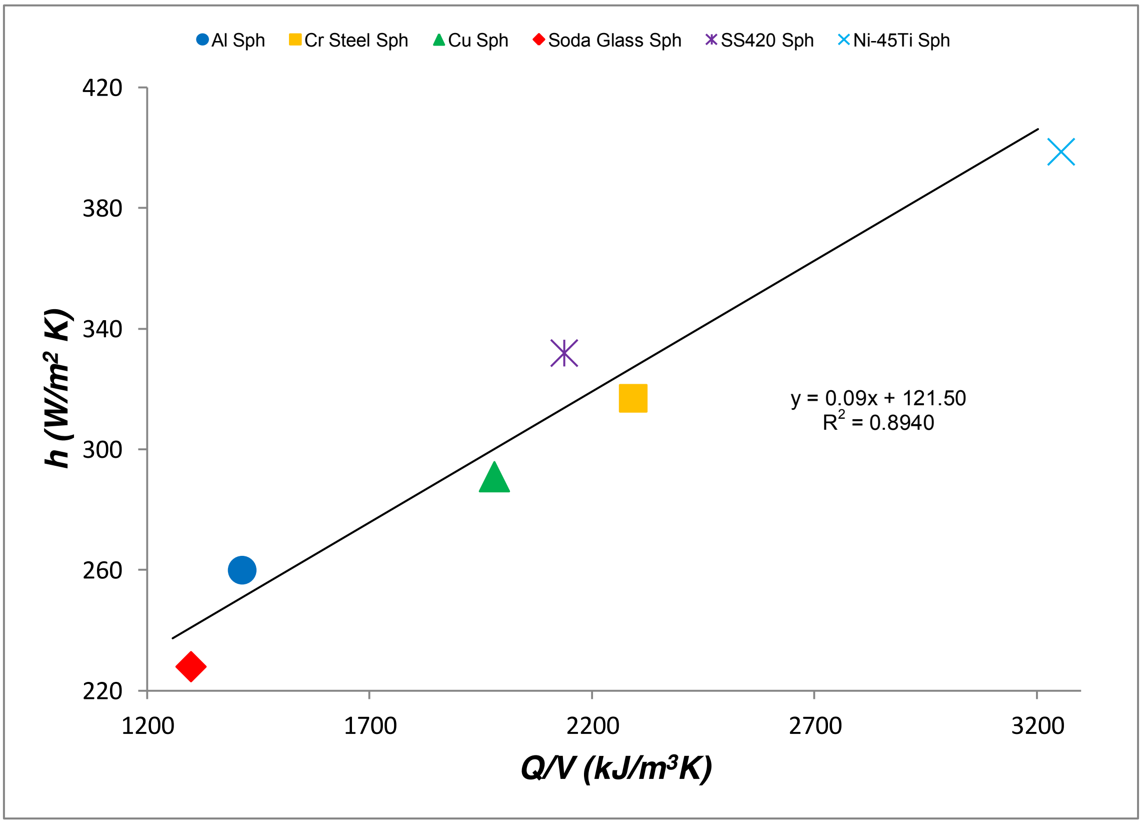

Figure 8.17 - Material effect on heat transfer coefficients of the packed spheres samples at 2.55 m/s.

From Table 8.3 it can be seen that the heat transfer coefficients follow a trend when multiplying the specific heat of the material times the density of the material times the solid volume fraction, this is known as the volumetric heat capacity or energy density.

In a comparison for example, the specific heat of the aluminium is the highest of the group at 0.90 kJ/kg K, the stainless steel 420 has a value of 0.46 kJ/kg K, approximately half of the aluminium. The density of aluminium is approximately a third of the stainless steel 420 (2700 kg/m^3 vs. 7750 kg/m^3). An empirical correlation relating the volumetric heat capacity to the heat transfer coefficient considering these five materials would be:

$$h = a * [0.09 c_R \rho_R (1 - \varepsilon) + 121.50] \qquad \text{Eq. 8.11}$$

From section 3.4, materials that theoretically would perform good as a regenerator in this case would be nickel and copper alloys, having high volumetric heat capacity values. For example, Nitinol (Ni-45Ti) is a nickel - titanium alloy with a density of 6475 kg/m^3 and a heat capacity of 0.838 kJ/kg K [180]; if considered a possible material to create a packed spheres sample and a porosity of 0.4 it would have a volumetric heat capacity of 3254 kJ/m^3 K and a heat transfer coefficient of 414 W/m^2 K on average, if fitted with Eq. 8.11.

If the material's density and specific heat increase, the heat transfer coefficient increases as well, these are two characteristics that are favoured among regenerators; in general terms by choosing a material with a high density and considerable specific heat value one may design a more efficient regenerator, as mentioned in Chapters 1 and 3.

8.6. Thermal Conductivity Change Effect on the Heat Transfer Coefficient

In a regenerator the effect of the longitudinal thermal conductivity is considered. In Table 8.4 and Figure 8.18 the samples' characteristics can be seen, these are made from the same material and have very similar porosities.

Sample	**k_R (W/mK)**	**$Q=c_R m_R \Delta T$ (kJ)**	**A_{HT} (m^2)**	**h (W/m^2K)**
Al Felt	6.51	0.036	0.23	261
A2 Rep	25.71	0.038	0.20	243
Al Sph	0.1	0.085	0.10	260

Table 8.4 - Thermal conductivity effect on the heat transfer coefficients of the aluminium samples at 2.55 m/s.

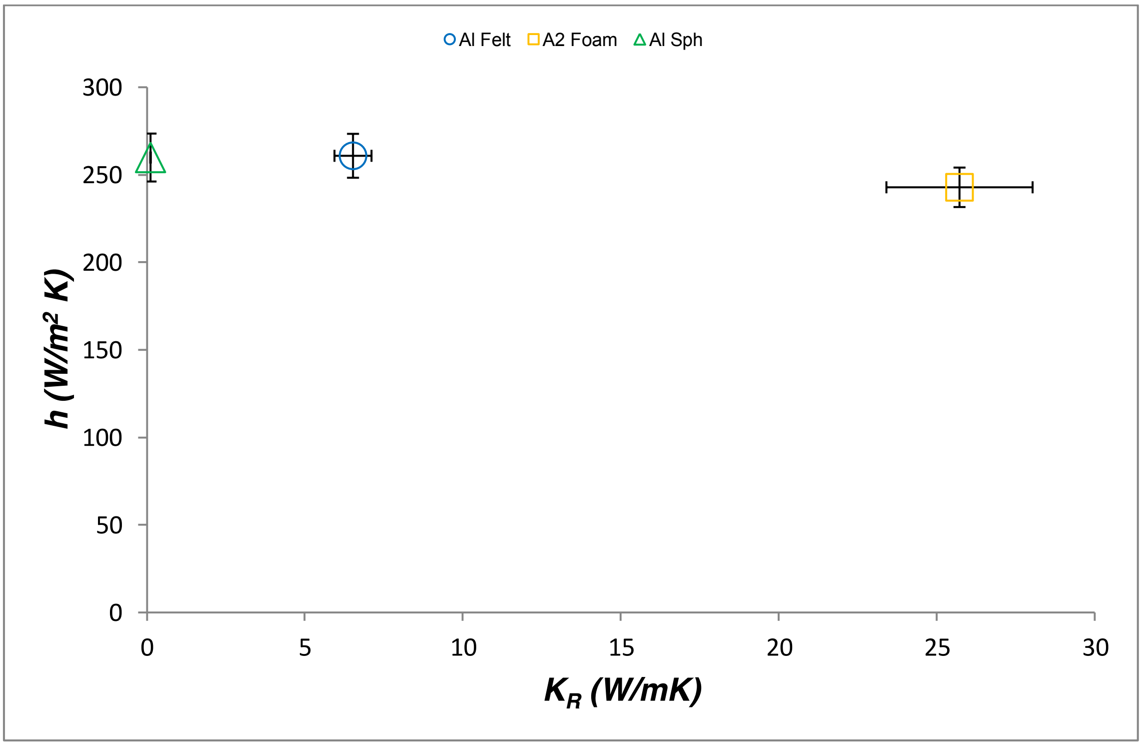

Figure 8.18 - Thermal conductivity effect on the heat transfer coefficients of the aluminium samples.

From Figure 8.18 it can be seen that the results do not show an obvious trend of the effect the longitudinal thermal conductivity has on the heat transfer coefficient, especially when considering the error, making it possibly a less considerable property when compared to density and specific heat.

8.7. Structure Change Effect on the Heat Transfer Coefficient

In a porous material the effect that the change in the structure provokes can be seen in Table 8.5 and Figure 8.19, four different structures (mesh, felt, packed spheres and replicated) made from different grades of stainless steels are compared and analysed.

Sample	**c_M (J/kg K)**	**ρ_M (kg/cm^3)**	**A_{HT} (m^2)**	***h* (W/m^{2}K)**
(SS304L) 30 Mesh	500	8030	0.205	509
SS304L Felt	500	8030	0.233	571
SS420 Sph	460	7740	0.105	332
SS316L (1)	500	7990	0.055	190

Table 8.5 - Structure change effect on the heat transfer coefficients of the stainless steel samples at 2.55 m/s.

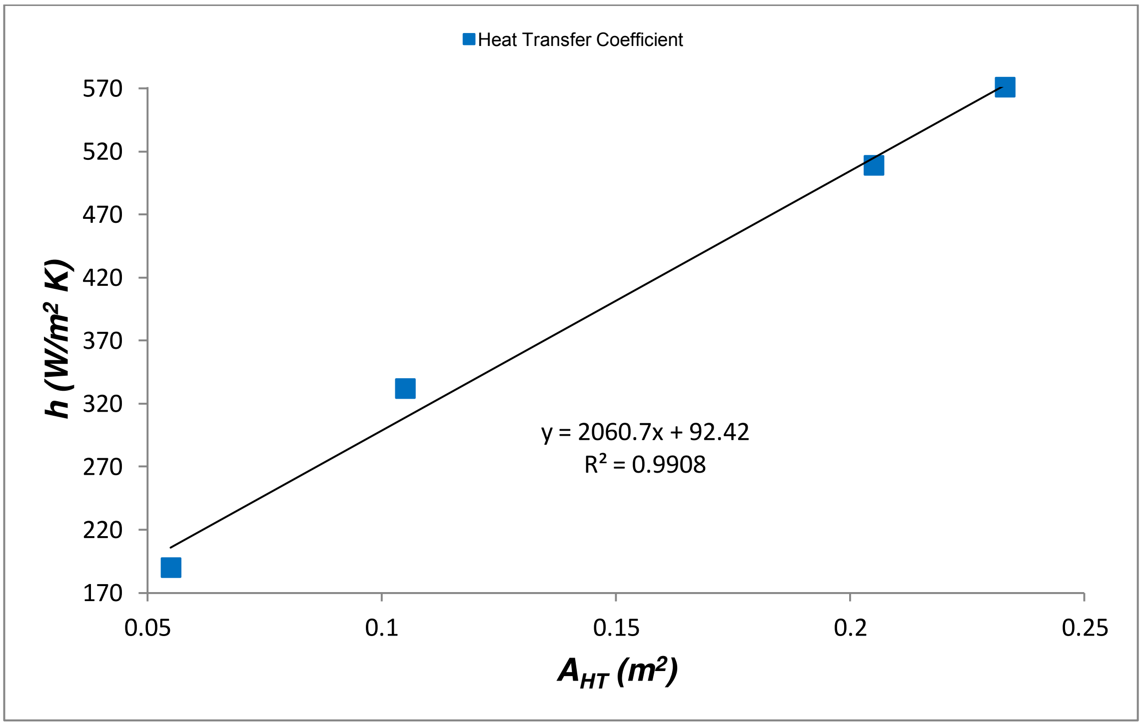

Figure 8.19 - Structure effect on the heat transfer coefficients of the stainless steel samples at 2.55 m/s.

From Table 8.5 it can be seen that the structure with the highest heat transfer coefficient in this group is the wire felt, this is due to its higher heat transfer area, it is followed by the 30 mesh; both these samples are made from wires showing similar behaviour in heat transfer situations.

The packed spheres sample has a high heat transfer coefficient because of its high mass, but it does not allow the air to pass as freely as the other samples., offering poorer performance. The ALM sample has the lowest heat transfer coefficient due to the lowest heat transfer area, this is caused by the large pore size of the sample, 3.9 mm. An empirical correlation relating the heat transfer area to the heat transfer coefficient considering these four samples would be:

$$h = a * [2060.7A_{HT} + 92.42] \qquad \text{Eq. 8.12}$$

In general terms the wire made samples due to their higher heat transfer area are the best choice as regenerators in this case, it could be possible for a replicated porous metal to challenge the wire made samples if a smaller pore size is used, at the moment this type of sample has not been produced.

8.8. ALM (SLM vs. EBM) Porous Samples' h Comparison

In Figure 8.20 the comparison between the ALM samples made from two different materials can be seen.

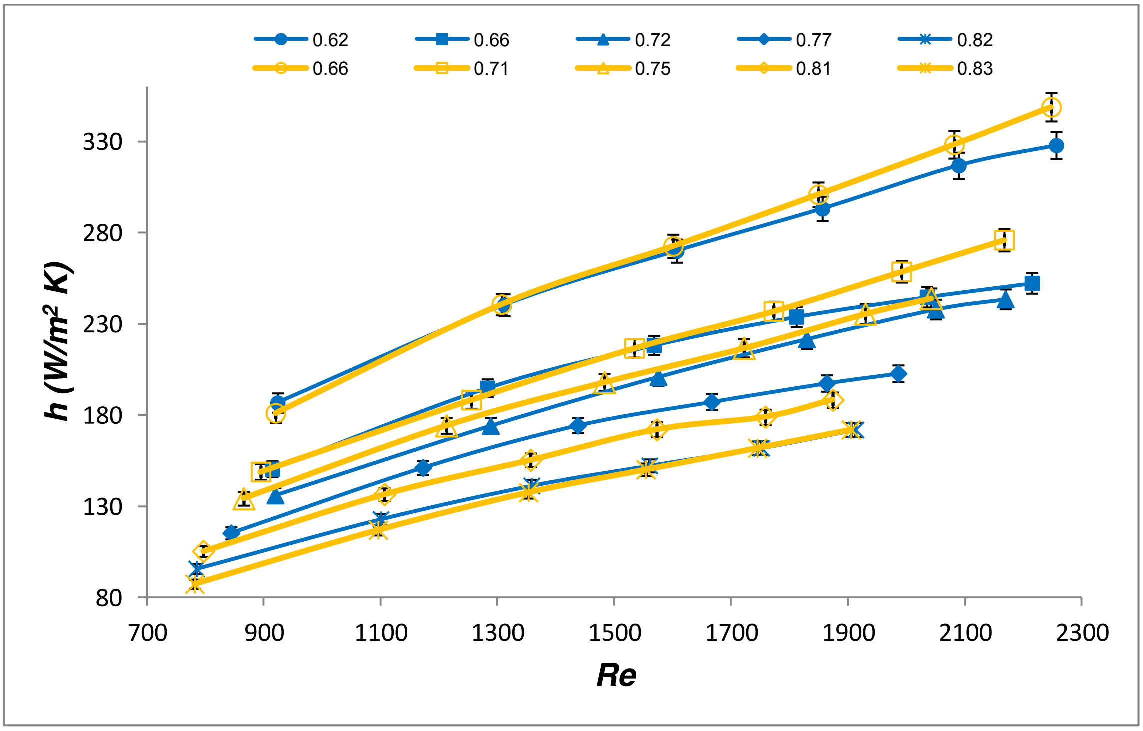

Figure 8.20 - Additive Layer Manufactured samples' h comparison.

In this graph when considering the heat transfer coefficients of both these sets of samples it can be noted that they are very similar, most falling between the acceptable error value. These samples were produced using the same CAD file, however, the manufacturing processes are different, SLM for the stainless steel samples and EBM for the Ti6Al4V samples.

In the SLM process the sample needs supports to hold its weight while being built, reason why the porosity of these is lower than the EBM made samples. A possible reason of why the EBM samples has similar h values throughout except in 4 points where it is higher may be due to the longitudinal thermal conductivity value, which is lower (6.7 W/mK) when compared to the stainless steel samples (16.2 W/mK).

8.9. General Performance of the Different Materials

It is clear that the heat transfer coefficient is affected by parameters such as the porosity and the pore size, as was shown in the work from Tong and London [125] and Kays and London [93] where the Stanton times the Prandtl number elevated to the 2/3 power were used; in Kays and London's work they propose a correlation applied to wire screens using 6 different porosities, from a range of 0.602 to 0.832 at different Reynolds numbers, showing that the heat transfer coefficient increases as the porosity decreases, the same occurs in Tong and London's work applied to a packed bed of lead spheres with a porosity value of 0.39, in both cases the heat transfer coefficient increases proportionally with the Reynolds number, as shown in Barari's work as well [120], confirming the samples' behaviour is consistent with that seen by other researchers.

With the heat transfer tests on the regenerator samples it can be clearly seen that the heat transfer coefficient increases when decreasing pore size, when decreasing pore size the area of heat transfer increases, allowing more heat to be captured by the sample as expected from the work done by Walker [19] in which he states that a more efficient regenerator needs a larger heat transfer area.

This effect can be seen for the porosity too, if the solid volume fraction increases there is more material present to capture more energy, this effect can be seen in the work done by Lu [205] on Duocel porous aluminium, by reducing sample porosity (higher material density) the heat transfer coefficient increases.

The effect of the thermal conductivity through the samples is not significant, the extraction of heat away from the surface is not the rate limiting behaviour, from Figure 8.19, the heat transfer coefficient is directly dependent on the heat transfer area, the most significant transfer of heat is from the air to the available area, if the value is large more heat is transferred, by the proposed equation in this graph the behaviour observed is of the linear nature.

In Table 8.6 the assessment of the performance of the different materials and structures against the baseline 200 Mesh regenerator sample is shown, the table lists the requirements for a regenerator from Table 1.1. In this assessment there is a number assigned from 1 to 10, in which 1 means very low performance and 10 means exceptionally good performance.

	High c_R	**High ρ**	**High ε**	**Low ε**	**High A_{HT}**	**Low k**	**Total Marks**
SS304L 200 Mesh	6	9	8	2	10	9	44
Rep Al	10	3	7	3	4	2	29
Rep Al (Vib)	10	3	8	2	3	2	28
SS304L 10 Mesh	6	9	8	2	2	9	36
SS304L 20 Mesh	6	9	8	2	3	9	37
SS304L 30 Mesh	6	9	8	2	4	9	38
Al Felt	10	3	7	3	5	2	30
Cu Felt	4	10	7	3	5	1	30
SS304L Felt	6	9	7	3	5	9	39
Al Sph	10	3	4	6	2	2	27
Cu Sph	4	10	4	6	2	2	28
Cr Steel Sph	5	9	4	6	2	7	33
Glass Sph	8	1	4	6	2	10	31
SS420 Sph	5	9	4	6	2	8	34
SS316L ALM (1)	6	9	7	3	1	8	34
Ti6Al4V ALM (1)	6	5	7	3	1	9	31

Table 8.6 - Performance of materials depending on the table of requirements for the regenerator application.

From this table it can be seen that the baseline material has the highest marks, the closest one after that is the SS304L felt, having a similar wire based structure and material properties falling behind only on the amount of heat transfer area, this is due to the wider wire diameter of the felt sample (0.25 mm) against the wire diameter of the mesh (0.075 mm), all the other samples perform lower. The weighting of each of the parameters is unknown [19], for example from tests in this work the importance of the thermal conductivity was less than the other parameters, caution needs to be taken in comparisons between results where the thermal conductivity changes significantly but other behaviours are similar.

With the knowledge gained here, the potential for development of replicated porous metals to act as regenerators can be discussed. The replicated porous metals have potential in gaining advantage in certain qualities such as a higher heat transfer area by reducing the pore size and if a better material were available (stainless steel) it could perform as well (or even better) as the baseline material, however it would be difficult to create since for replication a higher melting point material to serve as the preform is needed.

To consider the potential of replicated porous metal the following changes can be made, these are discussed in the context of the key dimensionless groups and the limits the process offers, their tentative location in comparison with the samples tested in this work is shown in Appendix 1 Figure A4c.

CHANGING THE PORE SIZE: It is possible to obtain the same specific surface area as the 200 mesh, simply by producing a replicated sample with a 180 μm pore size keeping the porosity the same, however because the material is aluminium the NTU_R value would not increase much, in total the NTU_R value only increases by 3.6 times (this when comparing the A samples vs. the C samples) according to NTU_R values, Stanton times Prandtl number elevated to the 2/3 would increase as Reynolds number lessens, the behaviour area is shown in Figure A4c (D_P Change).

CHANGING THE POROSITY: If the porosity is decreased to a value of approximately 64% (before the closing of the pores [7]) the effect is the increase of the NTU_R value, approximately by 2 full units for the replicated porous samples (this when comparing the B samples vs. the V samples, 70 vs. 76 % porosity), the behaviour area is shown in Figure A4c (ε Change).

CHANGE IN BOTH: If both properties are changed the replicated sample becomes more efficient having a higher heat transfer rate, however by its new location, it is obvious that pore size has the larger effect, since the Reynolds number drops closer to the area of the D_P Change, ideally the best replicated aluminium sample would have a lower porosity to keep the high flow rate, however it is impossible due to the closing off of the pores, the behaviour area is shown in Figure A4c (Change in Both).

In this chapter the results for heat transfer tests on the porous metal samples are presented, each section contains the experimental data given by the test rig and analysed in the terms which are of interest for the regenerator application, this being the heat transfer coefficient present in each sample at a certain velocity, next was to analyse the effect of pore size, porosity, material and structure change effects on the heat transfer coefficient finally concluding with a property comparison between the two sets of samples with very similar structure and different material (ALM porous metals); following in Chapter 9 the conclusions and future work are presented. A wide range of porous structures can now be directly compared, for full details see the graphs on Appendix 1 for comparisons of pressure drop, NTU_R and heat transfer coefficients.

Chapter 9. Conclusions and Future Work

9.1. Conclusions

This work encompasses the subject of the production and fluid and heat transfer behaviour of various groups of porous structures and materials. The results obtained aim to help develop new ways to design and manufacture regenerator elements. In total 37 porous material samples with different methods of production made from different materials tested as regenerators has been achieved; this is the largest database obtained for this type of material.

The argon only replication method was modified to produce replicated porous metal samples with different porosities and pore sizes, establishing the requirements by developing the technique into four novel protocols (W, X, Y and Z), each one to produce porous metals with a different porosity, from 61 to 78% [149]. 12 replicated porous metal samples with three different pore sizes of 1.09 mm, 1.55 mm and 2.18 mm and two preform packing variations, random and vibrated have been produced. The argon only replication process has been improved to work more effectively, the production rate was increased from 2 samples per day to 5 samples per day and the rate of uniform samples produced was increased from 1 in 10 to 9 in 10.

Apart from the replicated porous metal samples and with the purpose of testing a wide array of structures made from different materials as regenerators, 25 additional porous samples were created using different methods; analysing the effects produced by changing these two characteristics (structure and material). The other structures and materials analysed were wire meshes (7) (stainless steel 304L), wire felts (3) (Al, Cu and stainless steel 304L), packed bed of spheres (5) (Al, chrome steel, Cu, soda glass and stainless steel 420) and additive layer manufactured porous metals following a particular random pattern (10) (stainless steel 316L and Ti6Al4V).

The wire meshes were selected with different open mesh space sizes (taken as a measure equivalent to the pore sizes; 2 mm, 1 mm, 0.5 mm and 0.075 mm) to study the effect that pore size has on regenerator efficiency. From this test it was determined that pore size has a large impact on regenerator efficiency, the smaller the pore size the larger the heat transfer surface area, hence a better regenerator. To fill a gap in the existing literature an empirical correlation relating the pore size to the pressure drop has been proposed, along with an empirical correlation relating the pore size to the heat transfer coefficient for the wire meshes.

The impact that porosity has on pressure drop is less significant than pore size however it still has an effect, as the porosity increases the pressure drop decreases. For heat transfer, increasing the porosity decreases the NTU_R and heat transfer coefficient. To fill a gap in the existing literature an empirical correlation relating the porosity to the pressure drop has been proposed and an empirical correlation relating the porosity to the heat transfer coefficient for the replicated porous metals as well.

The thermal conductivity values for the porous metal samples was measured improving the accuracy of the results, this data is a significant extension of the existing database. The effect that the material has on the regenerator samples has been determined, it was concluded that the materials most suitable for this purpose would be iron, copper and their alloys; preferably steels and stainless steels. The absolute maximum performance (ignoring cost and processing issues) for materials in the Cambridge Engineering Selector software database 2014 edition is for Nitinol (Ni-45-Ti), having the highest volumetric heat capacity.

The performance these samples have when considering pressure drop were compared against the literature and it was determined that they follow a similar trend, however, due to the randomness of the structure, and possibly the shape of the pores, some of the samples' permeability values proved better than expected, having a higher permeability value without losing thermal performance.

When considering heat transfer the samples were compared against results from other researchers using Stanton number, the results consistently show that the wire mesh samples perform better as regenerators; however, the replicated porous metals have the advantage of being tailored to a wide array of specifications, being able to reproduce behaviours of the meshes or the packed spheres samples respectively, their location in Figure A4c (in between all samples) allows for them to emulate the behaviour of other types of structures with certain modifications.

It is worth pursuing lower pore size replicated porous metals for regeneration, perhaps introducing new methods of production to accommodate other types of structures and materials, having a much lower cost in the end when compared to the additive manufactured porous metals. The extensive range of tests and results is aimed to help researchers design new regenerator samples based on the different properties and characteristics from the different porous materials and structures discussed in this work.

9.2. Future Work

To improve the results obtained from this research several suggestions can be made in the form of future work. These ideas require additional time and resources to implement, reason why they were not carried out during the course of this work.

Initial runs have been made to analyse the samples using an X-ray computational tomography scan based in the Medical Advanced Manufacturing Research Centre of the University of Sheffield; this would give the exact surface area of any tested sample, the results will be more accurate than the current ones. Several images have been taken of the porous samples, however, currently the resources are not enough to have the complete analysis, sample images can be seen in Figure 9.1.

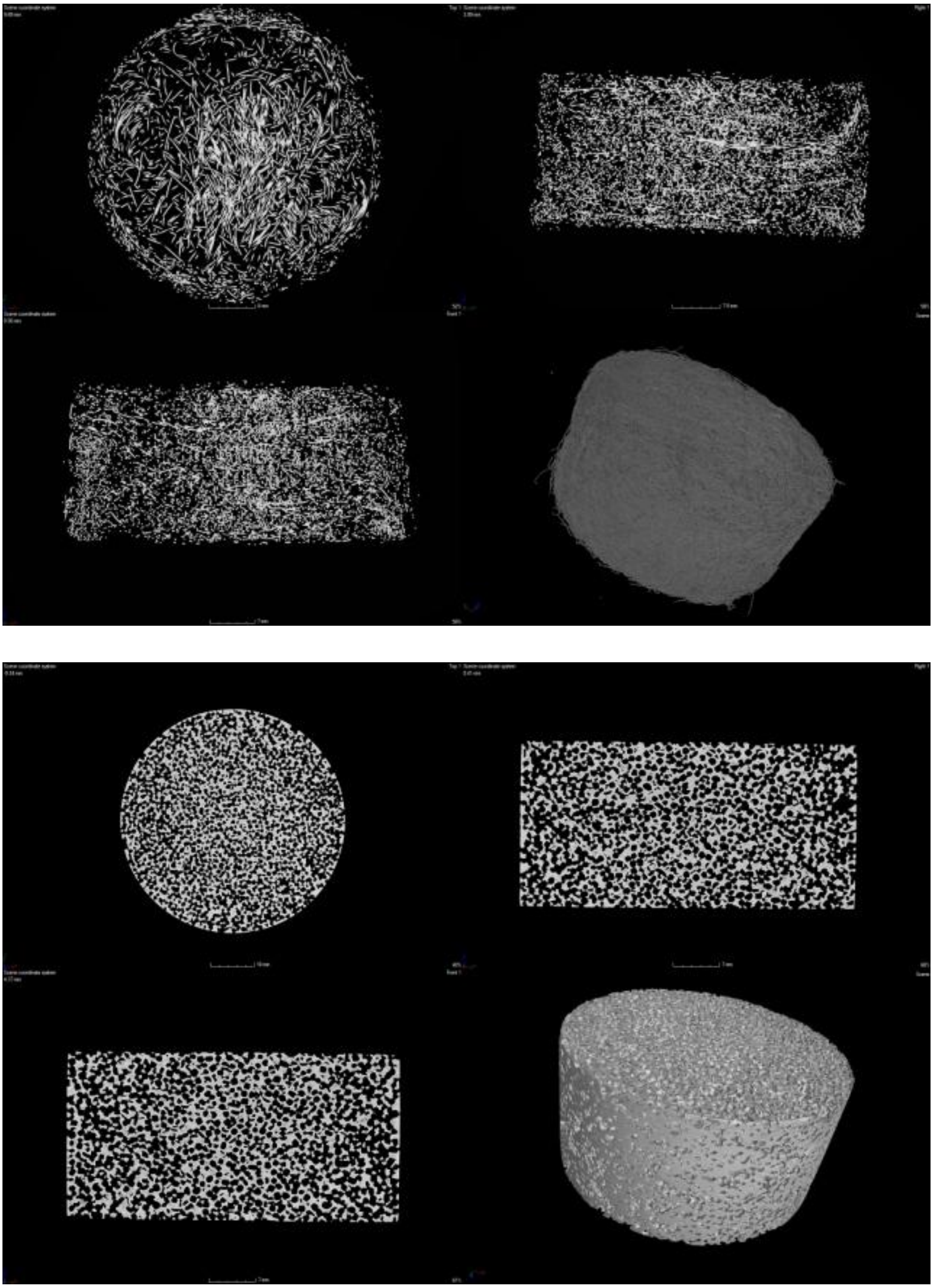

Figure 9.1 - X-Ray Computational tomography scans of the Al felt and A2 replicated samples.

The image clearly shows the internal structure of the samples, they can be used to detect poorly infiltrated regions of the porous metals and as an initial scan for future research using computational fluid dynamics, creating a model out of the different types of structures to understand the flow behaviour when it passes through the porous structure using the experimental data obtained from this work. By measuring the surface area of the porous metal samples, the values of the heat transfer coefficient will be closer to reality.

A hybrid sample made from layers of replicated porous aluminium and 20 Mesh has been manufactured to improve the replicated porous metal's heat transfer performance, however, the full analysis has not been performed yet due to time constraints, initial values of NTU_R at 2.55 m/s are around 9, above the replicated porous aluminium's highest value of 7.3 but lower than the 20 mesh's value of 11.5. Further analysis is needed.

The replicated vibrated samples (V group) show promise of good NTU_R values when compared to the non vibrated samples, especially the 2.18 mm pore size samples (C group) samples achieving lower pressure drop than them but around the same range of NTU_R values, new samples using vibration are suggested.

Replicated porous metal samples with smaller pore size should be made at the same level of porosity to improve the heat transfer performance, the challenge lies on the limitation of the replication process, which is followed due to its simplicity and low cost when compared for example with the additive layer manufactured samples.

Appendix 1. General Graphs and Data Tables

In Figure A1a and Figure A1b (log scale "Y" axis) the general pressure drop graphs including all produced samples can be seen.

In Figure A2a and Figure A2b (log scale "Y" axis) the general number of transfer units NTU_R graphs including all produced samples can be seen.

In Figure A3a and Figure A3b (log scale "Y" axis) the general heat transfer coefficient h graphs including all produced samples can be seen.

In Figure A4a (log scale) the Reynolds number against Stanton number times Prandtl number elevated to the 2/3 power including uncertainty values can be seen for wire meshes and packed spheres compared with the results from Kays and London.

In Figure A4b (log scale) the general Reynolds number against Stanton number times Prandtl number elevated to the 2/3 power including all produced samples can be seen. This is a common way to present this type of results (Kays and London).

In Figure A4c (log scale) the general Reynolds number against Stanton number times Prandtl number elevated to the 2/3 power including all produced samples by region can be seen.

In Figure A5 the pressure drop against heat transfer coefficient can be seen for all samples.

In Table A1 the experimental data for all samples can be seen.

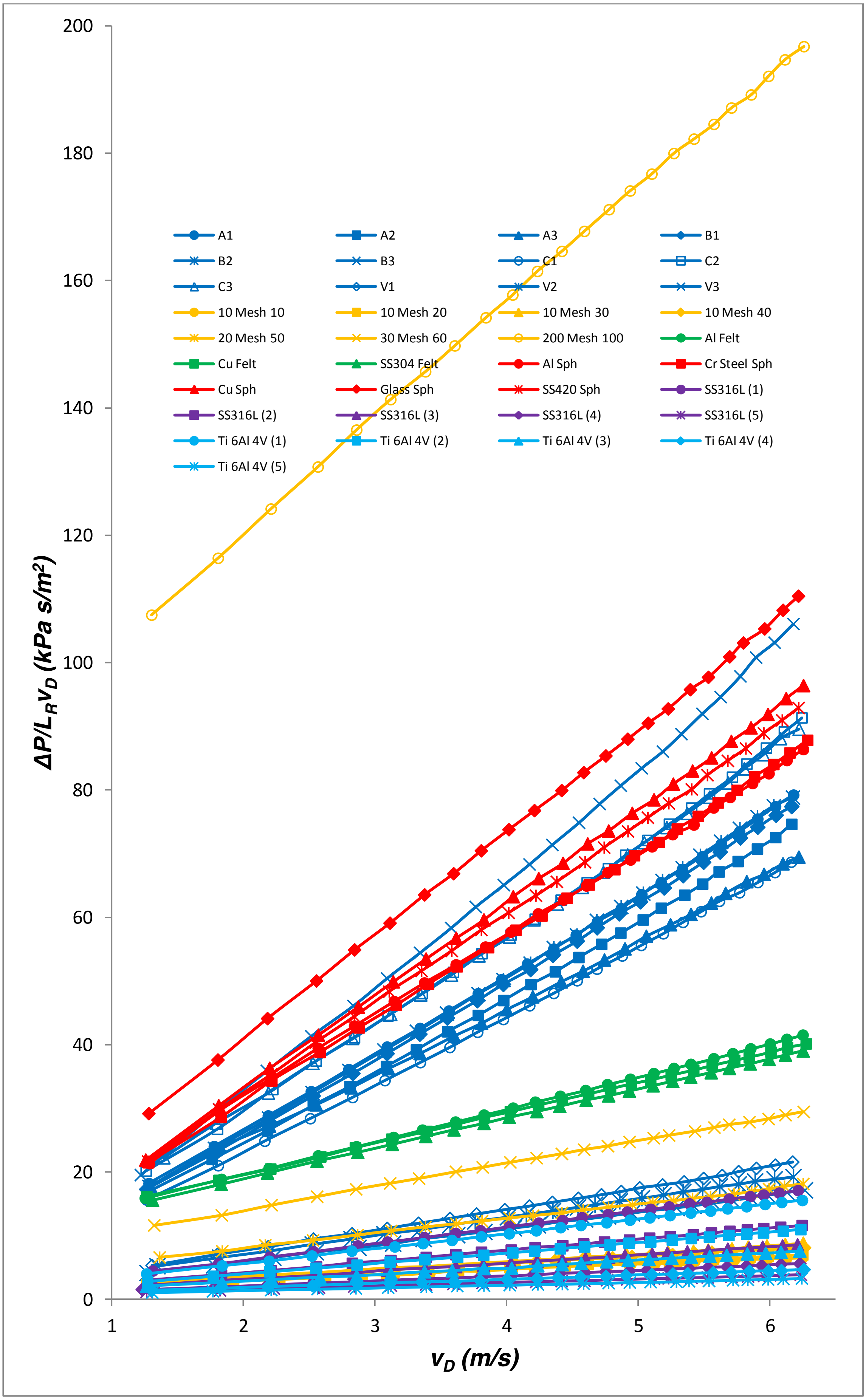

Figure A1a - General linear pressure drop graph.

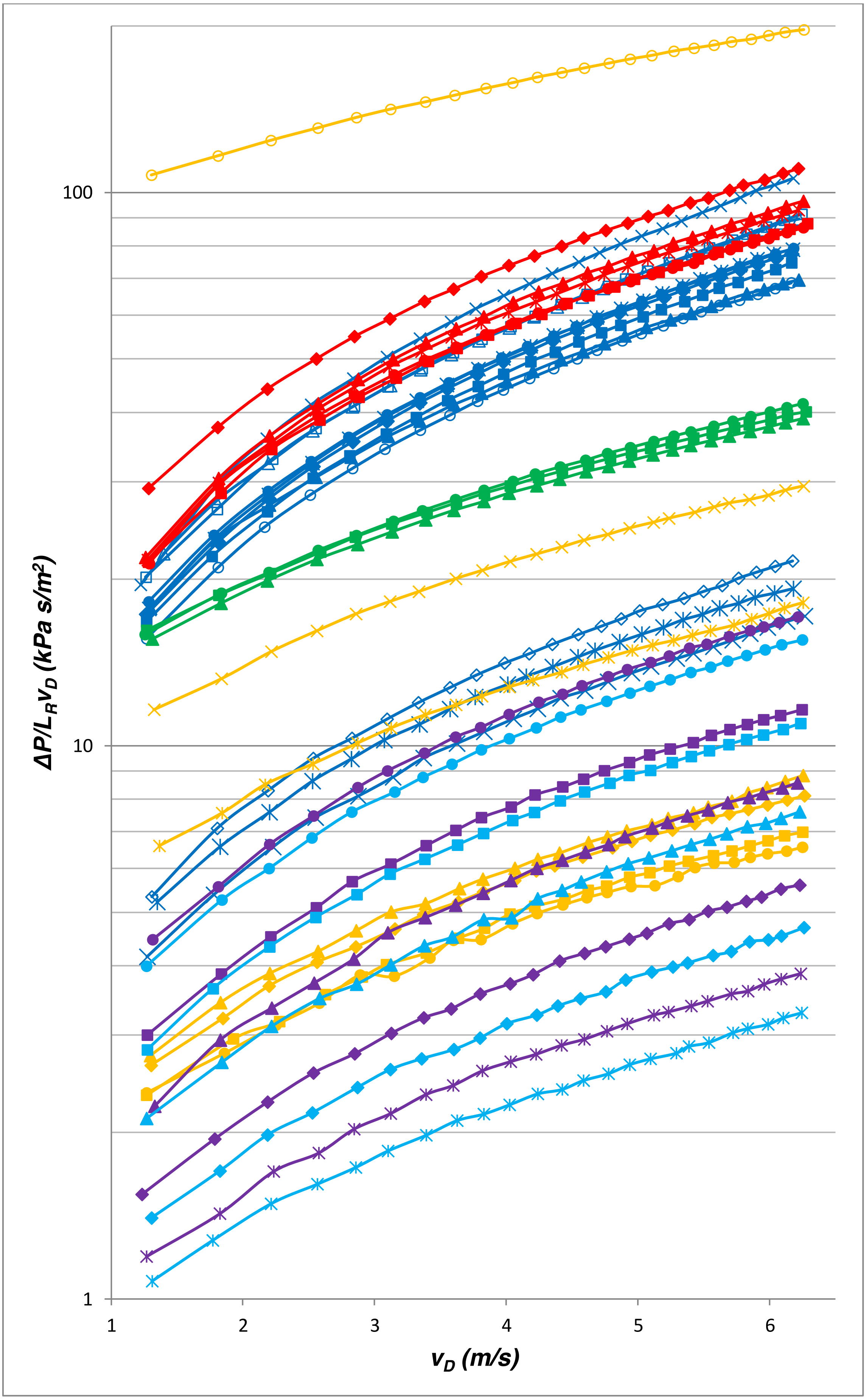

Figure A1b - General linear pressure drop graph (log scale).

In the general pressure drop graphs the performance of the six types of samples can be seen.

Group 1. Replicated porous metal samples

This group (blue) can be divided into two subgroups, the non vibrated and vibrated preform porous metals. Within all sample groups it has the second highest linear pressure drop. Considering only linear pressure drop, the best sample to be used as a regenerator would be the V3 sample.

Group 2 Wire mesh samples

For this group (orange) the difference between the samples relies on the pore size of the mesh, having the 200 mesh as the sample with the highest linear pressure drop caused by a pore size of 0.075 mm and the lowest linear pressure drop for the 10 mesh samples with a pore size of 2 mm. Within all sample groups its linear pressure drop range is present in all areas of the graph, due to the different pore sizes. Considering only linear pressure drop, the best sample to be used as a regenerator would be the 10 mesh 10 layer wire mesh.

Group 3 Wire felt samples

For this group (green) the felt structures were very similar in construction, reason why the linear pressure drop between them stays rather constant. Within all sample groups it has the third highest linear pressure drop. Considering only linear pressure drop, the best sample to be used as a regenerator would be the SS304L felt.

Group 4 Packed spheres samples

For this group (red) the packed spheres structures generate the highest linear pressure drop as a group. This is caused by the low porosity (≈ 40%) of the structures when compared to the others (> 61%). Considering only linear pressure drop, the best sample to be used as a regenerator would be the chrome steel sample.

Group 5 Stainless steel 316L samples

For this group (purple) the structure is based on a large pore size (3.9 mm), reason why the samples occupy the low linear pressure drop area of the chart, the difference between them is the porosity, ranging from 67 to 82%. Considering only linear pressure drop, the best sample to be used as a regenerator would be the SS316L (5) sample.

Group 6 Titanium alloy Ti6Al4V samples

This group's (light blue) structure is based on the same CAD files as the stainless steel samples, they have a very similar linear pressure drop as the previous group, having the same pore size of 3.9 mm they are present in the lower part of the graph. The porosity difference ranges between 68 and 83%. Considering only linear pressure drop, the best sample to be used as a regenerator would be the Ti6Al4V (5) sample.

From the graph it can be determined that the sample that generates the highest linear pressure drop is the 200 Mesh. The lowest linear pressure drop is caused by the Ti6Al4V (5) sample.

From the evidence it can be noted that the pore size plays a more important role than the porosity while generating a linear pressure drop. For example, the porosity of the 200 Mesh is 74.65%, compared to the porosity of the packed spheres of roughly 40%; the spheres generate a lower linear pressure drop than the mesh due to the larger space between the packed spheres when compared to the space between the wires of the mesh.

The porosity has an effect on linear pressure drop, as seen with the additive manufactured porous metals, only not as substantial as to when the pore size is changed dramatically.

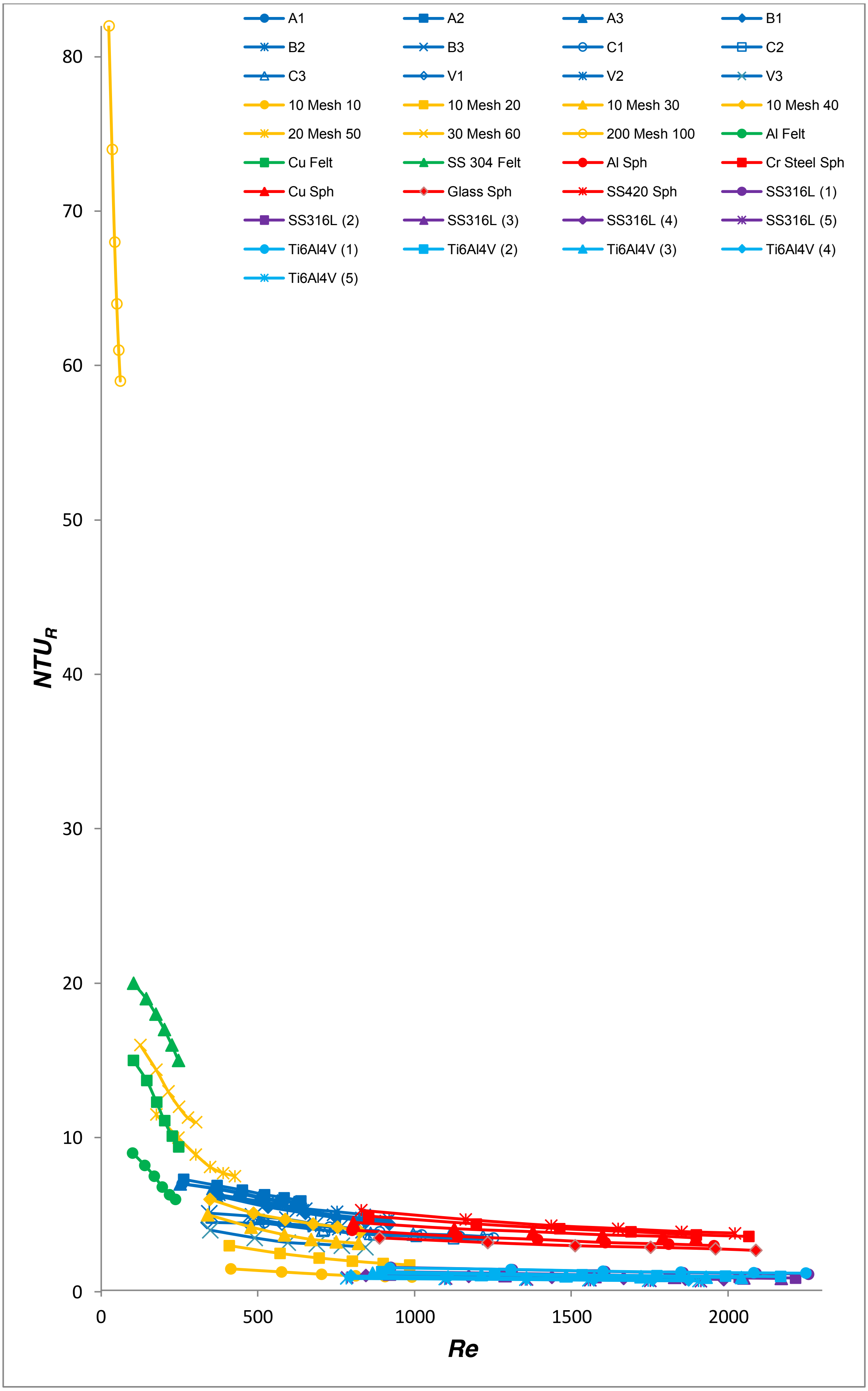

Figure A2a - General NTU_R value graph.

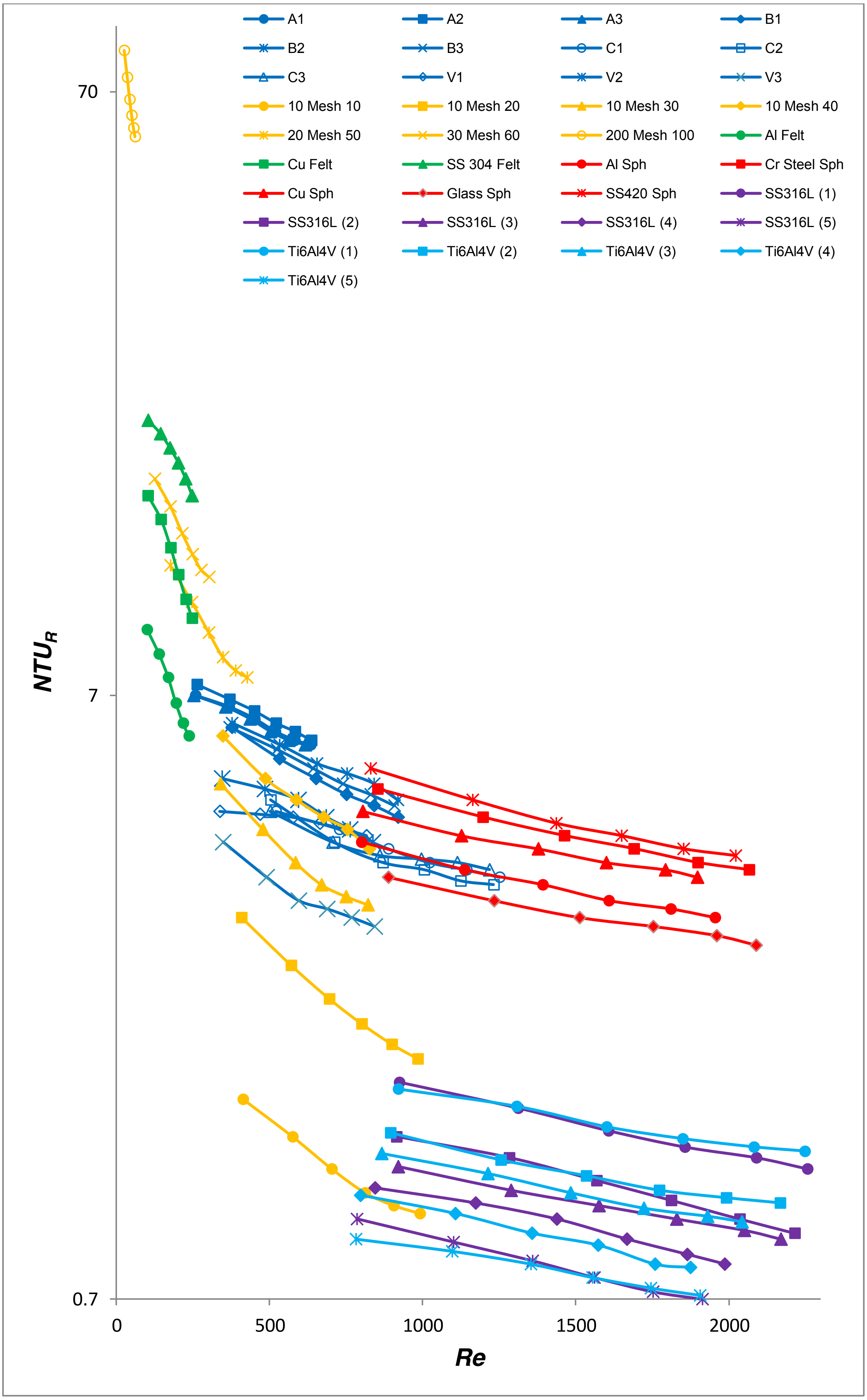

Figure A2b - General NTU_R value graph (log scale).

In the general NTU_R graphs the performance of the six types of samples can be seen. As a regenerator the important characteristic to have from this chart is a high NTU_R value at a low Reynolds number.

Group 1. Replicated porous metal samples

This group (blue) can be divided into four subgroups, the A, B, C and V samples. The A samples are the best performing samples of the group. The B samples are next in line, these samples have a larger pore size at 1.55 mm. Afterwards the C samples have a pore size of 2.18 mm. Finally the V samples have a higher porosity (≈ 76%) than the A, B and C samples (≈ 70%) and a pore size of 1.55 mm, they have approximately the same NTU_R range as the C samples, this occurs due to an increase in porosity and a decrease in pore size. The replicated porous metals performed well compared to most of the other groups, especially the A samples; the only samples that had higher NTU_R values were three mesh samples and the three felts. Considering only NTU_R value, the best sample to be used as a regenerator would be the A2.

Group 2 Wire mesh samples

For this group (orange) the difference between the samples relies on the pore size of the mesh; the 200 Mesh is the sample with the highest NTU_R range at the lowest range of Reynolds numbers of the group. The 30 and 20 mesh samples also performed at relatively high NTU_R values. From the 10 Mesh samples it was found that NTU_R value increases proportionally with the number of layers added. Considering only NTU_R value, the best sample to be used as a regenerator would be the 200 Mesh.

Group 3 Wire felt samples

For this group (green) the NTU_R values are noticeably different, their structure and porosities are similar, the difference relies on the material, having different thermal conductivities, densities and specific heat values, all having an impact on the resulting NTU_R. Considering only NTU_R value, the best sample to be used as a regenerator would be the SS304L sample.

Group 4 Packed spheres samples

For this group (red) the NTU_R value expand through a large range of Reynolds numbers, their structure and porosities are similar, the difference between them relies on the material, having different thermal conductivities, densities and specific heat values, all having an impact on the resulting NTU_R. Considering only NTU_R value, the best sample to be used as a regenerator would be the stainless steel 420, which has the lowest thermal conductivity, high density and mid range specific heat.

Group 5 Stainless steel 316L samples

For this group (purple) the NTU_R values are small, expanding through a large range of Reynolds numbers, their structure and material are similar, the difference between them relies on the porosity; it is inversely proportional to the NTU_R value. When considering only the NTU_R value, the best sample to be used as a regenerator would be the SS316L (1), which has the lowest porosity, giving the highest NTU_R value.

Group 6 Titanium alloy Ti6Al4V samples

This group's (light blue) structure is the same as the one used to produce the stainless steel samples, they have a very similar NTU_R value, the porosity in these samples is slightly higher due to the different manufacturing process. The SLM process needs supports to hold the samples while building, the EBM does not; reason why the SS316L samples are less porous. The NTU_R and Re have very little variation, slightly lower than the SS316L samples. Considering only NTU_R value, the best sample to be used as a regenerator would be the Ti6Al4V (1), having the lowest porosity and the highest NTU_R value.

From the chart the pore size and structure type have a large impact on the NTU_R, more so than porosity. The structures that favour a high NTU_R are the wire type structures, with the replicated porous metals closely following; the packed spheres while keeping up with the replicated porous metals in NTU_R value they deliver it at a much higher pressure drop, which is not convenient for regenerators.

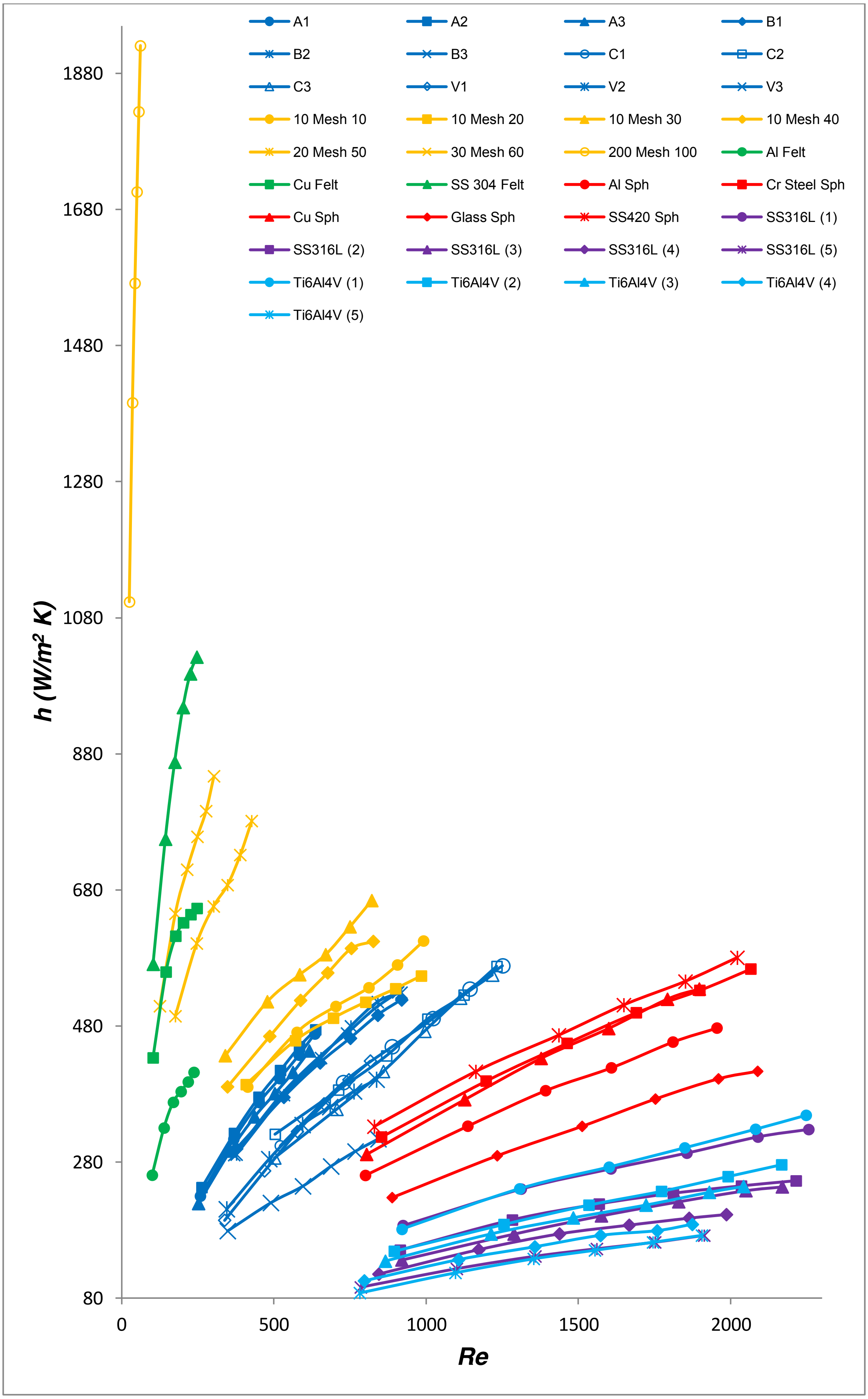

Figure A3a - General heat transfer coefficient value graph.

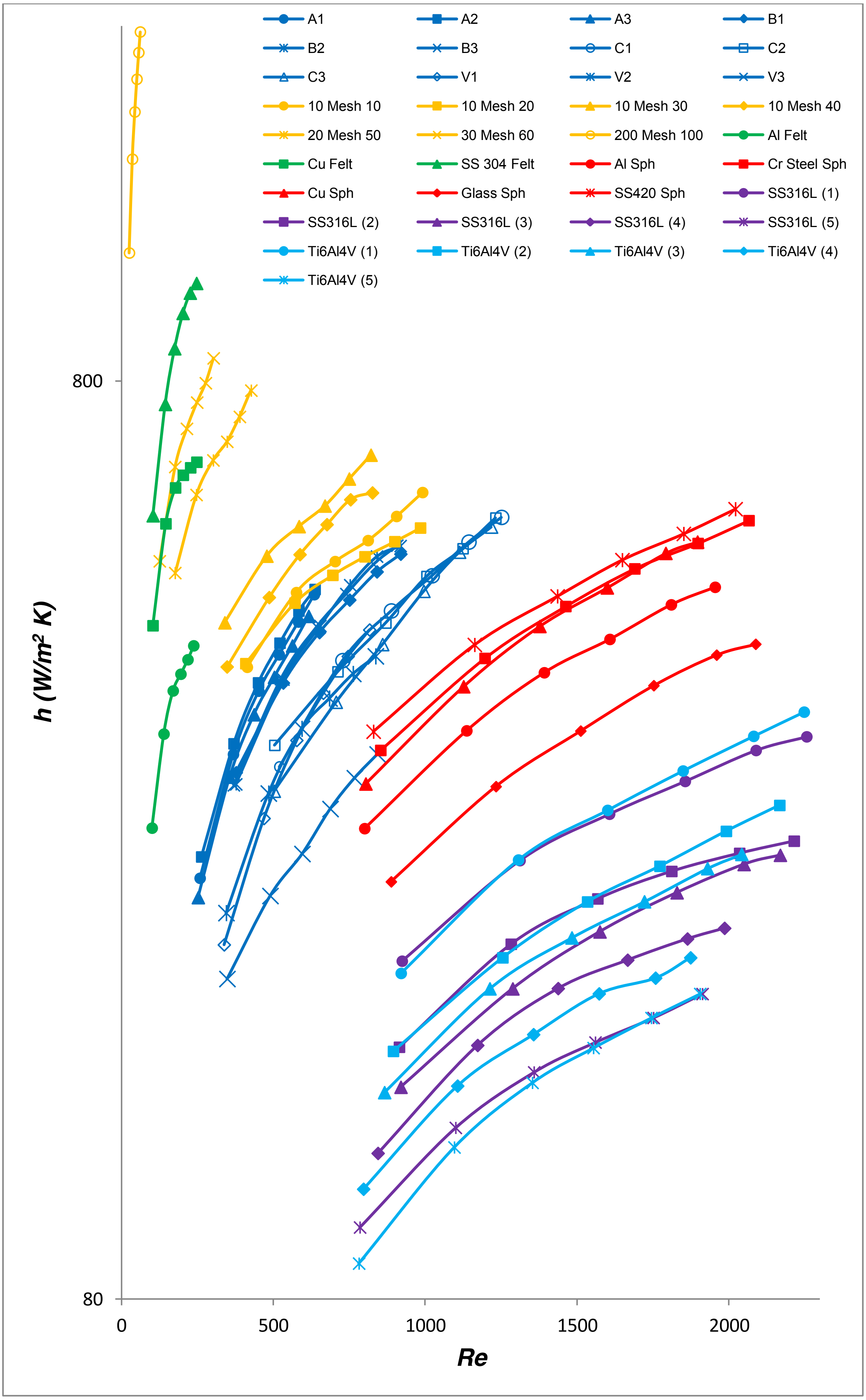

Figure A3b - General heat transfer coefficient value graph (log scale).

In the general heat transfer coefficient graphs the performance of the six types of samples can be seen. As a regenerator the important characteristic to have from this chart is a high heat transfer coefficient at a high Reynolds number.

Group 1. Replicated porous metal samples.

This group (blue) performed well compared to the other groups except the wire mesh and wire felt samples. With a smaller pore size, the replicated porous metals may challenge the heat transfer coefficient levels of the wire produced samples. For these porous metals, an empirical correlation to obtain the pore size necessary to match the heat transfer coefficient of the 200 mesh is given in Eq. A1.

$$h = a * (0.734 d_P^{-0.849}) \qquad \text{Eq. A1}$$

the sample would require to have a pore size of at least 5 times smaller to match the specific surface area (structure dependent) and an NTU_R value (material dependent) 13 times higher if it were made from aluminium. Considering only heat transfer coefficients, the best sample to be used as a regenerator would be the C2.

Group 2 Wire mesh samples

This group (orange) is the best performer in terms of heat transfer coefficient. Considering only heat transfer coefficients, the best sample to be used as a regenerator would be the 200 mesh.

Group 3 Wire felt samples

This group (green) performs better than most of the other samples except the some of the wire mesh samples. Considering only heat transfer coefficients, the best sample to be used as a regenerator would be the SS304L felt.

Group 4 Packed spheres samples

This group (red) performs worse than most of the other groups except the additive manufactured samples. They behave similar due to close porosity values between them and to their structure. The difference relies on the material properties. Considering only heat transfer coefficients, the best sample to be used as a regenerator would be the stainless steel 420.

Group 5 Stainless steel 316L samples.

For this group (purple) their structure and material are similar, the difference between them relies on the porosity; like the NTU_R value, it is inversely proportional to the heat transfer coefficient but directly proportional to the Reynolds number. When considering only the heat transfer coefficients, the best sample to be used as a regenerator would be the SS316L (1), which has the lowest porosity.

Group 6 Titanium alloy Ti6Al4V samples

This group's (light blue) structure is basically the same as the one used to produce the stainless steel samples, they have similar heat transfer coefficients, the porosity in these samples is slightly higher due to the different manufacturing process. Considering only heat transfer coefficients, the best sample to be used as a regenerator would be the Ti6Al4V (1), having the lowest porosity.

From the chart it can be seen that the pore size and structure type have a large impact on the heat transfer coefficient as it does with the NTU_R value explained in the previous graphs, more so than porosity. The structures that have a high heat transfer coefficient are the wire type structures and the replicated samples; the packed spheres have comparable heat transfer coefficient values to the replicated samples, however they display it at a much higher pressure drop values, which is not desirable for regenerators.

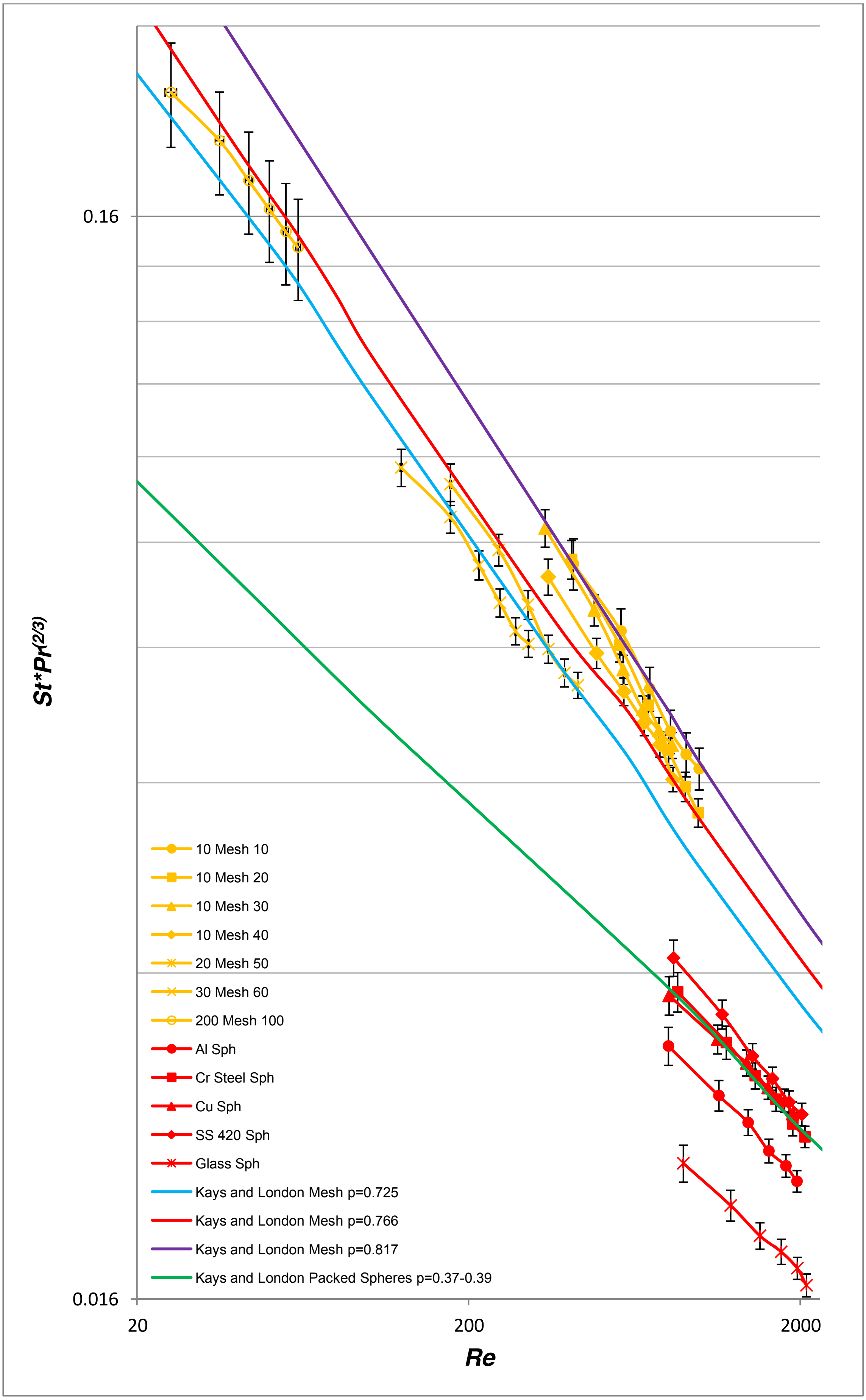

Figure A4a - Re vs. $St^{*} Pr^{2/3}$ for mesh and packed spheres [93].

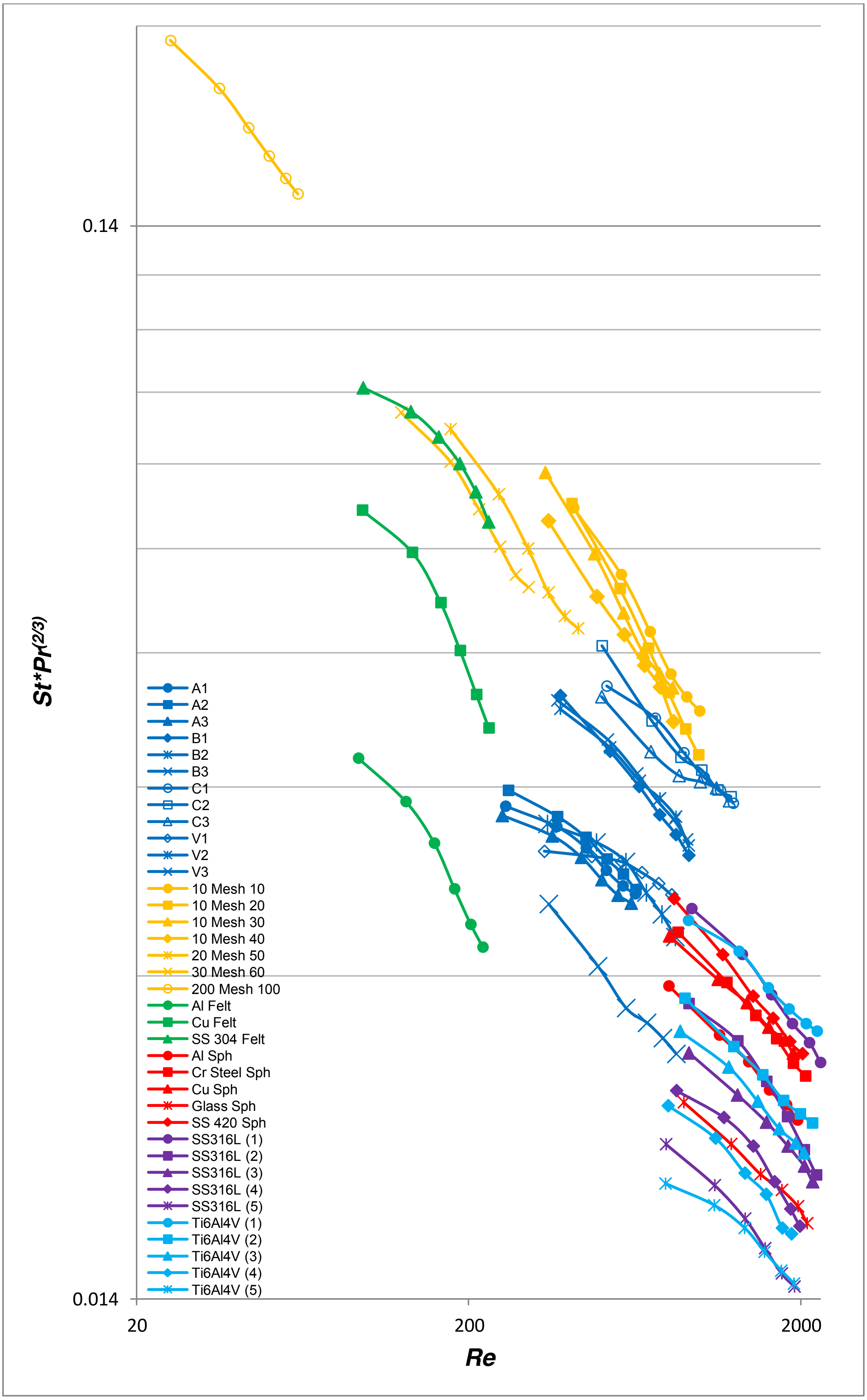

Figure A4b - *Re* vs. $St^{*}\,Pr^{2/3}$ for all samples.

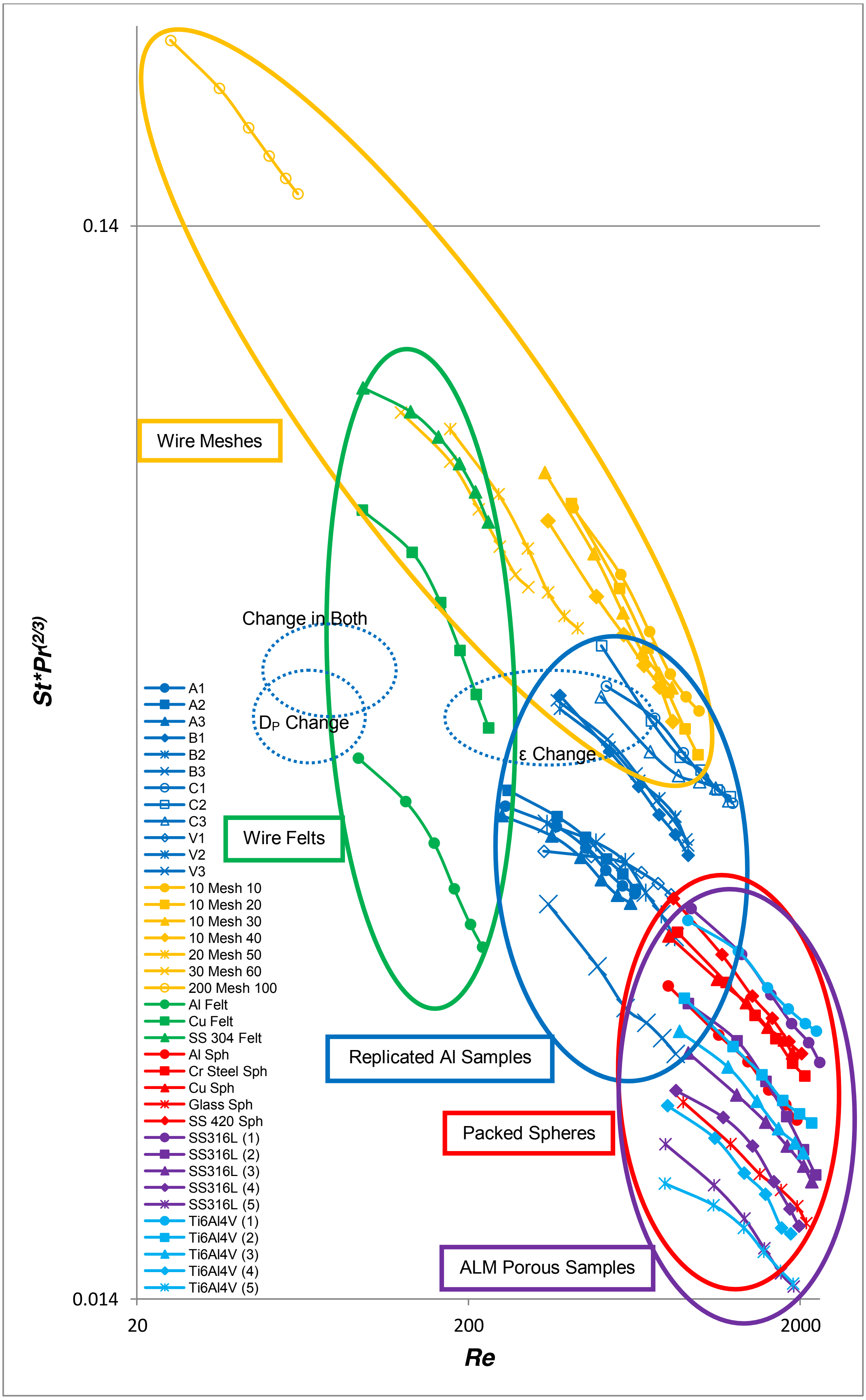

Figure A4c - Behaviour regions of all produced samples.

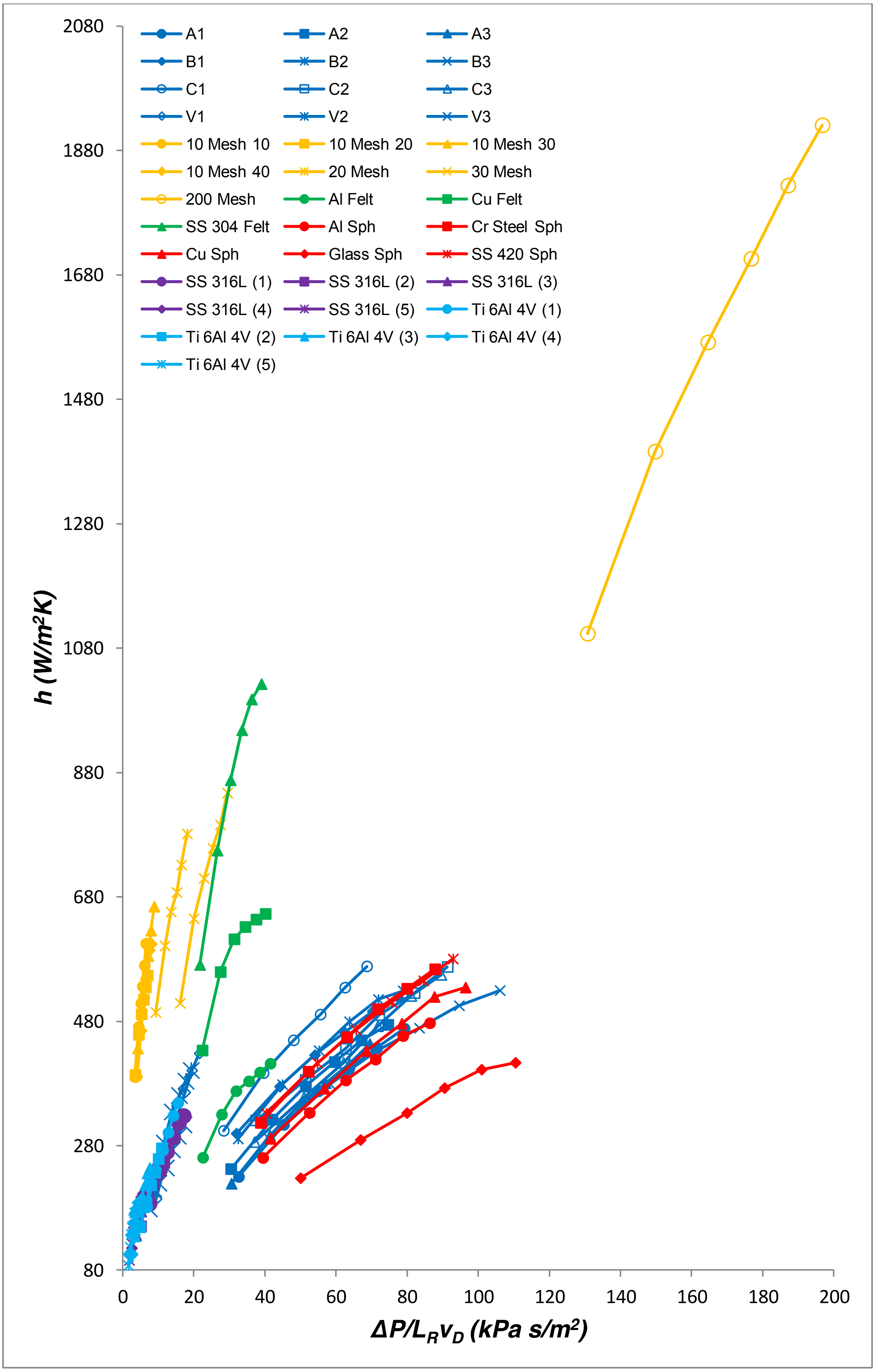

Figure A5 - Linearised pressure drop against heat transfer coefficient of all produced samples.

Figure A4a shows the gas flow through a randomly packed wire mesh layer structure at different porosities and a randomly packed spherical structure at a porosity range between 0.37 and 0.39 from Kays and London, the chart is obtained from experimental data and touching of the layers is considered.

In this chart the wire mesh samples and the packed spheres samples are included. They show a comparable correlation to the data presented by Kays and London [93].

In Figure A4b all the produced samples are present in the chart, clearly showing that every sample group is contained in a certain area.

In Figure A4c the different regions where the samples behave can be seen. The replicated porous metal samples' region falls in between the mesh and packed spheres, this indicates that, depending on the application, the replicated porous metals may be tailored to fit the requirements already presented by these two groups.

As a regenerator the baseline sample is the 200 Mesh, is located in the upper left corner of the graph, indicating a high Stanton number and low Reynolds number. The other wire meshes have a lower Stanton number, which is not desirable, they perform at a relatively high Reynolds number, which is desirable, however, priority is given to the Stanton number. The other wire produced structure, the felts, performed well, one of them, the SS304L felt, can rival the meshes. The other two, of different material characteristics, have lower Stanton numbers, becoming less effective for regeneration.

The packed spheres Reynolds and Stanton values places them on the lower right of the chart close to the additive manufactured samples, they have a relatively low Stanton number and high Reynolds number, qualities that are not desirable for a regenerator, the other way around is preferred, High Stanton number and low Reynolds number.

In Figure A5 the linearised pressure drop against heat transfer coefficient is shown, it can be seen that the baseline regenerator sample (200 Mesh) has a high pressure drop and high heat transfer coefficient as well, ideally the characteristics that would suit a regenerator would be a low pressure drop and a high heat transfer coefficient, the trade off in this case is the pressure drop, even if the process spends energy on passing the fluid through the porous matrix it is preferred over a low ability of heat transfer.

The effectiveness of a regenerator depends on the ability of receiving heat against the energy required to pass the fluid through it; pore size conflicts with the pressure drop, a balance between these two characteristics is needed.

The advantage of the replicated porous metals is that they can be tailored to have the desired characteristics for a regenerator, these are a small pore size, a high porosity, a material with a high density, considerable specific heat value, low thermal conductivity, high heat transfer area; all these leading to a high heat transfer coefficient, it also needs to generate a low pressure drop, however, aluminium is a very limited material for this application, as shown at the end of Chapter 8 while discussing the tentative regions for a replicated aluminium porous sample.

An advantage of the meshes compared to the replicated porous metals is the lack of longitudinal thermal conductivity; as the mesh layers are not bonded together they receive all the heat from the hot air and not the heat that travels by conduction through them, adding a material with low thermal conductivity such as stainless steel to the equation makes for a better regenerator. To counteract this effect, the replicated porous metal, instead of being one piece, could be cut into thin layers with a relatively free space in between, such as the mesh.

Superficial Velocity Parameter	v_D (2.55 *m/s*)	v_D (3.60 *m/s*)	v_D (4.40 *m/s*)	v_D (5.08 *m/s*)	v_D (5.69 *m/s*)	v_D (6.23 *m/s*)
REPLICATED POROUS ALUMINIUM SAMPLES						
A1						
$\Delta P/L_R v_D$ ($kPa\ s/m^2$)	32.62	45.29	55.02	63.57	71.50	79.20
Re	257.97	367.70	451.14	518.49	582.06	634.10
NTU_R	7.00	6.70	6.40	6.10	5.90	5.80
h (W/m^2K)	229.89	313.64	367.58	402.65	437.20	468.21
$St*Pr^{(2/3)}$	0.040	0.039	0.037	0.035	0.034	0.033
A2						
$\Delta P/L_R v_D$ ($kPa\ s/m^2$)	30.45	42.04	51.45	59.60	67.14	74.61
Re	263.04	369.61	450.24	521.01	583.40	636.60
NTU_R	7.30	6.90	6.60	6.30	6.10	5.90
h (W/m^2K)	242.53	322.11	375.32	414.57	449.48	474.39
$St*Pr^{(2/3)}$	0.042	0.039	0.038	0.036	0.035	0.034
A3						
$\Delta P/L_R v_D$ ($kPa\ s/m^2$)	30.57	41.36	49.87	57.04	63.77	69.46
Re	252.04	356.22	436.13	502.64	562.21	615.92
NTU_R	7.00	6.70	6.40	6.10	5.90	5.80
h (W/m^2K)	218.98	296.24	346.46	380.57	411.72	443.41
$St*Pr^{(2/3)}$	0.040	0.038	0.036	0.034	0.033	0.033
B1						
$\Delta P/L_R v_D$ ($kPa\ s/m^2$)	31.96	44.19	54.03	62.45	70.25	77.40
Re	376.99	532.14	651.28	750.78	840.81	919.03
NTU_R	6.20	5.50	5.10	4.80	4.60	4.40
h (W/m^2K)	299.58	375.14	425.73	461.91	495.75	518.31
$St*Pr^{(2/3)}$	0.051	0.045	0.042	0.040	0.038	0.036
B2						
$\Delta P/L_R v_D$ ($kPa\ s/m^2$)	32.43	44.89	55.19	63.75	71.87	78.82
Re	376.78	532.27	654.01	752.32	840.63	918.29
NTU_R	6.30	5.80	5.40	5.20	5.00	4.70
h (W/m^2K)	290.96	378.41	432.90	479.53	515.21	529.03
$St*Pr^{(2/3)}$	0.050	0.046	0.043	0.041	0.039	0.037
B3						
$\Delta P/L_R v_D$ ($kPa\ s/m^2$)	41.33	58.33	71.37	83.42	94.61	106.07
Re	369.07	523.93	642.41	739.43	829.55	907.46
NTU_R	6.20	5.70	5.30	5.00	4.80	4.60
h (W/m^2K)	290.27	378.84	431.91	469.00	505.11	529.53
$St*Pr^{(2/3)}$	0.051	0.047	0.043	0.041	0.039	0.038
C1						
$\Delta P/L_R v_D$ ($kPa\ s/m^2$)	28.38	39.56	48.05	55.59	62.52	68.67
Re	520.56	728.05	888.04	1022.22	1143.38	1251.16
NTU_R	4.50	4.20	3.90	3.70	3.60	3.50
h (W/m^2K)	304.06	396.90	449.55	490.94	534.28	568.41
$St*Pr^{(2/3)}$	0.052	0.049	0.045	0.043	0.042	0.041
C2						
$\Delta P/L_R v_D$ ($kPa\ s/m^2$)	37.44	51.38	62.71	72.09	82.02	91.33
Re	503.79	711.93	869.74	1004.79	1123.98	1231.96
NTU_R	4.70	4.00	3.70	3.60	3.45	3.40
h (W/m^2K)	320.83	385.86	436.04	490.13	525.43	567.56
$St*Pr^{(2/3)}$	0.057	0.048	0.045	0.044	0.042	0.041

C3						
$\Delta P/L_R v_D$ (kPa s/m^2)	37.09	50.93	62.10	71.73	81.11	89.55
Re	502.27	706.29	859.21	995.10	1112.55	1217.87
NTU_R	4.50	4.00	3.80	3.75	3.70	3.60
h (W/m^{2}K)	285.97	357.46	413.11	472.15	520.84	554.73
$St*Pr^{(2/3)}$	0.051	0.045	0.043	0.042	0.042	0.041
V1						
$\Delta P/L_R v_D$ (kPa s/m^2)	9.49	12.73	15.25	17.53	19.48	21.58
Re	337.55	468.67	576.53	664.08	745.64	816.31
NTU_R	4.50	4.45	4.40	4.30	4.20	4.10
h (W/m^{2}K)	194.50	267.06	324.83	365.65	401.01	428.57
$St*Pr^{(2/3)}$	0.037	0.036	0.036	0.035	0.034	0.033
V2						
$\Delta P/L_R v_D$ (kPa s/m^2)	8.63	11.65	13.88	15.90	17.73	19.22
Re	344.62	484.13	593.67	684.25	762.41	836.60
NTU_R	5.10	4.90	4.70	4.40	4.20	4.00
h (W/m^{2}K)	210.67	284.34	334.45	360.87	383.82	401.11
$St*Pr^{(2/3)}$	0.039	0.037	0.036	0.033	0.032	0.030
V3						
$\Delta P/L_R v_D$ (kPa s/m^2)	7.42	10.09	12.19	13.91	15.52	17.15
Re	347.84	489.54	594.95	687.45	767.49	842.69
NTU_R	4.00	3.50	3.20	3.10	3.00	2.90
h (W/m^{2}K)	178.56	219.89	244.33	273.49	295.49	313.62
$St*Pr^{(2/3)}$	0.033	0.029	0.026	0.025	0.025	0.024
WIRE MESH SAMPLES						
10 Mesh 10						
$\Delta P/L_R v_D$ (kPa s/m^2)	3.43	4.45	5.16	5.59	6.16	6.55
Re	413.43	575.34	702.98	811.57	905.31	990.97
NTU_R	1.50	1.30	1.15	1.05	1.00	0.97
h (W/m^{2}K)	390.28	470.71	508.77	536.29	569.74	604.95
$St*Pr^{(2/3)}$	0.076	0.066	0.059	0.054	0.051	0.049
10 Mesh 20						
$\Delta P/L_R v_D$ (kPa s/m^2)	3.55	4.49	5.29	5.90	6.45	6.98
Re	408.44	570.45	695.08	800.99	899.36	983.91
NTU_R	3.00	2.50	2.20	2.00	1.85	1.75
h (W/m^{2}K)	393.84	458.38	491.51	514.91	534.78	553.44
$St*Pr^{(2/3)}$	0.077	0.064	0.057	0.051	0.048	0.045
10 Mesh 30						
$\Delta P/L_R v_D$ (kPa s/m^2)	4.25	5.52	6.40	7.20	7.94	8.84
Re	339.68	477.92	584.26	669.53	749.48	820.93
NTU_R	5.00	4.20	3.70	3.40	3.25	3.15
h (W/m^{2}K)	436.35	515.69	555.38	584.84	625.80	664.36
$St*Pr^{(2/3)}$	0.082	0.069	0.061	0.056	0.054	0.052
10 Mesh 40						
$\Delta P/L_R v_D$ (kPa s/m^2)	4.06	5.22	6.07	6.89	7.53	8.12
Re	346.96	485.79	587.03	676.03	753.84	825.88
NTU_R	6.00	5.10	4.70	4.40	4.20	3.90
h (W/m^{2}K)	390.60	464.86	517.68	558.11	594.06	604.34
$St*Pr^{(2/3)}$	0.074	0.063	0.058	0.055	0.052	0.048
20 Mesh						
$\Delta P/L_R v_D$ (kPa s/m^2)	9.27	11.86	13.58	15.20	16.52	18.13

Re	175.99	246.18	301.66	347.31	388.85	426.49
NTU_R	11.50	10.00	8.90	8.10	7.70	7.50
h (W/m^{2}K)	494.32	601.26	655.73	687.10	731.29	781.25
$St*Pr^{(2/3)}$	0.091	0.079	0.070	0.064	0.061	0.059
30 Mesh						
$\Delta P/L_R v_D$ (kPa s/m^2)	16.13	20.03	22.86	25.33	27.43	29.45
Re	125.04	176.00	214.54	248.25	276.74	302.60
NTU_R	16.00	14.40	13.00	12.00	11.30	11.00
h (W/m^{2}K)	509.14	644.98	709.77	758.10	795.82	847.09
$St*Pr^{(2/3)}$	0.094	0.084	0.076	0.070	0.066	0.064
200 Mesh						
$\Delta P/L_R v_D$ (kPa s/m^2)	130.73	149.75	164.59	176.73	187.11	196.74
Re	25.25	35.40	43.37	50.02	56.10	61.09
NTU_R	82.00	74.00	68.00	64.00	61.00	59.00
h (W/m^{2}K)	1103.22	1395.97	1571.57	1705.86	1823.71	1920.70
$St*Pr^{(2/3)}$	0.208	0.188	0.173	0.163	0.155	0.150
WIRE FELT SAMPLES						
Al Felt						
$\Delta P/L_R v_D$ (kPa s/m^2)	22.55	27.86	31.90	35.48	38.59	41.51
Re	100.00	138.95	169.30	194.72	217.94	236.97
NTU_R	9.00	8.20	7.50	6.80	6.30	6.00
h (W/m^{2}K)	260.69	330.05	367.79	383.55	397.71	411.85
$St*Pr^{(2/3)}$	0.045	0.041	0.037	0.034	0.031	0.030
Cu Felt						
$\Delta P/L_R v_D$ (kPa s/m^2)	22.39	27.49	31.37	34.47	37.55	40.14
Re	102.78	145.32	177.10	202.57	226.84	247.17
NTU_R	15.00	13.70	12.30	11.10	10.10	9.40
h (W/m^{2}K)	433.15	559.33	612.00	631.74	643.68	652.76
$St*Pr^{(2/3)}$	0.076	0.069	0.062	0.056	0.051	0.048
SS 304 Felt						
$\Delta P/L_R v_D$ (kPa s/m^2)	21.72	26.63	30.32	33.55	36.28	39.02
Re	103.26	143.70	174.44	201.81	225.59	246.59
NTU_R	20.00	19.00	18.00	17.00	16.00	15.00
h (W/m^{2}K)	570.70	754.53	867.69	948.08	997.49	1022.18
$St*Pr^{(2/3)}$	0.099	0.094	0.089	0.084	0.079	0.074
PACKED SPHERES SAMPLES						
Al Sph						
$\Delta P/L_R v_D$ (kPa s/m^2)	39.45	52.54	62.73	71.08	78.83	86.36
Re	800.19	1136.30	1391.81	1607.79	1809.99	1954.55
NTU_R	4.00	3.60	3.40	3.20	3.10	3.00
h (W/m^{2}K)	260.37	332.77	384.95	418.53	456.44	476.99
$St*Pr^{(2/3)}$	0.027	0.025	0.023	0.022	0.021	0.021
Cr Steel Sph						
$\Delta P/L_R v_D$ (kPa s/m^2)	38.79	52.25	63.02	71.77	79.94	87.81
Re	852.92	1196.38	1462.37	1689.61	1898.15	2065.75
NTU_R	4.90	4.40	4.10	3.90	3.70	3.60
h (W/m^{2}K)	316.82	399.06	454.52	499.53	532.41	563.76
$St*Pr^{(2/3)}$	0.031	0.028	0.026	0.024	0.023	0.023
Cu Sph						
$\Delta P/L_R v_D$ (kPa s/m^2)	41.52	56.72	68.49	78.47	87.64	96.40
Re	804.01	1126.16	1377.11	1599.08	1792.07	1896.55
NTU_R	4.50	4.10	3.90	3.70	3.60	3.50

h (W/m^{2}K)	291.24	371.67	432.32	476.27	519.32	534.33
$St{*}Pr^{(2/3)}$	0.031	0.028	0.026	0.025	0.024	0.024
Glass Sph						
$\Delta P/L_R v_D$ (kPa s/m^2)	50.01	66.86	79.92	90.49	100.91	110.44
Re	887.69	1232.84	1511.70	1752.44	1959.53	2088.15
NTU_R	3.50	3.20	3.00	2.90	2.80	2.70
h (W/m^{2}K)	227.83	289.30	332.56	372.67	402.34	413.44
$St{*}Pr^{(2/3)}$	0.021	0.020	0.018	0.018	0.017	0.016
SS 420 Sph						
$\Delta P/L_R v_D$ (kPa s/m^2)	40.36	54.73	65.59	75.65	84.59	92.89
Re	829.41	1162.67	1435.44	1648.82	1851.12	2021.54
NTU_R	5.30	4.70	4.30	4.10	3.90	3.80
h (W/m^{2}K)	332.04	412.77	466.23	510.63	545.32	580.25
$St{*}Pr^{(2/3)}$	0.033	0.029	0.027	0.026	0.024	0.024
SELECTIVE LASER MELTING (SLM) SAMPLES						
SS 316L (1)						
$\Delta P/L_R v_D$ (kPa s/m^2)	7.47	10.37	12.39	14.15	15.75	17.10
Re	923.65	1311.62	1606.56	1855.86	2089.25	2256.12
NTU_R	1.60	1.45	1.33	1.25	1.20	1.15
h (W/m^{2}K)	186.72	240.29	269.96	293.10	316.76	327.81
$St{*}Pr^{(2/3)}$	0.029	0.026	0.024	0.023	0.022	0.021
SS 316L (2)						
$\Delta P/L_R v_D$ (kPa s/m^2)	5.10	7.03	8.43	9.63	10.70	11.62
Re	914.42	1282.64	1567.82	1811.44	2035.02	2214.71
NTU_R	1.30	1.20	1.10	1.02	0.95	0.90
h (W/m^{2}K)	150.47	194.82	218.30	233.87	244.71	252.30
$St{*}Pr^{(2/3)}$	0.025	0.023	0.021	0.019	0.018	0.017
SS 316L (3)						
$\Delta P/L_R v_D$ (kPa s/m^2)	3.72	5.15	6.21	7.10	7.89	8.57
Re	919.56	1288.01	1575.02	1828.89	2049.62	2169.12
NTU_R	1.16	1.06	1.00	0.95	0.91	0.88
h (W/m^{2}K)	136.09	174.18	200.94	221.66	237.95	243.52
$St{*}Pr^{(2/3)}$	0.024	0.022	0.020	0.019	0.019	0.018
SS 316L (4)						
$\Delta P/L_R v_D$ (kPa s/m^2)	2.56	3.34	4.08	4.58	5.11	5.60
Re	844.11	1172.32	1437.50	1666.42	1863.34	1985.65
NTU_R	1.07	1.01	0.95	0.88	0.83	0.80
h (W/m^{2}K)	115.29	151.14	174.31	187.18	197.41	202.77
$St{*}Pr^{(2/3)}$	0.022	0.021	0.019	0.018	0.017	0.016
SS 316L (5)						
$\Delta P/L_R v_D$ (kPa s/m^2)	1.84	2.43	2.87	3.26	3.56	3.87
Re	784.77	1100.10	1358.19	1560.09	1751.50	1912.75
NTU_R	0.95	0.87	0.81	0.76	0.72	0.70
h (W/m^{2}K)	95.74	122.91	141.28	152.26	161.94	171.94
$St{*}Pr^{(2/3)}$	0.020	0.018	0.017	0.016	0.015	0.014
ELECTRON BEAM MELTING SAMPLES						
Ti 6Al 4V (1)						
$\Delta P/L_R v_D$ (kPa s/m^2)	6.81	9.26	11.27	12.81	14.22	15.54
Re	920.17	1306.69	1600.52	1848.88	2081.40	2247.64
NTU_R	1.56	1.46	1.35	1.29	1.25	1.23
h (W/m^{2}K)	181.08	240.66	272.57	300.87	328.21	348.75
$St{*}Pr^{(2/3)}$	0.032	0.030	0.027	0.026	0.025	0.025

Ti 6Al 4V (2)						
$\Delta P/L_R v_D$ (kPa s/m^2)	4.89	6.61	7.95	9.03	10.05	10.97
Re	894.75	1255.05	1534.09	1772.47	1991.23	2167.06
NTU_R	1.32	1.19	1.12	1.06	1.03	1.01
h (W/m^{2}K)	148.91	188.31	216.63	236.89	258.59	275.96
$St*Pr^{(2/3)}$	0.027	0.024	0.023	0.021	0.021	0.020
Ti 6Al 4V (3)						
$\Delta P/L_R v_D$ (kPa s/m^2)	3.49	4.51	5.48	6.27	6.93	7.60
Re	865.65	1212.50	1482.69	1721.68	1929.47	2041.96
NTU_R	1.22	1.13	1.05	0.99	0.96	0.94
h (W/m^{2}K)	134.27	174.20	197.94	216.71	235.50	244.04
$St*Pr^{(2/3)}$	0.025	0.023	0.021	0.020	0.020	0.019
Ti 6Al 4V (4)						
$\Delta P/L_R v_D$ (kPa s/m^2)	2.17	2.82	3.39	3.90	4.25	4.69
Re	796.52	1106.22	1356.45	1572.46	1758.28	1873.69
NTU_R	1.04	0.97	0.90	0.86	0.80	0.79
h (W/m^{2}K)	105.38	136.50	155.30	172.02	178.93	188.29
$St*Pr^{(2/3)}$	0.021	0.020	0.018	0.018	0.016	0.016
Ti 6Al 4V (5)						
$\Delta P/L_R v_D$ (kPa s/m^2)	1.61	2.10	2.39	2.72	3.03	3.29
Re	781.64	1095.70	1352.76	1553.86	1744.50	1905.10
NTU_R	0.88	0.84	0.80	0.76	0.73	0.71
h (W/m^{2}K)	87.45	117.02	137.59	150.15	161.91	171.97
$St*Pr^{(2/3)}$	0.018	0.017	0.016	0.015	0.015	0.014

Table A1 - General experimental data for all tested samples.

Appendix 2. Porous Metal Sample Characteristics

#	Sample	Type	Material	c_M (J/kg K)	k_M (W/mK)	k_R (W/mK)
1	**A1**	Replication	Al	900[184]	205.0[190]	26.4
2	**A2**	Replication	Al	900	205.0	25.7
3	**A3**	Replication	Al	900	205.0	18.8
4	**B1**	Replication	Al	900	205.0	27.3
5	**B2**	Replication	Al	900	205.0	28.9
6	**B3**	Replication	Al	900	205.0	28.2
7	**C1**	Replication	Al	900	205.0	25.0
8	**C2**	Replication	Al	900	205.0	24.7
9	**C3**	Replication	Al	900	205.0	26.0
10	**V1**	Replication	Al	900	205.0	19.9
11	**V2**	Replication	Al	900	205.0	16.6
12	**V3**	Replication	Al	900	205.0	20.0
13	***10 Mesh 10***	Mesh	SS304L	500[185]	16.2[185]	< 0.1
14	***10 Mesh 20***	Mesh	SS304L	500	16.2	< 0.1
15	***10 Mesh 30***	Mesh	SS304L	500	16.2	< 0.1
16	***10 Mesh 40***	Mesh	SS304L	500	16.2	< 0.1
17	***20 Mesh***	Mesh	SS304L	500	16.2	< 0.1
18	***30 Mesh***	Mesh	SS304L	500	16.2	< 0.1
19	***200 Mesh***	Mesh	SS304L	500	16.2	< 0.1
20	***Al Felt***	Felt	Al	900	205.0	6.5
21	***Cu Felt***	Felt	Cu	386[184]	385.0[190]	19.4
22	***SS304L Felt***	Felt	SS304L	500	16.2	1.1
23	***Al Sph***	Packed Spheres	Al	900	205.0	< 0.1
24	***Cr Steel Sph***	Packed Spheres	Cr Steel	464[186]	46.6[194]	< 0.1
25	***Cu Sph***	Packed Spheres	Cu	386	386.0	< 0.1
26	***Glass Sph***	Packed Spheres	Soda Glass	990[191]	1.0[191]	< 0.1
27	***SS 420 Sph***	Packed Spheres	SS420	460[187]	24.9[187]	< 0.1
28	***SS316L (1)***	SLM	SS316L	500[188]	16.2[188]	2.4
29	***SS316L (2)***	SLM	SS316L	500	16.2	2.1
30	***SS316L (3)***	SLM	SS316L	500	16.2	1.6
31	***SS316L (4)***	SLM	SS316L	500	16.2	1.3
32	***SS316L (5)***	SLM	SS316L	500	16.2	0.9
33	***Ti6Al4V (1)***	EBM	Ti6Al4V	526[189]	6.7[189]	0.9
34	***Ti6Al4V (2)***	EBM	Ti6Al4V	526	6.7	0.7
35	***Ti6Al4V (3)***	EBM	Ti6Al4V	526	6.7	0.6
36	***Ti6Al4V (4)***	EBM	Ti6Al4V	526	6.7	0.4
37	***Ti6Al4V (5)***	EBM	Ti6Al4V	526	6.7	0.3

#	Sample	ρ (g/cm^3)	m_R (g)	L_R (mm)	D_R (mm)	ε (%)
1	**A1**	2.70[192]	42.22	25.1	51.0	69.6
2	**A2**	2.70	41.71	25.3	50.8	69.9
3	**A3**	2.70	38.02	25.6	50.9	73.0
4	**B1**	2.70	42.53	25.0	50.9	69.0
5	**B2**	2.70	44.03	26.1	50.8	69.2
6	**B3**	2.70	41.29	25.2	50.9	70.2
7	**C1**	2.70	41.66	25.0	51.0	69.7
8	**C2**	2.70	38.79	23.9	51.1	70.8
9	**C3**	2.70	38.95	25.6	50.9	72.2
10	**V1**	2.70	34.10	26.7	50.4	76.3
11	**V2**	2.70	30.96	25.8	50.7	78.0
12	**V3**	2.70	33.89	25.2	50.7	75.3
13	***10 Mesh 10***	8.03[185]	29.00	9.0	51.0	81.0
14	***10 Mesh 20***	8.03	57.33	18.0	51.0	81.0
15	***10 Mesh 30***	8.03	86.09	24.0	51.0	78.0
16	***10 Mesh 40***	8.03	115.32	33.0	51.0	78.0
17	***20 Mesh***	8.03	110.35	26.0	51.0	75.0
18	***30 Mesh***	8.03	115.20	26.0	51.0	73.0
19	***200 Mesh***	8.03	50.49	12.0	51.0	75.0
20	***Al Felt***	2.70	40.21	24.0	51.0	69.0
21	***Cu Felt***	8.96[193]	132.71	24.0	51.0	70.0
22	***SS304 Felt***	8.03	121.83	25.0	51.0	70.0
23	***Al Sph***	2.70	94.40	30.0	51.0	42.0
24	***Cr Steel Sph***	7.81[194]	265.28	27.0	51.0	39.0
25	***Cu Sph***	8.96	311.94	30.0	51.0	43.0
26	***Glass Sph***	2.48[191]	95.05	30.0	51.0	38.0
27	***SS 420 Sph***	7.74[187]	271.42	29.0	51.0	40.0
28	***SS316L (1)***	7.99[188]	134.81	25.6	51.1	61.8
29	***SS316L (2)***	7.99	125.31	25.5	51.0	65.7
30	***SS316L (3)***	7.99	116.41	25.3	50.8	71.5
31	***SS316L (4)***	7.99	93.32	25.3	51.0	77.3
32	***SS316L (5)***	7.99	73.72	25.2	51.0	82.0
33	***Ti6Al4V (1)***	4.43[189]	74.16	25.6	51.5	66.4
34	***Ti6Al4V (2)***	4.43	67.64	25.6	51.3	70.9
35	***Ti6Al4V (3)***	4.43	56.31	25.4	51.0	75.3
36	***Ti6Al4V (4)***	4.43	43.08	25.4	51.2	81.3
37	***Ti6Al4V (5)***	4.43	39.89	25.4	51.0	82.5

#	**Sample**	**K x 10^{-8} (m^2)**	**δK x 10^{-8} (m^2)**	**C x 10^{-3} (m^{-1})**	**δC x 10^{-3} (m^{-1})**	**St*$Pr^{2/3}$ (at 2.55m/s)**	**δSt*$Pr^{2/3}$ (at 2.55m/s)**
1	**A1**	1.4	± 0.4	10	± 1	0.040	± 0.002
2	**A2**	3.8	± 0.3	10	± 1	0.042	± 0.002
3	**A3**	0.48	± 0.03	8.7	± 0.5	0.040	± 0.002
4	**B1**	2.8	± 0.1	10.1	± 0.5	0.051	± 0.002
5	**B2**	3.7	± 0.2	10	± 1	0.050	± 0.002
6	**B3**	0.7	± 0.2	14	± 1	0.051	± 0.002
7	**C1**	1.7	± 0.3	8.9	± 0.4	0.052	± 0.002
8	**C2**	2.8	± 0.2	12	± 1	0.057	± 0.002
9	**C3**	1.26	± 0.04	12	± 1	0.051	± 0.002
10	**V1**	1.8	± 0.1	2.7	± 0.1	0.037	± 0.001
11	**V2**	1.50	± 0.04	2.4	± 0.1	0.039	± 0.002
12	**V3**	2.5	± 0.2	2.2	± 0.1	0.033	± 0.001
13	***10 Mesh 10***	1.5	± 0.1	0.7	± 0.1	0.076	± 0.004
14	***10 Mesh 20***	1.67	± 0.04	0.79	± 0.05	0.077	± 0.003
15	***10 Mesh 30***	1.5	± 0.1	1.0	± 0.1	0.082	± 0.003
16	***10 Mesh 40***	1.52	± 0.02	0.94	± 0.03	0.074	± 0.003
17	***20 Mesh***	0.53	± 0.01	1.9	± 0.1	0.091	± 0.004
18	***30 Mesh***	0.266	± 0.002	3.0	± 0.1	0.094	± 0.004
19	***200 Mesh***	0.0216	± 0.0001	15	± 1	0.21	± 0.02
20	***Al Felt***	0.190	± 0.001	4.3	± 0.1	0.045	± 0.002
21	***Cu Felt***	0.182	± 0.001	4.1	± 0.1	0.076	± 0.003
22	***SS304 Felt***	0.190	± 0.001	4.0	± 0.1	0.099	± 0.004
23	***Al Sph***	0.27	± 0.01	11	± 1	0.027	± 0.001
24	***Cr Steel Sph***	0.42	± 0.02	10.4	± 0.4	0.031	± 0.001
25	***Cu Sph***	0.52	± 0.03	12.6	± 0.4	0.031	± 0.001
26	***Glass Sph***	0.22	± 0.01	13.8	± 0.5	0.021	± 0.001
27	***SS 420 Sph***	0.48	± 0.03	12.0	± 0.4	0.033	± 0.001
28	***SS316L (1)***	2.0	± 0.1	2.2	± 0.1	0.032	± 0.001
29	***SS316L (2)***	2.7	± 0.1	1.47	± 0.05	0.026	± 0.001
30	***SS316L (3)***	3.7	± 0.2	1.08	± 0.05	0.024	± 0.001
31	***SS316L (4)***	3.9	± 0.2	0.68	± 0.04	0.022	± 0.001
32	***SS316L (5)***	3.8	± 0.1	0.45	± 0.03	0.020	± 0.001
33	***Ti6Al4V (1)***	2.0	± 0.1	1.96	± 0.05	0.032	± 0.001
34	***Ti6Al4V (2)***	2.6	± 0.1	1.37	± 0.03	0.027	± 0.001
35	***Ti6Al4V (3)***	3.1	± 0.2	0.9	± 0.1	0.025	± 0.001
36	***Ti6Al4V (4)***	3.7	± 0.2	0.55	± 0.04	0.021	± 0.001
37	***Ti6Al4V (5)***	3.8	± 0.1	0.42	± 0.03	0.018	± 0.001

Appendix 3. Uncertainty Analysis

To obtain the uncertainty values for permeability (K), form drag (C) and Stanton number (St) given in Appendix 2 the uncertainties provided by the equipment manufacturers and the uncertainties from each of the variables present in the parameter calculations were considered, calculating them using the root sum squares method explained by Taylor [183].

For the mass flow rate:

$\sqrt{2\rho\Delta P}$:
$$\frac{\delta_{\sqrt{2\rho\Delta P}}}{\sqrt{2\rho\Delta P}}=\frac{1}{2}\sqrt{\left(\frac{\delta_{\rho}}{\rho}\right)^{2}+\left(\frac{\delta_{\Delta P}}{\Delta P}\right)^{2}} \qquad \text{Eq. A3a}$$

A_{CS}:
$$\frac{\delta_{A_{CS}}}{A_{CS}}=2\frac{\delta_{D_R}}{D_R} \qquad \text{Eq. A3b}$$

C_d:
$$0.632\pm0.5\%=0.632\pm\frac{0.5}{100}\rightarrow\delta_{C_d}=\frac{0.5}{100} \qquad \text{Eq. A3c}$$

$\dot{m}$:
$$\frac{\delta_{\dot{m}}}{\dot{m}}=\sqrt{\left(\frac{0.5}{100}\right)^{2}+\left(2\frac{\delta_{D_R}}{D_R}\right)^{2}+\frac{1}{2}\sqrt{\left(\frac{\delta_{\rho}}{\rho}\right)^{2}+\left(\frac{\delta_{\Delta P}}{\Delta P}\right)^{2}}} \qquad \text{Eq. A3d}$$

For the replicated and ALM porous metals:

V_R:
$$\frac{\delta_{V_R}}{V_R}=\sqrt{\left(\frac{\delta_{A_{CS}}}{A_{CS}}\right)^{2}+\left(\frac{\delta_{L_R}}{L_R}\right)^{2}} \qquad \text{Eq. A3e}$$

m_M:
$$\frac{\delta_{m_M}}{m_M}=\frac{\delta_{V_R}}{V_R} \qquad \text{Eq. A3f}$$

ε:
$$\frac{\delta_{\varepsilon}}{\varepsilon}=\sqrt{\left(\frac{\delta_{m_R}}{m_R}\right)^{2}+\left(\frac{\delta_{m_M}}{m_M}\right)^{2}} \qquad \text{Eq. A3g}$$

A_{Sp}:

$$\frac{\delta_{A_{Sp}}}{A_{Sp}} = \sqrt{\left(\frac{\delta_{\varepsilon}}{\varepsilon}\right)^2 + \left(\frac{\delta_{L_C}}{L_C}\right)^2}$$

Eq. A3h

A_{HT}:

$$\frac{\delta_{A_{HT}}}{A_{HT}} = \sqrt{\left(\frac{\delta_{V_R}}{V_R}\right)^2 + \left(\frac{\delta_{A_{Sp}}}{A_{Sp}}\right)^2}$$

Eq. A3i

Re:

$$\frac{\delta_{Re}}{Re} = \sqrt{\left(\frac{\delta_{\dot{m}}}{\dot{m}}\right)^2 + \left(\frac{\delta_{L_C}}{L_C}\right)^2 + \left(\frac{\delta_{\varepsilon}}{\varepsilon}\right)^2 + \left(\frac{\delta_{A_{CS}}}{A_{CS}}\right)^2}$$

Eq. A3j

v_D:

$$\frac{\delta_{v_D}}{v_D} = \frac{\delta_{\dot{m}}}{\dot{m}}$$

Eq. A3k

$\frac{\Delta P}{L_R v_D}$:

$$\frac{\delta_{\frac{\Delta P}{L_R v_D}}}{\frac{\Delta P}{L_R v_D}} = \sqrt{\left(\frac{\delta_{\Delta P}}{\Delta P}\right)^2 + \left(\frac{\delta_{L_R}}{L_R}\right)^2 + \left(\frac{\delta_{v_D}}{v_D}\right)^2}$$

Eq. A3l

NTU:

$$\frac{\delta_{NTU}}{NTU} = \sqrt{\left(\frac{\delta_{m_R}}{m_R}\right)^2 + \left(\frac{\delta_{A_{CS}}}{A_{CS}}\right)^2 + \left(\frac{\delta_{\dot{m}}}{\dot{m}}\right)^2 + \left(\frac{\delta_{L_R}}{L_R}\right)^2 + \left(\frac{\delta_{k_R}}{k_R}\right)^2}$$

Eq. A3m

h:

$$\frac{\delta_h}{h} = \sqrt{\left(\frac{\delta_{\dot{m}}}{\dot{m}}\right)^2 + \left(\frac{\delta_{A_{HT}}}{A_{HT}}\right)^2 + \left(\frac{\delta_{NTU}}{NTU}\right)^2}$$

Eq. A3n

St:

$$\frac{\delta_{St}}{St} = \sqrt{\left(\frac{\delta_h}{h}\right)^2 + \left(\frac{\delta_{A_{CS}}}{A_{CS}}\right)^2 + \left(\frac{\delta_{\varepsilon}}{\varepsilon}\right)^2 + \left(\frac{\delta_{\dot{m}}}{\dot{m}}\right)^2}$$

Eq. A3o

For the wire meshes and wire felts several of the equations used are the same as for the replicated and ALM porous metals, they will not be repeated. The new equations are:

A_{HT}: $$\delta_{A_{HT}} = \sqrt{\left(\delta_{V_R}\right)^2 + \left[\left(\frac{4}{D_W}\right)\varepsilon V_R \sqrt{\left(\frac{\delta_\varepsilon}{\varepsilon}\right)^2 + \left(\frac{\delta_{V_R}}{V_R}\right)^2}\right]^2}$$ Eq. A3p

D_H: $$\frac{\delta_{D_H}}{D_H} = \sqrt{\left(\frac{\delta_\varepsilon}{\varepsilon}\right)^2 + \left[\frac{\delta_\varepsilon}{\Phi(1-\varepsilon)}\right]^2}$$ Eq. A3q

Re: $$\frac{\delta_{Re}}{Re} = \sqrt{\left(\frac{\delta_{\dot{\mathrm{m}}}}{\dot{\mathrm{m}}}\right)^2 + \left(\frac{\delta_{D_H}}{D_H}\right)^2 + \left(\frac{\delta_{A_{CS}}}{A_{CS}}\right)^2}$$ Eq. A3r

For the packed spheres:

A_{HT}: $$\frac{\delta_{A_{HT}}}{A_{HT}} = 2\frac{\delta_{D_{Sph}}}{D_{Sph}}$$ Eq. A3s

To calculate the uncertainty values for the permeability (*K*) and the form drag (*C*) from the curve fitting derived from the pressure drop and superficial velocity values, the linearised form of the Darcy-Forchheimer equation is used (Eq. 4.7):

$$\frac{\Delta P}{L_R v_D} = a + b v_D$$ Eq. A3t

where *a* and *b* are the constant values obtained from the fitted curve, having the form of the least squares fitting equation:

$$y = a + bx$$ Eq. A3u

the uncertainties for *K* and *C* are calculated from:

$$K = \frac{\mu}{a} \quad and \quad C = \frac{b}{\rho} \qquad \text{Eq. A3v}$$

assuming zero uncertainty for the dynamic viscosity and density:

$$\frac{\delta_K}{K} = \frac{\delta_a}{a} \quad and \quad \frac{\delta_C}{C} = \frac{\delta_b}{b} \qquad \text{Eq. A3w}$$

$$a = \frac{\sum x^2 \sum y - \sum x \sum xy}{\Delta} \qquad \text{Eq. A3x}$$

$$b = \frac{N \sum xy - \sum x \sum y}{\Delta} \qquad \text{Eq. A3y}$$

$$\Delta = N \sum x^2 - \left(\sum x\right)^2 \qquad \text{Eq. A3z}$$

$$\delta y = \sqrt{\frac{1}{N-2} \sum_{i=1}^{N} (y_i - a - bx_i)^2} \qquad \text{Eq. A3aa}$$

$$\delta a = \delta y \sqrt{\frac{\sum x^2}{\Delta}} \qquad \text{Eq. A3ab}$$

$$\delta b = \delta y \sqrt{\frac{N}{\Delta}} \qquad \text{Eq. A3ac}$$

References

[1] L. Polonsky, S. Lipson and H. Markus, "Lightweight cellular metal", *Modern Castings*, vol. 39, pp. 57-71, 1961.

[2] J. Banhart, "Manufacture, characterisation and application of cellular metals and metal foams", *Progress in Materials Science*, vol. 46, pp. 559-632, 2000.

[3] Y. Conde, J-F. Despois, R. Goodall, A. Marmottant, L. Salvo, C. San Marchi and A. Mortensen, "Replication processing of highly porous materials", *Advanced Engineering Materials*, vol. 8, no. 9, pp. 795-803, 2006.

[4] R. Goodall and A. Mortensen, "Chapter 24 - Porous Metals", in *Physical Metallurgy*, 5th ed., D.E. Laughlin and K. Hono Eds., Oxford: Elsevier, 2014, pp. 2399-2595.

[5] C. San Marchi and A. Mortensen, "Chapter 2.6 - Infiltration and the Replication Process for Producing Metal Sponges", in *Handbook of Cellular Metals - Production, Processing, Applications*, H.P. Degischer and B. Kriszt Eds., Weinheim: Wiley-VCH, 2002, pp. 44-56.

[6] C. Galliard, J-F. Despois and A. Mortensen, "Processing of NaCl powders of controlled size and shape for the microstructural tailoring of aluminium foams", *Materials Science and Engineering A*, vol. 374, no. 1 and 2, pp. 250-262, 2004.

[7] J-F. Despois and A. Mortensen, "Permeability of open-pore microcellular materials", *Acta Materialia*, vol. 53, no. 5, pp. 1381-1388, 2005.

[8] R. Goodall, J-F. Despois, A. Marmottant, L. Salvo and A. Mortensen, "The effect of preform processing on replicated aluminium foam structure and mechanical properties", *Scripta Materialia*, vol. 54, no. 12, pp. 2069-2073, 2006.

[9] R. Goodall, A. Marmottant, L. Salvo and A. Mortensen, "Spherical pore replicated microcellular aluminium: Processing and influence on properties", *Materials Science and Engineering A*, vol. 465, no. 1 and 2, pp. 124-135, 2007.

[10] J-F. Despois, A. Marmottant, L. Salvo and A. Mortensen, "Influence of the infiltration pressure on the structure and properties of replicated aluminium foams", *Materials Science and Engineering A*, vol. 462, pp. 68-75, 2007.

[11] C. San Marchi, J-F. Despois and A. Mortensen, "Uniaxial deformation of open-cell aluminium foam: the role of internal damage", *Acta Materialia*, vol. 52, no. 10, pp. 2895-2902, 2004.

[12] R. Goodall, L. Weber and A. Mortensen, "The electrical conductivity of microcellular metals", *Journal of Applied Physics*, vol. 100, no. 4, pp. 044912-1 - 044912-7, 2006.

[13] C. Kadar, F. Chmelik, J. Kendvai, G. Voros and Z. Rajkovits, "Acoustic emission of metal foams during tension", *Materials Science and Engineering A*, vol. 462, no. 1 and 2, pp. 316-319, 2007.

[14] R. Goodall and A. Mortensen, "Microcellular aluminium? - Child's play!", *Advanced Engineering Materials*, vol. 9, no. 11, pp. 951-954, 2007.

[15] J.D. DeFouw and D.C. Dunand, "Processing and compressive creep of cast replicated IN792 Ni-base superalloy foams", *Materials Science & Engineering A*. vol. 558, pp. 129-133, 2012.

[16] A.J. Organ, *The Regenerator and the Stirling Engine*. London: Mechanical Engineering Publications Limited, 1997, pp. 1-26.

[17] G. Walker, *Stirling Engines*. New York: Oxford University Press, 1980, pp. 1-10.

[18] R. Goodall, "Chapter 10 - Porous Metals: Foams and Sponges", in I.T. Chang and Y.Y. Zhao eds. *Advances in powder metallurgy: Properties, processing and applications*, Cambridge: Woodhead Publishing Limited, 2013, pp. 273-307.

[19] G. Walker, *Stirling Engines*. New York: Oxford University Press, 1980, pp. 124 - 159.

[20] H.J. McQueen, "Successful transition from wrought iron to steel in hot work processing with mechanism differences", *Materials Science Forum*, vol. 638-642, pp. 3380-3387, 2010.

[21] M.F. Ashby, A.G. Evans, N.A. Fleck, L.J. Gibson, J.W. Hutchinson and H.N.G. Wadley, *Metal Foams: A Design Guide*, Boston: Butterworth-Heinemann, 2000, pp. 1-39.

[22] A. Czyzewski. (2011, August 1). *Nature inspires new methods of making porous materials* [Online]. Available: http://www.theengineer.co.uk/civil/news/nature-inspires-new-methods-of-making-porous-materials/1009543.article.

[23] J. Rouquerol, D. Anvir, C.W. Fairbridge, D.H. Everett, J.H. Haynes, N. Pernicone, J.D.F. Ramsay, K.S.W. Sing and K.K. Unger, “Recommendations for the characterization of porous solids”, *Pure & Applied Chemistry*, vol. 66, no. 8, pp. 1739-1758, 1994.

[24] P. Liu, B. Yu, A. Hu, K. Liang and S. Gu, “Development in applications of porous metals”, *Trans. Nonferrous Met. Soc. China*, vol. 11, no. 5, pp. 629-638, 2001.

[25] 3M Inc. (2012). *3M Micropore Surgical Tape Applications*. [Online]. Available:https://solutions.3m.com/wps/portal/3M/en_EU/Healthcare-Europe/EU-Home/Products/ProductCatalogue/?PC_Z7_RJH9U52300PI40IA1Q602S28E7000000_nid=34DDVZ1Q1ZbeP7FT9L23G3gl.

[26] Z.A. ALOthman, “A review: Fundamental aspects of silicate mesoporous materials”, *MDPI Materials*, vol. 5, no. 12, pp. 2874-2902, 2012.

[27] R.D. Arrua, M.C. Strumia and C.I. Alvarez-Igarzabal, "Macroporous monolithic polymers: Preparation and applications", *MDPI Materials*, vol. 2, no. 4, pp. 2429-2466, 2009.

[28] Y.Y. Zhao and D.X. Sun, "A novel sintering-dissolution process for manufacturing Al foams", *Scripta Mater.*, vol. 44, pp. 105-110, 2001.

[29] E. Arzt, "The influence of an increasing particle coordination on the densification of spherical powders", *Acta Metallurgica*, vol. 30, no. 10, pp. 1883-1890, 1982.

[30] R. Higginson and M. Sellars, *Worked Examples in Quantitative Metallography*, 6th ed., London: Maney, 2003.

[31] N. Tuncer, G. Arslan, E. Maire and L. Salvo, "Investigation of spacer size effect on architecture and mechanical properties of porous titanium", *Materials Science and Engineering: A*, vol. 530, pp. 633-642, 2011.

[32] T. Miyoshi, M. Itoh, S. Akiyama and A. Kitahara, "Aluminium Foam, "ALPORAS": The Production Process, Properties and Applications", in D.S. Schwarz, D.S. Shih, A.G. Evans and H.N.G. Wadley eds. *Porous and Cellular Materials for Structural Applications*, MRS Symposium Proceedings Vol. 521, 1998, pp. 133-138.

[33] P. Asholt, "Aluminium foam produced by the melt foaming route process, properties and applications", in J. Banhart, M.F. Ashby and N.A. Fleck eds. *Proc. of Int Conf. on Metal foam and porous metal structures*, Bremen, Germany, 1999, pp. 133-140.

[34] Kenny L.D., *Materials science forum*, vol. 217-222. Switzerland: Transtec Publications, 1996.

[35] K. Naplocha and K. Granat, "The structure and properties of hybrid preforms for composites", *JAMME*, vol. 22, no. 2, pp. 35-38, 2007.

[36] S. Pratapa, K. Umaroh and F.E. Herdiyanti, "Synthesis of rutile-rich corundum/rutile functionally-graded materials with different precursors", *Indonesian Journal of Physics*, vol. 22, no. 2, pp. 81-84, 2011.

[37] Y.J. Lin and L.B. Chang, "Alumina/glass composites fabricated by melt-infiltration of glass into porous alumina", *Key Engineering Materials*, Vol. 313, pp. 129-138, 2006.

[38] D.L. Goodstein, W.D. McCormick and J.G. Dash, "Sintered copper sponges for use at low temperature", *Cryogenics*, vol. 6, no. 3, pp. 167-168, 1966.

[39] I-H. Oh, N. Nomura, N. Masahashi and S. Hanada, "Mechanical properties of porous titanium compacts prepared by powder sintering". *Scripta Mater.*, vol. 49, no. 12, pp. 1197-1202, 2003.

[40] A. Arockiasamy, S.J. Park and R.M. German, "Viscoelastic behaviour of porous sintered steels compact". *Powder Metall.*, vol. 53, no. 2, pp. 107-111, 2010.

[41] M. Thieme, K.-P. Wieters, F. Bergner, D. Scharnweber, H. Worch, J. Ndop, T.J. Kim and W. Grill, "Titanium powder sintering for preparation of a porous functionally graded material destined for orthopaedic implants", *Journal of Materials Science: Materials in Medicine*, vol. 12, pp. 225-231, 2001.

[42] J.S. Hirschhorn, *Introduction to Powder Metallurgy*. New York: The Colonial Press Inc., 1969, pp. 96-154.

[43] M. Kobashi and N. Kanetake, "Processing of intermetallic foam by combustion reaction". *Adv. Eng. Mat.*, vol. 4, no. 10, pp. 745-747, 2002.

[44] F. Thümmler and W. Thomma, "The sintering process", *Metallurgical Reviews*, vol. 12, no. 1, pp.69-108, 1967.

[45] L.K. Barrett and C.S. Yust, "Progressive shape changes of the void during sintering", *Transactions of AIME*, vol. 239, pp. 1172-1180, 1967.

[46] H.H. Hausner, "Basic studies in linear shrinkage behavior during sintering", *Progress in Powder Metallurgy*, vol. 19, pp. 67-85, 1963.

[47] W.D. Jones, *Fundamental Principles of Powder Metallurgy*, London: Edward Arnold Publishers Ltd., 1960, Chapters IV and V.

[48] A. Laptev, M. Bram, H.P. Buchkremer and D. Stöver, "Study of production route for titanium parts combining very high porosity and complex shapes", *Powder Metall.*, vol. 47, no. 1, pp. 85-92, 2004.

[49] Y.Y. Zhao, "Stochastic modelling of removability of NaCl in sintering and dissolution process to produce Al foams", *Journal of Porous Materials*, vol. 10, pp. 105-111, 2003.

[50] Y.Y. Zhao, F. Han and T. Fung, "Optimisation of compaction and liquid-state sintering in sintering and dissolution process for manufacturing Al foams", *Mat. Sci. Eng. A*, vol. 364, no. 1 and 2, pp. 117-125, 2004.

[51] D.C. Dunand, "Processing of titanium foams", *Adv. Eng. Mat.*, vol. 6, no. 6, pp. 369-376, 2004.

[52] H.I. Bakan, "A novel water leaching and sintering process for manufacturing highly porous stainless steel", *Scripta Mater.*, vol. 55, pp. 203-206, 2006.

[53] I. Mutlu and E. Oktay, "Production and characterisation of Cr-Si-Ni-Mo steel foams", *Indian Journal of Engineering & Materials Sciences*, vol. 18, no. 3, pp. 227-232, 2011.

[54] B. Arifvianto and J. Zhou, "Fabrication of metallic biomedical scaffolds with the space holder method: A review", *MDPI Materials*, vol. 7, no. 5, pp. 3588-3622, 2014.

[55] B. Ye and D.C. Dunand, "Titanium foams produced by solid-state replication of NaCl powders", *Materials Science and Engineering A*, vol. 528, no. 2, pp. 691-697, 2010.

[56] Z. Esen and S. Bor, "Processing of titanium foams using magnesium spacer particles", *Scripta Mater.*, vol. 56, pp. 341-344, 2007.

[57] H.Ö. Gülsoy and R.M. German, "Sintered foams from precipitation hardened stainless steel powder". *Powder Metall.*, vol. 51, no. 4, pp. 350-353, 2008.

[58] M. Hakamada, Y. Asao, T. Kuromura, Y. Chen, H. Kusuda and M. Mabuchi, "Density dependence of the compressive properties of porous copper over a wide density range", *Acta Materialia*, vol. 55, no. 7, pp. 2291-2299, 2007.

[59] B. Jiang, N.Q. Zhao, C.S. Shi, X.W. Du, J.J. Li and H.C. Man, "A novel method for making open cell aluminium foams by powder sintering process", *Materials Letters*, vol. 59, no. 26, pp. 3333-3336, 2005.

[60] C.E. Wen, Y. Yamada, K. Shimojima, Y. Chino, H. Hosokawa and M. Mabuchi, "Compressibility of porous magnesium foam: dependency on porosity and pore size", *Materials Letters*, vol. 58, no. 3 and 4, pp. 357-360, 2004.

[61] B. Jiang, N.Q. Zhao, C.S. Shi and J.J. Li, "Processing of open cell aluminium foams with tailored porous morphology", *Scripta Materialia*, vol. 53, no. 6, pp. 781-785, 2005.

[62] Y.Y. Zhao, T. Fung, L.P. Zhang and F.L. Zhang, "Lost carbonate sintering process for manufacturing metal foams", *Scripta Materialia*, vol. 52, no. 4, pp. 295-298, 2005.

[63] X. Ma, A.J. Peyton and Y.Y. Zhao, "Eddy current measurements of electrical conductivity and magnetic permeability of porous metals", *NDT & E International*, vol. 39, no. 7, pp. 562-568, 2006.

[64] B. Yuan, C.Y. Chung and M. Zhu, "Microstructure and Martensitic Transformation Behaviour of Porous NiTi Shape Memory Alloy Prepared by Hot Isostatic Pressing Processing", *Mat. Sci. Eng. A*, vol. 382, no. 1 and 2, pp. 181-187, 2004.

[65] X. Zhao, H. Sun, L. Lan, J. Huang, H. Zhang and Y. Wang, "Pore structures of high-porosity NiTi alloys made from elemental powders with NaCl temporary space-holders", *Materials Letters*, vol. 63, no. 28, pp. 2402-2404, 2009.

[66] J.A. Scott and D.C. Dunand, "Processing and mechanical properties of porous Fe-26Cr-1Mo for solid oxide fuel cell interconnects", *Acta Materialia*, vol. 58, no. 18, pp. 6125-6133, 2010.

[67] Z.S. Rak and J. Walter, "Porous Titanium Foil by Tape Casting Technique", *J. Mater. Proc. Tech.*, vol. 175, no. 1 to 3, pp. 358-363, 2006.

[68] S. Guo, B. Duan, X. He and X. Qu, "Powder injection molding of pure titanium", *Rare Metals*, vol. 28, no. 3, pp. 261-265, 2009.

[69] G. Engin, B. Aydemir and H.Ö. Gülsoy, "Injection molding of micro-porous titanium alloy with space holder technique", *Rare Metals*, vol. 30, no. 6, pp. 565-571, 2011.

[70] A. Manonukul, N. Muenya, F. Léaux and S. Amaranan, "Effects of replacing metal powder with powder space holder on metal foam produced by metal injection moulding", *Journal of Materials Processing Technology*, vol. 210, pp. 529-535, 2010.

[71] Y. Chino and D.C. Dunand, "Directionally freeze-cast titanium foam with aligned, elongated pores", *Acta Materialia*, vol. 56, no. 1, pp. 105-113, 2008.

[72] D. Driscoll, A.J. Weisenstein and S.W. Sofie, "Electrical and flexural anisotropy in freeze tape cast stainless steel porous substrates", *Materials Letters*, vol. 65, no. 23 and 24, pp. 3433-3435, 2011.

[73] D.C. Dunand and J. Teisen, "Superplastic foaming of titanium and Ti-6Al-4V", in D.S. Schwarz, D.S. Shih, A.G. Evans and H.N.G. Wadley eds. *Porous and Cellular Materials for Structural Applications*, MRS Symposium Proceedings Vol. 521, San Francisco, CA, USA, 1998, pp. 231-236.

[74] S.M. Oppenheimer, J.G. O'Dwyer and D.C. Dunand, "Porous, superelastic NiTi produced by powder metallurgy", *TMS Letters*, vol. 1, no. 5, pp. 93-94, 2004.

[75] N.G. Davis, J. Teisen, C. Schuh and D.C. Dunand, "Solid-state foaming of titanium by superplastic expansion of argon-filled pores", *J. Mater. Res.*, vol. 16, no. 5, pp. 1508-1519, 2001.

[76] N.G.D. Murray and D.C. Dunand, "Microstructure evolution during solid-state foaming of titanium", *Comp. Sci. Tech.*, vol. 63, no. 16, pp. 2311-2316, 2003.

[77] D.K. Pattanayak, A. Fukuda, T. Matsushita, M. Takemoto, S. Fujibayashi, K. Sasaki, N. Nishida, T. Nakamura and T. Kokubo, "Bioactive Ti metal analogous to human cancellous bone: Fabrication by selective laser melting and chemical treatments", *Acta Biomaterialia*, vol. 7, no. 3, pp. 1398-1406, 2011.

[78] S.J. Li, L.E. Murr, X.Y. Cheng, Z.B. Zhang, Y.L. Hao, R. Yang, F. Medina and R.B. Wicker, "Compression fatigue behavior of Ti-6Al-4V mesh arrays fabricated by electron beam melting", *Acta Materialia*, vol. 60, no. 3, pp. 793-802, 2012.

[79] L.E. Murr, K.N. Amato, S.J. Li, Y.X. Tian, X.Y. Cheng, S.M. Gaytan, E. Martinez, P.W. Shindo, F. Medina and R.B. Wicker, "Microstructure and mechanical properties of open-cellular biomaterials prototypes for total knee replacement implants fabricated by electron beam melting", *Journal of the Mechanical Behaviour of Biomedical Materials*, vol. 4, pp. 1396-1411, 2011.

[80] D.A. Ramirez, L.E. Murr, S.J. Li, Y.X. Tian, E. Martinez, J.L. Martinez, B.I. Machado, S.M. Gaytan, F. Medina and R.B. Wicker, "Open-cellular copper structures fabricated by additive manufacturing using electron beam melting", *Materials Science and Engineering A*, vol. 528, no. 16 and 17, pp. 5379-5386, 2011.

[81] Y.Q. Fu, Y.W. Gu, C. Shearwood, J.K. Luo, A.J. Flewitt and W.I. Milne, "Spark plasma sintering of TiNi nano-powders for biological application", *Nanotechnology*, vol. 17, no. 21, pp. 5293-5298, 2006.

[82] A. Jinnapat and A. Kennedy, "Characterisation and mechanical testing of open cell Al foams manufactured by molten metal infiltration of porous salt bead preforms: Effect of bead size", *MDPI Metals*, vol. 2, no. 2, pp.122-135, 2012.

[83] M.A. Marletta, *The Merck Index. An encyclopedia of chemicals, drugs and biologicals*. 10th ed. Rahway, New Jersey: Merck Co. Inc., 1983., p. 1229.

[84] Ohio University. (2010). *Stirling Engine Alpha Configuration Image* [Online]. Available: http://www.ohio.edu/mechanical/stirling/engines/alpha.gif.

[85] Y. Timoumi, I. Tlili and S.B. Nasrallah, "Performance optimization of Stirling engines", *Renewable Energy*, vol. 33, no. 9, pp. 2134-2144, 2008.

[86] D.G. Thombare and S.K. Verma, "Technological development in the Stirling cycle engines", *Renewable Sustainable Energy Rev.*, vol. 12, no. 1, pp. 1-38, 2008.

[87] A.J. Organ, *The Regenerator and the Stirling Engine*. London: Mechanical Engineering Publications Limited, 1997, pp. 553 - 589.

[88] MSI News. (2008). *Air Power Cooler Image* [Online]. Available: http://www.msi.com/news/591.html.

[89] American Stirling Company. (2000). *Stirling Engine Operation Image* [Online]. Available: http://www.stirlingengine.com/faq.

[90] A.J. Organ, *The Regenerator and the Stirling Engine*. London: Mechanical Engineering Publications Limited, 1997, pp. 27 - 56.

[91] H. Nakahara, University of British Columbia. (2012). *Pressure - Volume Diagram of the Stirling Cycle* [Online]. Available: https://people.ok.ubc.ca/jbobowsk/Stirling/how.html.

[92] H. Nakahara, University of British Columbia. (2012). *Stirling Cycle Schematic Diagram* [Online]. Available: https://people.ok.ubc.ca/jbobowsk/Stirling/how.html.

[93] W.M. Kays and A.L. London, *Compact Heat Exchangers*. 2nd ed., New York: McGraw-Hill, 1964.

[94] M. Tanaka, L. Yanashita and F. Chisaka, “Flow and heat transfer characteristics of the Stirling engine regenerator in an oscillating flow”, *JSME International Journal*, vol. 33, no. 2, pp. 283-289, 1990.

[95] H. Darcy, *Les fontaines publiques de la ville de Dijon*. Paris: Dalmont, 1856.

[96] K. Boomsma and D. Poulikakos, "The effects of compression and pore size variations on the liquid flow characteristics in metal foams", *J. Fluids Eng.*, vol. 124, no. 1, pp. 263-272, 2002.

[97] A.E. Scheidegger, *The Physics of Flows Through Porous Media*, 3rd. ed., Toronto: University of Toronto Press, 1974.

[98] G.P.J. Diedericks and J.P. Du Plessis, "Modelling of flow through homogeneous foams", *Mathematical Engineering in Industry*, vol. 6, no. 2, pp. 133-154, 1997.

[99] J. Dupuit, *Etudes Theoriques et Pratiques sur le Mouvement des Eaux*, Paris: Dunod, 1863.

[100] A. Dybbs and R.V. Edwards, "Department of Fluid, Thermal, and Aerospace Report", *Workshop on Heat and Mass Transfer in Porous Media*, FTAS/TR (Case Western Reserve University), Springfield, VA, USA, 1975, pp. 75-117.

[101] R.M. Fand, B.Y.K. Kim, A.C.C. Lam and R.T. Phan, "Resistance to the flow of fluids through simple and complex porous media whose matrices are composed of randomly packed spheres", *ASME J. Fluids Eng.*, vol. 109, no. 3, pp. 268-274, 1987.

[102] N. Dukhan and P. Patel, “Equivalent particle diameter and length scale for pressure drop in porous metals”, *Exp. Therm. Fluid Sci.*, vol. 32, no. 5, pp. 1059-1067, 2008.

[103] J.L. Lage, B.V. Antohe and D.A. Nield, “Two types of nonlinear pressure-drop versus flow-rate relation observed for saturated porous media”, *ASME J. Fluid Eng.*, vol. 119, no. 3, pp. 700-706, 1997.

[104] P. Forchheimer, "Wasserbewegung durch Boden", *Z. Ver. Deutsch. Ing.*, vol. 45, pp. 1736-1741 & 1781-1788, 1901.

[105] S. Ergun, “Fluid flow through packed columns", *Chem. Eng. Prog.*, vol. 48, no. 2, pp. 89-94, 1952.

[106] N. Dukhan, “Correlations for the pressure drop for flow through metal foam”, *Exp. Fluids*, vol. 41, no. 4, pp. 665-672, 2006.

[107] A. Bhattacharya, V.V. Calmidi and R.L. Mahajan, “Thermophysical properties of high porosity metal foams”, *International Journal of Heat and Mass Transfer*, vol. 45, no. 5, pp. 1017-1031, 2002.

[108] J.P. Bonnet, F. Topin and L. Tadrist, “Flow laws in metal foams: Compressibility and pore size effects”, *Transp Porous Med.*, vol. 73, no. 2, pp. 233-254, 2008.

[109] T.S. Zhao and P. Cheng, “Oscillatory pressure drops through a woven-screen packed column subjected to a cyclic flow”, *Cryogenics*, vol. 36, no. 5, pp. 333-341, 1996.

[110] P-H. Chen and Z-C. Chang, “Measurements of thermal performance of cryocooler regenerators using an improved single-blow method", *Int. J. Heat Mass Transf.*, vol. 40, no. 10, pp. 2341-2349, 1997.

[111] P. Du Plessis, A. Montillet, J. Comiti and J. Legrand, “Pressure drop prediction for flow through high porosity metallic foams”. *Chem. Eng. Sci.*, vol. 49, no. 21, pp. 3545-3553, 1994.

[112] K. Boomsma, D. Poulikakos and F. Zwick, “Metal foams as compact high performance heat exchangers”, *Mechanics of Materials*, vol. 35, no. 12, pp. 1161-1176, 2003.

[113] D.J. Thewsey and Y.Y. Zhao, "Thermal conductivity of porous copper manufactured by the lost carbonate sintering process", *Phys. Stat. Sol. A*, vol. 205, no. 5, pp. 1126-1131, 2008.

[114] B.Q. Li and X. Lu, "The effect of pore structure on the electrical conductivity of Ti". *Transport in Porous Media*, vol. 87, no. 1, pp. 179-189, 2011.

[115] H. Chen, C. Chang and J. Huang, "Effect of oversize in wire-screen matrix to the matrix holding tube on regenerator thermal performance", *Cryogenics*, vol. 36, no. 5, pp. 365-372, 1996.

[116] C.Y. Zhao, “Review on thermal transport in high porosity cellular metal foams with open cells", *Int. J. Heat Mass Transf.*, vol. 55, no. 13 and 14, pp. 3618-3632, 2012.

[117] T.E.W. Schumann, “Heat transfer: A liquid flowing through a porous prism", *J. Franklin Inst.*, vol. 208, no. 3, pp. 405-416, 1929.

[118] H. Hausen, *Heat transfer in counterflow, parallel flow and cross flow*. New York: McGraw Hill, 1983.

[119] K. Krishnakumar, A.K. John and G. Venkatarathnam, "A review on transient test techniques for obtaining heat transfer design data of compact heat exchanger surfaces", *Experimental Thermal and Fluid Science*, vol. 35, no. 4, pp. 738-743, 2011.

[120] F. Barari, E.M. Elizondo Luna, R. Goodall and R. Woolley, "Metal foam regenerators; heat transfer and storage in porous metals", *J. Mater. Res.*, vol. 28, pp. 2474-2482, 2013.

[121] Z.H. Cai, M.L. Li, Y.W. Wu and H.S. Ren, "A modified selected point matching technique for testing compact heat exchanger surfaces", *Int. J. Heat Mass Transfer*, vol. 27, no. 7, pp. 971-978, 1984.

[122] C.C. Furnas, "Heat transfer from a gas stream to a bed of broken solids", Ind. Eng. Chem., vol. 22, no. 1, pp. 26-31,1931.

[123] G.L. Locke, *Heat transfer and flow friction characteristics of porous solids*. Stanford, CA, USA: Stanford University. Dept. of Mechanical Engineering, 1950.

[124] J.E. Coppage and A.L. London, “Heat transfer and flow friction characteristics of porous media", *Chem. Eng. Prog.*, vol. 52, no. 2, pp. 57-63, 1956.

[125] L.-S. Tong and A.L. London, “Heat transfer and flow friction characteristics of woven-screen and crossed-rod matrices", *Trans. ASME*, vol. 79, no. 10, pp. 1558-1570, 1957.

[126] C. Chang, S. Hung, P. Ding and H. Chen, “Experimental evaluation of thermal performance of Gifford-McMahon regenerator using an improved single-blow model with radial conduction", *Int. J. Heat Mass Transf.*, vol. 42, no. 3, pp. 405-413, 1999.

[127] L.B. Younis and R. Viskanta, “Experimental determination of the volumetric heat transfer coefficient between stream of air and ceramic foam", *Int. J. Heat Mass Transf.*, vol. 36, no. 6, pp. 1425-1434, 1993.

[128] X. Fu, R. Viskanta and J.P. Gore, “Measurement and correlation of volumetric heat transfer coefficients of cellular ceramics", *Exp. Therm. Fluid Sci.*, vol. 17, no. 4, pp. 285-293, 1998.

[129] P.-H. Chen and Z.-C. Chang, “An improved model for the single-blow measurement including the non-adiabatic side wall effect", *Int. Commun. Heat Mass Transf.*, vol. 23, no. 1, pp. 55-68, 1996.

[130] R.I. Loehrke, “Evaluating the results of the single-blow transient heat exchanger test", *Exp. Therm. Fluid Sci.*, vol. 3, no. 6, pp. 574-580, 1990.

[131] F.W. Schmidt and A.J. Willmott, *Thermal Energy Storage and Regeneration*. New York, NY, USA: Mc Graw-Hill, 1981.

[132] G.F. Kohlmayr, “Exact maximum slopes for transient matrix heat-transfer testing", *Int. J. Heat Mass Transf.*, vol. 9, no. 7, pp. 671-680, 1966.

[133] C.Y. Liang and W.J. Yang, “Modified single-blow technique for performance evaluation on heat transfer surfaces", *ASME J. Heat Transf.*, vol. 97, no. 1, pp. 16-21, 1975.

[134] R.S. Mullisen and I.R. Loehrke, “A transient heat exchanger evaluation test for arbitrary fluid inlet temperature variation and longitudinal core conduction", *ASME J. Heat Transf.*, vol. 108, no. 2, pp. 370-376, 1986.

[135] R.E. Sonntag, C. Borgnakke and G.J. Van Wylen, *Fundamentals of Thermodynamics*. 5th. ed., New York, NY, USA: John Wiley & Sons Inc., 1998.

[136] P.F. Pucci, C.P. Howard and C.H. Piersall, “The single-blow transient testing technique for compact heat exchanger surfaces", *ASME J. Eng. Power*, vol. 89, no. 1, pp. 29-40, 1967.

[137] J.D. Hoffman, *Numerical Methods for Engineers and Scientists*. 2nd. ed., New York, NY, USA: Marcel Dekker, 2001.

[138] S.C. Chapra and R.P. Canale, *Numerical Methods for Engineers*. 5th Ed., Singapore: McGraw Hill, 2006.

[139] F. Darabi, “Heat and momentum transfer in packed beds", Ph.D. thesis, Leeds University, United Kingdom, 1982.

[140] B.S. Baclic, D.D. Gvozdenac and D. Vadlja, “Performance identification of the apparatus for testing compact heat exchanger surfaces", *ASME Adv. Heat Exch. Des.*, vol. 66, pp. 13-20, 1986.

[141] P.J. Heggs and D. Burns, “Single-blow experimental prediction of heat transfer coefficients a comparison of four commonly used techniques", *Exp. Therm. Fluid Sci.*, vol. 1, no. 3, pp. 243-251, 1988.

[142] K. Shaji and S.K. Das, “The effect of flow maldistribution on the evaluation of axial dispersion and thermal performance during the single-blow testing of plate heat exchangers", *Int. J. Heat Mass Transf.*, vol. 53, no. 7 and 8, pp. 1591-1602, 2010.

[143] J. Zhou, C. Mercer and W.O. Soboyejo, “An investigation of the microstructure and strength of open-cell 6010 aluminum foam”, *Metall. Mater. Trans.*, vol. 33, no. 5, pp. 1413-1427, 2002.

[144] X. Ma, A. Peyton and Y. Zhao, "Measurement of the electrical conductivity of open-celled aluminium foam using non-contact eddy current techniques", *NDT & E International*, vol. 38, no. 5, pp. 359-367, 2005.

[145] M.A. El-Hadek and S. Kaytbay, "Mechanical and physical characterization of copper foam", *Int. J. Mech. Mater. Des.*, vol. 4, no. 1, pp. 63-69, 2008.

[146] C.-F. Li and Z.-G. Zhu, "Apparent electrical conductivity of porous titanium prepared by the powder metallurgy method", *Chinese Phys. Lett.*, vol. 22, no. 10, pp. 2647-2650, 2005.

[147] J. Banhart, “Properties and applications of cast aluminium sponges", *Advanced Engineering Materials*, vol. 2, no. 4, pp.188-191, 2000.

[148] H. Seliger and U. Deuther, "Die Herstellung von Schaum und Zell aluminium". *Feiburger Forschungshefte*. vol. 1, pp. 103-129, 1965.

[149] E.M. Elizondo Luna, F. Barari, R. Woolley and R. Goodall "Casting protocols for the production of open cell aluminum foams by the replication technique and the effect on porosity", *J. Vis. Exp.*, vol. 94, no. e52268, pp. 1-12, 2014.

[150] R. Goodall, J.-F. Despois and A. Mortensen, “Sintering of NaCl powder: Mechanisms and first stage kinetics", *J. Eur. Ceram. Soc.*, vol. 26, no. 16, pp. 3487-3497, 2006.

[151] G.Y. Zaragoza Reyes “Aluminium Foams For Heat Transfer Applications", Ph.D. thesis, Dept. of Mat. Sci. and Eng., The University of Sheffield, United Kingdom, 2012.

[152] T. Abdulla, “The Effect of Pulsed Bipolar Plasma Electrolytic Oxidation Coatings on the Mechanical Properties of Open Cell Aluminium Foams", Ph.D. thesis, Dept. of Mat. Sci. and Eng., The University of Sheffield, United Kingdom, 2013.

[153] D.G. Eskin, L. Katgerman, Suyitno and J.F. Mooney, "Contraction of aluminum alloys during and after solidification", *Metallurgical and Materials Transactions A*, vol. 35, no. 4, pp. 1325-1335, 2004.

[154] E. Hernandez-Nava, C. Smith, F. Derguti, S. Tammas-Williams, F. Leonard, P. Withers, I. Todd and R. Goodall, "The effect of density and feature size on mechanical properties of isostructural metallic foams produced by additive manufacturing", *Acta Materialia* vol. 85, pp. 387-395, 2015.

[155] D. Tsarouchas and A. Markaki, "Extraction of fibre network architecture by X-ray tomography and prediction of elastic properties using an affine analytical model", *Acta Materialia*, vol. 59, no. 18, pp. 6989-7002, 2011.

[156] S.S. Al-Bermani, "An investigation into microstructure and microstructural control of additive layer manufactured Ti-6Al-4V by electron beam melting", Ph.D. thesis, Dept. of Mat. Sci. and Eng., The University of Sheffield, United Kingdom, 2011.

[157] F. Barari, "Metal foam regenerators; heat transfer and pressure drop in porous metals", Ph.D. thesis, Dept. of Mechanical Eng., The University of Sheffield, United Kingdom, 2014.

[158] *Measurement of fluid flow by means of pressure differential devices*, BS EN ISO 5167-1:1997, 1992.

[159] H.T. Aichlmayer and F.A. Kulacki, “The effective thermal conductivity of saturated porous media", *Adv. Heat Transf.*, vol. 39, no. C, pp. 377-460, 2006.

[160] K. Boomsma and D. Poulikakos, “On the effective thermal conductivity of a three - dimensionally structured fluid-saturated metal foam", *Int. J. Heat Mass Transf.*, vol. 44, no. 4, pp. 827-836, 2001.

[161] E.G. Alexander, *Structure-property relationships in heat pipe wicking materials*. Raleigh, NC, USA: North Carolina State University, 1972.

[162] E. Sadeghi, S. Hsieh and M. Bahrami. "Thermal contact resistance at a metal foam-solid surface interface". in *ASME/JSME 2011 8th Thermal Engineering Joint Conference*, Honolulu, HI, USA, 2011.

[163] B. Manshoor, N. Ihsak and A. Khalid, "Experimental study of the metal foam flow conditioner for orifice plate flowmeters", *World Academy of Science, Engineering and Technology*, vol. 6, pp. 1307-1310, 2012.

[164] F.E. Grubbs, "Sample criteria for testing outlying observations". *Annals of Mathematical Statistics*, vol. 21, no. 1, pp. 27-58, 1950.

[165] S. Makridakis, S.C. Wheelwright and R.J. Hyndman, *Forecasting: methods and applications*, 3rd. ed. New York, NY, USA: John Wiley & Sons Inc., 1998.

[166] MathWorks, *Curve Fitting Toolbox User's Guide*. Natick, MA, USA: The MathWorks, Inc., 2002.

[167] N.R. Draper and H. Smith, *Applied Regression Analysis*, 3rd. ed. New York, NY, USA: John Wiley & Sons Inc., 1998.

[168] S.A. Glantz and B.K. Slinker, *Primer of Applied Regression & Analysis of Variance*, 2nd. ed. New York, NY, USA: McGraw-Hill, 2001.

[169] J.O. Osorio-Hernández, M.A. Suarez, Goodall, G.A. Lara-Rodriguez, I. Alfonso and I.A. Figueroa, "Manufacturing of open-cell Mg foams by replication process and mechanical properties". *Materials and Design*, vol. 64, pp. 163-141, 2014.

[170] A. Mortensen and I. Jin, "Solidification processing of metal matrix composites", *International Materials Reviews*, vol. 37, no. 3, pp. 101-128, 1992.

[171] J.-M. Hugo, E. Brun and F. Topin, "Metal foam effective transport properties". in *Evaporation, Condensation and Heat Transfer*, A. Ahsan, Ed., InTech, 2011, pp. 279-303.

[172] V.A. Patil and J.A. Liburdy, "Turbulent flow characteristics in a randomly packed porous bed based on particle image velocimetry measurements", *Physics of Fluids*, vol. 25, no. 4, pp. 043304 - 1 to 043304 - 23, 2013.

[173] R.A. Wirtz, C. Li, J.-W. Park and J. Xu, "High Performance Woven Mesh Heat Exchangers". *Mechanical Engineering Dept. University of Nevada.* Reno, NV, USA, pp. 1-7, 2002.

[174] S. Lowell and J.E. Shields, *Powder Surface Area and Porosity*, 2nd. ed. London: Chapman and Hall, 1984.

[175] A. Elsner, A. Wagner, T. Aste, H. Hermann and D. Stoyan, “Specific surface area and volume fraction of the cherry-pit model with packed pits", *J. Phys. Chem. B*, vol. 113, no. 22, pp. 7780-7784, 2009.

[176] S.Y. Kim, J.W. Paek and B.H. Kang, "Flow and heat transfer correlations for porous fin in a plate-fin heat exchanger", *J. Heat Transfer*, vol. 122, no. 3, pp. 572-578, 2000.

[177] J.L. Sommer and A. Mortensen, "Forced unidirectional infiltration in deformable porous media", *J. Fluid Mech.*, vol. 311, pp. 193-215, 1996.

[178] J.W. Paek, B.H. Kang, S.Y. Kim and J.M. Hyun, "Effective Thermal Conductivity and Permeability of Aluminum Foam Materials", *Int. J. Thermophysics*, vol. 21, pp. 453-463, 2000.

[179] J.G. Fourie and J.P. Du Plessis, "Pressure drop modelling in cellular metallic foams", *Chem. Eng. Science*, vol. 57, no. 14, pp. 2781-2789, 2002.

[180] CES EduPack (2014). *Nickel-titanium alloy, austenitic*. Granta Design Limited, UK, Available: www.grantadesign.com.

[181] F.M. White, *Viscous Fluid Flow*, 3rd. ed. New York, NY, USA: McGraw-Hill, 2006.

[182] G.F. Hewitt, G.L. Shires and T.R. Bott, *Process Heat Transfer*, Boca Raton, FL, USA: CRC Press, 1994.

[183] J.R. Taylor, *An Introduction to Error Analysis - The Study of Uncertainties in Physical Measurements*, 2nd. ed., USA: University Science Books, 1997.

[184] W.D. Callister, *Materials Science and Engineering: An Introduction*, 7th. ed., New York, NY, USA: John Wiley & Sons Inc., 2007, p. 717.

[185] AK Steel Corporation. (2007). *Product Data Sheet 304/304L Stainless Steel* [Online]. Available: http://www.aksteel.com/pdf/markets_products/stainless/austenitic/304_304l_data_sheet.pdf.

[186] R.G.P. International. (2013). AISI *52100 100Cr6 Chrome Steel Balls* [Online]. Available: http://www.rgpballs.com/en/products/BALLS/QUICK-SELECTION/STEEL/CHROME-STEEL/AISI-52100-100Cr6-CHROME-STEEL-BALLS.

[187] AK Steel Corporation. (2007). *Product Data Sheet 420 Stainless Steel* [Online]. Available: http://www.aksteel.com/pdf/markets_products/stainless/martensitic/420_data_sheet.pdf.

[188] AK Steel Corporation. (2007). *Product Data Sheet 316/316L Stainless Steel* [Online]. Available: http://www.aksteel.com/pdf/markets_products/stainless/austenitic/316_316l_data_sheet.pdf.

[189] M. Yan and P. Yu, "Chapter 5 - An Overview of Densification, Microstructure and Mechanical Property of Additively Manufactured Ti-6Al-4V — Comparison among Selective Laser Melting, Electron Beam Melting, Laser Metal Deposition and Selective Laser Sintering, and with Conventional Powder Metallurgy", in *Sintering Techniques of Materials*, Dr. Arunachalam Lakshmanan Ed., InTech [Online]. Available: http://www.intechopen.com/books/sintering-techniques-of-materials/an-overview-of-densification-microstructure-and-mechanical-property-of-additively-manufactured-ti-6a, 2015, pp. 77-106.

[190] H.D. Young, University Physics, 7th. ed., Reading, MA, USA: Addison Wesley, 1992, Table 15-5.

[191] M.F. Ashby and D.R.H. Jones, *Engineering Materials 2 An Introduction to Microstructures Processing and Design*, Oxford: Pergamon Press, 1986.

[192] P.G. Sheasby and R. Pinner, *The Surface Treatment and Finishing of Aluminium and Its Alloys*, 6th. ed., ASM International [Online]. Available: http://www.asminternational.org/documents/10192/1849770/06945G_Sample.pdf/9c7a7f57-5508-43fa-9d8f-3e5a2dc57ec7, 2001, p. 2.

[193] J.F. Shackelford, Y.-H. Han, S. Kim and S.-H. Kwon, *CRC Materials Science and Engineering Handbook*, 4th ed., Boca Raton, FL, USA: CRC Press, 2015, p. 32.

[194] GMS Ball Co. Ltd. (2015). *Specification AISI 52100* [Online]. Available: http://www.gmsball.co.uk/index1.php?wd=950&ht=991#.

[195] Keene, B.J. Review of data for the surface tension of pure metals. Int. Mater. Rev. 1993, 38, 157–192.

[196] A. Jinnapat and A. Kennedy, "The Manufacture and Characterisation of Aluminium Foams Made by Investment Casting Using Dissolvable Spherical Sodium Chloride Bead Preforms", *MDPI Metals*, vol. 1, pp.49-64, 2011.

[197] B. Donohue, "Developing a Good Memory: Nitinol Shape Memory Alloy", Today's Machining World, How It Works, pp. 42-48, 2009 [Online]. Available: http://jmmedical.com/images/uploads/pages/File/TMW%20 Article09-03-Shape-memory-alloys.pdf.

[198] E.L. Furman, A.B. Finkelstein and M.L. Cherny, "Permeability of Aluminium Foams Produced by Replication Casting", *MDPI Metals*, vol. 3, pp. 49-57, 2012.

[199] A. Boschetto, L. Bottini, F. Campana and L. Consorti, "Morphological Characteristics of Aluminium Foams Produced by Replication Casting", Conregno Nazionale IGF XXII, Rome, Italy, pp. 297-305, 2013.

[200] National Physical Laboratory. *Kaye & Laby Tables of Physical & Chemical Constants* [Online]. Available: http://www.kayelaby.npl.co.uk/ general_physics/2_2/2_2_3.html.[201] C. San Marchi and A. Mortensen, "Deformation of Open-Cell Aluminium Foam", *Acta Materialia*, vol. 49, pp. 3959-3969, 2001.

[202] J.F. Despois, Y. Conde, C. San Marchi and A. Mortensen, "Tensile Behavior of Replicated Aluminium Foams", *Advanced Engineering Materials*, vol. 6, No. 6, pp. 444-447, 2004.

[203] E. Artz, "The Influence of an Increasing Particle Coordination on the Densification of Spherical Powders", *Acta Metall.*, vol. 30, pp. 1883-1890, 1982.

[204] B. Dietrich, "Pressure Drop Correlation for Ceramic and Metal Sponges", *Chemical Engineering Science*, vol. 74, pp. 192-199, 2012.

[205] T.J. Lu, H.A. Stone and M.F. Ashby, "Heat Transfer in Open-Cell Metal Foams", *Acta Mater.*, vol. 46, pp. 3619-3635, 1998.

[206] R. Gheith, F. Aloui and S.B. Nasrallah, "Study of the Regenerator Constituting Material Influence on a Gamma Type Stirling Engine", *Journal of Mechanical Science and Technology*, vol. 26, No. 4, pp. 1251-1255, 2012.